Developments at the Cologne 10 MV AMS system for ^{60}Fe measurements

Inaugural-Dissertation

zur
Erlangung des Doktorgrades
der Mathematisch-Naturwissenschaftlichen Fakultät
der Universität zu Köln

vorgelegt von:

Susan Herb
aus Köln

Köln, 2022

Diese Arbeit stellt eine von der Mathematisch-Naturwissenschaftlichen Fakultät der Universität zu Köln angenommene Dissertation dar.

Berichterstatter:	Prof. Dr. Alfred Dewald
	Prof. Dr. Andreas Zilges
Tag der letzten mündlichen Prüfung:	23.08.2022

Ein guter Forscher muß nach der Wahrheit streben und wissen, daß er ihr immer nur nahe kommen kann. Er muß Tatsachen anerkennen, gleichgültig, ob diese seinem Denken und seinen Wünschen entgegenkommen oder nicht, das heißt, er muß selbstlos sein. Und er muß die Fähigkeit haben, sich über das Naturgeschehen zu wundern und es zu bewundern.

Lise Meitner

Abstract

The focus of this thesis is the development of ^{60}Fe isotopic ratio measurements with Accelerator Mass Spectrometry (AMS) at the Cologne 10 MV tandem accelerator system. Within this work an extensive range of investigations and developments of the 10 MV AMS system were conducted. These increased the reachable statistics and enables the necessary system stability to allow long-term measurements and especially low-level isotopic ratio measurements. The comparison between initial and latest conducted ^{60}Fe AMS measurements revealed a significant decrease of required measurement duration by at least 95%, a factor of 20, to 1.49 days on average for a theoretical ^{60}Fe event of a $1 \cdot 10^{-16}$ ^{60}Fe/Fe ratio. Therefore, the system is now capable of similar statistics in reasonable measurement duration as established AMS laboratories. For the first time, full reference sample sequence measurements were conducted at the system which is a mandatory criterion for a functioning AMS system. Furthermore, the data acquisition was coupled to the 10 MV AMS control system. With that, automated AMS measurements of ^{60}Fe and ^{14}C were conducted for the first time at the 10 MV AMS system.

The key component for isobar suppression of ^{60}Ni in ^{60}Fe measurements at the Cologne setup is the gas-filled magnet. For the optimization of the used gas parameters for ^{60}Fe measurements and for a deeper understanding of the inner processes of particles passing the gas-filled magnet, a wide range of investigations were conducted. Thereby, the ion beam shape of ^{60}Ni particles a from a ^{60}Fe blank material was investigated after the gas-filled magnet and for the first time within the gas-filled magnet for different gas pressures and gas types. The measurements in the gas-filled magnet investigated the beam shape and trajectory in the dispersive axis. For the first time, it was possible to measure the ions deviation from the magnet optical axis which increases with increased gas pressure to outer trajectories. In nitrogen gas, the ion widths show a characteristic shape including a minimum in comparison to the gas pressure. For the first time, it was determined that the minimum of this shape shifts for different passed gas paths. The measurements with helium gas showed smaller positional deviations from the optical axis and significantly larger widths for the measured gas pressure range. The analysis of the two-dimensional profiles after the magnet was used to determine the optimal gas settings in terms of transmission for a subsequent symmetrical detector window. From the investigations, the optimum gas parameter from the measured options is nitrogen gas at 3 mbar gas pressure. The additional measurements of the separation factor between ^{60}Fe and ^{60}Ni in dependence of different nitrogen gas pressures revealed an increase in separation factor up to a pressure of 5 mbar with increased gas pressure. Finally, the two-dimensional profile of ^{60}Fe was analyzed and compared to the available subsequent detector entrance windows. It revealed that the high transmission loss in the initially conducted ^{60}Fe measurements were caused by the size of the respective entrance window. The experiments were simulated with an in-house code, which was further developed within this thesis, and an externally available simulation code. The approaches for the in-house code including a semi-empirical approach for the mean charge

states, for inclusion of the gas density effect, and charge state distribution widths was revised. It enables sufficient qualitative and moderate quantitative agreement with the experimental values for nitrogen gas. The measured separation factors could be qualitatively reproduced by the in-house code. The investigations made clear that a general full established description of the inner processes within the gas-filled magnet is not sufficiently possible at the present state of research for a range of the required approaches. Finally, ^{60}Fe AMS measurements were developed at the 10 MV AMS system. Therefore, a characterization of the system for iron measurements was conducted. The values for the present system are comparable to values given for larger AMS systems measuring ^{60}Fe. Thereby, for the first time successful AMS measurements using the gas-filled magnet at the Cologne 10 MV setup were conducted. Furthermore, for the first time in Cologne, successful AMS measurements of ^{60}Fe reference sample sequences were achieved. Thereby, two sample sequence measurements of standard and background samples were conducted using different-sized detector entrance windows. For the smaller window a transmission from the measurement position of the stable reference isotope to the particle detector of 28.41% was achieved with a corrected background level of $^{60}\mathrm{Fe/Fe}=4.53^{+3.85}_{-1.46}\cdot10^{-15}$. With the larger window a transmission of 45.11% at a corrected background level of $^{60}\mathrm{Fe/Fe}=1.46^{+0.47}_{-0.30}\cdot10^{-14}$ was determined.

Kurzzusammenfassung

In dieser Arbeit liegt der Fokus auf der Entwicklung von ^{60}Fe-Isotopenverhältnis-Messungen mit Beschleuniger-Massenspektrometrie (AMS) am Kölner 10 MV-Tandem-Beschleuniger-AMS-System. Es wurden eine umfangreiche Reihe von Untersuchungen und Verbesserungen des AMS-Systems durchgeführt. Diese erhöhten die erreichbare Statistik und die nötige Systemstabilität, die für Langzeitmessungen von niedrigsten Isotopenverhältnissen benötigt werden. Dabei zeigte der Vergleich von initialen und aktuellen ^{60}Fe-Messungen eine Reduktion der Messzeit um mindestens 95%, einen Faktor 20, auf 1,49 Tage für ein hypothetisches ^{60}Fe-Teilchen aus einem Isotopenverhältnis von ^{60}Fe/Fe=$1 \cdot 10^{-16}$. Somit erreicht das System ähnliche Statistiken in angemessenen Messzeiten für ^{60}Fe wie größere, etablierte AMS-Labore. Mit dem aktuellen System wurden zum ersten Mal vollständige Sequenzen an Referenz- und Untergrundproben gemessen. Dies stellt ein zwingendes Kriterium für ein funktionierendes AMS-System dar. Im Zuge dieser Entwicklungen wurde die Datenaufnahme in das 10 MV-AMS-Kontrollsystem eingebunden. Damit wurden zum ersten Mal an diesem System erfolgreich automatische AMS-Messungen von ^{60}Fe und ^{14}C durchgeführt. Das Schlüsselelement zur Isobarenunterdrückung von ^{60}Ni in ^{60}Fe-Messungen am Kölner System ist der gasgefüllte Magnet. Zur Optimierung der Gasparameter für ^{60}Fe-Messungen und für ein tieferes Verständnis der Ionenstrahl-Entwicklung im gasgefüllten Magneten wurde ein ^{60}Ni-Teilchenstrahl aus einer ^{60}Fe-Untergrundprobe hinter und zum ersten Mal im gasgefüllten Magneten für verschiedene Gastypen und Gasdrücke untersucht. Innerhalb des Magneten wurde das dispersive Ionenstahlprofil und dessen Trajektorie vermessen, außerhalb des Magneten das zweidimensionale Ionenstahlprofil. Durch die Messungen innerhalb des Magneten wurde zum ersten Mal nachgemessen, dass ein erhöhter Gasdruck zu einer erhöhten radialen Abweichung in Richtung Außenbahn im Vergleich zur optischen Achse des Magneten führt. Die Ionenstrahlbreiten im Stickstoffgas zeigten im Vergleich zum gemessenen Druck einen charakteristischen Verlauf mit einem Minimum. Es wurde zum ersten Mal gemessen, dass sich dieses Minimum mit steigender durchlaufener Gasmenge verschiebt. Die Nutzung von Heliumgas führte zu schwächeren radialen Abweichungen und zu einer signifikanten Verbreiterung des Profils für den gemessenen Druckbereich. Aus den Messungen des zweidimensionalen Profils hinter dem Magneten konnte der optimale Gastyp und Gasdruck in Bezug auf Transmission für ein nachfolgendes, symmetrisches Detektorfenster bestimmt werden. Aus den Untersuchungen wurde von den gemessenen Optionen 3 mbar Stickstoffgas als optimale Gasoption bestimmt. Die Messung des Separationsfaktors von ^{60}Fe und ^{60}Ni in Abhängigkeit zu verschiedenen Stickstoffdrücken zeigte, dass sich die Separation bis zu einem Druck von 5 mbar mit steigendem Gasdruck erhöht. Final wurde das zweidimensionale ^{60}Fe-Profil hinter dem gasgefüllten Magneten vermessen. Dies zeigte, dass die hohen Transmissionsverluste der initial durchgeführten ^{60}Fe-Messungen durch die Größe des Detektoreingangsfensters hervorgerufen wurden. Die Experimente wurden mit einem internen, in dieser Arbeit weiterentwickeltem, Code und einem extern entwickelten Code simuliert und verglichen. Die Ansätze des internen Codes, inklusive semiem-

pirischer Formel für den mittleren Ladungszustand zur Einbeziehung des Gasdichteneffekts und der Ladungszustandsverteilungsbreite, wurden überarbeitet. Dies führte zu guter qualitativer und in weiten Bereichen auch quantitativer Übereinstimmung zu experimentellen Werten für Stickstoffgas. Der Separationsfaktor für Stickstoffgas konnte durch den intern entwickelten Code erfolgreich wiedergegeben werden. Die Untersuchungen haben gezeigt, dass eine vollständige Beschreibung der internen Prozesse im gasgefüllten Magneten mit dem aktuellen Forschungsstand nicht zufriedenstellend möglich ist. Final wurden ^{60}Fe-Messungen am 10 MV-AMS-System entwickelt. Zu diesem Zweck wurden in Voruntersuchungen die Schlüsselparameter für die Messungen bestimmt. Diese sind vergleichbar zu etablierten Messungen größerer AMS-Labore. Anschließend wurden zum ersten Mal am Kölner System erfolgreich AMS-Messungen mit einem gasgefüllten Magneten durchgeführt und darüber hinaus erfolgreich vollständige Probensequenz-AMS-Messungen von ^{60}Fe erreicht. In diesen wurden zwei Probensequenz-Messungen von Standard- und Untergrundmaterialien durchgeführt mit zwei verschieden großen Detektoreingangsfenstern. Mit dem kleinen Fenster wurde eine Transmission von 28,41% vom Messort des stabilen Referenzisotops zum Teilchendetektor erreicht, bei einem korrigierten Untergrundverhältnis von $^{60}\mathrm{Fe/Fe}=4{,}53^{+3{,}85}_{-1{,}46}\cdot10^{-15}$. Mit dem großen Fenster wurde eine Transmission von 45,11% bei einem korrigierten Untergrundverhältnis von $^{60}\mathrm{Fe/Fe}=1{,}46^{+0{,}46}_{-0{,}29}\cdot10^{-14}$ erzielt.

Contents

Acronyms in this work

ADC	Analog to digital converter
AMS	Accelerator mass spectrometry
BPM	Beam profile monitor
ERAWAST	Exotic Radionuclides from Accelerator Waste for Science and Technology
ESA	Electrostatic analyzer
FC	Faraday cup
FWHM	Full width half maximum
GFM	Gas-filled magnet
GVM	Generating voltmeter
HE	High energy
LE	Low energy
MC-ICPMS	Multicollector-Inductively Coupled Plasma Mass Spectrometry
NEC	National Electrostatic Corporation
NMR	Nuclear magnetic resonance
MC-SNICS	Multi-Cathode Source for Negative Ions by Cesium Sputtering
MLL	Maier-Leibnitz-Laboratorium
MSA	Magnetostatic analyzer
OPC	OLE for Process Control
OLE	Object Linking and Embedding
PDB	Pee Dee Belemnite
PLC	Programmable Logic Controllers
PSI	Paul-Scherrer institute
ROI	Region of interest
TCP/IP	Transmission Control Protocol/Internet Protocol
VERA	Vienna Environmental Research Accelerator
VI	Virtual instrument

1 Introduction

Accelerator mass spectrometry (AMS) is a highly sensitive technique for the determination of isotopic ratios of a rare isotope of interest in comparison to a reference isotope. The atoms or molecules of a material are, usually negatively, ionized and extracted as a defined ion beam. Thereby, a specific ion beam species is selected by use of electric and magnetic fields by its mass over charge ratio. By use of the stripping process in the accelerator, limiting molecule interferences are suppressed. Remaining mass interferences like an abundant isobar are further separated by a range of dedicated suppression techniques exploiting differences in the ion properties like the nuclear charge. The final identification of the isotope of interest is done by a differential energy loss separation in matter. Thereby, isotopic ratios down to 10^{-16} are achievable with highest efficiencies. In AMS, if a stable reference isotope is present, it is macroscopically measured in a Faraday cup (FC) while isotopes of interest are individually counted. In case of long-lived isotopes and especially for difficult to measure β-emitters, AMS is superior compared to decay counting concerning sensitivity and efficiency. These requirements are demanded in a wide range of applications in which AMS is used. Prominent examples are geology, [1], [2], environmental science, [3], nuclear waste investigations, [4] or nuclear astrophysics, [5], [6], [7]. For the latter, ^{60}Fe became an isotope of high interest for supernovae and galactic cosmic rays investigations. Thereby, the ^{60}Fe/Fe ratios are between $10^{-14} - 10^{-16}$ which is the lower limit of AMS measurement feasibility. Moreover, due to the presence of the highly abundant isobar ^{60}Ni in this mass region, ^{60}Fe is currently only measurable at largest AMS facilities, [8]. Due to the high demands in measurement qualities, successful AMS measurements of ^{60}Fe require a highly stable system. Since real sample ratios have to be measured against reference standard materials and background materials (blanks), the system must not change during related sample sequence measurements. The Cologne AMS system at the 10 MV FN tandem accelerator can be classified to the high voltage AMS facilities, even when it provides only lower acceleration voltages than facilities which formerly measured ^{60}Fe, [8], [9]. Nevertheless, it is predestined for demanding medium-mass isotope measurements in which high energies for isobar suppression are required. The AMS system was for the first time completely operated in 2018 and initial individual standard sample measurements were performed, [10]. It is therefore a young system in comparison to well established large AMS facilities.

In the beginning of this thesis, the measurement possibilities with the system were highly limited. Ion source instabilities and general instabilities in the ion transport inhibited any long-term measurements or even mandatory sample sequence measurements. In addition with the lack of reproducibility of the system, AMS measurement developments and systematic investigations for improvements were hindered for any desired isotope. For the initially performed and occasionally successful individual measurements of ^{60}Fe, an immense transmission loss of the particle beam revealed. Since these were the first performed AMS measurements with a gas-filled magnet at the system, the ion beam development inside the gas-filled magnet was not known well enough

and the ideal gas type and pressure range for the used energy range for mass 60 was not known. Additionally the in-house developed simulation code for the ion transport through the gas-filled magnet revealed implausible values for the trajectory. In combination, the first ever conducted gas-filled magnet AMS measurement of ^{60}Fe at the 10 MV AMS system revealed that a measurement duration of weeks would be necessary for even single counts of the desired lowest ratios. This thesis will report on these issues and how they were overcome to yet allow long term sample sequence measurements in general, by additional use of the gas-filled magnet and in respect to ^{60}Fe measurements in reasonable measurement times.

2 Basic Concepts

Accelerator mass spectrometry is a method for the determination of isotopic ratios of low-abundant isotopes in sample material. For mass discrimination, an interplay of magnetic and electric fields is used. They discriminate over the momentum to charge ratio $\frac{\mathrm{p}}{\mathrm{q}}$ and energy to charge ratio $\frac{\mathrm{E}}{\mathrm{q}}$ which results in a mass over charge ratio $\frac{\mathrm{m}}{\mathrm{q}}$ discrimination. In advantage over other mass spectrometry methods, AMS overcomes the limits set by molecular mass interferences by use of the stripping process in tandem accelerators. Primarily left with the discrimination of atomic mass interferences, mainly the respective stable isobars, see subsec. 2.3, AMS is capable of measuring isotopic ratios down to 10^{-16}. Thereby, the crucial values for each AMS measurement are the achievable background level and the required statistics, expressed by the measurement duration for the desired precision. Their defining values and dependencies within the measurement will be shortly explained in the following.
The AMS technique only performs relative measurements in various forms. First, the isotope of interest is measured to a reference isotope which is, if available, a stable natural abundant nuclide, that produces an electrically measurable macroscopic ion beam. Exceptions to this rule occur for example in the high mass region where no abundant isotope is present. For these, an excess of one of the rare isotopes is artificially added, which is called spiking. In every method, the isotopes are measured sequentially, whereby due to statistics reasons the most measurement time is used for the isotope of interest. Looking at the first case of an abundant reference isotope the measured isotopic ratio is defined as:

$$R_{meas.} = \frac{N_R}{N_S} \tag{2.1}$$

In this ratio, N_R is the number of particles of the rare isotope of interest and N_S the number of the stable, abundant isotope particles. The latter is calculated by:

$$N_S = \dot{N}_S \cdot t = \frac{I_S}{q \cdot e} \cdot t \tag{2.2}$$

The value N_S can be expressed as the product of particle rate $\dot{N}_S$ multiplied with the measurement time t. In a measurement, the particle rate is derived by the recorded macroscopic, electric ion beam current I_S, the chosen charge state q and the elemental charge e. As the second relativity in AMS measurements, the sample material ratio is not measured absolutely but against a reference material, so-called standard material, with a well known ratio. Additionally, within every measurement, the background is determined by measuring so called blank materials which do not contain the isotope of interest or at least in a significantly less amount. From these, a normalized background counting rate $\dot{N}_B$ can be determined. It is derived by measured background events N_B in the blank material normalized to the respective measurement time t_B and the ion beam current

for the abundant reference isotope $I_{S,B}$, see eq. 2.3a.

$$\dot{N}_B = \frac{N_B}{I_{S,B} \cdot t_B} \tag{2.3a}$$

$$N_R = N_{Ioi} - N_B = N_{Ioi} - \dot{N}_B \cdot I_S \cdot t \tag{2.3b}$$

This value is used to correct the measured isotope of interest particle number N_{Ioi} of each sample, see eq. 2.3b. For the respective number of background events N_B, the normalized background rate is multiplied by the stable reference ion current and measurement time of the respective sample. This value is finally subtracted from the measured events to result in the final background-corrected number of rare isotope particles N_R. These values are used to determine the background-corrected ratios of samples and standards. The measured and corrected standard sample ratio is then used to account for transmission loss from the stable reference isotope measurement up to the identification of the isotope of interest. This sums up transmission losses up to the detection system as well as intentional identification conditions of the isotope of interest for isobar suppression. The so-called correction factor cf is numerically described as the factor between measured isotopic ratio $R_{meas.,std.}$ and the literature value $R_{theo.,std.}$ of the reference material:

$$cf = \frac{R_{theo.,std.}}{R_{meas.,std.}} \tag{2.4}$$

Finally, the measured background level $R_{meas.,blank}$ has to be corrected by the correction factor which gives then the lower limit of the measurement:

$$R_{blank} = R_{meas.,blank} \cdot cf \tag{2.5}$$

The last two values are used to classify the developed and performed AMS measurements in this work. The upcoming chapter presents physical background theory important for understanding the used isotope identification and isobar separation and suppression techniques. Furthermore, the separation quantities are defined and the analysis for their determination is explained. A short presentation of the separation techniques used within this thesis will be given. Finally, theoretical background for the data analysis concerning uncertainty treatment in AMS and a description of the χ^2 analysis for offline data analysis is given.

2.1 Low energy ion interactions in matter

The interaction of accelerated charged particles with matter plays an important role in every field of nuclear physics using an accelerator setup. This starts with the creation of a charged ion beam, considers evocation of nuclear reactions and goes up to the detection and characterization of particles. In the case of AMS, the considered particle energies are in general too low for nuclear reactions. Therefore, this section will only deal with interactions such as energy loss as well as energy and angular straggling which are crucial for particle identification or isobar separation and

suppression techniques. Detailed explanations of theories are given if they were revised or replaced in the simulation code for the gas-filled magnet, see sec. 4.3. A special consideration will thereby be given to charge changing processes and charge state distributions in matter.

2.1.1 Energy loss

Almost any isobar separation technique used after the accelerator in AMS is based on the differential energy loss of the different isobars in matter. At the considered energies the dominant process is the electronic stopping in which the ions scatter at the Coulomb field of the target atom electrons. The first classical theoretical approach tackling the description of the energy loss was done by Bohr, [11]. This was later complemented by Bethe for the non-classical case, [12], and Bloch for a joint description of the differential energy loss $\frac{\mathrm{dE}}{\mathrm{dx}}$, [13]. For the calculation of the total energy loss over a distance d the differential energy loss has to be integrated:

$$\Delta E = \int_0^d \frac{dE}{dx}\Big(E\Big)\, dx \tag{2.6}$$

It has to be taken into account that the differential energy loss is again dependent on the respective energy. For practical use different investigations were conducted which mostly differentiate in the considered energy range and are implemented in the LISE++ software for inter- and extrapolated calculations, [14]. In the energy range around 1 MeV/u used in the AMS experiments in Cologne, the implemented codes based on Ziegler, [15], are adequate from their given applicability and used in this thesis.

2.1.2 Energy loss straggling

The energy loss straggling has a high impact on the separation quality of the detector system and leads to a worsening of the separation. It has direct influence on the separation possibilities using a gas ionization detector measuring the differential energy loss. As an indirect impact considering the gas-filled magnet the straggling in energy loss leads to wider charge change distribution, see subsec. 2.1.4, and thereby an additional spatial broadening of the beam. The straggling is defined as the mean square deviation of the occurred energy loss:

$$\Omega^2 = \Big\langle (\Delta E - \langle \Delta E \rangle)^2 \Big\rangle$$

The straggling described by Bohr was derived under the assumptions of equally distributed target atoms, fully stripped ions and that the energy loss in comparison to the incident energy can be neglected, [16]. The following formula was derived:

$$\Omega_B^2 = 4\pi \cdot Z_1^2 \cdot Z_2^2 \cdot e^2 \cdot N \cdot x \tag{2.7}$$

Thereby, Z_1 and Z_2 are the nuclear charges of projectile and target, N is the atomic density and x is the target thickness. From that, Yang, [17], derived a scaling law on the basis of calculations by Chu, [15], and empirical formulas for hydrogen as well as helium and heavy ions. Formulas were

derived for solid and gaseous targets. For the latter, the following formula is given:

$$\Omega_Y^2 = \Omega_B^2 \frac{(Z_1^{\frac{4}{3}}/Z_2^{\frac{1}{3}}) \cdot C_1 \cdot \Gamma}{(\epsilon - C_2)^2 + \Gamma^2} \tag{2.8}$$

$$\text{with } \Gamma = C_3 \cdot (1 - e^{-C_4 \epsilon}) \text{ and } \epsilon = E/Z_1^{\frac{3}{2}} \tag{2.9}$$

Thereby, sets of coefficients for atomic and molecular gases and solids are provided.

2.1.3 Angular straggling

The interaction between ions and atoms leads to spatial scattering with each collision. The type of description has to be chosen by the number of collisions. In most practical cases multiple scattering can be considered. As a reference for its definition, a value of at least 20 collisions can be found, [18]. For the energy and target thickness ranges used in AMS measurements within this thesis, the formulas derived by Green are the suitable, [19]. It is derived from the tabulated angular distributions calculated by Sigmund, [20], which are based on the theory of Meyer, [18]. The basic assumptions of the theory are homogeneity of the target material, collisions occur only between two particles in azimuthal symmetry, the energy loss is neglected and small scattering angles, less than 20°. The theory is based on a classical approach which is valid for:

$$\alpha = \frac{Z_1 \cdot Z_2}{137 \cdot \beta} > 1 \tag{2.10}$$

The value α is the Born parameter, Z_1 and Z_2 the nuclear charges of the collision partners and $\beta = \frac{v}{c}$ with v the ions velocity and c the speed of light. From that a rule for the suitable energy range can be derived, [18]:

$$E < A_1 Z_1^2 Z_2^2 \cdot 25[keV] \tag{2.11}$$

The value A_1 is the mass of the incident particle in atomic units. For the cases considered in this thesis this assumption is always valid. As an example a ^{60}Ni projectile on a nitrogen target inside the gas-filled magnet is given:

$$A_1 \cdot Z_1^2 \cdot Z_2^2 \cdot 25[keV] = 60 \cdot 28^2 \cdot 7^2 \cdot 25[keV] = 57624[MeV] \tag{2.12}$$

This value is far above any energy available at the Cologne setup. Therefore, Greens theory can be used which derived the following formula for half angles:

$$\alpha_{1/2} = 1.1 \cdot 10^{-3} \frac{Z_1 \cdot Z_2 \cdot Z}{E} \cdot \tau^N \tag{2.13}$$

$$\text{with } \tau = 41.5 \frac{T_2}{Z^2 \cdot M_2}, \tag{2.14}$$

$$Z = (Z_1^{\frac{2}{3}} + Z_2^{\frac{2}{3}})^{\frac{1}{2}}, \tag{2.15}$$

$$N = (\ln(1.03 + \tau))^{-0.115} - 0.115 \tag{2.16}$$

The value T_2 is the passed target thickness in [µg/cm^2], E is the energy of the incident particle in [MeV] and M_2 is the mass of the target in atomic mass units.

2.1.4 Charge state distribution of ions after passing matter

The investigation and prediction of charge state distributions of ions passing matter is of great importance in many applications of accelerator physics. In tandem accelerators the resulting charge state distribution after the stripper medium highly impacts the accessibility of certain energies with a statistically reasonable amount for specific isotope beams. In AMS the choice of charge state is always challenged between the need for high energies leading to higher isobar separation and high statistics for short or even reasonable measurement times. Furthermore, charge changing processes become even more crucial when using a gas-filled magnet for isobar suppression. Unless otherwise stated the following information are taken from [21] and [22]. Ions passing matter run through multiple ion atom collisions while only in a fraction of these, charge changing processes occur. The probability for a charge change in a collision is related to the total charge changing cross section σ_t which is defined by:

$$\sigma_t = \sigma_l + \sigma_c \tag{2.17}$$

The values σ_l and σ_c are the electron loss and electron capture cross sections for the collision process. The cross sections normally lay in the order of $10^{-18}\,cm^2$. A resulting charge state fraction Y_q of an ion beam passing matter is theoretically described by use of a set of coupled differential equations, see eq. 2.18. These are dependent on the passed material distance x which comprises all possible charge changing processes corresponding to the resulting charge state q.

$$\frac{dY_q(x)}{dx} = \sum_{q' \neq q} [\sigma(q', q) \cdot Y_{q'}(x) - \sigma(q, q') \cdot Y_{q'}(x)] \tag{2.18}$$

For the applications at the 10 MV AMS system, including the foil stripper and dense gases within the gas ionization detector and gas-filled magnet, the formation of charge state equilibrium is assumed. Presuming a Gaussian distribution, the fraction of a respective charge state can be calculated by:

$$F_{q,equil.} = \frac{1}{\sqrt{2\pi} \cdot d} \cdot e^{-\frac{(q-\bar{q})^2}{2 \cdot d^2}} \tag{2.19}$$

The value $\bar{q}$ is called mean equilibrium charge state and d is the width of the distribution represented by its standard deviation σ . For this case the cross section dependency on the momentary charge state can be assumed exponentially:

$$\sigma_l = A_l \cdot e^{-b_l(q-\bar{q})} \tag{2.20}$$

$$\sigma_c = A_c \cdot e^{b_c(q-\bar{q})} \tag{2.21}$$

One approach for a simplified determination, [23], takes into account that for $q = \bar{q}$, the capture and loss cross sections are equal, $\sigma_c = \sigma_l$. As a result the parameter A_c equals A_l. Since at $q = \bar{q}$, the capture cross section is equal to these parameters, $\sigma_c = A_c = A_l$, they can be calculated by using the semi-empirical capture cross section approach by Schlachter, [24]. The exponential coefficients b_l and b_c are calculated by a semi-empirical approach derived in [23]. In reality, the charge changing cross sections are dependent on the projectiles energy, the density of the target material, precisely on the time until the next collision occurs, and on the shell configurations of projectile and target.

Besides their measurements, the only way for their determination are demanding calculations, performed numerically by codes like CAPTURE and LOSS, [25], [26]. For the determination of the final charge state distribution the cross section values can be used as input parameters to codes like the BREIT code from GSI, [27]. This procedure requires the knowledge of a whole range of single and multiple electron loss and capture cross section which is time-costing using the numerical codes and experimentally often not available. A more practical approach is the determination of semi-empirical formulas. These are derived by fits over a wide range of experimental values differing between solid and diluted gaseous targets. The approach by Sayer, [28], is widely used for stripper materials:

$$q_{mean} = Z_p \cdot \left(1 - 1.03 \cdot e^{(-47.3 \cdot Z^{-0.380} \cdot \beta^{0.860})}\right) \text{ for carbon foils} \tag{2.22}$$

$$q_{mean} = Z_p \cdot \left(1 - 1.08 \cdot e^{(-80.1 \cdot Z^{-0.506} \cdot \beta^{0.996})}\right) \text{ for diluted gases} \tag{2.23}$$

While Sayer does not include target properties, besides the physical state, Dmitriev, [29], determined different coefficients in their fits for different targets. A more recent approach by Schiwietz, [30] uses general target properties in their formulas. For the latter, the approach for the calculation of the charge state distribution width should be emphasized here. An approximated formula for the reduced width w including the explicit charge state distribution width d and target nuclear charge Z_t for solids is given:

$$w = d \cdot Z_p^{-0.27} \cdot Z_t^{0.035 - 0.0009 Z_p} \cdot f(q_{mean}) \cdot f(Z_p - q_{mean}) \tag{2.24}$$

with

$$f(x) = \sqrt{\frac{x + 0.37 \cdot Z_p^{0.6}}{x}} \tag{2.25}$$

Thereby, the reduced width was measured in dependence of the remaining bound electrons, [30]. The shown measurement values within the reference can be manually parameterized for the calculation of the width d.

2.2 Isotope transmission and isobar separation

The measurement of low isotopic ratios is highly dependent on the counting statistics of the isotope of interest as well as the suppression of the isobar. Thereby, the total transmission of the system can be a limiting factor. The term transmission is defined as the percentage of the particles which are transported from one point of the system to another. The total transmission $T_{tot.}$ is defined as:

$$T_{tot.} = \prod_{i=1}^{n} T_i \tag{2.26}$$

The individual transmissions T_i describe the different transport mechanisms through the system where losses of initial target particles occur. This starts with the process from extracting the sample material as an analyzed beam species which will be referred to as the extraction efficiency. This includes the ionization efficiency of the material in the used ion source and the efficiency for the extraction as a defined ion beam. It further compromises the real ion beam transport and also

unavoidable losses by the used separation and suppression techniques. Examples for the latter are the mandatory choice of injected molecule on the low energy side or the charge state dependent beam analysis on the high energy side. The last contribution to the transmission is always the fraction of detector signals which can be clearly identified as the isotope of interest by use of data acquisition software conditions. These software cuts are individually called region of interest (ROI). This discrimination may be modified dependent on the necessary suppression of the isobar. The suppression of the interfering isobar is one of the biggest challenges in low level AMS measurements. The isobar separation S_I of an individual suppression step can be given by the factor of the isobar amount before $N_{I,\,before}$ and after $N_{I,\,after}$ the suppression step. The suppression through the system up to the detector can be given as their multiplication:

$$S_I = \left(\prod_i S_{I,i}\right) = \prod_i \frac{N_{I,\,before,i}}{N_{I,\,after,i}} \tag{2.27}$$

The isobar suppression in the detector was defined as the acceptance of the isotope of interest by the chosen ROI, $T_{Ioi,\,Det.}$, divided by the acceptance of included isobars in comparison to the total isobar amount in the spectra, $T_{I,Det.}$, [31], :

$$S_{I,\,Det.} = \frac{T_{Ioi,\,Det.}}{T_{I,\,Det.}} \tag{2.28}$$

The suppression in the final detector spectra is mainly determined by the cut-off condition for separation from the isobar and by identifying the isotope of interest. The suppression of the overall AMS system can be given as the multiplication of all suppression factors:

$$S_{tot} = \left(\prod_i S_{I,i}\right) \cdot S_{I,\,Det.} \tag{2.29}$$

Assuming Gaussian distributions for the considered signals the separation can be quantitatively described by the distance between the distribution centers and their widths. Examples of separated distributions for the one- and two-dimensional case are shown in fig. 2.1. For one-dimensional signals, e.g. from the energy loss over a certain distance, the separation factor S_f can be calculated by eq. 2.30a as proposed by Knie, [32], or by eq. 2.30b as proposed by Feuerstein, [23]. Unless otherwise stated, the value σ always refers to the σ interval of the corresponding Gaussian distribution. The first representation of the separation factor by Knie is used in this thesis for calculating the separation factor of one- and two-dimensional Gaussian distributions.

$$S_f = \frac{\mu_1 - \mu_2}{0.5 \cdot (FWHM_1 + FWHM_2)} \tag{2.30a}$$ or $$S_f = \frac{\mu_1 - \mu_2}{0.5 \cdot (\sigma_1 + \sigma_2)} \tag{2.30b}$$

In the one-dimensional case the distributions are fitted to a one-dimensional non-normalized Gaussian function which are found in two different forms:

$$gauss1d(x) = A \cdot e^{-\frac{(x-\mu)^2}{2\cdot\sigma^2}} \tag{2.31a}$$ or $$gauss1d(x) = \frac{A}{\sqrt{\sigma \cdot \pi}} \cdot e^{-\frac{(x-\mu)^2}{2\cdot\sigma^2}} \tag{2.31b}$$

Thereby, in eq. 2.31a A is the area under the Gaussian curve and in eq. 2.31b A is the height of the

curve. In the two-dimensional case the significant separation has to be determined along a specific chosen axis. Thereby, the connection line of the centers, see fig. 2.1 b), is used. Furthermore, the shape of the two-dimensional Gauss can vary from circular up to an ellipsoid shape in dependence on the considered separation quantities. The σ value is determined on the respective axis of connection and equals the length between the center of the distribution to the intersection with its σ ellipse. From that, the FWHM is determined. For fitting the two-dimensional non-normalized Gaussian the following formula is used in this thesis:

$$gauss2d(x,y) = Ae^{-a(x-\mu_x)^2-b(x-\mu_x)(y-\mu_y)-c(y-\mu_y)^2} \tag{2.32}$$

$$\text{with: } a = \left(\frac{cos^2(\theta)}{2\sigma_x^2} + \frac{sin^2(\theta)}{2\sigma_y^2}\right)$$

$$b = \left(\frac{sin(2\theta)}{2\sigma_x^2} - \frac{sin(2\theta)}{2\sigma_y^2}\right)$$

$$c = \left(\frac{sin^2(\theta)}{2\sigma_x^2} + \frac{cos^2(\theta)}{2\sigma_y^2}\right)$$

Thereby, the values refer to the center of an ellipses at (μ_x,μ_y) with its semi-axes (σ_x,σ_y) which is rotated by the angle θ. From (σ_x,σ_y) the values ($FWHM_x$, $FWHM_y$) are determined. Since the available implementation of the separation factor determination, [33], only allowed the analysis of formerly online derived spectra, it was converted to a python code which allowed the analysis of an arbitrary spectrum derived from the offline data, see the appendix 7.1.1 for the code. It has to be mentioned that the separation values are quantitative indicators for the suppression ability and helpful in the comparison to other laboratories but limited in their significance. They are unsuitable to predict if a certain background limit is feasible since the amount of isobar is several magnitudes higher and the corresponding distribution can show significant tailing.

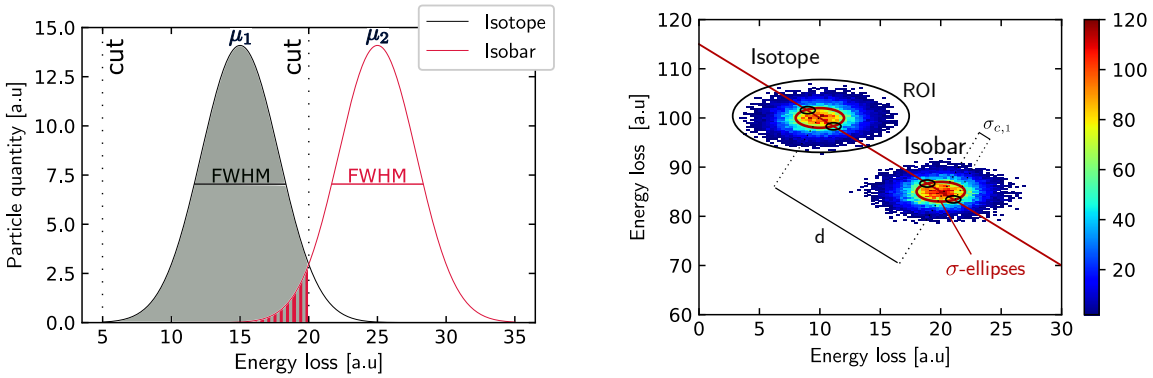

(a) (b)

Figure 2.1: Plot a) shows an example of one-dimensional Gaussian distributions representing signals of isotope and isobar in the final detector. It shows exemplary equally high distributions with $S_f = 1.5$, $T_{Ioi} = 96.13\%$ and $S_I = 24.84$ when using the indicated cuts as ROI. Plot b) shows an example of two-dimensional Gaussian distribution histograms resulting from the comparison of different separation quantities such as energy loss of different differential energy losses. Indicated are an exemplary ROI, the σ ellipses of the distributions, the connection line between the means and the intersections used for determination of the width σ_c along the connection line. The separation factor of the shown distributions is $S_f = 3.83$.

2.3 Isobar separation and suppression techniques

In comparison to other mass spectrometry techniques, the AMS technique normally does not have to deal with molecular mass interference by use of tandem accelerators since the molecular bonds are broken when passing the stripper medium in the middle of the accelerator. But even with that advantage the suppression of atomic mass interferences and especially the isobar passing all mass filters up to the detection system is a crucial challenge. This section will present isobar separation techniques which are applied concerning different sections of the setup. The focus will be on techniques used within this thesis.

2.3.1 Negative ion extraction

The ionization efficiency of different negative atoms or molecules in the ion source is a strong tool for interference suppression. In the cesium sputter ion source the ionization efficiency is selective in terms of atom and molecule type from respective materials. Therefore, the choice of extracted molecule and sample material determines the achievable ion yield. Furthermore, several magnitudes up to full suppression of the isobar is achievable. Since atomic nitrogen does not form negative ions while the atomic carbon ion yield is high, ^{14}C became the most prominent AMS nuclide. Wide investigations concerning the negative ionization properties of elements were performed by Middleton, [34]. The choice of material and extracted ion type in this thesis will be discussed in the respective sections, see subsec. 3.2.3.2 and 5.3.

2.3.2 Gas-filled magnet

The separation technique of gas-filled magnets is widely used in AMS for a range of isotopes from aluminum up to nickel to add a further isobar suppression step to the system, [35], [36], [37]. In general magnetostatic analyzers (MSA) are momentum over charge filters and electrostatic analyzers (ESA) are energy over charge filters for ion beams passing them. One way to use them for isobar suppression is to place a foil in front of these components. The isotope and isobar experience different energy loss and corresponding charge distribution formation in dependence of their nuclear charge. Subsequently, they become distinguishable by MSAs or ESAs. This process is used in the so called degrader foil technique which can be used on its own or in combination with a time-of-flight system, [10], [38]. Within this methods, transmission losses have to be accepted since only one charge state can be analyzed subsequently. Furthermore, the charge state distributions of isotope and isobar overlap and the chosen isotope charge state can experience interferences from other isobar charge states, compare [33] for stable nickel and iron. Having access to a magnet prepared for gas-mode can overcome these problems. Ions passing the entrance foil will equivalently occupy the corresponding charge state distribution. In contrast to vacuum the subsequent gas collisions lead to a recombination of the different charge states, so that the ions occupy a mean charge state on average. A scheme of both situations can be found in fig. 2.2. The reason for this is that the formation of the charge state distribution is dependent on the energy and nuclear charge but only negligible on the initial charge state, see sec. 2.1.4. On a macroscopic scale this effect manifests in the isotopes and isobars different energies and occupied mean charge states which are separated by

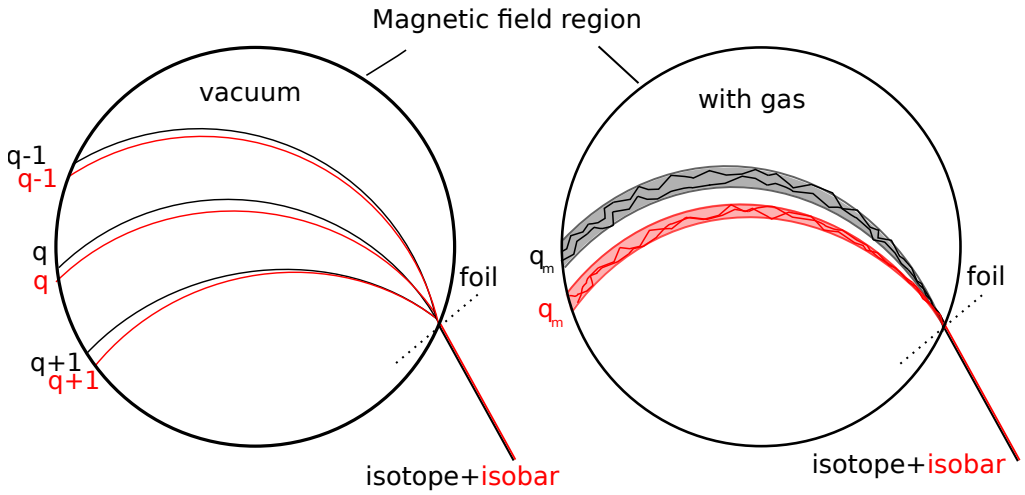

Figure 2.2: Scheme of the different behaviors of isotope and isobar passing the magnet with entrance foil in vacuum on the left or in gas-filled mode on the right. In vacuum it is displayed how the charge states produced in the entrance foil are separated due to their different magnetic rigidities. The difference in energy loss in the entrance foil causes the separation between isotope and isobar component. By use of gas-mode, it is shown how the isotopes are fluctuating around a formed mean charge state due to charge changing collisions in the gas. Since this mean charge state is energy and nuclear charge dependent but only negligible on the initial charge the different isotope charge states are recombined. Furthermore, the isobar is more significantly positionally separated due to its different energy loss and corresponding mean charge state. The subsequent energetic separation is thereby worsened by the additional energy loss.

the magnetic field. Furthermore, due to the energy loss the occupied mean charge state decreases along the flightpath through the gas. On a microscopic scale concerning an individual ion, the ion undergoes numerous collisions. Only a fraction of these collisions lead to a charge change which is dependent on the respective cross sections. The ions charge state then fluctuates around the respective mean charge state. The momentary charge state determines the momentary flight direction of the ion due to the magnetic fields impact. The charge state and corresponding direction fluctuation rate on the one side and angular straggling on gas molecules on the other side lead to a spatial broadening of the beam. A more detailed visualization of a microscopic ion path inside the gas-filled magnet can be found in subsec. 4.3.1. The recombination of the charge states allows for an increase in transmission in contrast to the degrader foil technique. On the downside the ion beam experiences significant broadening due to energy and angular straggling which impacts isobar separation negatively. Furthermore, due to the high energy loss while passing the entrance foil and gas length of the magnet as well as the detector entrance foil, the energetic separation of isobars which are not suppressed by the magnet becomes significantly worse.

2.3.3 Gas ionization detector

The last step of every AMS measurement is the particle counting of the isotope of interest. Therefore, the particles must be identified and remaining isobars and interferences have to be separated. A commonly used detector type for this application is the gas ionization detector. Like the gas-filled magnet, it is based on the difference in the differential energy loss dependent on the nuclear charge. In the gas ionization detector the differential energy loss is captured along individual gas distance

sections up to the stopping of the ion in the gas. For that, a sealed chamber containing a parallel plate capacitor setup with a segmented anode structure is used. Isobutane gas is mainly used as gas-filling. The interaction of the incoming ions with the gas releases electrons proportional to the deposited energy transferred due to the deceleration. Due to a perpendicular applied electric field the electrons are attracted to the anode structure. To compensate for the distance between the release of the electrons and the anode which would influence the measured signal height, a so called Frisch grid is used in front of the anodes. By taking the signal between anode and Frisch grid the height dependence is minimized. Besides the separation on the individual anodes, the comparison of different anode signals to each other or the complete energy signal can be used to differentiate between the signals of isobar and isotope. Comparing the energy loss of isobar and isotope over the length of the detector at ideal gas pressures, the energy loss curves show an intersection. A good differential energy loss isobar separation is then achieved by comparing the highest difference in differential energy losses before and after the intersection. Advantages of the gas ionization detector are its robustness. This is crucial if the isobar is not sufficiently suppressed beforehand. It offers a high versatility for the measurement of a wide range of incoming energies by adaption of the used gas pressure. Furthermore, due to the anode segmentation it offers multiple ΔE information whereby the differential energy loss signal can be moved along the detector by changing the gas pressure. The gas pressure variations are normally only limited by the tensile strength of the used entrance foil. The five anode gas ionization detector used in this work will be described in more detail in subsec. 3.2.2.

2.4 Data analysis

2.4.1 Uncertainty treatment in AMS measurements

Since the final isotopic ratio is derived by a variety of different values its uncertainty treatment is shortly discussed. Thereby, the uncertainty of the stable isotope current from manual read-off as well as the treatment of counting statistics in case of a low amount of events will be explained. As a systematic error the given error from the standard sample values which is based on its production and value determination, [39], [40], has to be taken into account. The presented uncertainty treatment is taken from the analysis for ^{60}Fe performed at the MLL (Maier-Leibnitz-Laboratorium), [41] [42], and adapted to the Cologne measurements.

2.4.1.1 Uncertainty of the stable isotope current determination

Within the manual measurements the stable reference isotope current is read manually from a pico-amperemeter. Thereby, a certain random error which is influenced and caused by high-frequency fluctuations during reading time and low-fluctuations due to slow drifts is unavoidable. It is hereby conservatively estimated to be around 10%. For each measurement the current is read at least twice, in the beginning, I_1, and at the end, I_2. Assuming the current does not differ highly between these read-offs also taking into account the mentioned uncertainty ($I_1 \approx I_2$), the final uncertainty can

be given as:

$$\frac{\Delta I}{I} = \frac{1}{\sqrt{2}} \cdot \frac{\Delta I_1}{I_1} = 7.1\% \tag{2.33}$$

2.4.1.2 Uncertainty in setup transmission

The transmission uncertainty in AMS measurements should compensate for long-term drifts and fluctuations of the system. For an assumption of this value the standard sample sequence measurements are considered. As an estimation for the setups transmission uncertainty, the standard deviation from the uncorrected ratios of measurements without gas-filled magnet, represented by the performed ^{14}C measurements, see subsec. 3.2.3.3, and with gas-filled magnet by the performed ^{60}Fe measurements, see subsec. 5.6.3, are used individually for each measurement type. The highest standard deviation from the different standard sample measurements is taken as a conservative approach. Therefore, the transmission uncertainty without using a gas-filled magnet is assumed to be 6% and 15% by use of the gas-filled magnet.

2.4.1.3 Uncertainty for high and low counting statistics

In counting experiments with high statistics the uncertainty for n events in an individual measurement, which is assumed to follow a Gaussian distribution, can be given as $\sqrt{n}$, [43]. In the performed AMS measurements the standard sample events uncertainty could be defined by this definition since at least 100 counts were measured. In the case of the background events, the statistics do not exceed several events per measured sample. For these the confidence intervals by Feldman et al. [44] were adapted as described in reference [41]. These are designated for small amount of events in which the counting statistics dominates the uncertainty. Additionally, the previous described uncertainties were combined by quadratic addition to 9% for the carbon measurements and 17% for the iron measurements and quadratically added to the limit values from Feldman. The results for event numbers up to $n = 20$ can be found in the appendix in subsec. 7.1.

2.4.2 χ^2 analysis

The final identification of the isotope of interest can be achieved by the investigation of individual separation values or their combination. This is usually done by defining ROIs in one- or two-dimensional spectra. As an additional useful tool the χ^2 analysis of the signals in dependence on individual separation properties like energy loss on single anodes of the gas ionization detector or position information, was used for the analysis of ^{60}Fe measurements, [41], [42]. Thereby, a standard sample measurement with clearly identifiable ^{60}Fe is used for defining the expectation values. The individual signals are assumed to be Gaussian so that the χ^2 analysis determines the deviation of the compared signals mean values to the expected mean values. It is therefore used to reduce the multi-dimensional problem of i separation information to an one-dimensional.

Within this thesis only energy loss signals within the gas ionization detector were used, so that the corresponding calculation for the χ^2 of one event takes the form:

$$\chi^2 = \sum_{i=0}^{N} \left(\frac{(E_i - \mu_i)^2}{\sigma_i^2} \right) \tag{2.34}$$

The value E_i represents the compared energy signal value of the event on an individual anode or the summed energy loss. Thereby, μ_i are the means from the given standard sample distribution signals and σ_i are corresponding σ values. The χ^2 analysis for ^{60}Fe was implemented into a python code for this thesis. The expectation values are defined by use of a high standard sample. Thereby, for each separation value one-dimensional cuts can be set graphically or taken from a priory created text file. The distribution within the cut is fitted to determine its Gaussian parameters. These are subsequently used for the χ^2 analysis. Thereby, besides the standard sample data for the expectation values, two additional measurements can be analyzed. The code delivers the respective resulting χ^2 distributions. Furthermore, it is possible to define two-dimensional spectra with a corresponding ROI and define in a rerun of the program a cut condition on the χ^2 distribution. The resulting two-dimensional spectra without cuts, with only the one-dimensional cuts and with the additional χ^2 cut can be extracted as well as the respective counts within the chosen ROI. It is furthermore possible to analyze the sum of several measurements which has to be used when investigating low statistics samples like blanks. Examples of the resulting distributions can be found in subsec. 5.6.5.5 and of the resulting spectra in the appendix in subsec. 7.4.5.

3 Experimental Setup and Developments

At the Institute for Nuclear Physics two accelerator systems are available to perform AMS measurements. The CologneAMS setup containing a 6 MV Tandetron accelerator is in routine operation for the isotopic ratio measurements of light nuclides up to aluminum and heavy nuclides like Actinides. For the coverage of nuclides in the middle mass region a new AMS setup was built at the 10 MV FN tandem accelerator which takes advantage of the higher achievable energies. All measurements performed in this thesis were conducted at the 10 MV AMS system. Therefore, this chapter is only dedicated to this setup. It will shortly present the current status of the system by presenting its layout with indicated hardware changes, the used gas ionization detectors and the control system. The larger part of this chapter will concentrate on the investigations and improvements performed at the setup. In the beginning of this thesis the system was capable of individual sample measurements of isotopic ratios. It lacked a sufficient degree of stability required for the measurement of sample sequences necessary for AMS. Furthermore, the reproducibility within measurements and moreover between measurements was often not given. This chapter will present the results of the corresponding investigations and how the former limits were overcome. The current degree of stability and reproducibility was testified within an extended test measurement and finally within a comprehensive ^{14}C standard sample sequence measurement.

3.1 The 10 MV AMS setup and control system

Over the course of several theses since 2011 a whole new AMS setup was built up at the 10 MV FN accelerator system of the University of Cologne, [45], [46], [23], [10], [33]. These theses handled the planning, the construction and the control of the AMS system as well as first tests and AMS measurements of individual standard and blank samples. In the following the layout, the gas ionization detector and the control system will be described since many developments have been introduced to these aspects.

3.1.1 Layout of the setup

AMS setups can be separated in different segments including the ion source, the low energy mass spectrometer, the accelerator, the high energy mass spectrometer and the detection system. The current layout of the 10 MV AMS system is shown in fig. 3.1 whereby all modifications made to the system during this thesis are indicated in the layout. The injector section was initially incorporated on the low energy side of the 10 MV accelerator in 2011, [45]. It contains a Multi-Cathode Source for Negative Ions by Cesium Sputtering (MC-SNICS) which can hold up to 40 samples. The ion source is followed by the low energy mass spectrometer with a 90° electrostatic analyzer (ESA)

and a 90° magnetostatic analyzer (MSA). One way to perform the switching between stable and rare isotope is changing the magnetic field. However, due to the inertia of the magnetic field the waiting for identical stable magnetic field strengths for each switch is time-costing. Therefore, the so-called bouncing method is used at the 10 MV AMS setup. Due to electric isolation of the magnet vacuum chamber a voltage can be applied for additional acceleration or deceleration of the ions in front of and after passing the magnetic field. The selected ion beam can be switched without changing the magnetic field. For macroscopic ion beam measurement, Faraday cups are placed at positions where the beam should have a waist. Within the injector two Faraday cups are used, one after the ESA (FC ESA) and one after the analyzing magnet (FC Magnet). After the injector the beam is transported through the low energy side containing different lenses and is measured in the low energy Faraday cup (FC LE). Thereby, it has to pass the switched off 20° magnet for ion beams produced by the second ion source for nuclear physics experiments and the duoplasmatron source. The upcoming accelerator is a 10 MV FN tandem accelerator from *National Electrostatics Corporation* (NEC) which is charged by use of pelletron chains. The charge reversal is done by use of carbon stripping foils. For beam times using the AMS beam line the terminal voltage stabilization is controlled by a generating volt meter (GVM) which aims to an uniformly stabilization without analyzing slits. The measured transmission with protons through the machine is around 50%, [10]. The first Faraday cup on the high energy side is positioned after the accelerator (FC HE). Subsequently the beam has to pass the switched off first high energy magnet, used for nuclear structure experiments, and enters the high energy mass spectrometer. The key elements of the high energy mass spectrometer are the second 90° analyzing magnet, in this thesis only referred to as HE analyzing magnet if not stated differently, and the 30° electrostatic analyzer. For ion-optical purpose several magnetic quadrupole lenses, mostly quadrupole doublets, are integrated. The formerly used quadrupole triplet lens was replaced by a quadrupole doublet lens required for ^{90}Sr AMS measurements[1] and is used for the carbon and latest iron measurements, see subsec. 3.2.3 and 5.6.2. For beam tuning several Faraday cups are available. The high energy magnet is followed by the analyzing cup (FC ANA) which is used for beam identification. For the measurement of the stable isotope within the AMS measurement two individual Faraday cups, referred to as offset-cups, are positioned in a dedicated chamber after the high energy analyzing magnet in the dispersive plain. This allows the measurement of the stable reference isotope without changing the accelerator voltage. They are manually set to the expected stable isotope position on the dispersive plane and can be finely positioned with dedicated piezo motors, [47]. The next Faraday cup is positioned between the quadrupole lenses prior to the ESA (FC HE I). The subsequent one is positioned after the ESA (FC HE II) and the last one prior to the gas-filled magnet (FC HE III). Different types of detection methods and setups can be used with this AMS beam line. The most basic setup is achieved by positioning the gas ionization detector after the ESA, see subsec. 3.2.3. Within this configuration it is possible to add a suppression step by additional foils integrated for the degrader foil method which were used for ^{53}Mn/^{55}Mn ratio measurements of standard material, [10]. Furthermore, two Time-of Flight detectors can be integrated into the existing setup for further separation. In 2018, a new 135° gas-filled magnet was taken into operation which in combination with the gas ionization detector builds the second detection setup used for the measurements in this thesis, [33]. For the particle transport through the gas-filled magnet one silicon detector in front of its entrance is in routinely use and two further silicon detector can be installed. Since

[1] G. Hackenberg, PhD thesis, not submitted

LE - Low energy
HE - High energy
MC SNICS - Multi-cathode source for negative ion by cesium sputtering
ESA - Electrostatic analyzer
FC - Faraday cup
EL - Einzel lens
FC Ana - Analyzing cup
BPM - Beam profile monitor
Sili - Silicon detector

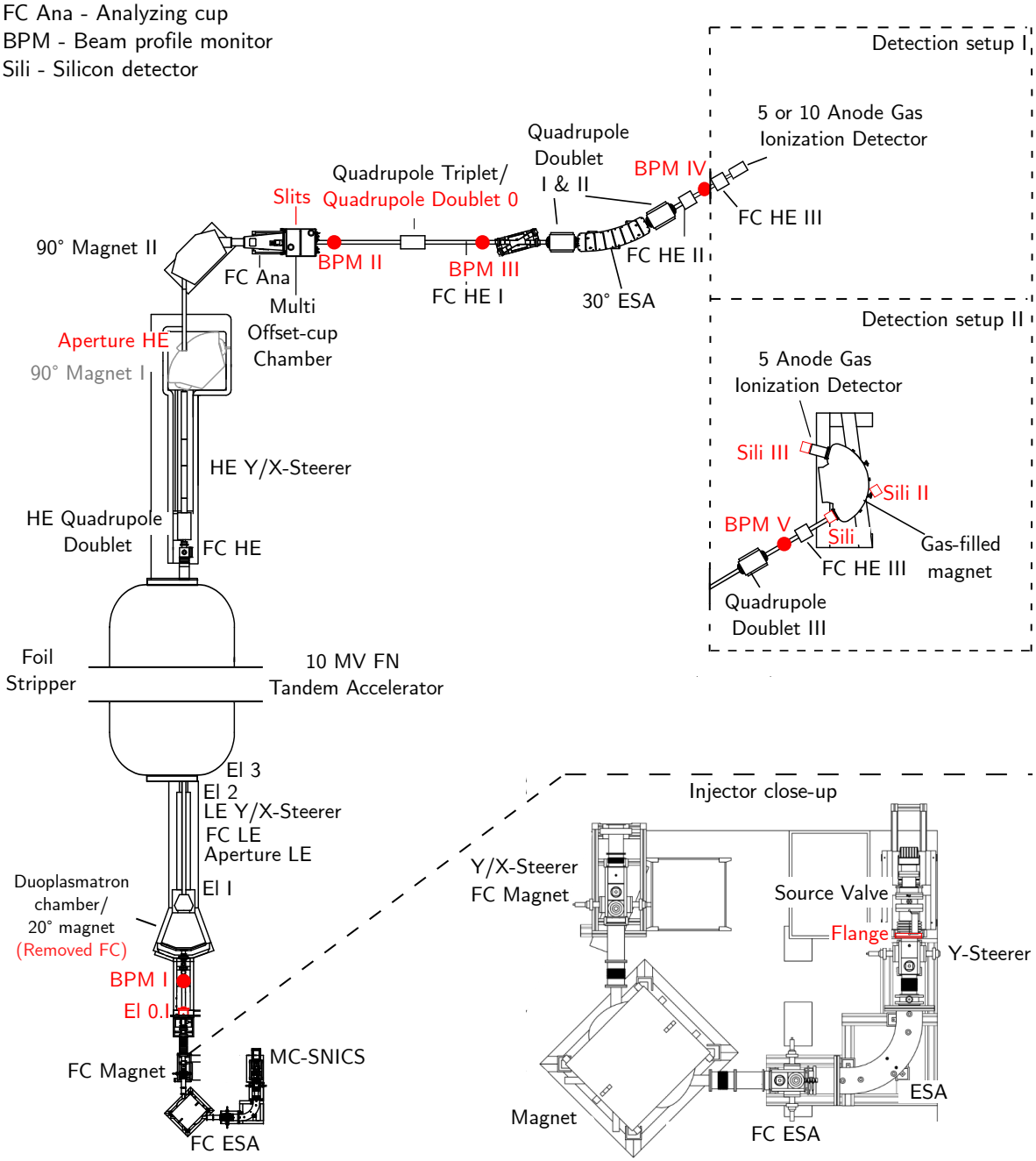

Figure 3.1: Layout of the AMS setup at the 10 MV accelerator. The red marked components are the hardware elements modified or added at the setup in this thesis described in the subsec. 3.2.1, adapted from [10]. The zoomed in injector layout was adapted from [45]. The two used detection setups requires the temporary rebuilding of the beam line at the indicated cut.

the modifications of the setup also concerns ion-optical components the current ion optics was simulated with LIMIOPTIC2, [48]. It was based on the calculations performed in [10] and adapted to the current setup. The overall setup simulation can be found in the appendix in subsec. 7.2.2. Furthermore, the code including all parameters can be found in the appendix, see subsec. 7.2.1, where all component modifications are highlighted. The parameters of the initial beam width in the simulations were conservatively assumed from phase space measurements of hafnium, [49]. Modifications with special impact on the ion optics between the former and current status are individually compared and discussed within the subsections.

3.1.2 Gas ionization detector

The gas ionization detector represents the final particle identification and counting tool in the majority of AMS setups. Recently, two different gas ionization detectors are available at the 10 MV AMS setup. When measuring after the ESA a 10 anode detector, [33], is used. In the AMS measurements with the gas-filled magnet the 5 anode gas ionization detector is used. A technical drawing can be found in fig. 3.2.

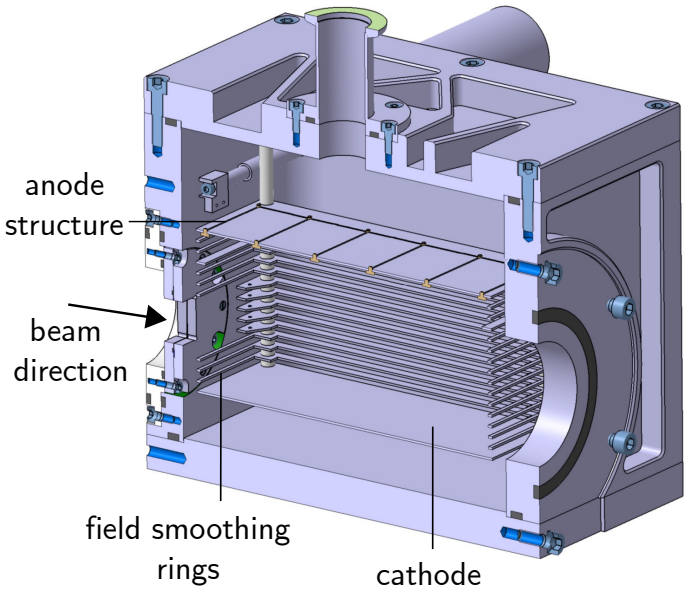

Figure 3.2: The figure shows an adapted technical drawing of the 5 anode gas ionization detector. Thereby, a vertical cut through the detector housing is displayed. The shown anode structure is the newly built with geometrically equal anodes. Two further anode structures are currently available. The beam enters the detector from the left. The entrance window can be changed by exchanging the removable holding frame.

It will be described in more detail due to the performed modifications on the layout for signal quality improvement, see subsec. 3.2.2. The 5 anode gas ionization detector formerly came with two different layouts of the anode structure and was built to fulfill a compact design for multiple installment possibilities along different beam lines, [33] and [50]. A new anode layout was introduced which consist of geometrically equal anodes. Different entrance windows can be integrated by a removable window frame at the entrance of the detector. Available windows are rectangular 8x8 mm^2, 10x10 mm^2, 12x12 mm^2, 20x20 mm^2 and a round window with a diameter of 45 mm.

Both former anode layouts featured two anodes which were split diagonally to enable position-sensitive signals. In total the vertical detector structure consists of 16 layers in total. The anode structure at the top, the Frisch grid, the cathode at the bottom and 13 layer of stainless steel rings. Each layer is separated by insulators with a spacing of 5 mm and electrically connected by according resistors. The additional rings should ensure an evenly decreased voltage for example from Frisch grid to cathode and aims for smoothing of the electric field. In the area of injection five rings have an opening for the beam to pass through. By the possibility to install slits between the entrance window, the distance between entrance and inlaying structure measures around 15 mm.

3.1.3 Control system and software

The control system of the 10 MV AMS setup was constructed and built over different theses covering the hardware components, its linkage and the user software, [45], [23]. Most of the setup hardware components can be controlled by analog or digital voltage signals and otherwise provide themselves voltage signals proportional to their set values. These function can be used to built up a computer-driven control of the setup which will be described in the following. The intersection for use of the provided signals within the software is a combination of Programmable Logic Controllers (PLC), Siemens Simatic S7-200, and an OPC (OLE (Object Linking and Embedding) for Process Control) server on the computer itself. For that, the PLCs are used to digitize the voltages and submit the data to the OPC server. This OPC server builds the interface for providing the data on the computer. Exceptions of this procedure are the low energy magnet power supplies, the gas-filled magnet power supplies and the read-back of the Faraday cup currents by Keithley 6485 Picoammeter which are connected over Ethernet. Additionally, the read-back of the offset-cup currents can be provided by a combination of a RedLab system and a current integrator, [47]. Components which are shared with the nuclear physics beam line are not integrated at the moment. The control software, the so-called Phoenix software, is written in LabView and allows the control and read-out of the connected hardware components. It provides a graphical interface and its functions were inspired on the control software used at the 6 MV AMS setup, [23]. More details of available functions are given in subsec. 3.2.4.1.

3.2 Improvement of the 10 MV AMS setup

Unlike the commercially purchased 6 MV Tandetron accelerator AMS system, the 10 MV AMS system was built up from provided sections of the university of Utrecht and additionally purchased components. Subsequently it was further developed in-house. This provides a high variety of possible developments and improvements. On the downside the setup did not show the same high degree of stability and reproducibility in the beginning necessary for long-term low level isotopic ratio measurements of sample sequences. This section will report on the encountered issues that limited the initial measurements and the current status after their investigation, resolution and further improvements. This will cover every aspect of the beam line, the ion source stability and output, the low energy mass spectrometers and high energy mass spectrometer stability, reproducibility and transmission as well as the inner detector layout. The gas-filled magnet as the new

key component was investigated separately, see chap. 4. For characterizing the current status extensive test measurements using different beam species as well as an AMS measurement of a ^{14}C sample sequence of standard and blank materials were performed. Furthermore, the incorporation of the data acquisition into the control software will be described which offers a range of new possibilities like automatic AMS measurements at the 10 MV accelerator.

3.2.1 Hardware setup developments

The AMS setup at the 10 MV accelerator is dedicated to medium mass isotopes which comes with higher difficulty in the separation and suppression of the isobar due to the lower $\frac{\delta Z}{Z}$ and $\frac{\delta m}{m}$ ratios. The most basic but mandatory prerequisite is the stability and reproducibility of the system. In the lower limits of AMS, the low counting statistics requires also high ion source output and high transmission to even enable measurements in a reasonable time. The first AMS standard material measurements of ^{60}Fe showed that the system could not fulfill the mentioned requirements over sufficient time spans, described in subsec. 5.6.1. The development procedure and the first measurements were strongly challenged and even limited, on the one side by persistent problems and on the other side by dynamically occurring problems. This concerned for the most cases the quantitative output and the stability of the ion source as well as the transport though the system.

3.2.1.1 Source stability improvement

The ion source used at the 10 MV AMS system is a Multi-Cathode Source for Negative Ions by Cesium Sputtering (MC-SNICS). The main problem of the ion source was its stability. The indicators for ion source stability is the extracted ion beam current itself and more importantly the sputter current provided by the sputter voltage power supply. While the ion beam output can also be impacted by transport mechanism, the sputter current is directly proportional to the quality of the sputter process. The first investigated effect was the long-term fluctuations of the measured ion beam current output. It was observed that the fluctuations were not dependent on the status of the sample lifespan or the sample position nor were they mirrored within the sputter current. This indicated a problem in the ion transport instead and was actually resolved within the low energy side transmission investigations in which the steerer setup was modified, see subsec. 3.2.1.2. The most dominant problem with the ion source was the behavior when newly started at the beginning of a measurement period or at the morning of a new measurement day. At its worst the ion sources output was nearly unusable for the standard ratio measurements of ^{60}Fe which are still 4 orders of magnitudes higher than the aimed real sample ratios. The following paragraphs will report on the modifications done to the ion source setup and the operation routine which in summary resolved the problematic behavior. The first modification concerns the improvement of the vacuum pumping for the ion source. The injector design intends that the directly connected small vacuum pump on top of the ion source is supported by the next larger vacuum pump in the beam line, [45]. The two vacuum sections were connected by an adapter flange with different sized diameters. Thereby, the inner diameter of the whole flange was the same as at the smaller adapter side. This flange was redesigned with an open inner structure which provides better vacuum

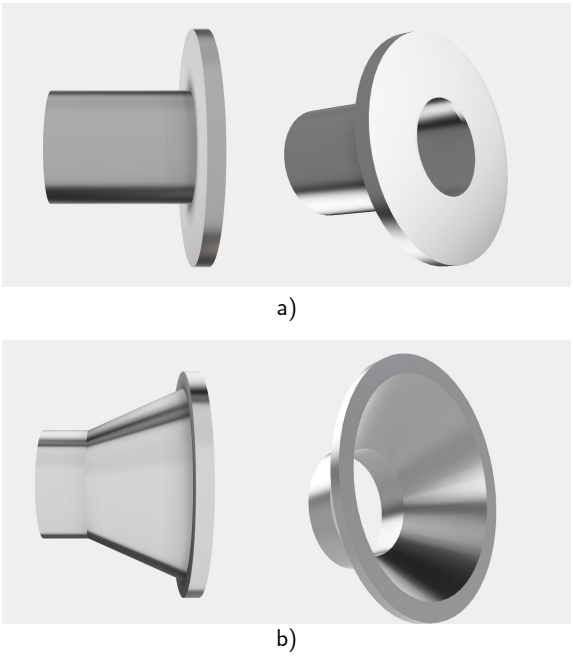

Figure 3.3: a) shows a simplified rendered visualization of the former adapter flange. b) shows a simplified rendered visualization of the redesigned adapter flange, adapted from a technical drawing, for better vacuum pumping of the sensitive source section.

pumping, see fig. 3.3. The stronger vacuum pumping power is of special importance after ion source maintenance or sample wheel replacements and especially in the process of heating up the ionizer and corresponding structures. In a next step the cesium flow continuity into the ion source was improved. Within starting the ion source, in respective heating up the ionizer and cesium oven, the ion source often showed unexpected behavior. The sputter current stayed low until the ionizer and cesium oven was heated over normal operation temperatures. A similar behavior is expected and observed after maintenance of the ion source including cesium refill when the most upper layer in the oven experiences oxidization which has to be broken up by higher temperatures, [51]. Since there was no reason for this behavior when the ion source was under vacuum before, the key parameters for possible oxidization, the vacuum and the temperature of the cesium oven structure, were investigated. At first, the valve separating the sample wheel to the remaining ion source structure, see fig. 3.1, in case of wheel replacement was deconstructed and investigated. It was deeply cleaned and its sealing ring was replaced. The vacuum tightness of this valve is one of the most important factors since vacuum-breaks near the ion source structure can lead to oxidization of the cesium reservoir and even harm or destroy the wire of the ionizer when in operation. The double-walled cesium feedthrough is indirectly heated by the ionizer from inside the source and the cesium oven located at the cesium reservoir on the other side. The current revision of the ion source does not provide additional heating of the cesium feedthrough. A cooling connection for the incorporated sealing ring was used which was also connected to the outer wall of the cesium feedthrough. For a more reliable heating of the feedthrough the formerly used water-cooling, with a temperature of 14-17°C, was disconnected. In order to preserve the sealing ring in long-term, the feedthrough should be cooled by the Syltherm XLT cooling fluid used for the sample wheel cooling which is operated at room temperature. Finally, an existing temperature sensor was mounted at the outer oven structure and integrated into the setup control system so that the cesium oven temperature can be digitally read out. This reference temperature improved the reproducibility

of the ion source behavior in terms of routine operation and breaking of built cesium oxide after refilling. Since this value is logged the comparison of temperature to ion beam output on a long time range indicates the need for cesium refill. In the matter of operating the ion source, different test measurements and the year-long experience led to changes in the routine ion source handling. The finally determined parameter set delivers the highest stable output which can be easily transported through the system, see for example the parameter set for the carbon measurements in tab. 7.3 in the appendix. A significant difference to formerly used settings, [33] and [38], is an increased ionizer current to 25 A. It was observed that a further increase of the ionizer current is still followed by an increased ion beam output. Since the actual ionizer current value is the upper limit of the manufacturer specifications, a far further increase was not tested. For the future, it is important to investigate the actual limits of the used ionizer since an increased ionizer current promises a further increase of the ion beam output. Furthermore, it can be reported that for heavy molecules like SrF_3 an even higher extraction voltage value can lead to higher analyzed ion beam output. However, it was not possible to transport the beam further through the system. It is planned to investigate this effect by simulating the source inspired by the investigation of the gas ion source at the 6 MV AMS system, [52]. Besides the quantitative differences in values, the routine for ion source handling at the beginning and during a measurement week was revised. When firstly starting up the ion source, only the ionizer is heated until the sputter current and the source output shows saturation effects. Only then the cesium oven is turned on. This led to the most reproducible way for fast stable operation at first start which is also used for the two 6 MV Tandetron accelerator ion sources[2]. Furthermore, the ion source is no longer shut down over night during measurements but held on minimal operation conditions. The ionizer is set to 21 A and the cesium oven current to 0.15 A. By that, the ion source is ready to use in about half an hour in the morning instead of 1 to 2 hours. This routine will become obsolete when measurements will be carried out continuously during beam times. In the current state the ion source runs stable and is ready to use within 1 to 2 hours when firstly started up and after half an hour after the minimal operation conditions. The ion source output is sufficiently high for reasonable measurement duration and almost only dependent on the life-span of the sample when in routine operation. The output and stability were successfully tested and will be reported and discussed in subsec. 3.2.1.5.

3.2.1.2 Low energy side transmission investigations and modifications

At the limit of AMS at isotopic ratios of 10^{-16} the overall transmission through the system is crucial to allow reasonable measurement times. In the beginning of this thesis the systems transmission was overall not sufficient for lowest isotopic ratios. Moreover, systematic investigations of the system and of the actual measurements themselves were strongly hindered by the low energy side transmission reproducibility and stability. The dominant transmission loss and instabilities occurred from the FC Magnet up to the FC LE. Typical transmissions ranged between 30% and 55%. The rarely achieved better transmission values could not be reproduced between individual days of measurement, nor did it stay stable over the course of a complete measurement day. For the investigation of the quantitative beam transport problems, the key parameters are the beam position and its shape. Routinely used components for this type of diagnostic are movable slits and apertures which in combination with an additional Faraday cup enable conclusions about

[2]Dr. S. Heinze and Dr. A. Stolz, Private communication

beam size, position and rudimentary about the shape. Due to given limits in its interpretation, more sophisticated beam diagnostic tools were required. In the following it will be reported on the performed investigations and the corresponding modifications to the system which currently allows high, stable and reproducible transmission which was testified in subsec. 3.2.1.5. In the following, the beam direction will be identified as z-axis, the dispersive axis will be called x-axis and the remaining perpendicular direction y-axis. Initially, the ion beam spot was visualized by use of a quartz crystals which illuminate at beam exposure due to scintillation effects. Therefore, two crystals were installed on the low energy side, the first in front the duoplasmatron chamber and the second one after the FC LE to allow independent investigation of injector components and remaining low energy side components. The crystals were mounted under 45° with respect to the beam direction which allowed its inspection with a camera set up under 45°. For the investigation the beam was cut in x-direction by the slits after the low energy magnet since it was not possible to produce a sharp beam spot on either of the two crystals. The cut beam was pictured centrally on the first crystal. By this the achieved transmission to the next Faraday cup within the duoplasmatron chamber was only 10% although no further ion optical component lies in between. By use of an additional steerer between crystal and duoplasmatron chamber the transmission could be increased up to 50%. By a trace of the steerer a double peak structure was observed. The addition of both peaks resulted in 90% transmission of the initial beam. Therefore, the setup was simplified by replacing the quadrupole triplet lens at the end of the injector by an einzel lens. With this modification the double peak structure could be eliminated. This effect could have been caused by passing the quadrupole lens with a prior misaligned beam, [53]. By calculating the magnetic potential of an assumed quadrupole field for an initial misaligned beam it can be seen that while the original higher order field is still preserved additional lower order terms in the potential appears. This so called spill-down effect can explain further misalignment and distortion in the focusing. With the simplification and a tuning procedure using the first quartz as a starting point and then respectively to the ion beam current on the FC LE, the transmission was increased over 84%. For a more sophisticated further investigation and to ensure that the beam is injected straightly into the subsequent low energy einzel lens a beam profile monitor (BPM) was installed between the injector einzel lens and the 20° magnet. Its layout and functionality is described in more detail in subsec. 3.2.1.4. The second problem which had to be tackled was the instability of the low energy side transmission again between the FC Magnet and the FC LE which was not resolved by the prior modifications. Since these fluctuations could be already observed on the BPM the origin had to be in the injector. Due to former reported power supply instabilities of the ESA for large ion beam output from the source, [46], it was decided to connect additional resistors in parallel to the power supply since it needs a certain load for its control mode. Subsequently, it revealed that the fluctuations disappeared by shortening of the injector steerer units. Therefore, the electrostatic analyzer and the electrically isolated magnet vacuum chamber could be excluded as candidates. Until this point in each steerer unit one plate was set on ground and one was set on potential. If the polarity of the steerer unit was set to the opposite polarity, the plate formerly on ground was set on the opposite potential polarity and the plate formerly on potential was set on ground. The potentials with different polarities were provided by the same power supply. The switchover between the power units at the zero position for the steerer voltages was not clearly defined at 0 V and the units overall showed instabilities. Therefore, for each steerer pair a new sufficiently stable power supply was integrated. They deliver voltages with negative polarity for

one of the plates from 0 to -500 V for each steerer pair respectively. The other plate in each steerer pair is charged by one single power supply providing -250 V. The resulting applicable potential difference is ±250 V. As an additional candidate for unintentional charging and according steering the intermediate Faraday cup inside the duoplasmatron chamber was removed since it was not used anymore. With these modifications, by use of the newly installed BPM and by use of the bigger aperture on the low energy side of 7 mm, a reproducible and stable transmission of nearly 100% is achieved for masses up to the iron oxide range, see subsec. 3.2.1.5.

3.2.1.3 New defined focal points and new effective radius measurement

The transmission of analyzed beams in AMS is divided into two sections. The first part is the transmission up to the position of the stable reference isotope measurement, in case of the 10 MV setup at the offset-cups. It includes the low energy side transmission and the transmission through the accelerator and the first section of the high energy side. The second section is from the offset-cups up to the detection setup which is expressed as the correction factor. The latter is used for correcting real sample measurements by use of standard samples with well-known isotopic ratios. In the first measurements a high transmission on the high energy side was not reproducible. Nevertheless, high transmission could be again achieved with adapted values. An exception was the transmission from the FC HE II up to the FC HE III, which hardly showed good transmission and will be discussed in more detail in subsec. 3.2.1.4. It was assumed that the low reproducibility of the high energy mass spectrometer was caused by the fact that the trajectory through the high energy magnet could not be defined reproducible enough. Since neither the injection nor the ejection was clearly defined by slits or similar components the chosen beam energy was as well not well-defined. This directly influences the reproducibility of further components. Therefore, it was decided to build a structure for fixed focal point definition and accordingly define the effective magnetic radius for the newly fixated trajectory. The successful transport of the ion beam is grounded on the principle of conserving image attributes between points where waists of the beam should be created. Concerning the magnetic sector field a point-to-point image is produced by choosing the object distance equal to the image distance which is chosen to the double radius, $d = 2\rho$. For the second high energy magnet the effective radius was previously determined to 1101(1) mm, [10]. Thereby, the ideal object point of the system would lay inside the vacuum chamber of the first 90° high energy magnet for nuclear physics which is complicated to conduct and therefore formerly not installed. It was decided to implement an aperture system in a t-cross flange closely after the first analyzing magnet. The aperture system consists of a tantalum metal sheet with an area of 4 cm x 3 cm with two round apertures with 3 mm and 5 mm diameter. It is mounted on a manually movable feedthrough. The aperture was aligned by the procedure described in [10]. For the image point, remote-controlled electrically movable slits in front of the plane in which the offset-cups lay were installed[3]. The ion optics simulation of the ideal case and the current case with the shifted focal point can be found in fig. 3.4. With these new components the effective radius of the ions fixated trajectory through the magnet was remeasured. In equivalent to the procedure in [10] a well-defined proton beam was used. For that, the beam was firstly analyzed with the second high energy magnet to ensure that no remaining magnetic field from the first analyzing magnet is affecting the measurement. Therefore, an additional Faraday cup was installed on the

[3]G. Hackenberg, PhD thesis, not submitted

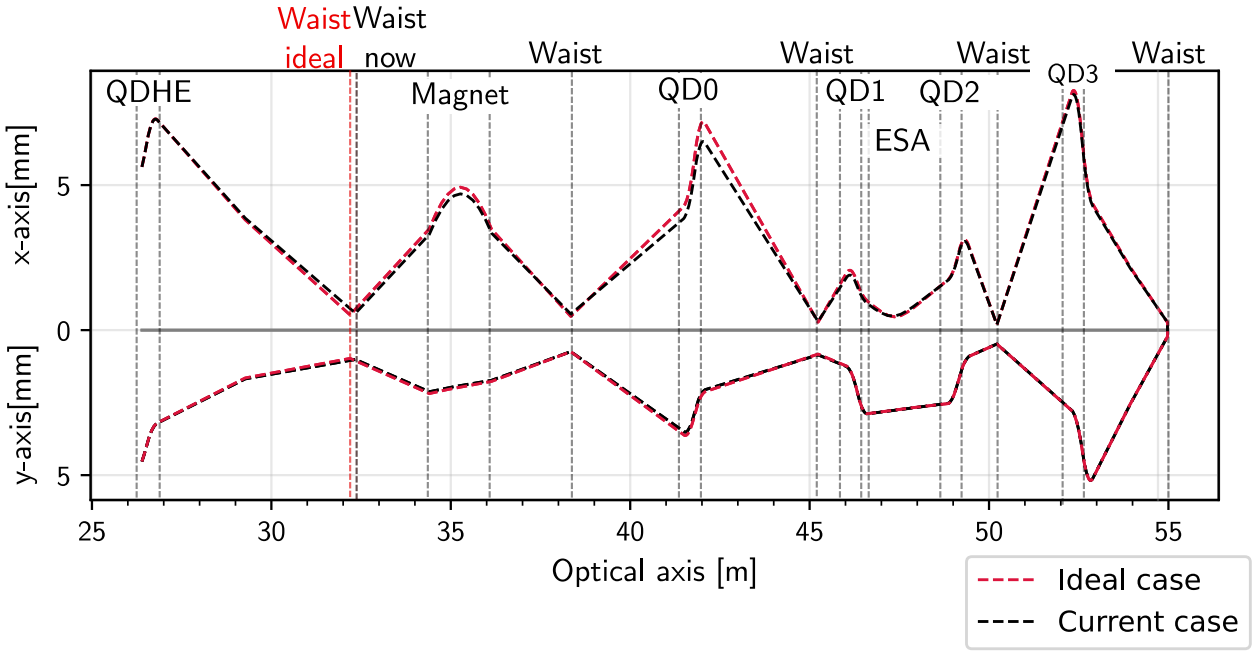

Figure 3.4: Comparison between the ion-optic simulations by LIMIOPTIC2 with ideal and shifted focal point in front of the second analyzing magnet. The lines represent the outer envelopes of the simulated beam for the dispersive x-axis on the upper half and non-dispersive y-axis on the lower half, where the red line shows the case of the optimal positions object point and the black line with the currently defined object point. For this, the optimization procedure of LIMIOPTIC2 was used to define the best focused beam for both cases.

optical axis on the plane of the offset-cups to make use of the newly installed analyzing slits. For the measurement, the small aperture was used and the analyzing slits were equivalently set to ±1.5 mm. The corresponding magnetic field was measured by a nuclear magnetic resonance (NMR) probe and the value was noted. Subsequently, the beam was analyzed at the first high energy magnet with the slits before and after the magnet opened to ±1.5 mm. Its effective radius is well-defined to 1016 mm which was determined by an energy calibration using a resonance in the ^{27}Al(p,γ)^{28}Si reaction, [54]. Equivalently the magnetic field was measured by a NMR probe and its value was noted. With these information, the exact proton energy and therefore the offset of the terminal voltage to the currently displayed value was determined. The proton beam energy was 14.39 MeV at a displayed terminal voltage of 6.97 MV. Including the injection energy of 92.5 kV, an offset to the real terminal voltage of -180 kV in this measurement is calculated. The effective radius of the second high energy analyzing magnet with the new fixated-trajectory-defining components was determined to 1103.9(14) mm. The measurement values can be found in tab. 3.1. With the performed simulation of optimized beam transport, it can be observed that the beam is slightly larger at the object point for the shifted position. The rigidity resolution Δ_{min} can be derived by the ion beams transfer matrix assuming a double focusing magnetic sector field with additional drift path, [55]. It is respectively calculated by eq. 3.1, [45].

$$\Delta_{min} = -\frac{x_0}{2\rho_0} \tag{3.1}$$

With the values from the simulations and the new radius, the absolutes of the rigidity resolution for the ideal case is $|\Delta_{min}|$=0.236‰ and for the current case only slightly higher with $|\Delta_{min}|$=0.263‰.

Ion	E[MeV]	Magnet	B[G]	Effective radius[mm]
p	14.39	1	5413(11)	1016 [4]
		2 (New Value)	4982(7)	1103.9(14)
		2 (Old Value)		1101(1)

Table 3.1: The table shows the measured magnetic field values for a proton beam on the corresponding beam axis for each magnet at a beam energy of 14.39 MeV. The energy was defined by the magnetic field of the first magnet since its effective radius is precisely defined. With the energy and the magnetic field of the second magnet the measured effective radius with the newly fixated focal points was determined. The errors of the magnetic field are dominated and determined by the measured beam width. For comparison the old determined value of the effective radius is given.

3.2.1.4 High energy side transmission improvements

Through the installation of the trajectory fixing components, injection aperture and analyzing slits, and the definition of the magnetic effective radius from the corresponding fixated ion beam curve, the magnetic field calculation became more reliable and reproducible. As a further result the reproducibility of subsequent ion-optical settings is also improved. The second irregularity in beam transport was the difficulty to achieve reproducible high transmission through the last quadrupole lens between FC HE II and FC HE III. For its investigation and for further general routine ion beam inspection, it was decided to integrate additional beam profile monitors into the beam line which will be shortly described. The used system is the BPM system 5000 from *Danfysik* which includes the BPM unit 517, the corresponding preamplifier and the BPM electronics 519 which can handle two BPM signals. The BPM consists of an ellipsoidal formed tungsten wire loop, see fig. 3.5 a) which rotates with a frequency of 25 Hz. It passes two positions per rotation in which it measures the x-fraction of the beam while it is aligned with the x-axis and vice versa with the y-axis, see fig. 3.5 b). The resulting electric signal can be read out by an oscilloscope which shows two separated signals each corresponding to one axis. An example of the signals can be seen in fig. 3.5 c). The signals give qualitative information about beam shape and beam position. A centered symmetrical beam will form one single symmetrical signal per axis. A deviation from the center is expressed by a second peak appearing while asymmetries are mirrored within each respective signal shape symmetry. Furthermore, the signal width is proportional to the beam width. The BPM systems were already available but not ready for use. Within this thesis 5 beam profile monitors were put into operation and integrated in the beam line, see fig. 3.1. The investigations with the BPM revealed that using quadrupole lens settings that lead to a centered symmetric beam up to the BPM before quadrupole lens III hindered high transmission between the surrounding two Faraday cups. The last BPM after quadrupole lens III showed that it was not possible to create a symmetric beam but that the beam is skewed in one of the directions dependent on the set quadrupole lens values. An irregularity was found by investigation of the interplay of the different high energy mass spectrometer quadrupole lens patterns. The pole pattern of the lenses of the former sections including the first quadrupole lens after the high energy analyzing magnet, in the following referred to as QD 0, QD I and QD II can be described as DFFDDF in the x-axis in which "D" stands for a quadrupole lens with a defocusing effect in the x-axis and "F" a quadrupole lens

[4] 10 MV accelerator laboratories ion-specific energy-magnetic field conversion tables for the first analyzing magnet.

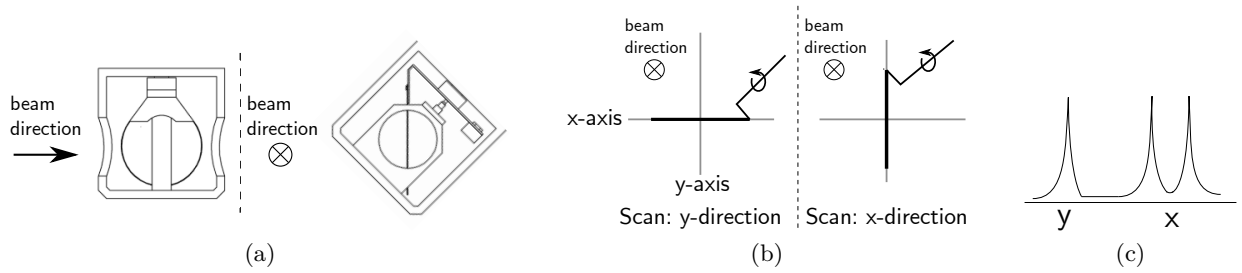

Figure 3.5: The figure shows the layout of the beam profile monitors (a), adapted from [56]. The beam profile monitor is positioned under 45% to the beam line. The measurement procedure by an ellipsoidally formed rotating wire loop is shown in (b) and an example of the produced signal in (c). In the example signals the beam is in center in the y-direction and off-center in x-direction. The peak widths are proportional to the beam width in the corresponding direction.

with a focusing effect in the x-axis. The ion-optical calculations of the current system showed that this only builds an one-folded telescopic image in one of the directions dependent on the lenses settings. Thereby, the outgoing beam does not have an equally symmetric x- and y-phase space. Therefore, the QD III can not be treated as an independent lens but it is has to continue the pole pattern so that the focusing properties of the latter lens of QD II matches the focusing properties of the first lens in QD III. This translates to the an aimed pole pattern of DFFD in the x-axis for QD II and QD III. The desired pole pattern and the ion-optical simulation of both cases, if the poles match or not, are shown in fig. 3.6. With this knowledge the polarity of the QD III poles were switched to achieve similar phase spaces for x- and y-direction. Since then a reproducible high transmission up to 100% to the last Faraday cup is achieved easily and the corresponding BPM signal for both directions are identical.

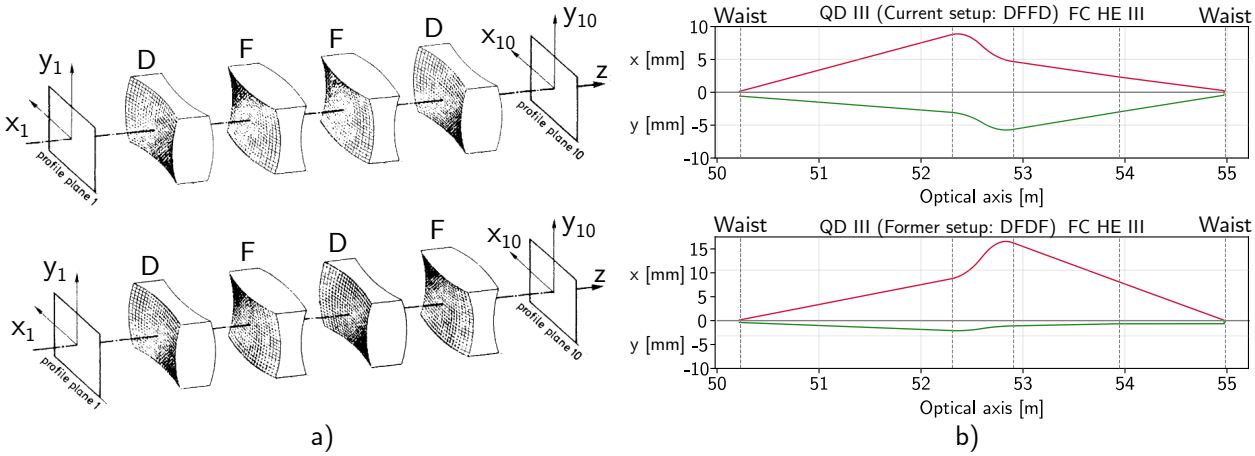

Figure 3.6: Plot a) shows the layouts of a system of two quadrupole doublet lenses which fulfill the condition for point-to-point transformation in DFFD layout (upper) and in DFDF layout (lower), adapted from [55]. This concludes in equal magnification in x and y. Plot b) shows the ion transport simulations with LIMIOPTIC2 from the waist in front of the quadrupole doublet 3 to the waist at the entrance of the magnet. The upper image shows the case if QD II and QD III are arranged like the DFFD layout which is the current setup. This configuration leads to more similar phase spaces of the x- and y-direction at the waist and produces a smaller beam along the flight path and in its waist. The lower image shows the case if the poles are switched and the poles of QD II and QD III are arranged as DFDF which was the status in the beginning of the thesis.

3.2.1.5 Long-term stability test

The formerly described modifications and improvements aimed primarily for a high degree of stability and reproducibility. Therefore, the systems status was put to test by use of different macroscopic ion beams. At first, different type of ion beams were produced and transported up until the FC LE to determine their quantitative output and transmission. The results can be found in tab. 3.2. The ion source output was in a sufficient range for measurements and the transmission up to the FC LE using the low energy side aperture with 7 mm diameter was continuously greater than 92%. Since the 20° magnet was in use until a few hours prior to the tests due to a former nuclear structure experiment, it influenced the light ion beams with masses below oxygen negatively. By a fast manually performed demagnetization, the influence on the carbon beam could be highly reduced while for the proton beam an additional steerer had to be set up in front of the 20° magnet for compensation. Since the setup is dedicated to medium mass isotopes the magnet influence is not a problem in current applications. Subsequently, the system was left unchanged for 16 hours and the measurement was repeated with the same settings. The determined ion source output and high transmission were identical.

Isotope	Material	Sputtercurr.[mA]	FC ESA[nA]	FC Magnet[nA]	FC LE[nA]	T[%]
^{12}C	C	0.88	20 500	11 400	11 000	96
^{16}O	FeO	0.95	21 000	11 195	10 600	95
^{56}Fe	FeO	0.95	21 000	760	740	97
^{48}Ti	TiH	0.7	18 150	128	125	98
p	TiH	0.7	14 860	2380	2200	92

Table 3.2: The table shows the ion source output and transmission up until the FC LE for different isotopes. Thereby, the ion source settings remained the same with exception for the analyzing magnet for choosing the injected mass. Also the transmission up to FC LE was continuously over 92%. For light isotopes, the 20° switching magnet can influence the beam negatively. Within the test measurement the proton and carbon beams were influenced. The shown transmission could only be achieved by manual demagnetization for carbon and an additional steerer for protons. The setup remained unchanged and the ion source output and transmission values were equally reproduced after 16 hours.

In a next step, the transmission through the whole system was investigated. Therefore, a $^{54}Fe^{10+}$ beam was used. It was tuned up until FC HE II after the high energy ESA with high transmission and all Faraday cup values were repeatedly logged to investigate the systems stability over the course of 9 hours. The results of the different transmissions can be found in fig. 3.7. All transmissions are given in percent from the indicated Faraday cup to the former one. One exception to this is transport through the accelerator indicated by the comparison of FC LE to FC HE. For this, the plane factor between them is given instead, since the different incoming isotopes can not be separated at the FC HE. Its transmission is finally included in the value of the FC ANA which gives the transmission from the FC LE to the FC ANA. After the initial beam tuning, the transmission is nearly 100% on the low and high energy side respectively. From the FC LE until the FC ANA the transmission is around 6.9% including the charge state fraction and the loss due to coulomb explosions in the stripper foil of the accelerator. Corrected by the charge state fraction

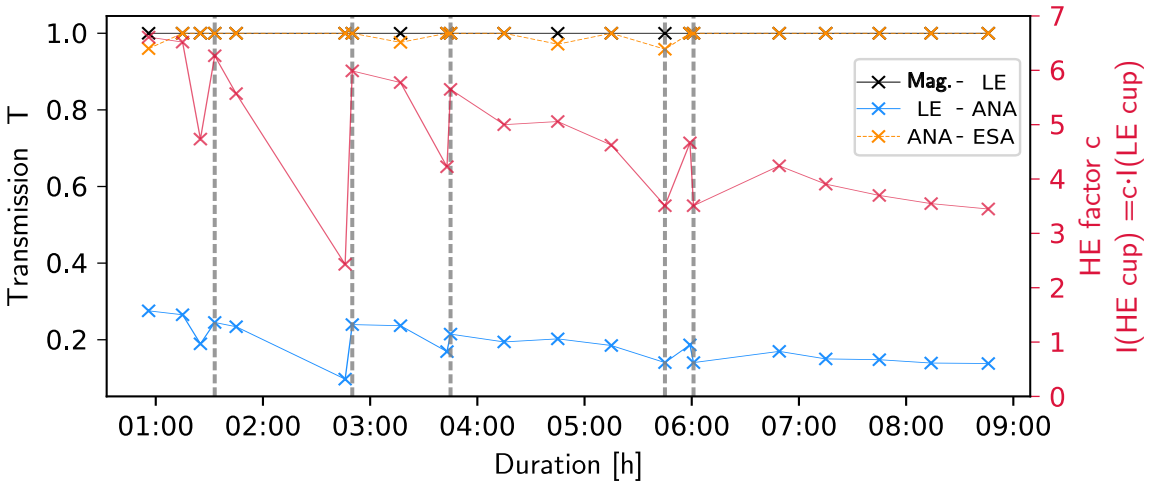

Figure 3.7: The plot shows the transmission and stability test of the 10 MV AMS system over the course of around 9 hours for different sections of the beam line. The transmissions from the indicated Faraday cup to the former are given in percent on the left axis. The only exception is the value of the FC HE to the FC LE which is given as a plain factor on the right axis, since the current on the FC HE includes all incoming isotopes and charge states. The transmission on the low energy side and high energy side is very stable and almost 100% over the whole measurement time. The transmission through the accelerator has rapid high decreases. The transmission could be restored by stripper foil exchange, indicated by vertical gray dotted lines. The more slowly decrease cannot clearly be traced down to a final explanation. Options are discussed in the text.

the transmission is around 27.5%. Over the course of the 9 hours the high transmission on the low energy side and high energy side remained stable. The source of instability is the transmission throughout the accelerator. This transmission loss has to be divided into two effects. On the one side there are several rapid decreases due to exhausting of the stripper foil. It was mainly brought back by changing the explicit foil. Additionally, a slow decrease can be observed over the whole measurement time. This effect can be caused by the quality of the stripper foils which were poorly within this measurement since they were at the end of their lifespan and renewed shortly after. Furthermore, it could be caused by accelerator instabilities expressed by long-term shifts starting shortly after these measurements. At last it could be dependent on the lifespan of the explicit sample which causes differences in the sputter process. This is supported by similar transmission loss effects for different sample wheel positions described in investigations later described in subsec. 3.2.1.6.

3.2.1.6 Sample wheel position dependence measurement

The next investigation in terms of stability and reproducibility was the dependence between the sample position on the wheel and the transmission. It was formerly shown that the wheel eccentricity of the cathode wheel of the MC-SNICS has an influence on the correction factor in the per mil range, [57]. For the investigation in this work, identical new samples were placed on four positions of the wheel each shifted by 90° and the respective transmissions were logged. The ion current and transmissions can be found in tab. 3.3. Significant deviations can be observed from the FC LE up to the FC ANA. The low energy side transmission and the high energy side otherwise were stably high. Fortunately the high deviations in their extent will only effect the measurement time but not

Pos.	I(ESA) [nA]	I(Magnet) [nA]	I(LE)|T [nA|%]	I(HE)|factor [nA|w.u.]	I(Ana)|T [nA|%]	I(ESA II)|T [nA|%]	T_{tot} [%]
21	21500	46	46|100	240|5.22	28|25.36	28|100	25.36
31	19000	37	37|100	190|5.14	25|28.15	25|100	28.15
1	26000	36	36|100	90|2.50	9|10.42	9|100	10.42
11	18500	41	41|100	120|2.93	13|13.21	13|100	13.21

Table 3.3: The table shows the measured Faraday cup currents for $^{54}Fe^{10+}$ and the according transmission to the former Faraday cup or in case of the FC HE the factor to the FC LE (without unit) for different wheel positions. All currents are given in electric nanoampere. By dividing this value with its charge state 10^+ the particle nanoampere values can be calculated. The transmissions after the accelerator are given with consideration to the charge state fraction and therefore by the explicit value of 24%. The last column gives the total transmission through the system. Huge effects can be seen on the transmission between FC LE and FC ANA while the low and high energy side transmission remained stable.

in equal degree the correctness of the result which was also shown in the performed test measurements, see subsections 3.2.3.3 and 5.6.2. Nevertheless resolving this impact is necessary since the measurement time is one crucial limit within low-level AMS measurements. Additionally during the investigations concerning the sample cathode size, an additional sample wheel dependence of the ion beam current amount itself was observed, see subsec. 3.2.1.8.

Two effects come into play concerning the sample wheel position. On the one side a systematic misalignment of the sample wheel which influence all samples on the wheel. It is not possible to reproducibly position the sample wheel sufficiently. Even when a sample wheel is replaced, it is manually aligned by use of a single additional alignment pin. An example for the reproducibility improvement of these alignments could be an additional second alignment pin for a tight fit of the wheel inside the ion source for a well-defined reproducible position. While this circumstance can influence the overall ion source performance, the observed sample position dependence on the wheel has to be originated by an eccentricity of the wheel position. One reason for this is the alignment routine. Even with specified routines for these operations, [51], the reproducibility is limited since some of the steps are dependent on subjective senses instead of objective quantities. Investigation and resolving of the problems are undergoing. The ion source has three additional alignment rods at its outer side which can be used for alignment adjustment while in operation. Since their manual usage is unhandy because the ion sources high voltage has to be shut off every time and the result of the adjustment can not be seen synchronously, the rods are newly equipped with motors for remote usage[5]. The ion source output or even the transmission through the system could be used for alignment corrections. This procedure is successfully used at the Vienna Environmental Research Accelerator (VERA) using the same source type.

3.2.1.7 Tuning procedure test measurement

In the final step the tuning procedure for particle beam was testified. Concerning the used mass spectrometers the beam can be defined by its discrimination parameters $\frac{E}{q}$ and $\frac{p}{q}$. Therefore, the setup parameters for particle beams can be determined by use of macroscopic so-called pilot beams.

[5] G. Hackenberg, PhD thesis, not submitted

Thereby, it is possible to tune an arbitrary beam and scale all components in respect to the $\frac{E}{q}$ and $\frac{p}{q}$ difference or to choose different beams with each equal $\frac{E}{q}$ or $\frac{p}{q}$ values. Both methods were used at the 10 MV AMS setup. For testifying the tuning procedure a macroscopic pilot beam was used for a different macroscopic beam. In case of failure, the test would reveal remaining dysfunctions of setup components. Therefore, a $^{47}Ti^{8+}$ was used as pilot beam for $^{48}Ti^{8+}$. The isotopes were injected into the accelerator as TiH. For the aimed $^{48}Ti^{8+}$ beam, an energy of 64.31 MeV at a terminal voltage of 6.98 MV was chosen. While tuning discriminating components, like MSA and ESA, the corresponding slits were set to ±1 mm. For the tuning procedure of components like lenses, the slits were opened to ±2 mm. At the HE analyzing magnet II, the 3 mm injection aperture was used. First the $^{47}Ti^{8+}$ with the same $\frac{E}{q}$ was chosen at a magnetic field of the high energy magnet of 8964 G. It was used to tune the ESA and HE steerer pairs. Subsequently, the magnetic field was set to 9059.5 G and the terminal voltage was set to 7.139 MV to create a pilot beam with the same $\frac{p}{q}$. This beam was used for tuning of the remaining magnetic components like the lenses. The final parameter set can be found in the appendix in tab. 7.2. With the pilot beam a high energy side transmission from FC ANA to FC HE II of 87% was achieved. By changing the bouncer voltage on the low energy side from the set 1386 V to the calculated value for $^{48}Ti^{8+}$ of 1009 V an equal HE transmission of 87% was achieved. This confirmed the functioning of this tuning procedure at the current setup. In addition, the low energy side transmission and the factor from the FC LE to the FC HE were compared between ^{48}TiH, ^{47}TiH and ^{46}TiH. For all three isotopes the transmissions and factors were almost identical.

3.2.1.8 Cathode size investigations

The newly achieved stability of the ion source and the system enabled the possibility for investigations for ion beam output increase. The goal is to maximize the ion beam output which can be fully transported through the whole system. For its improvement a test measurement was performed to investigate the dependence of the ion beam output to the sample cathode bore diameter. It has to be mentioned that the MC-SNICS can be equipped with a cathode wheel for large samples with cathode opening diameters of several millimeters. Such large cathodes are not suitable for AMS measurements since a high amount of material is needed per cathode and a significant fraction is not used. Therefore, it was investigated if only a slight enlarging of the cathode opening size would result in an improvement which outweighs the cost of larger required sample amounts, provided that it is available, or the redesign of the cathodes in terms of cathode depth. This investigation was inspired by similar investigations for ^{41}Ca AMS measurements at Malt (Micro Analysis Laboratory, Tandem accelerator, University of Tokyo)[6]. For the tests in Cologne, standard copper sample cathodes from NEC with a diameter of 1.1 mm were drilled out to larger diameters. Several pairs of cathodes with 1.3 mm, 1.5 mm, 1.7 mm, and 1.9 mm diameter respectively were produced. The final samples were made by pressing iron oxide material manually into the cathodes with fitted pressing rods, a pair of pliers and a hammer since no commercial pressing tool for variable sizes is available. Additionally, a pair of standard-sized samples using the commercial sample press was produced. The samples were distributed along the sample wheel. For the measurement a mass spectrum of the whole iron oxide pattern was recorded for each cathode. The peak height of mass 72, mainly $^{56}Fe^{16}O$, was taken as an indicator for the output investigations. The recorded mass

[6] T. Yamagata, AMS-15 conference talk

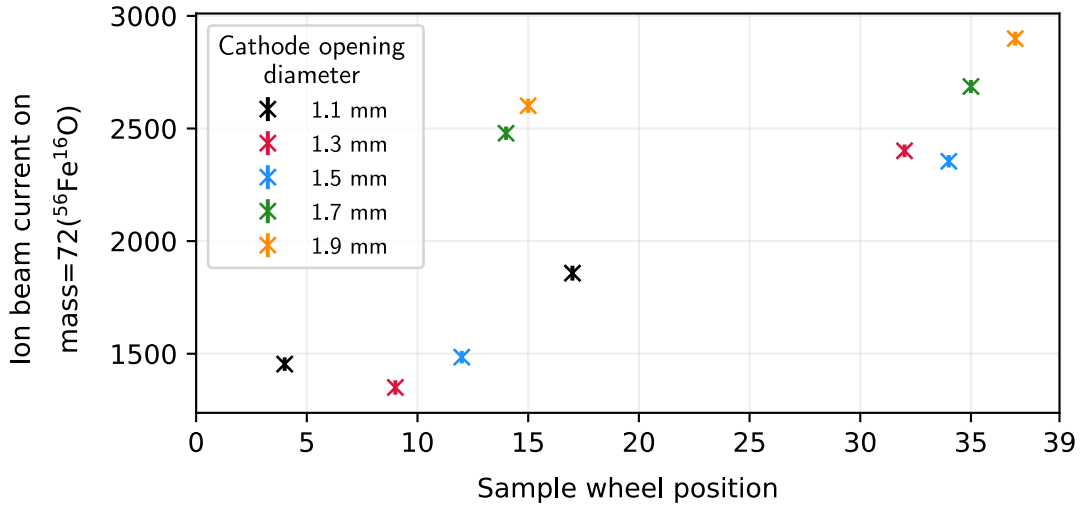

Figure 3.8: The plot shows the result of the cathode diameter size investigation for the current output of the ion source. The ion beam current on mass 72, mainly $^{56}Fe^{16}O$, is plotted against the sample wheel position since an significant dependence was found in the data. The different colors indicate different-sized cathode opening diameters. Firstly, comparing close-lying cathodes from position 4 to 15 and position 32 to 37 individually, the pattern looks similar for each data cluster. While the currents for 1.3 mm and 1.5 mm show only a small increase or are even equal in their errors there is significant increase to 1.7 mm opening. From 1.7 mm again is only a slight increase to 1.9 mm. The 1.1 mm can only be compared within the first cluster where it lies in between 1.3 mm and 1.5 mm openings for the nearest positions. The second cathode with 1.1 mm on position 17 shows an increase to the first one only explainable by the momentary sample wheel position dependence. Furthermore, the data indicates that the dependence on the sample wheel position decreases significantly with increasing opening diameter. This can be explained since the cesium spot can not always be centered on an eccentric aligned wheel which has less impact on larger sample areas.

patterns showed that the sample cathode opening does not significantly impact the mass separation quality of the low energy mass spectrometer. The results of the quantitative investigations can be seen in fig. 3.8. It was observed that the data show a significant dependence on the sample wheel position. Therefore, the data are additionally put in relation to the position for interpretation. Classifying the data in clusters of close lying cathodes once from position 4 to 15 and secondly from position 32 to 37, similar patterns can be found for cathodes with diameters 1.3 mm to 1.9 mm. The openings from 1.1 mm up to 1.5 mm in the low-position cluster shows similar values with no significant trend to the cathode diameter. This is reproduced in the high-position cluster for the 1.3 mm and 1.5 mm currents which are equal within their error. From 1.5 mm up to the 1.7 mm openings a significant increase can be observed in both clusters and again a slight increase from 1.7 mm to 1.9 mm opening. Furthermore, the data indicate that the dependence on the sample wheel position is higher for small openings. The second cathode with 1.1 mm on position 17 shows an increase to the first one on position 4 which is only explainable by the momentary sample wheel position dependence. As in the transmission investigations, see subsec. 3.2.1.6, the significant sample position dependency is probably traced back to the eccentricity of the wheel which causes a shift in the cesium spot position. This will have smaller effects on bigger sample surface areas. Apart from the quantitative output, it was tested if the ion beam of different sized openings from the same cluster can be transported equally through the system up to the FC ANA. Thereby, the beam did not reach the same transmission with equal parameter settings but if newly tuned

equal transmissions were achieved. Overall the data indicate that it can be advantageous to use larger sputter surfaces. The ion beam current increased for diameters over 1.7 mm and the sample wheel dependency is less prominent. No continuous trend could be observed over the whole span of diameters which could be influenced by the inaccurate pressing for non-standard diameters or the sample position. The bigger surface area did not effect the spectrometers mass separation and equal transmission could be achieved by respective tuning. The measurement should be repeated when the sample wheel dependency is well investigated or even solved. In alternative it could be repeated by choosing only two different diameters for the opening but more samples per option for a better distribution along the wheel. Furthermore, if an ideal size is found a sophisticated pressing tool should be constructed to avoid the manual pressing since the method showed inaccuracies in the smoothness of the sample surface which is a critical criterion. A simple solution would be additional adapted components to the commercial press.

3.2.1.9 Conclusion of stability tests

The tests showed that the transport through the accelerator itself is an ongoing problem. On the one side a significant sample wheel dependence on this transmission leads in the worst case to extended required measurement duration. On the other side the stability of the accelerator and the impact on the transmission through the accelerator is a remaining uncertainty. Its current status and to what extent it could hinder aimed measurements has to be investigated in the future. Overall the results of all individual test measurements proved that the remaining AMS system itself has now the stability and reproducibility to perform long-term measurements mandatory for small isotopic ratios. It was shown that the ion source already delivers sufficient output and the transmission over the system is stably high. Also the tuning procedure was successfully confirmed which is an indirect test for the functioning of the whole system in terms of discrimination accuracy.

3.2.2 Improvement of the 5 anode gas ionization detector

In the use of the 5 anode gas ionization detector after the gas-filled magnet it revealed that signals of the first anode showed a severe disturbance, see fig. 3.11 a) for the signals in the initial configuration with and without using the gas-filled magnet. This manifested in a double peak structure which worsens the energy resolution to an extent that it is no longer usable for isobar separation, [33]. Therefore, the signals of the first anode were left out for the analysis in the first measurements. As a first step in the investigation the prior anode structure was replaced by a more simple layout in which all anodes have the same width and length of $30 \times 80\,\mathrm{mm}^2$, see layout in appendix in subsec. 7.4.2. By use of such an equally structured layout, the anodes capacities are equal. Therefore, with a simple calibration of the amplification setup by a pulser signal, the captured signals of all anodes are directly comparable. By comparing the detector with the available 10 anode gas ionization detector it stood out that the distance between the entrance window and the first anode is significantly larger in the 5 anode detector. Consequently, the volume in front of the detector is not covered by a homogeneous electric field which influences the produced electron transport properties. For investigation of this effect a test measurement was conducted. Therefore, the gas ionization detector was positioned as in the first detection layout, see fig. 3.1, subsequent

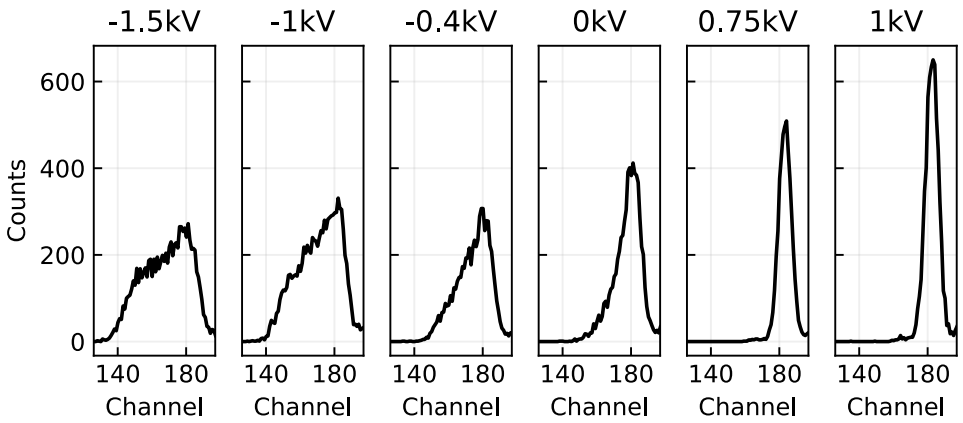

Figure 3.9: The plot shows the spectra of the first anode of the five anode gas ionization detector in dependence of the setting of the prior HE y-steerer. The signals shape and the quantitative width is significantly impacted. This is caused by the electrons produced in the volume in front of the inner detector layout which does not lay within the homogeneous electric field. This influences the produced electron transport and therefore the signal. Further simulations of this area showed even worse disturbance by the field smoothing rings when using the largest possible window.

to the ESA and quadrupole lens II. The entrance window for this measurement was a $10\,\mathrm{x}\,10\,\mathrm{mm}^2$ silicon foil with a thickness of 150 nm. For the tests a stable ^{54}Fe beam with an energy of 58 MeV was tuned to FC HE II in front of the detector. After reducing the beam intensity, the beam was tuned into the detector by help of an analog ratemeter analyzing the second anodes signal. By testing different components influence on the anode signals, a significant dependence was observed for the injection height of the beam, see fig. 3.9. In the measurement, the injection height was varied by use of the HE y-steerer located after the HE quadrupole doublet. Based on this finding the behavior in the first part of detector was simulated with SIMION which is a software for the calculation of electric fields and trajectories of charged particles within these fields. The detector layout from the cathode up to the Frisch grid was remodeled, inserted into the software and assigned with the applied voltages. Thereby, the electric potential is calculated and the trajectory of formerly defined particles are simulated. For realistic particle migration within gas, the viscous damping factor within SIMION was applied, [58]. For the given simulation it was chosen to 1000. Since the signals at the anodes are originated by the produced electrons and not by the beam itself, their behavior was simulated respectively. For that, the starting points of the electrons were set at different heights and depths of the detector. The simulations for different entrance layouts can be found in fig. 3.10. It was observed that inside the detector where the electric field is very homogeneous the electrons flight direction is only negligibly affected by the injection height. As expected the height has the largest impact on electrons produced between the window and the inner lying detector structure. Due to the non-homogeneous field these electrons are also guided to the anode structure. On the one side this leads to a broadening of the energy loss signal, on the other side for even larger height difference the simulation showed that a non-negligible part of the signal can be blocked by the rings used for smoothing the field, see fig. 3.10 a).

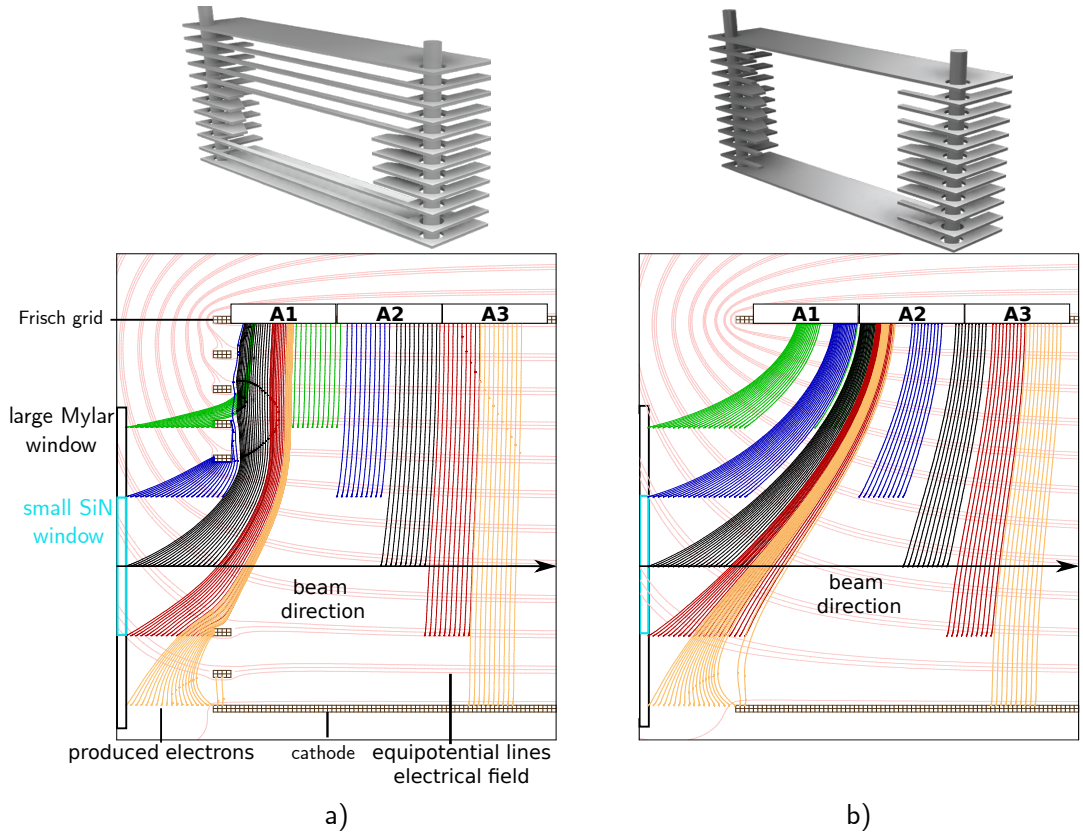

Figure 3.10: The upper drawings in a) and b) show the 5 anode detector structure at the front area prior to and after the modifications of the smoothing rings. The lower plots in a) and b) show the corresponding SIMION simulations of the produced electrons within the equipotential lines of the electric field. Thereby, the inner detector from Frisch grid to the cathodes and the outer housing was simulated and only a cut out of the front of it is shown. The positions of the above lying anodes are indicated on height of the Frisch grid. A viscous damping is used to simulate the particle migration within gas. The smaller 2 cm x 2 cm SiN window and the round large Mylar window with a diameter of 4.5 cm are drawn. Their widths are not to scale. The different colors indicate different heights of production for the electrons corresponding to different injection heights of the primary ion beam. In a homogeneous perpendicular electrical field the produced electrons traverse orthogonally to the initial beam towards the nearest anode. In case of the old configuration, a), this status is almost reached within the structure from the second anode on. The electrons produced in front of the detector structure describe a curved trajectory to the inside of the detector. This broadens the signal captured on the anodes and worsens the energy resolution. The severe disturbance in the former layout was caused due to the stopping of produced electrons by the smoothing rings. With the new structure, b), all produced electrons describe slightly curved trajectories. However, the severe disturbance at the first anode should not occur anymore. Still when the larger window should be used the detector has to be redesigned since the electrical field is not sufficiently homogeneous and for example incoming ions could collide with the cathode.

The lost electrons lead to a distinctly lowered energy loss signal. On basis of these results the formerly whole rings were cut to match the opening in x-direction in front of the detector at each height while the remaining electric field structure is mainly maintained, see fig. 3.10 b). Thereby, all the produced electrons describe slightly curved trajectories but the severe disturbance at the first anode should not occur anymore. Additional simulations were performed to investigate if

the electric field structure from the 10 anode gas ionization detector, characterized in [33], further improves the behavior. No difference between the anodes signal qualities were observed with this detector in the performed test measurements. Its inner layout consists of anodes, Frisch grid and a cathode which is formed like a tub. An equivalent electric structure within the 5 anode detector layout can be achieved by shortening the cathode with a specific number of smoothing rings above. This setup was simulated with the options of a shortening of two or four smoothing rings above the cathode.

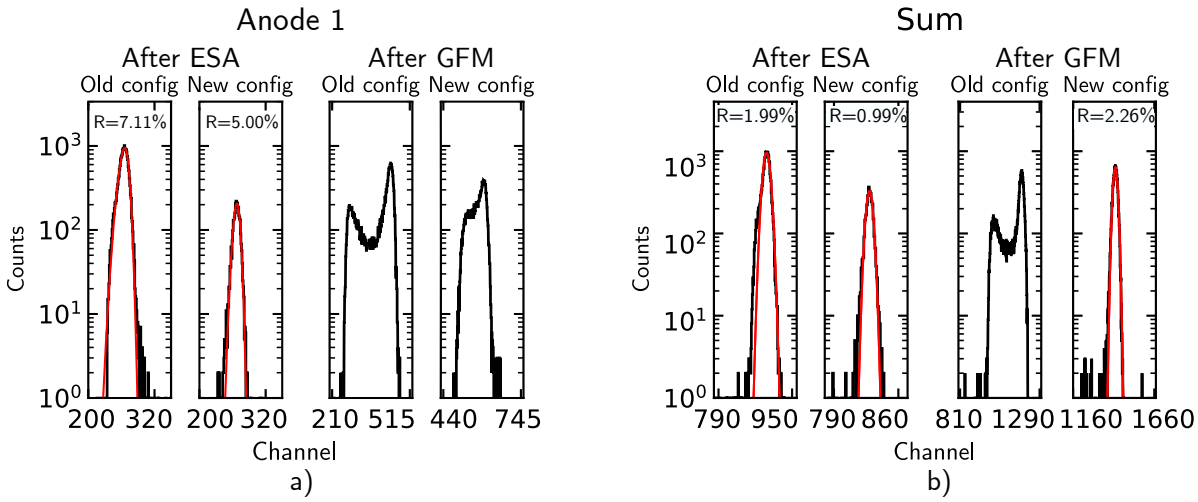

Figure 3.11: The different plots show the single spectra of anode 1, a), and total energy as the sum spectrum of all anodes, b) prior and after the adaptions. The two left plots in a) and b) show equivalent $^{54}Fe^{9+}$ test measurements after the ESA. The first anode signal is improved by the new configuration. The improvement of the first anode signal is affecting an improvement of the total energy resolution in the sum spectrum by a factor of two. The two right plots in a) and b) show the energy loss signals produced by $^{60}Ni^{10+}$ particles and $^{60}Fe^{10+}$ particles after passing an additional gas distance within the GFM. Thereby, the signals can only be compared qualitatively. The additional broadening due to the gas distance has a significant impact on the first anodes disturbance. The signal of the first anode and the total sum was not usable for discrimination in the old configuration. With the new configuration the first anode signal is improved and becomes available for discrimination but the resolution is still worse than other anodes. The total energy resolution can now be determined to $E_{res} = 2.26\%$ and the total energy sum signal can be used for discrimination.

By use of this configuration the effects from the front of the detector are mirrored at its end. Thereby, electrons produced at the end of the last anode or shortly after are guided back into the detector structure and can even reach the fourth anode. By this, the resolution of the energy loss signal on the fourth and fifth anodes became worse which decreases the quality of separation on the last two anodes. Therefore, according to the simulations, the equally distributed and cut smoothing rings are the best option of the discussed. To prove the findings and assumptions of the simulations, a second test measurement with stable ^{54}Fe with an energy of 51 MeV was conducted. Therefore, the smoothing rings were adapted as formerly described, see fig 3.10 b) and the option for shorten out the cathode with the two lowest or four lowest rings was prepared for mirroring the electric field of the 10 anode gas ionization detector. Comparable test measurements with and without using the gas-filled magnet were performed, see fig. 3.11 b). Similar to the first test measurement the anodes signals were investigated in dependence on the injection height varied

by use of the HE y-steerer. The severe disturbance of the first anode signal was not observed anymore. Furthermore, the total energy resolution could be improved to $E_{res} = \frac{FWHM}{\mu} = 0.99\%$ when positioned after the ESA. It is a factor two lower in comparison to the $E_{res} = 1.99\%$ in the initial test with the old configuration. While the total energy resolution in the configurations with shortened out rings is almost the same, the resolution on the last anode dramatically worsens by 30% with two shortened smoothing rings above the cathode and even 120% with four shortened rings as qualitatively expected by the simulations. For the detector position after the gas-filled magnet where the beam is much wider, the behavior impacted the discrimination abilities of the detector strongly. In most cases the first anode signal could not be used for discrimination. This also effected the total energy resolution which again was unusable for discrimination and no total energy resolution could be determined. With the new configuration the signal quality of the first anode improved strongly while the second one slightly worsened. Furthermore, all anode signals and the total energy loss signal became available for discrimination purpose by use of the small detector window. The total energy resolution is improved to $E_{res} = 2.26\%$ when used after the gas-filled magnet where even no total energy resolution could be determined beforehand. Even though the first anode signal became available for discrimination, it is still worse in comparison to other anodes resolution. For an equally good signal quality of all anodes the dead-volume within the detector has to be minimized. Therefore, the inner lying structure has to be set closer to the entrance window. For the use of the large detector window the structure has to be rebuilt completely since there are still signals produced on the bottom end of the inner detector structure which will lead to unclean signals.

3.2.3 AMS measurements of ^{14}C reference samples

Radiocarbon isotopic ratio measurements are one of the most common measurements performed in AMS laboratories. Due to the fact that the stable atomic isobar nitrogen is fully suppressed by the ion source sputter process and the carbon produces high ion beam currents, low-level AMS measurements can be performed with tabletop machines using accelerator voltages down to 200 kV, [59]. By that, a radiocarbon AMS measurement is an ideal candidate to test an AMS system for stability and overall performance. First tests using only macroscopic beam proved that stability, reproducibility and the transmission significantly improved and verified the applicability of the tuning procedure, see subsec. 3.2.1.7. Finally, the system should be verified for its capability of long term sample sequence AMS measurements. Therefore, the described improvements of the system were tested by performing a radiocarbon AMS measurement. The definitions and formulas given in this subsection regarding the calculations of the carbon ratios, if not other stated, are taken from [60].

3.2.3.1 ^{14}C standard materials

For radiocarbon AMS measurements a wide range of standard materials are available which are defined by their pMC (percent modern carbon) value and their δ^{13}C value in units of per mil. Within this measurement, two standard materials were used which passed the dedicated preparation

routine, [61]. Additionally, one blank material[7] was used. The standards values can be found in tab. 3.4.

Name	pMC	δ^{13}C[‰$_{PDB}$]	reference
NIST Ox-II	134.07	−17.8	[62]
IAEA C7	49.53	−14.48	[63]

Table 3.4: Standard material for radiocarbon AMS measurements used within this thesis and their given literature values.

The δ^{13}C value is based on the deviation in per mil to the reference material PDB (Pee Dee Belemnite) which is marine fossil with a ratio of $^{13}C/^{12}C = 0.0112372$. This normalization is necessary since the fractionation of the carbon isotopes is strongly dependent on the material type. The given δ^{13}C value for a sample is defined by eq. 3.2.

$$\delta^{13}C = \left(\frac{\frac{^{13}C}{^{12}C}(Sample)}{\frac{^{13}C}{^{12}C}(PDB)} - 1 \right) \cdot 1000[‰] \tag{3.2}$$

The definition of the pMC unit is traced back to the $^{14}C/^{12}C$ ratio of a theoretical wood sample from the year 1950. Its value is given as a specific carbon activity of $A = 226\,\frac{\mathrm{Bq}}{\mathrm{kg}}$. A respective ratio can be calculated from this value. For simplification an arbitrarily chosen mass of 1 kg is assumed. On the one side the number of ^{14}C atoms $N_{^{14}C}$ can be determined. It is calculated by using the half life of $T_{\frac{1}{2}} = 5700(30)\,y$, [64], with the formula:

$$N_{^{14}C} = \frac{A}{\lambda} = \frac{A \cdot T_{\frac{1}{2}}}{\ln(2)} \tag{3.3}$$

On the other side the total number of carbon moles n_C in the same mass $m_C = 1\,\mathrm{kg}$ can be calculated by use of the carbon molar mass $M_C = 12.0107(8)\frac{g}{mole}$, [65], the Avogadro constant $N_A = 6.02214179 \cdot 10^{23}\,\mathrm{mol}^{-1}$ and from that the total number of carbon atoms N_C:

$$n_C = \frac{m_C}{M_C} \tag{3.4}$$

$$N_C = n_c \cdot N_A \tag{3.5}$$

Subtracting the ^{14}C atoms and with consideration of the $\delta^{13}\mathrm{C} = -25‰$ for the theoretical material, the ^{12}C and ^{13}C atom numbers can be calculated. By these the $^{14}C/^{12}C$ ratio $\mathrm{R_{cal}}$ of the hypothetical sample in 1950 is determined to $\mathrm{R_{cal}} = 1.182(6) \cdot 10^{-12}$. With that, the $\mathrm{R_{14}} = ^{14}C/^{12}C$ ratios of the standards can be determined by using their pMC value, accounting for the current age by use of the half life and the year of measurement ($year$) and the isotope fractioning, see eq. 3.6.

$$R_{14} = \frac{N_{^{14}C}}{N_{^{12}C}} = R_{cal} \cdot EXP\left(-\frac{\ln(2)}{5730\,a} \cdot (year[y] - 1950) \right) \cdot \left(\frac{1 + \frac{\delta^{13}C[‰]}{1000}}{1 - \frac{25[‰]}{1000}} \right)^2 \cdot \frac{pMC}{100} \tag{3.6}$$

The $^{14}C/^{12}C$ and $^{14}C/^{13}C$ ratios for the standards in 2021 are given in tab. 3.5. Due to the

[7] Provided by Dr. Stefan Heinze

size of the offset-cup chamber only the measurement of $^{14}C/^{13}C$ is possible without changing the accelerator voltage. Therefore, the $^{14}C/^{13}C$ ratio is measured within this thesis.

Name	ID	$^{14}C/^{12}C\,[10^{-12}]$	$^{14}C/^{13}C\,[10^{-10}]$
NIST Ox-II	C1002	1.594(8)	1.444(7)
IAEA C7	C1007	0.593(3)	0.535(3)

Table 3.5: Explicit $^{14}C/^{12}C$ and $^{14}C/^{13}C$ ratios of standard material used within this thesis in 2021.

3.2.3.2 Tuning procedure and stable isotope transmission

For the tuning procedure a stable abundant ion beam was used to tune the beam throughout the accelerator setup optimizing the transmission between the ion beam currents measured by the Faraday cups along the beam line. The resulting parameters from the hereinafter described tuning procedure can be found in the appendix in subsec. 7.2.4. The chosen ion source parameters are set for maximal output and stable operation determined by the ion beam current at the FC Magnet. Carbon ions are extracted in atomic form while the isobar nitrogen does not form negative ions in its atomic form. For the tuning procedure the abundant ^{13}C was chosen. Regarding the ion source section only the einzel lens and y-steerer are tuned for new measurements. In the next step, the bouncer voltage is held fixed while the magnetic analyzer is traced to determine the desired mass component of the ion beam. A brief discussion of the low energy mass spectrum can be found later in this subsection. For the tuning up to the FC LE, firstly, the corresponding slits are set to ± 1 mm and the small aperture with a diameter of 4 mm was used to determine the direction by tuning the x- and y-steerer pairs in the injector. Thereby, the BPM is constantly used for intermediate beam inspection. Subsequently, the slits are opened up to at least ± 5 mm and the bigger aperture with 7 mm diameter was used for tuning the remaining components on the low energy side. For the standard material measurements a terminal voltage of 6.95 MV was used which led in combination with the 4+ charge state to a final ion energy of 35.57 MeV. The 4+ was chosen since it is the most abundant charge state for this terminal voltage, see fig. 3.12 c). Regarding the high energy side, the measurements were performed using detection setup I, see fig. 3.1, with the 10 anode gas ionization detector. Within the tuning procedure on the high energy side, available slits were chosen to ± 1 mm for tuning the dispersive ion-optical elements and between ± 2 mm and ± 3 mm for tuning other ion-optical components. The aperture in front of the high energy magnet had a diameter of 3 mm. The high energy steerer pairs and the electrostatic analyzer are tuned by a pilot beam with the same $\frac{E}{q}$ values. For that the stable isotope ion beam at the same terminal voltage and charge state was tuned in respect to a high transmission to the last available Faraday cup in front of the detector. In equivalent, a $^{13}C^{4+}$ beam at a terminal voltage of 7.547 MV producing a pilot beam with the same $\frac{p}{q}$ value as the later used $^{14}C^{4+}$ was used for tuning all quadrupole lenses in respect to high transmission. Subsequently, the $^{13}C^{4+}$ ion beam with the initial terminal voltage and the final HE magnet value was measured in the offset-cup. Thereby, the offset-cup was initially positioned at 16 cm on the right to the optical axis. The position was calculated using the formula derived in [10] for the second HE magnet at the FN. The offset-cup position was finally slightly adjusted to capture the maximum of the beam with dedicated motors, [47]. For switching between stable and rare isotope on the low energy side the bouncer unit was used. A final fine

tuning of the high energy mass spectrometer for the rare beam is done with respect to the detector rate. Thereby, the coupling to the data acquisition, see subsec. 3.2.4.1, was used due to the small counting rates of only a few Hertz. It has to be mentioned that the carbon ions were not stopped in the detector gas volume since the required pressure would be too high for the inserted $8\,\mathrm{x}\,8\,\mathrm{mm}^2$ SiN window with a thickness of 150 nm. This does not influence the counting ability of the detector but only the separation ability. Since no isobar is present, this configuration was sufficient for the presented measurement. The final set of measurement settings used for the carbon measurements

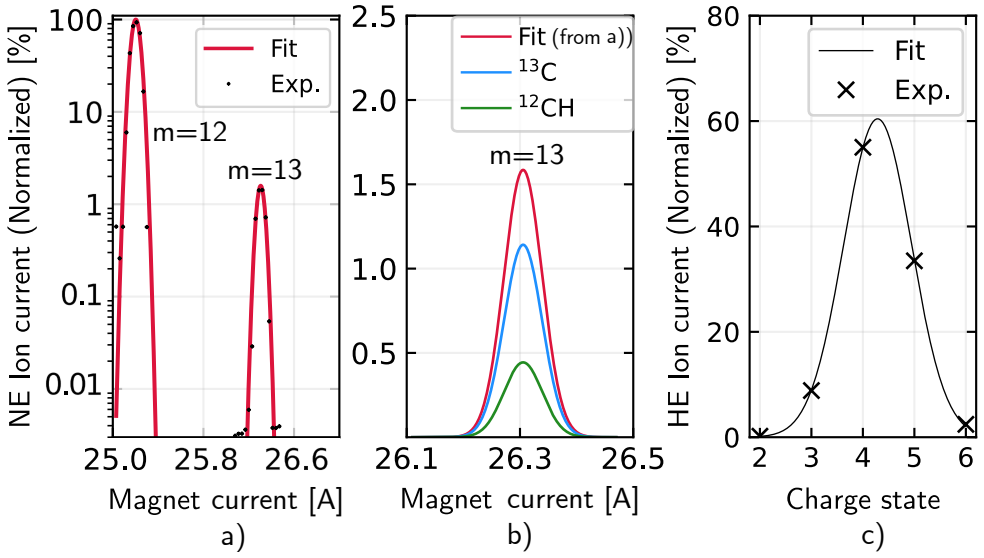

Figure 3.12: Plot a) shows a logarithmic mass spectrum of a carbon blank sample measured after the low energy analyzing magnet. While mass 12 only contains ^{12}C, the peak corresponding to mass 13 includes ^{12}CH and ^{13}C. By assuming the fraction of ^{13}C from the ^{12}C peak from their natural abundance, it can be deduced that 69% of the mass 13 peak corresponds to ^{13}C shown in b). In c) the charge state population of ^{13}C after the accelerator measured in the FC ANA is shown.

is given in the appendix in tab. 7.3. The achieved transmissions with the macroscopic ^{13}C beam can be found in tab. 3.6. The transmission on the low energy side from the FC Magnet up to the FC LE is 93.75 %. On the high energy side from the FC ANA up to the last Faraday cup the transmission is 96 %. For the transmission through the accelerator it has to be determined which fraction of the chosen mass 13 peak corresponds to ^{13}C and which to ^{12}CH. Therefore, the pattern of the mass spectrum after the low energy analyzing magnet is considered, see fig. 3.12 a). The amount of ^{13}C can be determined by applying the natural abundance ratio on the mass 12 peak which accounts for 69 % of the mass 13 peak, see fig. 3.12 a). This does not consider a differing δ^{13}C value which is in the order of per mil and neglected for these calculations. The transmission from the FC LE to the FC ANA for the 4^+ charge state is 29.76% which can be separated in the population of the charge state of 55%, see fig. 3.12 c), and a transmission through the accelerator of 54.11%. From that, the transmission up to the FC HE I is 96% and can be transported without losses to the FC HE II. The total absolute transmission with inclusion of the charge state fraction is 26.79%. By dividing this value by the corresponding charge state fraction a transmission of 48.7% is achieved from the FC Magnet up to the last Faraday cup. Overall, the system acted completely stable over the whole measurement period and no fluctuations or long-term shifts of the ion source or beam transport components occurred. Furthermore, the high transmission remained unchanged. Smaller exceptions to that have to be mentioned concerning the stability of the accelerator which

is described in subsec. 3.2.3.3.

Position	Transmission to last position[%]	Total transmission[%]
FC Magnet	-	-
FC LE	93.75	93.75
FC ANA	29.76	27.90
FC HE I	96.00	26.79
FC HE II	100.00	26.79

Table 3.6: The table lists the transmission between the different Faraday cup positions along the beam line for the carbon pilot beam. Thereby, for each position the transmission to the last position and the total transmission to the first Faraday cup (FC Magnet) is given. The transmissions on the high energy side are not divided by the charge state fraction of 55% for the used 4+ charge state.

3.2.3.3 Conduction, analysis and results

For the experiment two standard materials and one blank material were measured. Thereby, each material was split to several cathodes which were evenly distributed along the cathode wheel. The switching between ion beams by changing the bouncer voltage, the logging of the ion beam current from the picoamperemeter and the handling of the data acquisition was performed manually. To

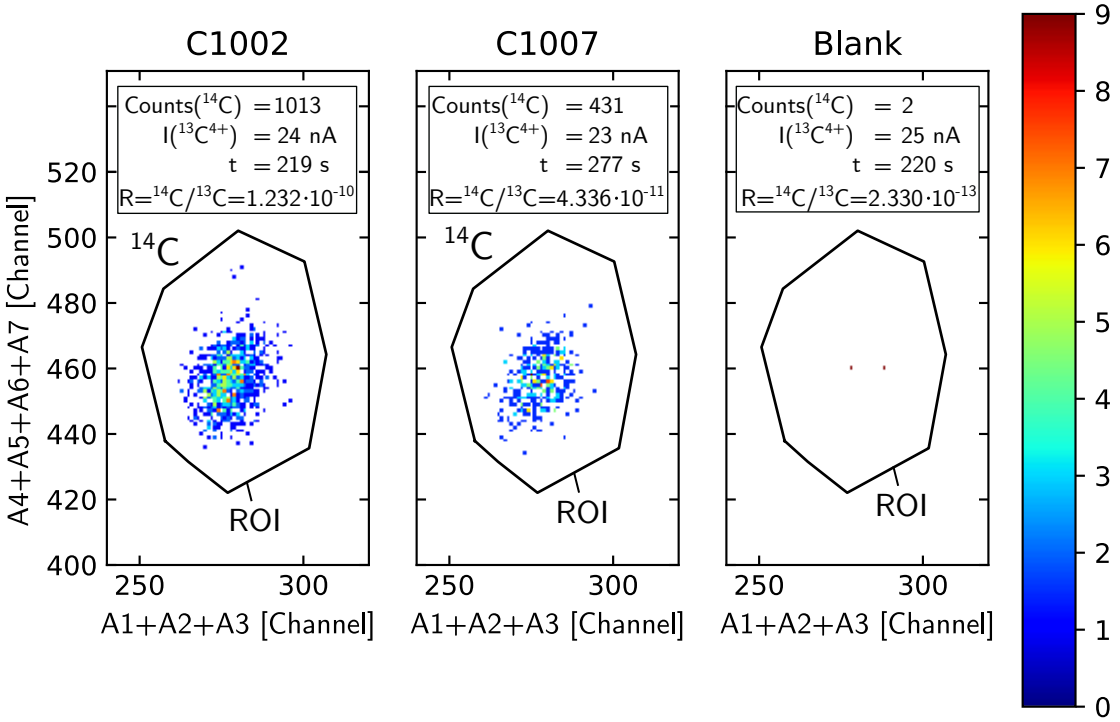

Figure 3.13: Examples of the gas ionization detector spectra used for particle identification of ^{14}C for the three measured materials. The two-dimensional spectra show the summed signals from the fourth to seventh anode against the summed signals from the first to third anode. Within these spectra a ROI is set represented by the black frame and the enclosed signals are identified as ^{14}C. The basic measurement values are given.

account for the stability of the beam or the samples lifespan for longer measurements this procedure

has to be repeated several times in which the data acquisition is paused when measuring the stable component. Thereby, all equipped samples were measured. For the particle identification two-dimensional spectra showing the summed signals from the fourth to seventh anode against the summed signals from the first to third anode were analyzed. A two-dimensional ROI was set and the enclosed signals were taken as the ^{14}C counts for this measurement. Examples of these spectra of the three different materials are shown in fig. 3.13. The first step of the final analysis was the background correction for each single measurement. The blank measurements were used to determine the background rate $\dot{N}_b$ which is used for the background correction. Therefore, the counts were divided by the measurement time and the measured stable ion beam. The corresponding error $\Delta\dot{N}_b$ was determined by error propagation, whereas the error of the counts is taken as the statistical error $\sqrt{N}$ for over 20 events and by use of limits for smaller event numbers, see subsec. 2.4.1.3. From these single values a weighted mean $\overline{\dot{N}_b}$ and its error $\overline{\Delta\dot{N}_b}$ were calculated by:

$$\overline{\dot{N}_b} = \frac{\sum_i (\dot{N}_b)_i \cdot \omega_i}{\sum_i \omega_i} \text{ with } \omega_i = \frac{1}{(\Delta\dot{N}_b)_i^2} \tag{3.7}$$

$$\Delta\overline{\dot{N}_b} = \frac{\sqrt{(\sum_i (\Delta\dot{N}_b)_i \cdot \omega_i)^2}}{\sum_i \omega_i} \tag{3.8}$$

These values were used for the background correction of the measurements as explained in chap. 2. The resulting isotopic ratios and their errors determined by error propagation from the single measurements can be seen in fig. 3.14. Concerning their scattering, the measured ratios of the highest standard have a standard deviation of 6.15% around their mean value, the ratios of the lower standard have a standard deviation of 0.93% and the uncorrected background ratios have a standard deviation of 39.51%. For every material the individual values were combined in a weighted mean value and corresponding error as in eq. 3.7. This value was used to determine the correction factors for the two standard materials from which the final weighted averaged correction factor of $c_f = 1.20(5)$ was calculated. It is comparable to the correction factor achieved at the 6 MV Tandetron accelerator AMS setup with 1.19[8]. This corresponds to a transmission of the high energy spectrometer including isotope identification of 83.33% for the value of this work. With that, the corrected background level was determined to $^{14}C/^{13}C = 4.52^{+0.78}_{-0.58} \cdot 10^{-13}$, ($^{14}C/^{12}C = 4.62 \cdot 10^{-15}$). The individual results for the standards can be found in tab. 3.7.

Material	Meas. $^{14}C/^{13}C$ Ratio	c_f	Corr. $^{14}C/^{13}C$ Ratio
Std. C1002	$1.22(3) \cdot 10^{-10}$	1.18(6)	$1.444(7) \cdot 10^{-10}$
Std. C1007	$0.43(2) \cdot 10^{-10}$	1.25(5)	$0.535(3) \cdot 10^{-10}$
Blank	$3.45^{+0.61}_{-0.43} \cdot 10^{-13}$		$4.15^{+0.74}_{-0.56} \cdot 10^{-13}$

Table 3.7: Measured ratios for the three materials. The correction factors of the two standards are equal within their error and resulted in a final factor for the measurements of $c_f = 1.20(5)$. This value was used for correcting the blank value which results in the corrected ratio of $^{14}C/^{13}C = 4.15^{+1.86}_{-3.59} \cdot 10^{-13}$. The correction factor is comparable to the value of 1.19 achieved for the routinely performed measurements at the 6 MV Tandetron accelerator AMS setup. The blank value is slightly higher which is sufficient for the shown magnitude of ratios and would have to be investigated for smaller ratios.

[8] Dr. Stefan Heinze, Private communication

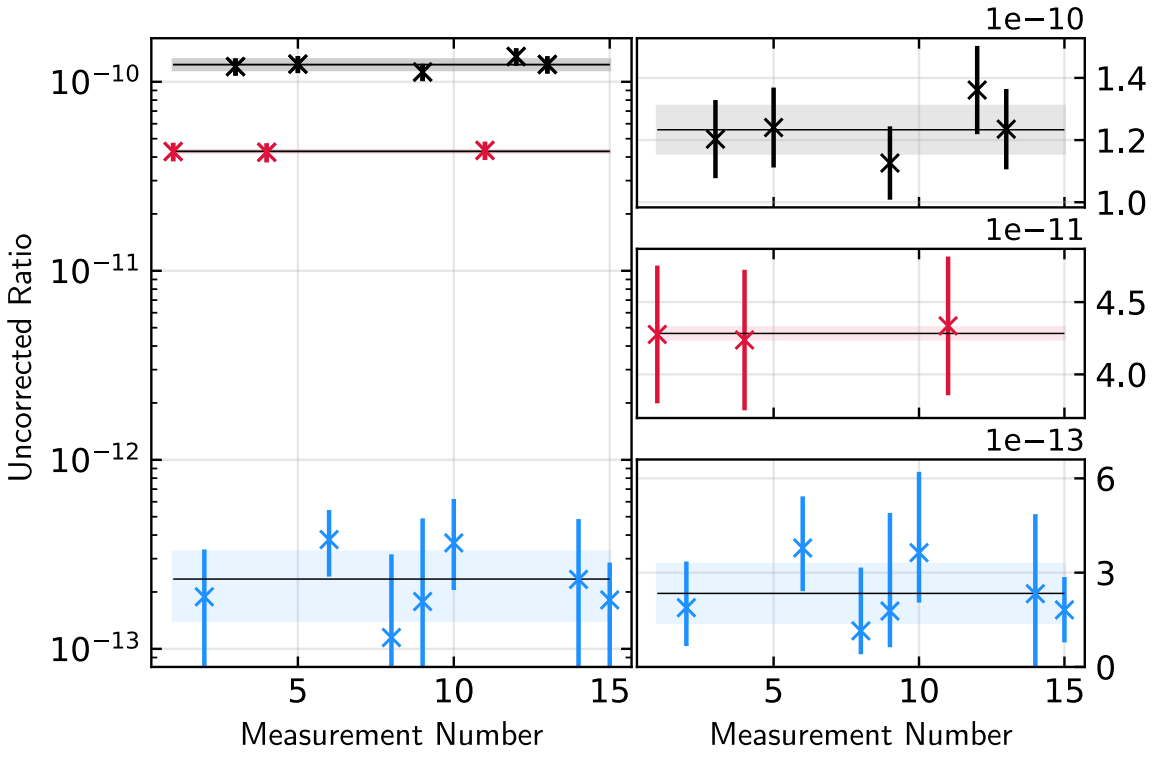

Figure 3.14: The left logarithmic plot shows the individual uncorrected $^{14}C/^{13}C$ ratios in order of their measurement. Thereby, the black ones correspond to the C1002 material with $^{14}C/^{13}C$=1.444(7)$\cdot 10^{-10}$, the red one to the C1007 material with $^{14}C/^{13}C$=0.5535(3)$\cdot 10^{-10}$ and the blue-colored values indicate the blank samples. The right plots show zoomed in versions of the three different ratios on a linear scale. The horizontal lines in all plots indicate the mean value and the underlying boxes indicate the standard deviation.

3.2.3.4 Background investigations

The measurements showed that the system is now capable of long-term routine AMS measurements of sample sequences. The correction factor and the corresponding transmission is comparable to the achieved transmission at the Cologne 6 MV Tandetron accelerator with a value of 1.19 where these measurements are performed routinely. The blank level is two to three orders of magnitudes lower than the measured standard values which would be sufficient for this level of ratios. Through measurement results from the 6 MV Tandetron accelerator it can be concluded that this background does not come from the material itself. There are several possible sources for this background. The first could be the preparation of the sample cathodes which may not be sufficiently clean concerning carbon contamination. Secondly, there could be a memory effect from within the ion source due the usage of the standard material with magnitudes up to 3 times higher than the achieved blank value. At last, it was reported that detector interferences were observed which was assigned to stable carbon ions which experience additional recharging in the second acceleration step of the tandem accelerator, [66]. For the inspection of the latter, a silicon detector was set up at the end of the offset-cup chamber at position of the optical axis and a $^{14}C^{4+}$ background energy spectrum was measured. The detector was equipped with a 3 mm aperture, so that explicitly the

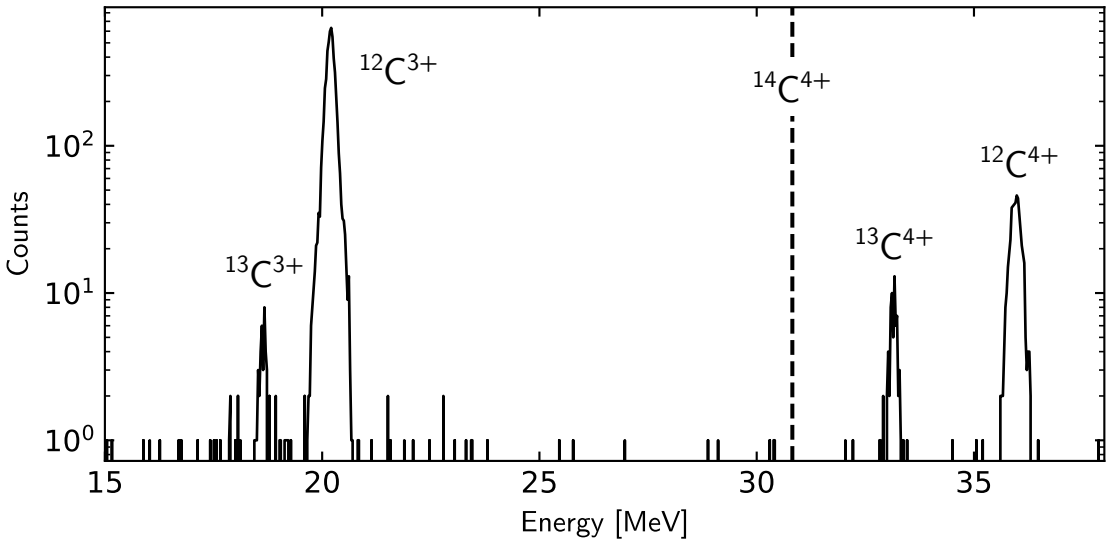

Figure 3.15: The plot shows the calibrated energy spectrum of carbon blank material after the high energy magnet. It was captured with a silicon detector on the optical axis at the end of the offset-cup chamber. All settings for the low and high energy side were set for $^{14}C^{4+}$ ions. The energy calibration was done by injecting the reduced macroscopic ion beams of $^{12}C^{3+}$,$^{12}C^{4+}$ and $^{12}C^{5+}$. The assignment of the peak is based on calculations at which energies the shown components would have the same $\frac{p}{q}$ value as $^{12}C^{4+}$ which fitted the peaks almost exactly, see tab. 3.8.

ions, which leave the high energy magnet straightly on the optical axis, are captured. Firstly, the reduced macroscopic ion beams of $^{12}C^{3+}$, $^{12}C^{4+}$ and $^{12}C^{5+}$ were injected into the silicon detector for calibration purpose. Subsequently, the setup parameters were set for $^{14}C^{4+}$ on the low and high energy side and a background spectrum after the high energy magnet was captured, see fig. 3.15. The captured ions must have the same $\frac{p}{q}$ value since they exit the HE analyzing magnet on the optical axis. Possible candidates are the abundant ^{12}C and ^{13}C which are also injected into the accelerator as $^{12}CH_2$ and ^{13}CH respectively. The energy which leads to the same $\frac{p}{q}$ values as $^{14}C^{4+}$ for the candidates are listed in tab. 3.8. They fit the measured peaks of the silicon detector spectrum almost perfectly. It is also stated which one-fold recharge process could have taken place and after which fraction of the second acceleration step it would have occurred to deliver the shown energy. Thereby, x is the fraction of the acceleration path in which the ion was in its initial charge state Cs_1 and the final charge state Cs_2. These can be calculated by the following equation:

$$E_{HE} = E_{LE} + x \cdot (TV \cdot Cs_1) + (1 - x) \cdot (TV \cdot Cs_2) \tag{3.9}$$

$$\Rightarrow x = \frac{E_{HE} - E_{LE}}{TV \cdot (Cs_1 - Cs_2)} - \frac{Cs_2}{Cs_1 - Cs_2} \tag{3.10}$$

In this E_{HE} is the final energy of the ion, E_{LE} is the energy corresponding to the energy of first acceleration step and TV the accelerator terminal voltage considering only one-fold electron capture and loss processes. Thereby, it is assumed that the component which leads to interference in the detector scatters at the end of the ESA at the outer plate, [66]. Since the ESAs voltage is set for the $\frac{E}{q}$ of $^{14}C^{4+}$ the positional deviation of other components can be calculated by their differing $\frac{E}{q}$ value. Therefore, the electric rigidity dispersion for the ESA was calculated within the LIMIOPTIC2 simulations which can be used for calculating other ion beam components deviations

	E(Calculated)[MeV]	E(Peak)[MeV]
$^{13}C^{3+}$	18.67	18.67(29)
$^{12}C^{3+}$	20.23	20.21(19)
$^{12}C^{4+}$	33.19	33.18(21)
$^{13}C^{4+}$	35.96	35.99(63)

	q_i	q_f	x[%]	$\Delta\frac{E}{q}$[‰]	Δd[mm]
$^{13}C^{3+}$	2	3	92	−19.23	48.08
$^{12}C^{3+}$	2	3	58	−12.50	31.24
$^{12}C^{4+}$	5	4	46	16.67	−41.68
$^{13}C^{4+}$	5	4	98	7.70	−19.24

Table 3.8: In the upper part of the table the stable carbon components are listed which have the same $\frac{p}{q}$ values as $^{14}C^{4+}$, their corresponding calculated energies and the calibrated energies from the peaks of the silicon detector energy spectrum. In the bottom table it is stated which charge state processes could lead to the explicit energies. Thereby, it is considered that the component is injected as a molecule with mass 14. The shown assumed processes consider one-fold electron capture and loss processes from the initial charge state Cs_1 to the final charge state Cs_2. Additionally, it is listed at which fraction x_1[%] of the second acceleration step this would have occurred. Additionally, the difference of the $\frac{E}{q}$ value and the corresponding deviation after the ESA to $^{14}C^{4+}$ is given.

from the optical axis:

$$D_E = 2.5\frac{mm}{‰} \tag{3.11}$$

$$\Delta d = D_E \cdot \Delta\frac{E}{q}[‰] \tag{3.12}$$

The values for the interference candidates can be found in tab. 3.8. The most probable candidate for this would be $^{13}C^{4+}$ which has the least deviation and therefore will hit the outer plate at the furthest back from all considered components. With the first automatic measurements, see subsec. 3.2.4.3, an interference was captured during the injection of ^{13}C into the accelerator, compare fig. 3.18. For a comparison the total deposited energy of the different components within the gas ionization detector was used. It was determined by the sum of all used anodes. These energy spectra were calibrated by the identified ^{14}C peak from the standard material and the respective energy deposition was calculated by use of LISE++. By assuming that the interference component is $^{13}C^{4+}$, the interference energy when entering the detector would be 34.9 MeV. Therefore, the $^{13}C^{4+}$ would have lost around 0.67 MeV in the scattering process at the ESA plate. In a next step this interference component was compared to the total energy deposition of the manually captured background of the blank material. Thereby, all blank measurement energy spectra were summed up to receive a higher statistic. For the final quantitative comparison of the spectra, Gaussian fits were performed for the C1002 standard ^{14}C peak and for the interference peak captured within the automatic measurement. The peak within the summed up blank measurements spectrum consists of only 21 events occupying the same channel. Therefore, no Gaussian fit was possible and the error was taken as half the channel size. The results can be found in tab. 3.9. While the ^{14}C peak of the standard and the unknown signals from the summed manually captured blanks fits within its errors, the interference peak does not fit with the blank signals within its σ interval. This could

Material	Injected mass (LE)	Mode	Mean (E(A1-A7)) [Channels]	Sigma(E(A1-A7)) [Channels]
C1002	14	Manual	105.36(5)	1.49(3)
Blank*	13	Auto	100.66(4)	1.39(2)
Blank	14	Manual	104.5(5)	-

Table 3.9: Comparison of the total deposited energies in the gas ionization detector of ^{14}C, the assumed interference component ^{13}C from the automatic measurements and the background from the blank measurements. The first two rows show the Gaussian fit values corresponding to ^{14}C in the C1002 material and assumable ^{13}C from the automatically captured blank material within the time period of injecting stable ^{13}C in the accelerator. The last row shows the value from all manually measured blank materials added up. Overall only 21 events were measured within the blank within the same channel which is taken as the mean. The error is given as half the bin size. It can be seen that the mean values of the ^{14}C and the background in the manual measurement matches well. Otherwise they do not fit with the assumed ^{13}C within its σ interval. This could be an indication that ^{13}C does not cause the interferences within the blank measurement.

be an indication that the interference in the manual blank measurement is indeed ^{14}C and not the observed interference of the automatic measurement. Since these are the only data to this question and the counting statistics of the blanks is low even when summed up (21 events), these results can only be taken as an indication rather than a final determination. If measurements with lower background level should be performed at the 10 MV AMS beam line, the different options have to be investigated further.

3.2.3.5 Discussion

The performed measurements showed the long-term stability of the system with high transmission which was the goal of the stated improvements in the chapter. Moreover, first sample sequence measurements could be performed. The ion source output was sufficiently high to perform measurements with statistical significance for ^{14}C/^{13}C ratios in the order of 10^{-10}, which can be translated to ^{14}C/^{12}C ratios in the order of 10^{-12}, in the range of 10 minutes or less. The transmission throughout the system remained stable at the reported high values. The correction factor of c_f=1.20(5), corresponding to a transmission of 83% on the high energy side, is equivalent to values reached at the tandetron system of c_f=1.19. The AMS system was stable and allowed measurements over the course of several days. The stability of the accelerator was the only drifting component. This effect especially impacts the AMS beam line since the accelerator can only be used in GVM control mode which does not keep the energy as exact as slit control. The long-term drifting effect could be seen in lowered correction factors and increasing blank values. The terminal voltage was subsequently corrected and the corresponding individual measurements were neglected. The reason for these drifts and their quantitative effect are not investigated in further detail. As long as the drifts are not resolved, especially for automatic measurements, see subsec. 3.2.4, it could be useful to introduce a condition to stop the acquisition at major differences in the particle rate of blank measurements. Furthermore, systematic investigations concerning the impact of these drifts should be performed. This could be possible using narrow analyzing slits and additionally their captured current values. A long-term logging of these values in combination with the value of

a subsequent Faraday cup and in addition to a digitized value of the terminal voltage could be used. Furthermore, in the course of these investigations, the comparison of energy spectra after the HE magnet by a silicon detector, like fig. 3.15, and one additionally positioned detector after the ESA would improve the understanding of the occurring background components. In summary, the system is now capable to perform long-term AMS measurements with high ion source output and high transmission and is only dependent on the stability of the accelerator. This enables the measurement of large sample sequences which is mandatory for every AMS measurement.

3.2.4 Automatic AMS measurements

A high degree of digitization of the setup control and the measurement data recording allows an advanced level of reproducibility and efficiency in experimental measurements. At the commercially purchased 6 MV Tandetron accelerator AMS setup, all crucial components are read out and controlled digitally. Due to the implemented connection to the data acquisition system MPA-3, [67], even low particle beams in the range of a few Hertz can be optimized by the existing software methods. Moreover, the final AMS measurement of samples can be performed automatically. Without automation of the AMS measurement, the experimenter has to switch between the different isotopic beams, log the electric current and handle the particle data acquisition manually. It requires permanent high concentration of the experimenter and leads to an unavoidable degree of uncertainty for the read-out and measurement time consistency. Therefore, in a stable setup there are only advantages in using automatic measurements since it provides a high degree of reproducibility and minimizes incomprehensible human errors. For that purpose, the 10 MV AMS setup control software already delivers the necessary degree of digitization. The basic framework of the components for automatic measurements except the rare isotope data acquisition were already set up. Thereby, the read-out of the offset-cup current was digitized by use of dedicated preamplifier from *Stanford Research Systems* for low-noise and fast read-out. The timing of the ion beam switching and the corresponding timed choice of used data acquisition is done by an Arduino micro controller. The Arduino is currently not coupled to the particle data acquisitions directly but only the main computer of the setup. A detailed explanation of this can be found in reference [47]. This subsection will explain how the MPA-3 data acquisition was coupled to the LabView control software. The new possibilities for particle beam tuning are described and the first performed automated measurements of ^{14}C and ^{60}Fe standard material and blanks are shown.

3.2.4.1 Coupling of the particle data acquisition

The data acquisition system used at the 10 MV AMS system is equivalent to the one used at the Tandetron AMS system. The MPA-3 Multiparameter system from FAST ComTec can handle up to 16 different ADC inputs and transfers them as listmode files to the acquisition computer. The available setup at the FN is equipped with 8 input channels. These inputs are analog to digital converter (ADC) signals in explicit. The related MPANT software is a graphical user interface and allows the online processing of the received information. The program provides the handling of the recorded events as single or coincident events. The data can be displayed live in one- and sorted two-dimensional spectra. In these spectra regions of interest (ROI) can be set and the

number of events inside the region is given directly. Both the raw and processed data is saved on the computer to allow offline analysis. By use of an additional available Dynamic Link Library (DLL) external control of the MPANT Software is possible. Therefore, a small in-house developed program is available which processes incoming TCP/IP (Transmission Control Protocol/Internet Protocol) commands and allows the communication with and control of the MPANT software[9]. Within this thesis the DLL was adapted and the command set was extended. These commands can be separated in the control of the data acquisition and the queries of acquisition information. The final command list which can be used from the LabView control software is the following:

- "Start" : Starts the data acquisition and erases previous recorded spectra
- "Stop" : Stops the data acquisition
- "Continue" : Continues a stopped acquisition
- "Livetime" : Provides the Livetime of a single ADC
- "Realtime" : Provides the Realtime of a single ADC
- "TotalCounts" : Provides the total number of counts in a specified spectrum
- "ROICounts" : Provides the number of counts in a specified supporting spectrum within MPANT associated with a ROI

It is not possible natively to receive counts within a ROI from an external source from the MPANT software, so a further step has to be prepared. An additional supporting spectrum has to be created which contains only counts associated with the ones in the ROI. This can be accomplished by adding a so-called condition relation to the set ROI within MPANT. Subsequently, a two-dimensional spectrum identical to the one in which the ROI is located has to be created with the given condition. By receiving its total counts, the ROI counts are given. Therefore, the command "ROICounts" is programmatically the same as "TotalCounts". The associated spectra for these commands can be set in an external setup file. Within the Phoenix software a set of subprograms so-called *Virtual instruments* (VI) are programmed for the communication with the data acquisition. Furthermore, the chosen ROI counts are included as a fixed variable within the Phoenix software, so that the established tuning methods can be used to process the data. The two most useful applications for that are given in the following subsections.

3.2.4.2 Detector rate tuning via the control software

For the optimization of particle beams an analog rate meter can be used for processing signals of one individual main amplifier. Since no sophisticated discrimination of the incoming signal is possible it can become impossible to optimize the desired isotope rate when interferences are present. In the case of low rates in the range of Hertz it is almost intrinsically impossible to optimize manually. By the performed coupling of the data acquisition to the setup control software every coincidence and condition chosen in MPANT can be transferred to the associated rate in the control software. With evaluating the corresponding timing information the rate of specific incoming particles can be determined. Thereby, the problem with interferences on single anodes

[9]Dr. S. Heinze, Private communication

vanishes and the discrimination is only limited by the detector or data acquisition limits. Also for the overall tuning procedure, the enabling of tuning methods like trending or tracing in dependence of the ROI rate significantly improved the particle beam optimization. In detection setup II, see fig. 3.1, it includes tuning to the gas-filled magnet entrance by a specially positioned silicon detector in front and finally into the gas ionization detector behind the gas-filled magnet. Over the course of subsequently tracing components and choosing the ideal values the best possible transmission is achieved. Example plots of the tuning process of the detector rate is shown in fig. 3.16. Thereby, examples of different traces of setup components are given and also examples of different magnitudes of count rates. Furthermore, an example of tracing with and without using the discrimination by a ROI condition is shown for the example of ^{60}Fe. Furthermore, in the case of low particle rates, which

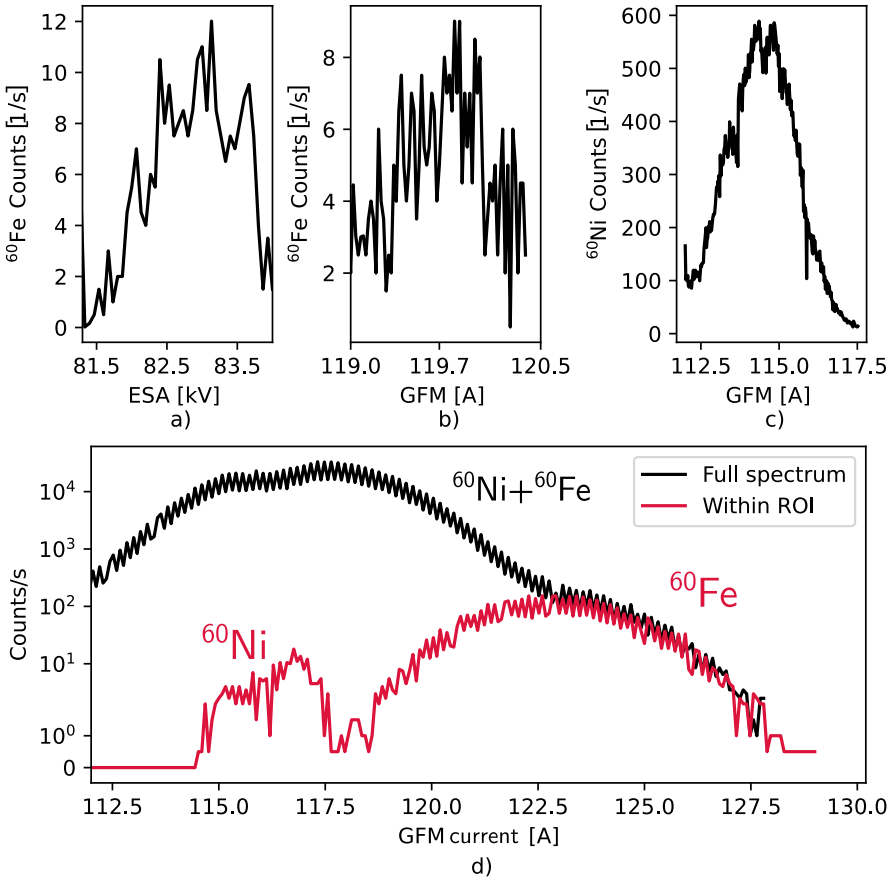

Figure 3.16: The upper plots show automatic traces on detector count rates. Thereby, plot a) and b) show the traces on detector count rates within a respective set ^{60}Fe ROI in dependence of the ESA and the GFM current values. For comparison an example of ^{60}Ni within a designated ROI with high statistics and low fluctuations is given in c). The fluctuations in the rate are caused by the low statistics within the measurements on the one side and by the timing of the interplay between control software and actualization time in MPANT. Plot d) shows the combined spectra of GFM traces on detector count rates with and without the discrimination to the ROI of ^{60}Fe. In the chosen example the plain separation of the GFM is not sufficient to identify the ^{60}Fe peak. Using the ROI within the tuning is the only way to determine the optimal magnet value for ^{60}Fe.

are challenged by their statistical fluctuations, the tuning procedure with the control software is the only practical option. It has to be mentioned that when using all available channels within MPANT the update times of an individual ADC channel is increased significantly. By reading information

from an external source like the control computer the readout can become faster than the MPANT actualization time. Currently this leads to small fluctuations in the rate. For compensation of these fluctuations or in case of smallest count rates, the possibility of using averaged values over a set number of last recorded values is implemented within the tuning methods. In the trending function the number of the averaged values can be changed dynamically while the program is running. In the tracing function the number of averaged values has to be set prior to starting the trace for consistency reasons within the trace.

3.2.4.3 First automatic measurements and limits

With the successful integration of the data acquisition to the control software, the option for automatic measurements became available. Therefore, subsequent to the two successfully performed AMS measurements of ^{14}C and ^{60}Fe, an additional automatic measurement was performed. Within an automated AMS measurement the injection of the different isotopes is handled automatically and combined with read-out and processing of the corresponding data acquisition results. The overall measurement time is chunked into smaller parts, called blocks, which holds the results of the respective measurement duration. In each block, several injection cycles of both isotopes with their specific data acquisition handling are performed with a prior defined schedule. Thereby, one single cycle consists of the measurement of injecting the abundant isotope and acquisition of the ion beam current and subsequently switching to the rare isotope and acquisition of the particles and the life acquisition time. The schedule should be chosen to consist of as many cycles within one block as reasonably possible. In preparation to an automated measurement the current integrator for the abundant reference isotope has to be set to the appropriate sensitivity for optimal ion beam current resolution. This can be done at the front panel of the dedicated preamplifiers and checked with the newly programmed digital current read-out program within the control software. Furthermore, the TCP connection to the data acquisition has to be established and the MPANT spectrum has to be prepared to provide the ROI count rate as described in subsec. 3.2.4.1. Ideally the general settings in MPANT are chosen for saving automatically at *Halt* and also incrementing the measurement number automatically. By starting the single measurement within the LabView control software the settings for the measurement have to be defined. A detailed explanation can be found in reference [47]. Firstly, the mode 'Stable and Rare' has to be chosen. In the next context menu, the sensitivity of the current integrator as formerly set is defined, so that the program interprets the acquired signal correctly. Furthermore, the stop condition, the block time and the location for saving the results has to be given. Thereby, the stopping conditions can be the number of blocks, the overall counts or both, which means the first met condition stops the measurement. The overall measurement time is defined by the stop condition and is at least the number of blocks multiplied by the block duration. In a last step the bouncer settings have to be defined by defining the cycle time for the abundant and rare isotope acquisitions in each cycle individually. By use of a gate signal to the control software the abundant isotope current is only acquired while injected. Since there is currently no continuous read-out of the particle counts by the control software but only the received total number of counts within its complete cycle time, a gate condition in the control software, equivalent to the case of stable beam acquisition, is not applied. The corresponding live time for the rare data acquisition is calculated within the control software. Furthermore, a waiting time should be defined which is used to compensate the time of

the ion beam switching. The sum of all timings defines the overall cycle duration. The settings for the performed automated measurement for each isotope are listed in tab. 3.10. At the end of the automated measurement the detector spectrum is saved within MPANT and a result file is saved on the setup control computer. Within this result file all general information is stored as well as the individual block values and the final result. By receiving these block results a more designated offline analysis is possible.

Isotope	Stop condition	block time[s]	Cycle time(Abundant)[ms]	Cycle time(Rare)[ms]
C	20 blocks	20	1400	7400
Fe	200 blocks	30	500	10000

Table 3.10: The list shows the settings of the automated measurements. The summed up acquisition times of rare and abundant isotope and the wait time gives the complete cycle time. It defines how often the beam is switched within one block. All data received within one block is averaged to receive one result per block. These parameters can be freely chosen.

First automatic measurements were performed at the end of each AMS measurement within this thesis, see subsec. 3.2.3 and 5.6.2. The recorded detector spectra and comparison of the manually captured data to the automatically acquired results for one standard and one blank material respectively can be found in fig. 3.18 for ^{14}C and fig. 3.17 for ^{60}Fe by use of the small detector window, as an example. The corresponding numerical results can be found in tab. 3.11. In both measurements the beam switching and synchronous recording of the respective injected beam worked successfully. Considering the ^{60}Fe measurements, the isotopic ratio results of manual and automatic measurements are equivalent within their errors by use of the gas-filled magnet in combination with the small detector entrance window. The other values, like the stable isotope current and the particle count rate, do not have to be the same in both measurements since they were not captured synchronously but subsequently. The automatic standard material measurements were performed at the end of the respective experiment weeks and the sample life approached its ending. Therefore, within the time span between the start of the manual measurement and automatic measurement the sample output may have decrease. In the ^{14}C measurement it revealed that an interference component occurred while injecting the stable isotope beam on the low energy side. Possible candidates for this interference were discussed in subsec. 3.2.3.4. By use of an adjusted ROI and the background correction the result for the standards are equivalent within their errors. The obvious disadvantage is unavoidable rejection of true signals which leads to a worse transmission and more important an order of magnitude higher background level. Both effects lead to unnecessarily worsened results but can fortunately be solved by further adjustments. While the stable isotope is injected the rare isotope in the chosen molecular form can not pass the low energy mass spectrometer and therefore no true signal can be recorded by the gas ionization detector. Therefore, there are different ways to solve the recording of the irrelevant interferences. One way could be to time the data acquisition per LabView-command. Thereby, a logic gate to the control software could be taken from the Arduino which manages the timing of the bouncer. The delay of the gate signal transfer has to be integrated into the wait time. In alternative the interference could be stopped before entering the detector by use of a Faraday cup or a steerer. The Faraday cup option was

tested but is not recommended due to the higher stress on the Faraday cups pneumatic which leads in the worst case to damages causing vacuum leakages. Both options will not allow bouncing in the lower millisecond region. A last option is already used at the 6 MV Tandetron accelerator where a logic gate is directly connected to the MPA data acquisition to inhibit signals. This is equivalently applicable at the 10 MV system and should be implemented in the future.

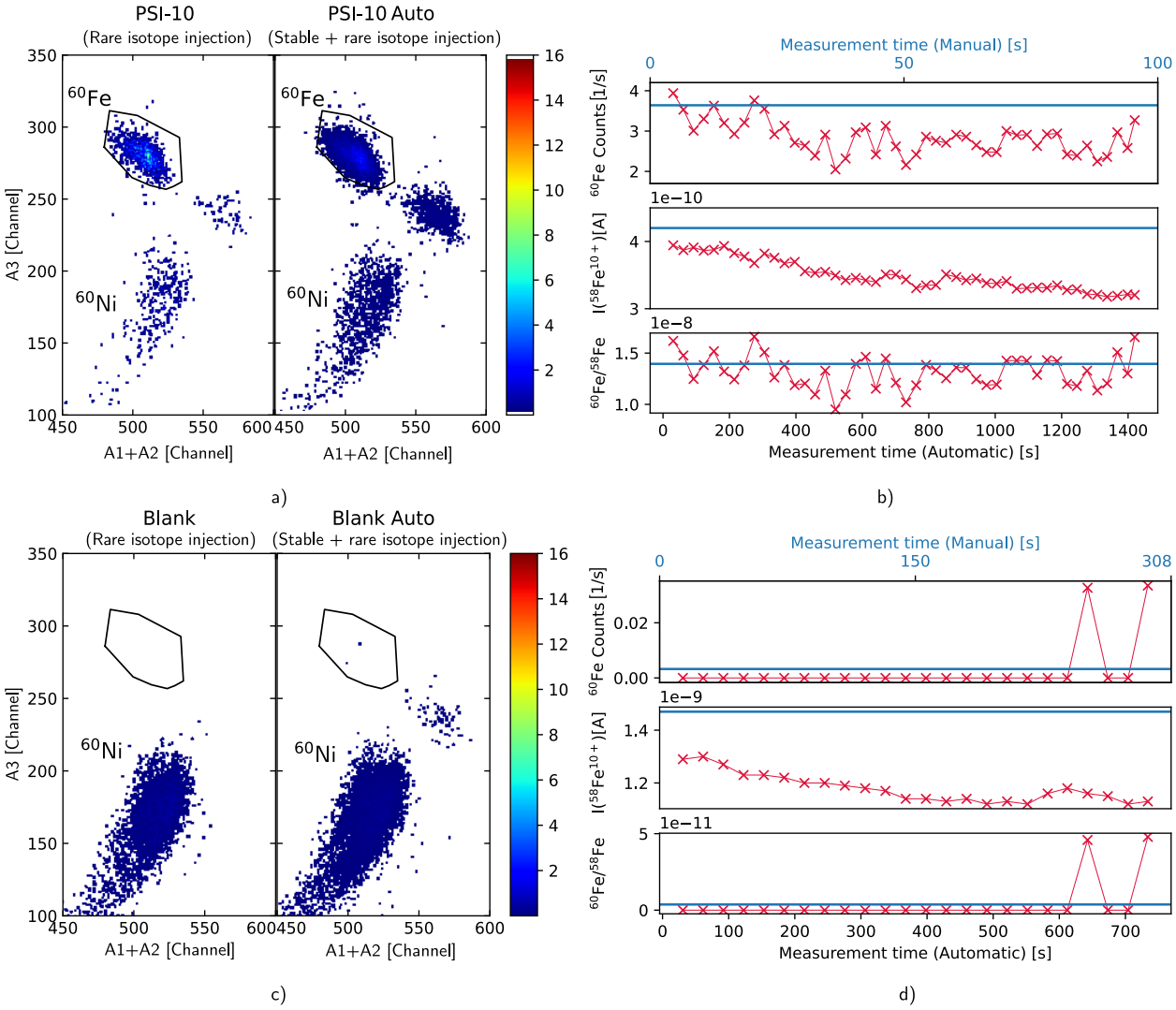

Figure 3.17: The plots show the comparison between subsequently performed manual and automatic AMS measurements of a ^{60}Fe standard (PSI-10: ^{60}Fe/Fe=1.124(3)·10^{-10}) by use of the small detector window, a) and b), and blank material, c) and d). Plots a) and c) show the respective detector spectra and ROIs for the measurements. Plots b) and d) present the taken values within the measurement times. In manual measurements the mean value of the rare isotope particle rate over the measurement time represents the whole measurement duration. The manual measurement values are indicated by the blue constant lines corresponding to the measurement duration above the plots. The red values represent the subsequently performed automatic measurement. The recorded values represent each an individual measurement block. The automatic measurement routine delivers the same results as the manually measured within their errors.

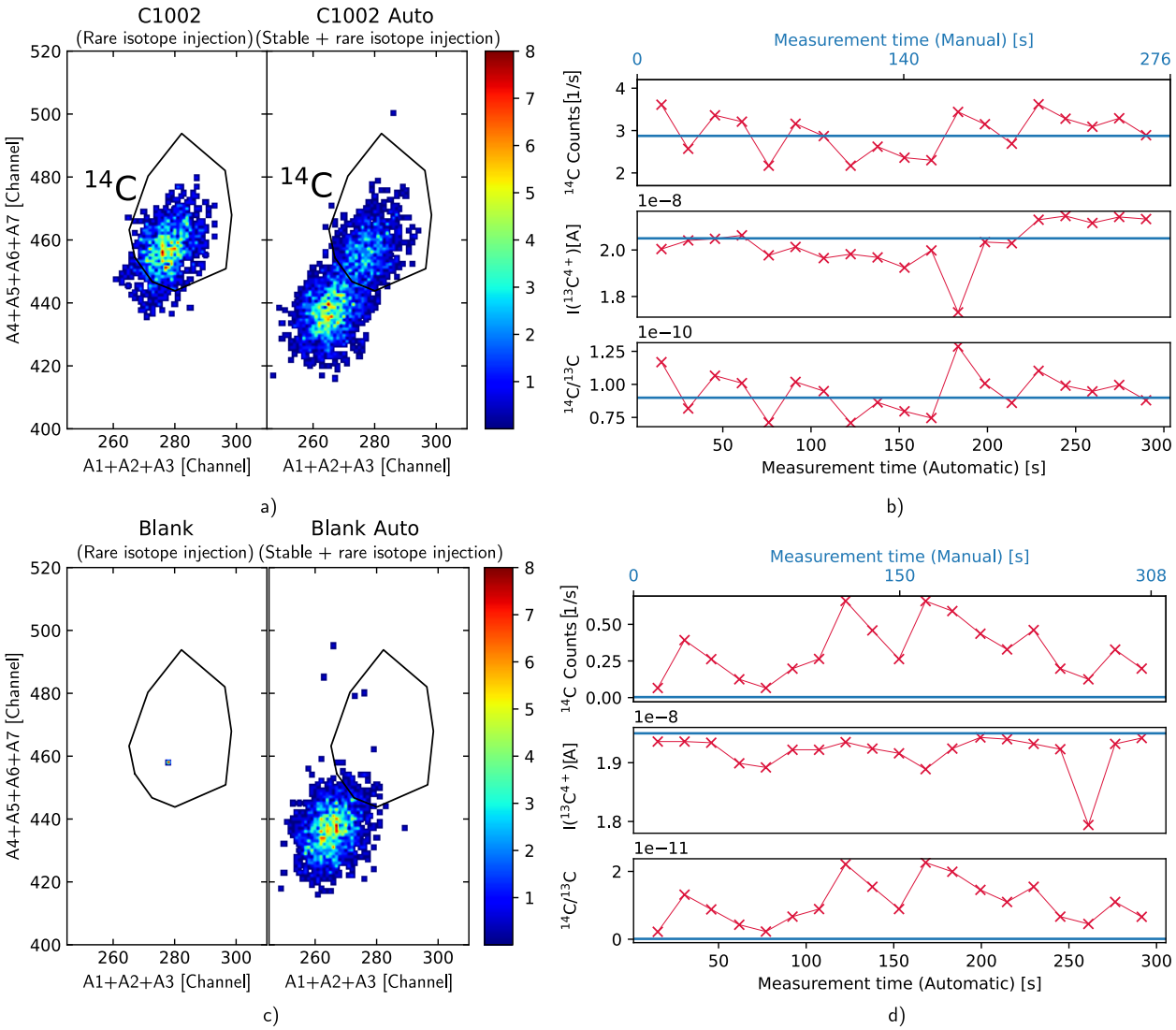

Figure 3.18: The plots show the comparison between subsequently performed manual and automatic AMS measurements of a ^{14}C standard (C1002: $^{14}C/^{13}C$=1.22(3)·10^{-10}), a) and b), and blank material, c) and d). Plots a) and c) show the respective detector spectra and ROIs for the measurements. Plots b) and d) present the taken values within the measurement times. In manual measurements the mean value of the rare isotope particle rate over the measurement time represents the whole measurement duration. The manual measurement values are indicated by the blue constant lines corresponding to the measurement duration above the plots. The red values represent the subsequently performed automatic measurement. The recorded values represent each an individual measurement block. While the automatic measurement routine worked well, it can be seen that an interference component disturbs the measurement while injecting the stable component. Future options to avoid this effect are described in the text.

Material	Meas. type	$\bar{I}$[nA]	Count rate[1/s]	Meas. Ratio:$^{14}C/^{13}C$
C1002	Manual	20.50(205)	2.871(98)	$8.97(95)\cdot10^{-11}$
	Auto	20.23(95)	2.760(100)	$8.74(52)\cdot10^{-11}$
C blank	Manual	19.50(195)	$0.003^{+0.006}_{-0.002}$	$1.09^{+1.90}_{-0.70}\cdot10^{-13}$
	Auto	19.18(33)	0.31(3)	$1.00(11)\cdot10^{-11}$
Material	Meas. type	$\bar{I}$[nA]	Count rate[1/s]	Meas. Ratio:$^{60}Fe/^{58}Fe$
PSI-10	Manual	0.42(4)	3.56(11)	$1.36(14)\cdot10^{-8}$
	Auto	0.35(2)	2.84(4)	$1.30(7)\cdot10^{-8}$
Fe blank	Manual	1.40(14)	$0.0032^{+0.0057}_{-0.0021}$	$3.72^{+6.55}_{-3.72}\cdot10^{-12}$
	Auto	1.18(5)	$0.0027^{+0.0031}_{-0.0017}$	$3.72^{+4.25}_{-2.46}\cdot10^{-12}$

Table 3.11: The table lists the result of the manually and automatically received results for AMS measurements of ^{14}C and ^{60}Fe standard and blank materials. The differing stable isotope currents $\bar{I}$[nA] within one sample are caused by the ending sample life span since the automatic measurements were performed subsequent to the manual measurements. The automatic measurements were successful and the results are similar and more accurate than the manually achieved one. An exception to this is the blank measurement of ^{14}C. While injecting the stable beam an interference component reached the detector and caused background. Different steps to avoid this are described in the text.

In conclusion, the structure of automated measurements was successfully tested and delivers accurate results. It could already be used by combining further suppression steps like the gas-filled magnet with a small detector entrance window, see subsec. 5.6.5.5 for an explanation of the impact of the used window size.

4 Investigation of the 135° gas-filled magnet

The gas-filled magnet is the key element for the isobar suppression in ^{60}Fe AMS measurements at the Cologne setup. The transmission loss up to the last Faraday cup in front of the gas-filled magnet was investigated and resolved, see subsec. 3.2.1.4. The remaining flightpath concerns the distance to and through the gas-filled magnet and subsequently into the gas ionization detector. Therefore, the goal of the presented investigations were the determination of the optimal gas properties for ^{60}Fe in Cologne and an overall better understanding of the inner lying ion beam development. This chapter describes the measurements conducted for the determination of the beam shape and trajectory development throughout the flightpath of the ions through the gas-filled region by newly built detector units. Thereby, two gas types, helium (He) and nitrogen (N_2) were used for a range of gas pressures. Furthermore, the beam shapes after passing the gas-filled magnet were captured at the same gas types but at higher ranges of pressures. At the determined best gas option the two-dimensional ^{60}Fe beam profile was captured and analyzed in terms of transmission to subsequent detector entrance windows. At a last experiment the separation factors between ^{60}Ni and ^{60}Fe were determined for different nitrogen gas pressures. The results from the measurements within the gas-filled magnet were used to improve a Monte Carlo code for gas-filled magnet isobar separation,[23]. Finally, all experimental values were simulated and compared with different available simulation codes.

4.1 Ion beam shape and trajectory investigation through the gas-filled magnet

The choice of gas type and pressure is a crucial condition when operating a gas-filled magnet for AMS. Both factors determine the discrimination between isotope and isobar and therefore the isobar suppression. Furthermore, they determine the beam shape and width after the magnet which has to be taken into account in the design of the subsequent isotope identification detector, for example the gas ionization detector. To get a better understanding of the beams behavior in terms of trajectory and width, respective measurements within the gas phase were conducted. Since this type of measurement was performed for the first time, a new detector setup was designed and built. It aims for measuring the position and width of the particle beam after different flightpaths inside the gas-filled magnet. In this section, the design and installation of these detector units at the 135° magnet will be described. Furthermore, it will be reported on the measurement conduction and the analysis. Finally, the results are presented and discussed.

4.1.1 Setup

The 135° dipole magnet at the Cologne 10 MV AMS system is equipped with seven outward ports. Two of these are viewing ports for the purpose of alignment and five are radial ports which are orthogonal to the optical axis and equally distributed by an angle of 22.5°. Therefore, the viewing ports were suitable candidates for the insertion of small detector units for the measurement of the beam position and beam shape. A drawing of the magnet design and the inserted detector setups for the measurement, described hereinafter, can be found in fig. 4.1 a). Due to the limited space, it was decided to measure the beam profile only in the dispersive axis. The dedicated detector units had to meet several requirements concerning the measurement process and the technical installment. For retaining the measurement conditions within related individual measurements, it was mandatory to keep the gas state. Furthermore, since the overall measurement of different gas properties requires an extensive range of individual measurements, the respective duration of each has to be kept as short as possible while still receiving sufficient statistics. Thereby, a balance has to be achieved between the size of the measured positional area and the degree of resolution since an increase in both corresponds to higher expenses in cost, construction and signal processing. For this first approach, it was decided to use a row of solar cells as particle counting detectors within each detector unit. By the assumption of a Gaussian beam profile, the number of signals in each cell delivers the integral over the respective Gaussian area, see an example in fig. 4.1 d). A dedicated mount was designed which can hold up to seven solar cells with each an area of $1\,\mathrm{x}\,1\,\mathrm{cm}^2$. Recesses were added for the guidance of signal cables of the solar cells which in summary lead to a compact design. A drawing of the mount of one detector unit can be seen in fig. 4.1 b). For the mounting at the magnet ports the detector units were placed in fixture pipes, see fig. 4.1 c) for a final picture of an individual detector unit. In the current design the outer cell projects over the edge of the mount, which has the risk of harming the cell in operation or installment. This should be improved in a future design step. To allow the fixtures movement along the dispersive axis without breaking the gas state, these are installed at the radial ports with manufactured feedthroughs. The concept is equivalent to the one used for the nuclear magnetic resonance (NMR) probes fixtures, [47]. At the outer end, an individually removable adapter was built with two fourfold Lemo vacuum feedthroughs which is again implemented with the formerly mentioned vacuum feedthrough design on the fixtures. The solar cell signal cables are connected to Lemo connectors. For an absolute scale of the position measurement, the fixtures were moved inwards as far as possible during the first installment and the position was marked outside as reference. Since the beam is blocked while being detected, it can only be captured at one single port position at a time. To allow subsequent measurements at different ports without breaking the gas state, four detector units were built. The last free radial port, port 2, was used for a NMR probe. The detector units were positioned at ports 1, 3, 4 and 5. The associated parameters for angle and assumed flightpath on the optical axis are found in tab. 4.1.

4.1.2 Conduction

For the measurement a ^{60}Ni particle beam was chosen since it was directly available as particle beam from the routinely used ^{60}Fe blank samples. Thereby, an energy of 100 MeV was used to reflect the used ^{60}Fe particle beam energy. It was decided to use the 11^+ charge state. Since the

Position	Port number	Angle [°]	Flightpath along optical axis [mm]
Foil		0	0
1	1	22.5	353
2	3	67.5	1060
3	4	90	1413
4	5	112.5	1767

Table 4.1: The table lists the used ports in the beam profile and trajectory measurements. The approximated flightpath is associated to the path along the optical axis in vacuum at the given angle.

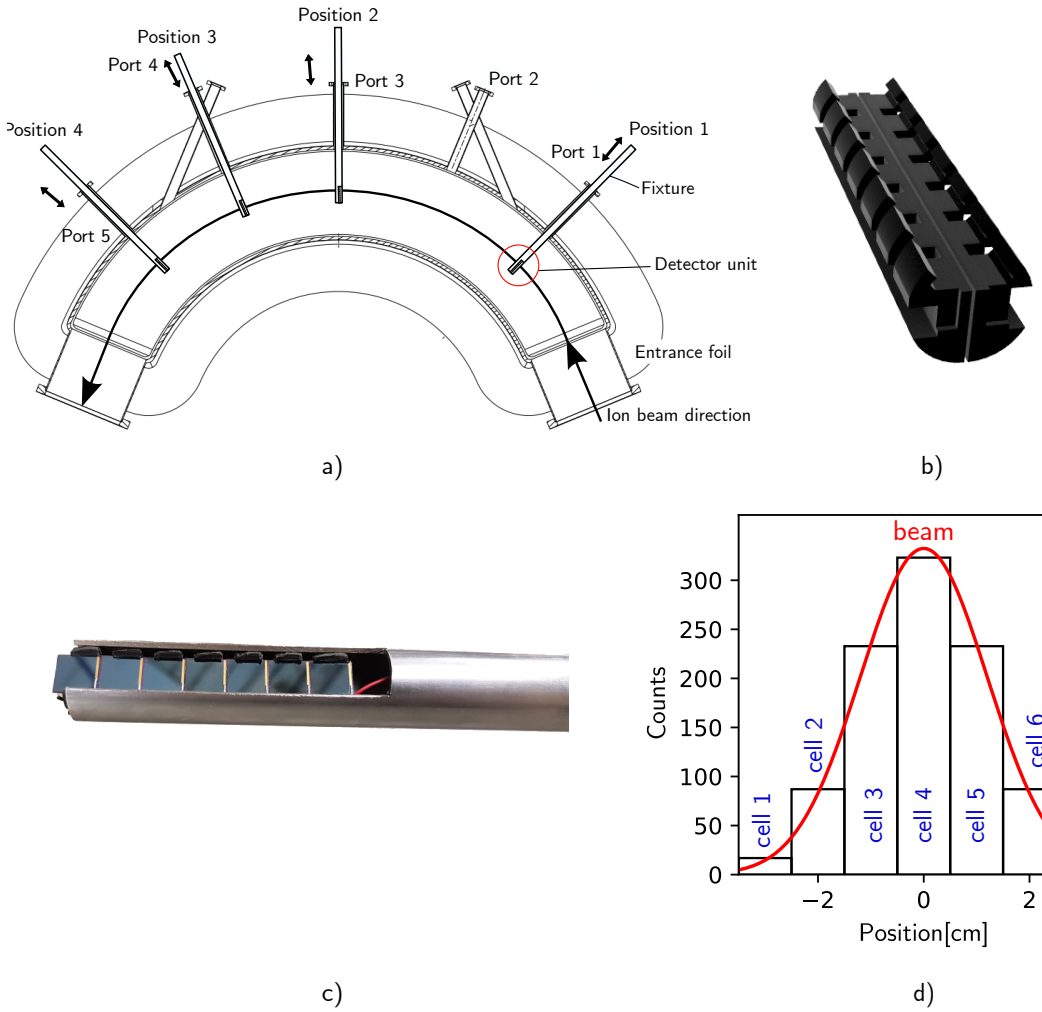

Figure 4.1: Plot a) shows an adapted technical drawing of the 135° magnet. The five radial ports are equally distributed with an angle of 22.5° and orthogonal to the optical axis. The optical axis and the ion beam direction is indicated while it does not represent a realistic particle beam trajectory in gas-filled mode. The solar cells are inserted into a dedicated mount, b). When assembled, this setup is referred to as one individual detector unit. These are again implemented into respective fixtures, c), which forms the final detector setup. Overall four of these were built and positioned at the indicated ports with manufactured feedthroughs at the positions indicated in a). This allowed movement along the dispersive axis without breaking the gas state at the different positions. Plot d) shows an example of the expected particle number spectra in an individual measurement at one position after the analysis. The red line indicates the beam as a Gaussian distribution. The bars correspond to the integral of the respective area indicating the particle number signal received by the individual solar cell.

suppression step of the gas-filled magnet is not yet surpassed in the measurements, interfering components can be observed in the captured energy spectra. For the 11^+ charge state only one other component was observed in the spectra which was clearly differentiable in position and size. By the comparison of the energy spectra different charge states on the silicon detector in front of the gas-filled magnet, the 11^+ was the most suitable. The 10^+ charge state showed several other components with different energies. The 9^+ charge state showed no other components but with the 10 MV FN accelerator 100 MeV are not available for this charge state. However, assuming the formation of the charge state equilibrium through the foil, the final distribution is only negligible dependent on the initial charge state, [21]. For the measurements the magnet entrance foil was a formerly equipped round 2 µm thick Mylar window with 5.8 cm diameter. In a first step the system was tuned using a macroscopic $^{54}Fe^{9+}$ at 90 MeV which has almost identical $\frac{E}{q}$ and $\frac{p}{q}$ ratios as $^{60}Ni^{10+}$, which was initially planned to be used. Subsequently, the ion beam on mass 76 ($^{60}Ni^{16}O$) was injected on the low energy side while the high energy mass spectrometers remained the same. Subsequently, $^{60}Ni^{10+}$ was initially tuned to the silicon detector in front of the magnet entrance. Accordingly, the components were scaled to the $\frac{E}{q}$ and $\frac{p}{q}$ of $^{60}Ni^{11+}$ at 100 MeV and the final particle beam was optimized on the silicon detector for each new measurement series. Within each series, for example the inner beam shape measurements for nitrogen gas, the high energy mass spectrometer settings were left untouched after this initial tuning to the silicon detector. For each new gas pressure only the magnetic field of the gas-filled magnet was adapted. The magnetic field was chosen for highest detector particle rate of the subsequent gas ionization detector with slits of ±1 mm. After the first conducted nitrogen gas measurement the rather large silicon detector, 2 cm in diameter, in front of the magnet was replaced by a smaller one, 0.5 cm in diameter, to define the injection more accurate. Within each gas type or pressure measurement the beam was captured at each angular position subsequently. Thereby, the fixtures were moved by 0.5 cm to achieve a better resolution than the solar cell width and compensate for beam intensity changes over the experiment time, see subsec. 4.1.3. Thereby, the extent of beam intensity fluctuation was inspected beforehand by using an analog rate meter which did not show significant short-term particle beam fluctuation for an integration duration of at least 30 seconds. Therefore, and to achieve enough statistics, the individual measurement duration was 2 to 5 minutes dependent on the beam intensity. The duration varied throughout the positions since the dispersive beam profile widens along the flightpath and spreads over the line of solar cells and in the y-direction. Therefore, the measurement time was prolonged with longer flightpath to reach the same statistics at the later positions. By this method the beam profile and position was measured for 1 to 5 mbar nitrogen gas pressure. For helium similar gas pressures were chosen for a direct comparison of both gases. The investigated pressures were 2, 4, 5 and 7 mbar. In the helium measurements some disturbances or total missing solar cell signals were observed. As formerly described one disadvantage of the design is the fragility of the outer solar cells. Furthermore, due to the compact layout of the solar cell row a certain tension of the cells was unavoidable by the current design. Within the experiment using helium gas it became present that some of the solar cells on the mount of the second position did not work properly anymore. For compensation more individual measurements were performed at this position but their results had to be still neglected in the final analysis.

4.1.3 Data analysis

For the capturing of each individual profile, a step wise scanning along the dispersive axis was performed. From each individual step, seven energy spectra corresponding to the seven solar cells were received. In each spectrum the ^{60}Ni peak was identified and its content was determined to receive the number of events, see fig. 4.2 a). The best approach for this was the sum of the peak counts. The counts in combination with the respective solar cell position can subsequently be used to receive the captured fraction of the beam profile from one individual measurement, see fig. 4.2 b). The combination of these fractions covers the whole measured beam profile, see fig. 4.2 c).

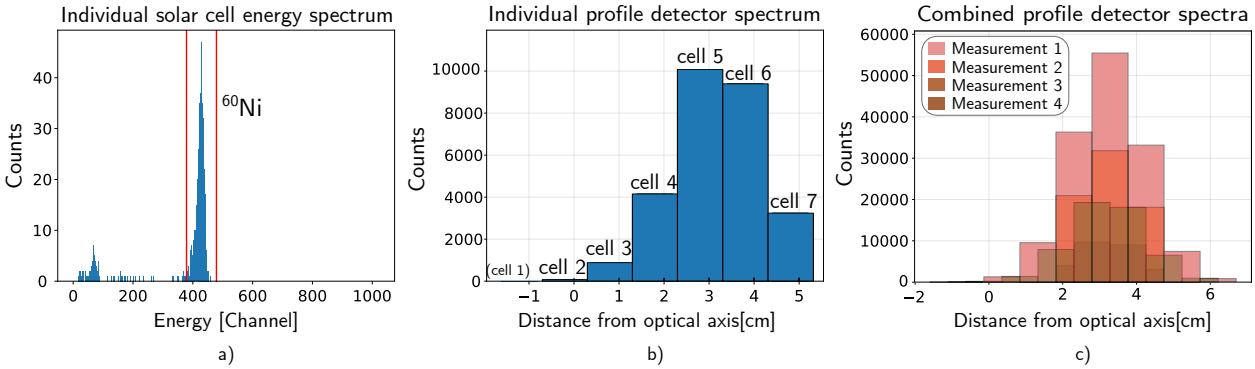

Figure 4.2: Plot a) shows an example of an energy spectrum of one solar cell with the given identification region for ^{60}Ni. Plot b) shows the most inner fraction of the ^{60}Ni particle distribution at the fourth port at 5 mbar N_2 gas pressure. The histogram represents the length of the solar cells on the dispersive plane in which the particles were captured. Plot c) shows all measured profile fractions which are combined to cover the whole profile at the fourth port at 5 mbar N_2 gas pressure.

For a final result, intensity fluctuations over a range of several minutes between different steps of the scanning have to be considered. Since no reference current could be measured due to practical reasons, a direct normalization between different related measurements of one profile is not possible. Furthermore, due to the step size of half a solar cell width not every position was measured within each scanning step which could otherwise have been used for normalization. Therefore, a dedicated analysis has been developed. Thereby, the beam shape is assumed as a Gaussian distribution, see eq. 2.31a, where A is the area under the function, μ is the mean of the distribution and σ the standard deviation. It is valid that the ratio between values at different positions in the distribution stays the same, independent of the total area A under the distribution. Therefore, these ratios were taken for the fit procedure. Thereby, for one profile the ratios of the captured counts between neighboring positions from left to right in beam direction, see eq. 4.1a, were determined in each captured fraction. Considering an underlying Gaussian distribution, the counts captured by a solar cell can be expressed as the integral of the Gaussian over the solar cell width around its position. Therefore, the error function is used which gives the integral from $-\infty$ to a given value of the Gaussian distribution, see eq. 4.1b. For the value of a solar cell at position pos_1, the error function value from its right edge in beam direction, $pos_1 + \frac{cell\ width}{2}$, was subtracted from the error function of the left edge, $pos_1 - \frac{cell\ width}{2}$. This results in the fraction of the Gaussian distribution over the length of the solar cell. Dividing these calculated fractions for neighboring

cells, see eq. 4.1c, give the ratios used for the fit.

$$Ratio(x_1, x_2)_{Exp} = \frac{N_{x_1}}{N_{x_2}} \quad \text{with} \quad x = pos_1 \quad \text{and} \quad pos_2 = pos_1 + width(solar\,cell)$$
$$Ratio(pos_1)_{Exp} = \frac{N_{pos_1}}{N_{pos_2}} = \frac{N_{pos_1}}{N_{(pos_1+width(solar\,cell))}} \tag{4.1a}$$

$$Ratio(x_1, x_2)_{Fit} = \frac{F\left(x_1 + \frac{width(solar\,cell)}{2}\right) - F\left(x_1 - \frac{width(solar\,cell)}{2}\right)}{F\left(x_2 + \frac{width(solar\,cell)}{2}\right) - F\left(x_2 - \frac{width(solar\,cell)}{2}\right)}$$
$$\text{With } F(z) = \frac{1}{2}\left(1 + erf\left(\frac{z-\mu}{\sigma\sqrt{2}}\right)\right) \tag{4.1b}$$
$$\text{and} \quad x_1 = pos_1 \quad \text{and} \quad x_2 = pos_2 = pos_1 + width(solar\,cell)$$

$$Ratio(pos_1)_{Fit} = \frac{F\left(pos_1 + \frac{width(solar\,cell)}{2}\right) - F\left(pos_1 - \frac{width(solar\,cell)}{2}\right)}{F\left(pos_1 + 1.5 \cdot width(solar\,cell)\right) - F\left(pos_1 + \frac{width(solar\,cell)}{2}\right)} \tag{4.1c}$$

An example for the this procedure is shown in fig. 4.3 a) for a solar cell at position pos_1= 2.3 cm from the optical axis and its neighboring cell at pos_2=pos_2+width(solar cell)= 3.3 cm. A final example fit for one complete profile is shown in fig. 4.3 b). For the error determination of the

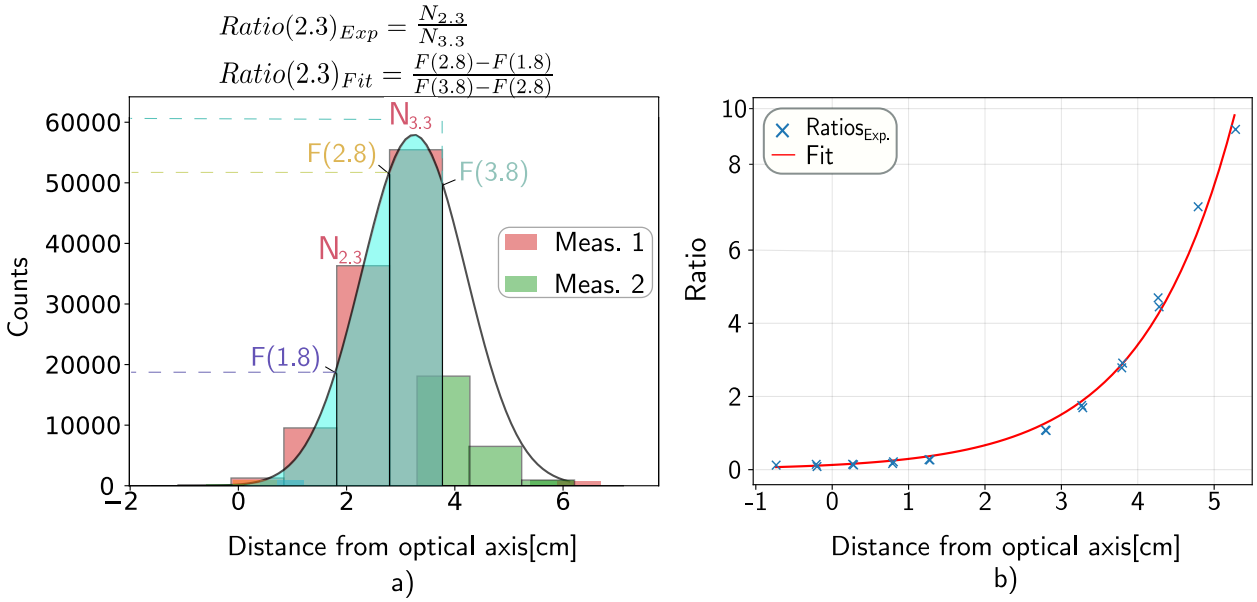

Figure 4.3: Plot a) shows an example of the fit procedure for the solar cell at position 2.3 cm from the optical axis for the first captured fraction of this profile, measurement 1. Exemplary a second measured fraction of the same profile is shown, measurement 2. For the experimental value the ratio is drawn to the subsequent solar cell position on the right in beam direction. For the fit the areas under the Gaussian from $-\infty$ up to the edges of the solar cells are subtracted to receive the value for the specific position. The resulting integral for F(3.8) is exemplary indicated as colored filling. The ratio of these subtractions results in the ratio which is used for fitting. Plot b) shows an example of the fitted curve for the given profile in a).

results a combination of experimental errors and fit accuracy has to be taken into account. For the experimental errors it is assumed that the determination of the solar cell positions has an uncertainty on the one side of a manual reading error of ±1 mm within the measurements and in addition an overall error of ±1 mm from the determination of the initial scale. The latter only influences the determined position but not the width since the width is not dependent on the actual position of the beam but only on the relative measured cell values to each other. Furthermore, the determined nickel counts N_{Ni} have in accordance with their counting statistics an error of $\pm\sqrt{N_{Ni}}$. To take these different error amounts into account a Monte Carlo principle for the fit was used. Therefore, the fit was performed 30 times, each time by a randomly distributed value for the solar cell detector unit position within its read-off error and a Gaussian randomly distributed value for the nickel counts of each cell individually within their statistical errors. The final values and errors were determined by the mean and standard deviation of these iterations. The number of iterations were determined beforehand by several repetitions of the fit for different iteration times. Performing at least 30 iterations, the final results did not further fluctuate outside of their errors. The final error of the mean, expressing the position, will be given as the error of ±1 mm from the scale uncertainty if the statistical fit error is smaller.

4.1.4 Results and discussion

From the analysis, the beam width in the dispersive axis and the beam position in comparison to the optical axis is derived. Thereby, for each measured gas pressure of each gas type, four sets of Gaussian parameters are received for the four measurement positions. The result of the widths are shown in fig. 4.4 a) for nitrogen gas and b) for helium gas. Thereby, the widths are presented in relation to the used gas pressure and for better comparison between the gases also to the corresponding gas density. The resulting course resembles the characteristic shape featuring a minimum, [68], [23], in the case of nitrogen. The shape is the result of opposite impacts on the beam broadening. Firstly, the ions averaged trajectory is defined by the averaged occupied mean charge, impacted by the ions energy and nuclear charge, see subsec. 2.3.2. Due to the numerous collisions on the flightpath and corresponding charge changing collisions, the ions charge repeatedly deviate from the mean charge for a short amount of time. Within this time frame, the ion also deviates from the corresponding trajectory. With increased gas pressure the charge state fluctuations increase and the mean free paths between charge changing collisions decrease. Thereby, the particles occupy differing charge states for a smaller amount of time and additionally achieve a smaller flight distance on the deviating trajectory. Therefore, the ions experience less positional deviation from the trajectory of the mean charge. This causes the beam narrowing with increasing gas pressure. On the other side, an increased gas pressure and and the corresponding higher number of collisions will cause increasing angular straggling of the beam which broadens the beam with increasing pressure. The interplay of these two effects causes the characteristic shape in which the minimum indicates the pressure after which the angular straggling becomes dominant. In the results for nitrogen the characteristic shape with the minimum is clearly observed. The gas pressure where the minimum occurs shifts with increased flightpath to higher pressures. This effect is observed for the first time in an experimental evaluation. The measured widths in helium in the similar gas pressure region are much broader than for nitrogen. In the considered region this is mainly originated in the significantly larger mean free paths caused by lower gas densities in helium compared to

nitrogen for the same gas pressures. With exception of the first measured position, a minimum is not observed within this pressure region, but a decrease of the width is observed. Due to the significantly smaller angular straggling in atomic helium gas (He) compared to molecular nitrogen gas (N_2) the angular straggling does not become dominant in this measured pressure region. The corresponding ion beam trajectories of these measurements can be seen in fig. 4.5.

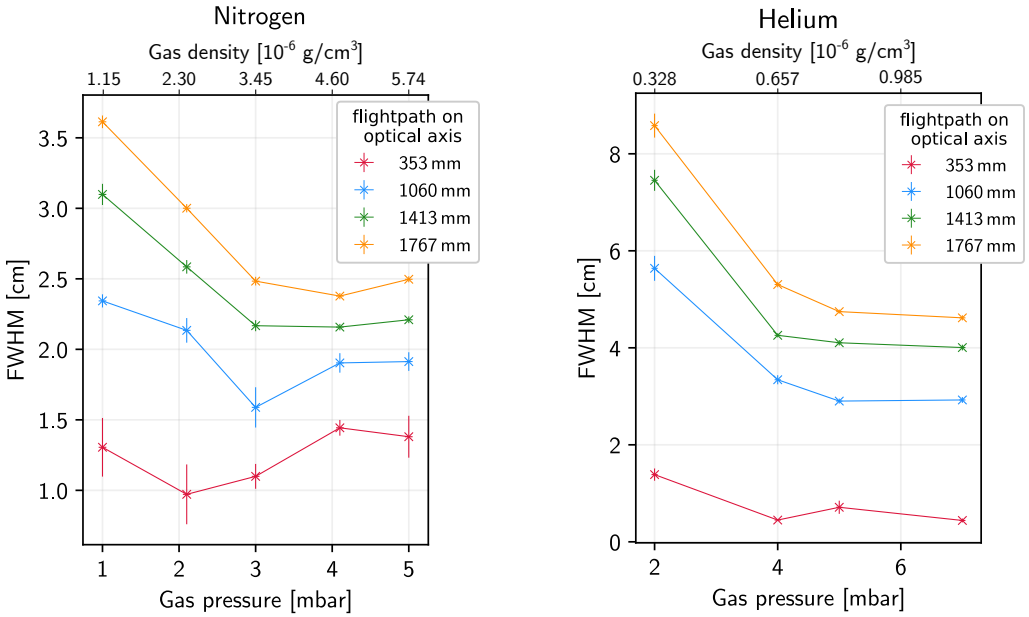

(a) (b)

Figure 4.4: The plots show the beam widths in the dispersive axis represented by their FWHM of the Gaussian fit in dependence of the gas pressure of nitrogen a) or helium gas b). The color scheme represents the different measured positions. The width development in nitrogen gas shows the characteristic shape. The minimums position shifts with the flightpath through the magnet to higher pressure values. The helium widths are significantly wider in this pressure region caused by the larger mean free path. No minimum is observed from the second position on(blue).

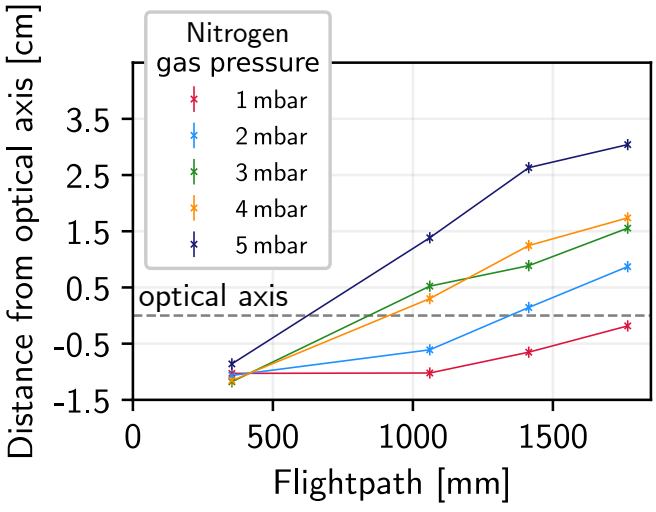

(a)

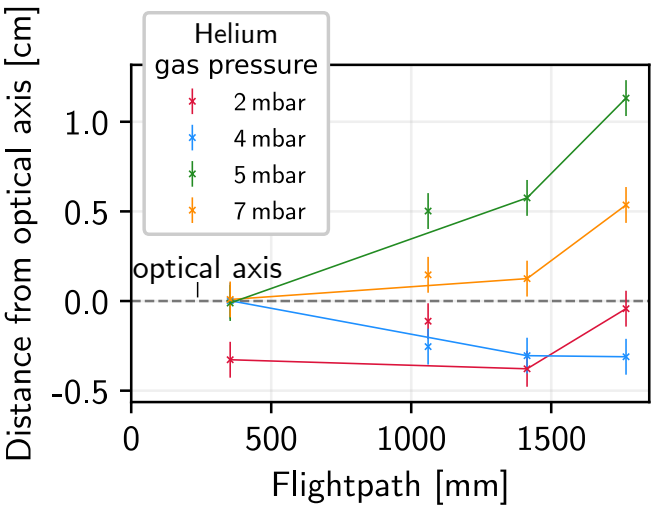

(b)

Figure 4.5: The plots show the beam trajectory measurements inside the GFM for nitrogen gas a), and helium gas b). Thereby, the beam position is represented by the deviation from the magnet optical axis. Positive values indicate an outer trajectory. The color scheme represents the used gas pressures. In nitrogen gas the beam is measured at inner trajectories on the first position caused by a systematic shift due to the tuning procedure up to the GFM. With increasing flightpath the beam the deviation increases. A back bending can be assumed by the last position. For helium the trajectories stay closer to the optical axis and there is no clear dependence between the pressure and captured trajectory. It is assumed that this corresponds to the inaccurate conditions for the trajectory fixations.

In the initial nitrogen gas measurement, the beam starts at an inner trajectory on the first position independent of the gas pressure. It is assumed that this is a systematic shift due to the tuning procedure. Since the initial beam injection remained constant during all measurements for one gas type, it is assumed that the beam was initially not injected centrally and straightly into the magnet in the first place. This could be caused by the tuning procedure using the large silicon detector in front of the magnet as the last reference point. For the initial measurement with the nitrogen gas, a silicon detector with a diameter of 2 cm was used. For a more centered tuning it was replaced by a silicon detector with a diameter of 0.5 cm which was used for further measurements. The ion beam trajectories in both cases trend to outer trajectories with increased gas pressures and additionally with increased flight path. At the last measured position, the ion beam position trend to bend again in direction to the optical axis. This is consistent with the knowledge that the beam reaches the centered detector after the gas-filled magnet and therefore the optical axis again. While this overshooting was calculated before, [36], it was also measured for the first time within this thesis. It can be explained since only a common magnetic field can be applied for the whole flightpath, but the ions experience significant energy loss through the magnet. Therefore, the ions can not be forced on the optical axis trajectory with a fixed radius. In the beginning the magnetic field is too weak for the particle energy to force them on the optical axis, therefore they deviate to outer trajectories. By loosing the energy the magnetic field will later be strong enough to force the ions back in direction to the optical axis. This effect becomes stronger for higher gas pressures due to the increased overall energy loss and therefore larger energy difference from beginning to

end. For helium the deviations are smaller since the energy loss in the observed pressure region is significantly less. The effect of the bending towards the optical axis was not observed so it is evident that it happens after the fourth measurement position since the beam again enters the gas ionization detector on the optical axis. Furthermore, the helium trajectories show inconsistencies between the positional deviation and gas pressures. It is assumed that the applied magnetic field was not chosen correctly for centered ejection to the gas ionization detector. The determination for each gas pressure was challenged since the energy loss difference between different pressures is small and therefore the magnetic field also does not vary significantly. This in combination with the systematic shift of the nitrogen gas pressure leads to the conclusion that for future investigations of the trajectory the injection and ejection of the particle beam from the gas-filled magnet has to be defined more accurate. This could be achieved by the use of small apertures or slits in front and after the gas-filled magnet.
Overall it can be said that the measurement was successfully conducted and delivers an insight to the beam shape in the dispersive axis and trajectory development. These investigations were determined for the first time experimentally. The deviation from the optical axis and the overshooting effect was experimentally observed for the first time. Furthermore, the general beam width development and the shift of the minimum of the width courses after different passed flightpaths was observed for the first time. The results were subsequently used for the revision of the in-house developed Monte Carlo code, see sec. 4.3. There are several disadvantages of the measurement technique in its current form. The fragility of the detector units and the missing initial protection of the solar cells led to damages and non-usability of individual cells. Furthermore, a more dedicated fixed scale should be equipped for easier and more reproducible read-out of the position. The most prominent disadvantage is the overall measurement time for the gained degree of achievable resolution. The measurement of higher gas pressures leading to broad beams in both axes and to a decrease in particle rate with increasing flightpath. Thereby, more individual measurements at longer duration become necessary and one gas pressure for one gas type required around an hour of overall measurement time. While these measurements were necessary for the revision of the simulations, the determination of the best gas type and pressure and moreover the width of the respective beam were performed in a second experiment, see sec. 4.2. Thereby, the beam shape was measured after the gas-filled magnet shortly before entering the gas ionization detector.

4.2 Ion beam profile measurements after passing the gas-filled magnet

The measurements of the beam profile in the dispersive axis improved the understanding of the inner beam shape and trajectory development. On the downside the measurements were time-consuming and therefore only a small range of pressures were investigated. Furthermore, the beam size after the gas-filled magnet can not be confidently extrapolated from this data. Therefore, a follow-up experiment was conducted in which experimentally the ideal gas type, comparing molecular nitrogen and atomic helium gas, and the ideal gas pressure were determined.

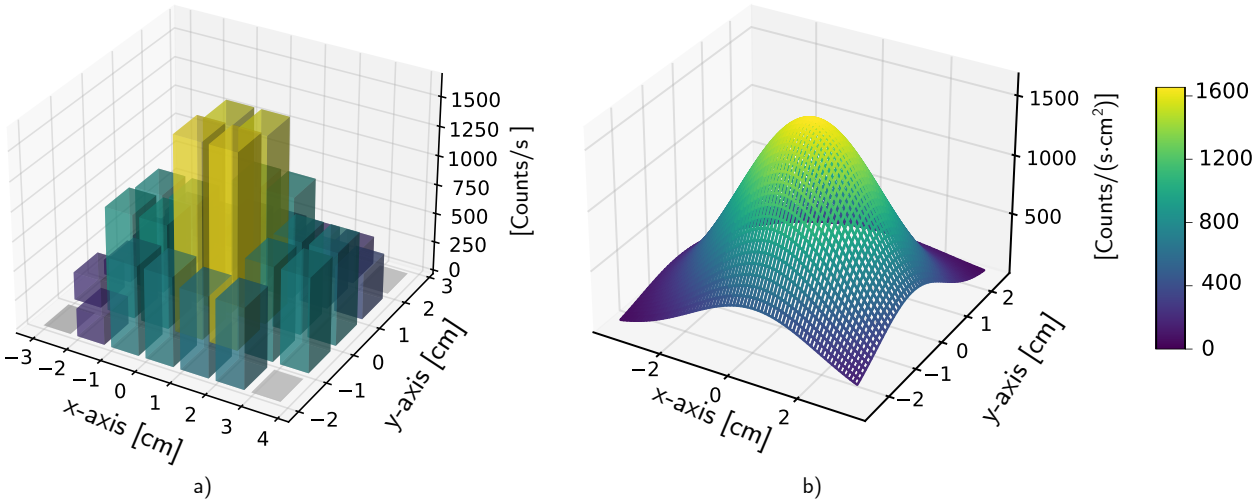

Figure 4.6: Plot a) shows the captured two-dimensional profile measurement of ^{60}Ni for 2 mbar nitrogen gas pressure which consists of the combination of two individual measurements. The x-axis represents the dispersive axis while the y-axis represents the non-dispersive axis. The two-dimensional Gaussian distribution which results from the performed fit is shown in plot b). The individual σ of each respective axis were determined by the semi-axes of the fitted σ ellipsoid and were used to calculate the full width at half maximums.

4.2.1 Setup, conduction and data analysis

For these measurements, a two-dimensional detector array was used which is integrated in a valve mounting and was already used for similar measurements at the 120° magnet at the 6 MV Tandetron accelerator setup, [23]. The valve was mounted at the same position as the 5 anode gas ionization detector while the latter was shifted further away for these measurements. The array consists of 32 solar cells which are chunked in 16 blocks. Since the current data acquisition system is only capable of measuring 8 signals at once, each measured profile was captured in two individual measurements which were combined in the analysis. Since the measurements only required around one minute the individual measurements for one profile were only one to two minutes apart so that no observable beam fluctuation was captured and the spectra could be combined without further normalization. In equivalent to the measurements inside the magnet a ^{60}Ni particle beam was used at an initial energy of 100 MeV. The particle beam was tuned to the small silicon detector in front of the magnet and all components values with exception of the gas-filled magnet remained the same. For each pressure and gas type the particle beams were tuned to the detector array center by changing the magnetic field. Thereby, gas pressures from 1 to 7 mbar were measured for nitrogen gas. For higher gas pressures the nickel particles were not measured in the array anymore and probably stopped within the magnet. For the helium gas pressure, a region between 1 to 20 mbar was measured. Higher gas pressures were not possible due to the stability of the magnet entrance window. For the data analysis the two separated measurements for one gas pressure and gas type were combined to one two-dimensional spectrum, see a resulting distribution in fig. 4.6. The data were fitted by a two-dimensional Gaussian distribution, see eq. 2.32. Thereby, the σ are given by the semi-axes of the σ ellipsoids of the fitted distribution and were used to calculate the full width at half maximums.

4.2.2 Results and comparison between gases

The beam widths after passing the magnet for nitrogen and helium can be seen in fig. 4.7. Each plot shows the width in the dispersive axis, indicated as x-axis in red, and the non-dispersive axis, the y-axis in blue. While the dispersive axis shows the combination of the competing narrowing and broadening effects, the linear increase in the non-dispersive axis is solely caused by the angular straggling. The crossing point of both curves in the nitrogen plots at around 3.1 mbar indicates the pressure from which the angular straggling dominates the beam width development. From the perspective of optimal transmission for an equally shaped detector entrance window, the crossing point of both curves is the ideal pressure when using nitrogen gas. For helium, it is again seen that the beam is broader at same pressure values and it decreases constantly with increasing the pressure. For equal gas densities the dispersive widths are in equal ranges. As expected, the angular straggling shows a much flatter increase than for nitrogen and does not become dominant in the measured pressure region up to 19.7 mbar. Therefore, also no minimum is observed in the dispersive axis widths. A value of 19.7 mbar is the best helium gas pressure in terms of transmission for a subsequent symmetrical detector entrance window. It was not possible to measure higher gas pressures due to the stability of the entrance window of the magnet.

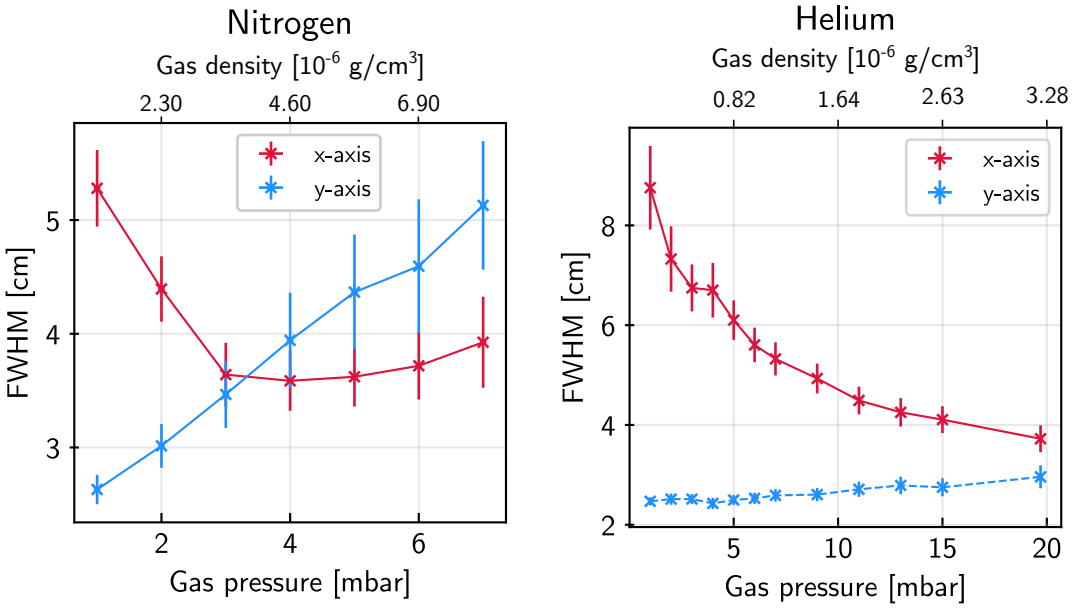

Figure 4.7: The plots show the results for the analyzed widths of the measured two-dimensional beam profiles after the gas-filled magnet in nitrogen a) and helium b). The red curves represent the dispersive x-axis and the blue curves represent the non-dispersive y-axis. While in the dispersive axis again the competing narrowing and broadening effects cause the characteristic width course shape, the y-axis shows a linear increase only caused by angular straggling.

For the determination of ideal gas type and pressures from the investigated ones, their results and further specifications are given in tab. 4.2. The x-width for the ideal nitrogen gas pressure is slightly smaller than for helium in the current setup configuration while the y-width of helium is 15% smaller. In case of spatial isobar separation the width in the dispersive x-axis is the key factor. Furthermore, the respective energy losses are calculated with LISE++ with the formalism by Ziegler

referring to an initial energy of 100 MeV lowered by the energy loss in the 2 µm thick Mylar detector entrance foil. The given energy loss values refer on the one side to the explicit loss in the gas for an approximated equal flight path on the optical axis of 2121 mm. On the other side gas type and gas pressure dependent deviations from the flightpath were observed influencing the final passed gas distance, see subsec. 4.1.4. Therefore, an additional energy loss value is given which accounts for different flight paths. The values for the flight paths are taken from the performed calculations, see sec. 4.3. The differences in energy loss between the gases for their optimal parameters in terms of transmission are significant. The explicit lower energy loss properties in helium can not compensate the necessary significant pressure difference between the gases for the same widths. In AMS measurements, the remaining energy determines the final energy separation quality between the isotope and the fraction of the isobaric beam which is not suppressed by the gas-filled magnet. Therefore, in combined terms of highest transmission and highest remaining energy for separation, nitrogen gas at 3 mbar is the optimal option for the investigated ion beam with an initial energy of 100 MeV and mass 60.

Gas	p[mbar]	FWHM[cm]		E-loss [MeV] (Optical axis)	E-loss [MeV] (Sim. flightpath)
		x	y		
N_2	3	3.64	3.47	29.87	30.24 (2147 mm gas path)
He	19.7	3.72	2.96	40.62	40.70 (2125 mm gas path)

Table 4.2: The table presents properties corresponding to the measured gas pressures which are nearest to the optimal pressures in terms of transmission. Thereby, the values of the analyzed widths are given for dispersive and non-dispersive axis. The energy loss was calculated by use of LISE++ with the formalism by Ziegler. An initial energy of 100 MeV was assumed which is lowered by the energy loss in the 2 µm Mylar entrance foil. The stated energy losses refer to an approximated flight path of 2121 mm on the optical axis on the one side. On the other side calculated flight paths resulting from the simulations, see sec. 4.3, were used to account for the different passed gas paths due to the different positional deviations. The x-widths of both gases are in a comparable range while the y-width is slightly smaller for helium. Nevertheless the energy loss at the respective helium gas is significantly higher. Taking both factors into account the nitrogen option is the favored one for AMS measurements in this energy and mass region of the ion beam.

4.2.3 Measurement of the ^{60}Fe beam profile

The investigations of the gas type and pressure revealed that the best choice for the energy and mass range comparable with the ^{60}Fe AMS measurements is nitrogen gas at a pressure of 3 mbar. With this result it was decided to perform an ion beam profile measurement of ^{60}Fe at the optimal parameters. Thereby, ^{60}Fe of a ^{60}Fe standard sample with ^{60}Fe/Fe=1.029(3) $\cdot 10^{-8}$, see subsec. 5.2, was tuned to the gas ionization detector while the magnet was filled with 3 mbar nitrogen gas. Subsequently, the two-dimensional profile was measured and analyzed as described in subsec. 4.2.1. A contour plot of the fitted Gaussian distribution and indications of the available detector entrance window can be found in fig. 4.8. Thereby, it was calculated which parts of the beam will pass the detector entrance windows to estimate the respective transmission loss. When using the smaller squared 1000 nm thick SiN detector entrance window with an area of 2 cm x 2 cm, 23% of the beam

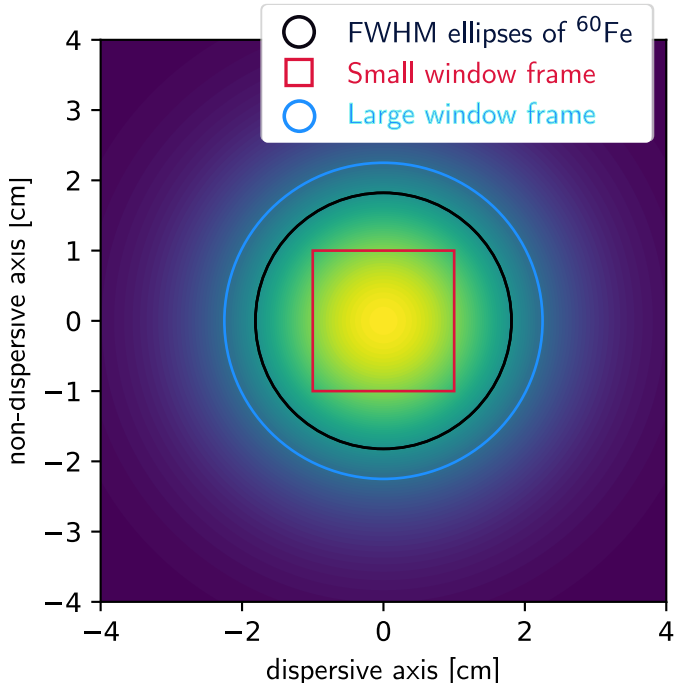

Figure 4.8: Interpolated contour plot of the fitted ^{60}Fe two-dimensional Gaussian position distribution. Its FWHM ellipse is indicated in black while the available window sizes of the detector entrance are indicated in red. They consist of the 2 cm x 2 cm squared SiN window and the round 4.5 cm in diameter Mylar window which is the largest available option for the current detector layout. Within the small window 23% of the beam passes the windows corresponding to the smaller window and 65% when using the large window.

should pass from the calculations. By use of the larger round 2 µm thick Mylar detector entrance window with 4.5 cm in diameter, 65% of the beam should pass from the calculations. The energy loss is similar in both windows, whereby calculations with LISE++ with the formalism of Ziegler gives 11.161 MeV energy loss in the SiN window and 11.757 MeV in the large round Mylar window. To achieve significant transmission near to 100% the window size has to be enlarged. It has to be considered that the Pole gap is 50 mm which represents a limit in the y width. For example to reach 89% transmission for the observed beam shape, a window size of (x=90 mm) x (y=50 mm) would be necessary. Therefore, the detector in general has to be enlarged including outer and inner layout.

4.2.4 Measurements of the separation factor for different N_2 gas pressures

While the former investigations placed the focus on the specific beam shape development dedicated to find the best parameters in terms of transmission, also the spatial separation between isotope and isobar is of special interest. Therefore, a measurement was conducted for the determination of the positional separation factor achieved by the gas-filled magnet for different nitrogen gas pressures. Thereby, the particle count rate within the gas ionization detector was logged while the magnetic field was traced over the combined ^{60}Ni and ^{60}Fe peak. The measurement was repeated by only capturing the count rate within the ROI to identify the minor ^{60}Fe peak clearly. The results of both traces and respective fits for further calculations can be found in fig. 4.9.

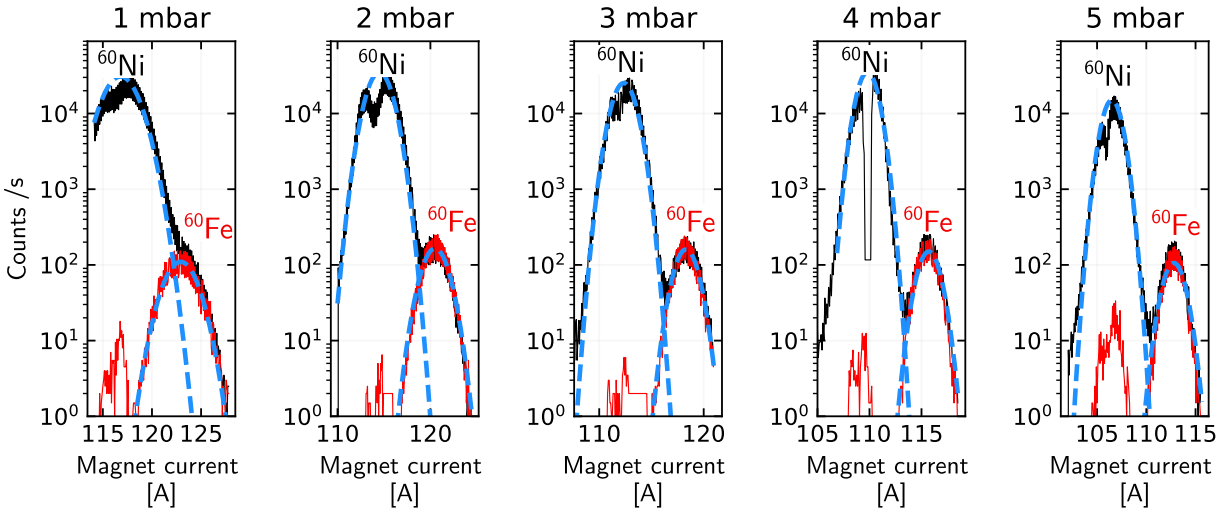

Figure 4.9: Plots of the captured count rates in the gas ionization detector without (black) and with (red) the condition of the ^{60}Fe ROI while tracing the GFM magnetic field for different nitrogen gas pressures. The black colored peaks consist of ^{60}Ni, left peak, and ^{60}Fe, right peak. The count rate with the ROI condition in red mainly consists of ^{60}Fe. Furthermore, the Gaussian fits of both peaks are indicated in blue. Their results were taken for the calculations of the separation factors.

Both peaks were fitted with an one-dimensional Gaussian function. The individual fits are plotted. The results were used to determine the separation factors in units of the set current of the magnetic field in ampere given in tab. 4.3. This value can be mainly used for qualitative comparison. The separation factor shows that up to 5 mbar nitrogen gas pressure the separation factor increases with increasing the gas pressure.

Gas pressure [mbar]	1	2	3	4	5
μ_{Ni} [A]	116.8	114.5	112.35	109.8	106.5
$FWHM_{\mathrm{Ni}}$ [A]	3.77	2.83	2.35	2.10	1.95
μ_{Fe} [A]	122.9	120.5	118.3	115.5	112.8
$FWHM_{\mathrm{Fe}}$ [A]	4.00	3.06	2.35	2.24	2.31
Separation factor	1.51	2.04	2.53	2.65	2.96

Table 4.3: Calculated separation factors for the GFM for ^{60}Fe and ^{60}Ni at different nitrogen gas pressures. The values refer to the separation concerning the magnetic field current. Up to the last pressure of 5 mbar the separation factor increases with increased gas pressure.

4.3 Ion beam development simulations through the gas-filled magnet

The quality of physical simulations has to be measured by their ability to reproduce experimental values and predict future results. In the case of ions passing a gas-filled magnets numerous effects impact the ion-gas interactions along large gas distances in a magnetic field. The first widely used simulation code for AMS applications was developed for the split-pole ENGE spectrometer, [69], [68], and over the last decades more codes for AMS and similar applications were developed, [36] or [70]. Furthermore, a simulation code was developed in-house dedicated to the 6 MV Tandetron

accelerator gas-filled magnet, [23]. These codes were used for calculation and subsequent comparison to experimental values of the beam width after the gas-filled magnet and in special case for the first mentioned code also for the spatial distance between isotope and isobar. The beam shape and trajectory development within a gas-filled magnet was neither calculated nor measured before. Furthermore, the quantitative comparison of calculated absolute positions was also not discussed before. This chapter will explain the revision of the in-house developed code by the inner gas-filled magnet beam shape and trajectory measurements, see subsec. 4.1.4. Thereby, special attention will be given to limiting factors for a full theoretical or semi-empirical description of these simulations. Subsequently, differing approaches from the former mentioned established simulation code, referred to as external code , will be given. Finally, simulations of all performed measurements from subsec. 4.1.4, 4.2.2 and subsec. 4.2.4 with the revised in-house code and the external code will be presented. The chapter will close with a discussion about the achievements and limits of these simulations.

4.3.1 In-house developed Monte Carlo code

The Monte Carlo method delivers numerical results by a statistical approach for complex and sometimes analytically non-solvable problems by random sampling. In the case of gas-filled magnet numerous gas interactions take place which can not be predicted deterministically. This is mirrored by the widely used formulas in ion beam physics for the processes of energy loss and angular straggling which are based on a certain statistics of ion-atom interactions, see sec. 2.1. Therefore, the simulation codes for gas-filled magnets do not simulate every ion-gas molecule interaction but only interactions which change the ions charge state. A comparison between the realistic flight path of an individual ion and the equivalent simulation is shown in fig. 4.10. The calculations within one simulation step will be briefly listed since the process is of importance for explanations of the explicit revision described in subsec. 4.3.1.2. Further details are explained in [23]. The initial ion at the beginning of each simulation is defined with its absolute velocity value, nuclear charge, charge state, mass, position and direction. Each step describes the distance between charge-changing collision whereby a significant number of intermediate collisions occur. In each of these steps, the calculations have the following order:

- Calculation of the mean charge state based on the ions velocity and the nuclear charge.
- Calculation of the charge state distribution width.
- Calculation of the electron capture and loss cross sections by use of the mean charge state, the current charge state and the charge state distribution width.
- Calculation of the total charge changing cross section from the electron capture and loss cross sections.
- Calculation of the passed gas distance to the next charge change by use of the cross section and the gas density.
- Calculation of the new energy after the passed distance.
- Calculation of the angular straggling over the passed distance.

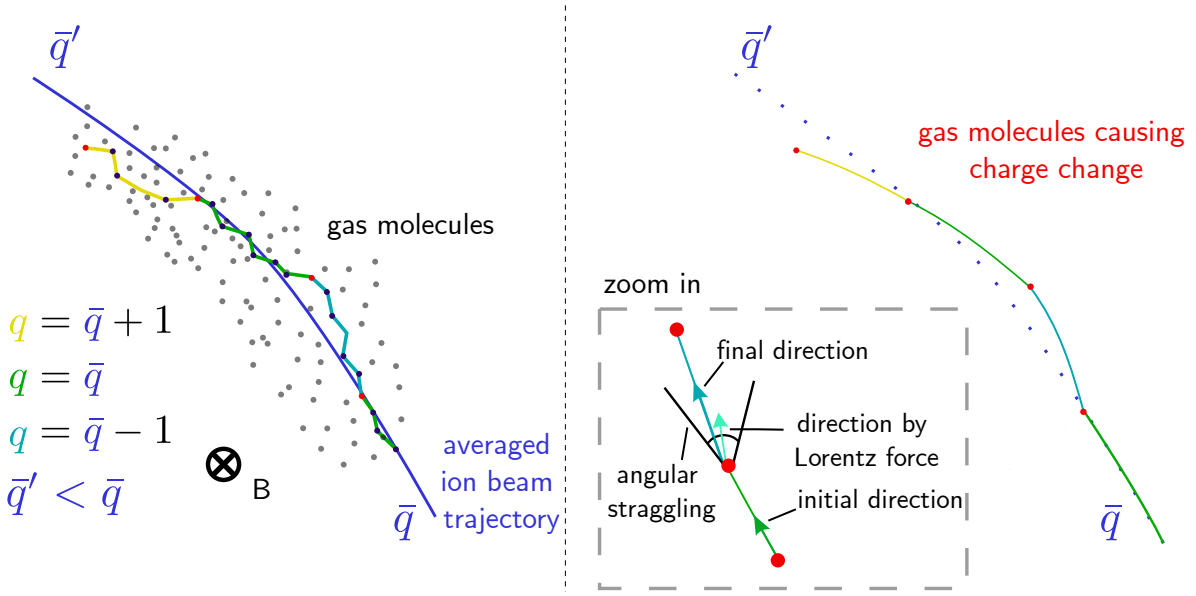

Figure 4.10: The plot shows a comparison between a realistic ion flight path through the GFM and the simulated ion path. On the left side the realistic ion path is shown in which the ion interacts with numerous gas atoms indicated in dark blue. Some of these interactions, indicated in red, change the charge state of the ion. On average the ion beam will follow the path of its mean charge state which decreases over the course of the flightpath due to the energy loss. Thereby, small fluctuations occur caused by angular straggling and larger deviations caused by the charge change fluctuations. Due to the statistic description of processes like energy loss and angular straggling the simulation code only simulates charge changing interactions, shown on the right. In between lying interactions are taking into account statistically averaged. An exemplary zoomed in interaction is shown. The final direction is a combination of the direction given by the Lorentz force taking into account the current energy, charge state and magnetic field which is then varied by the occurred angular straggling.

- Calculation of the new charge state (only ± 1).
- Calculation of the new direction by combining the direction from the Lorentz force varied with the angular straggling.

After each step the coordinates of the ion, given in a Cartesian coordinate system, are used to calculate the current radius and angle of its position in polar coordinates. By that certain termination conditions are checked. The steps are repeated until the ion either reaches a specified angle, for the 10 MV setup at 135°, is stopped within the gas, or by colliding with the magnet vacuum chamber wall. In each simulation at least several thousands of projectile particles will be simulated. The result is a histogram of the final ion positions on the dispersive axis from which the averaged ion beam position and width can be extracted. For comparison to results of this work, the code was adapted to match the gas-filled magnet setup at the 10 MV AMS system. Furthermore, its resulting output was extended to allow simulations of the received experimental values at different positions and the different used gas types. The comparison of the simulations from the initial code with the experimental results of this work showed moderate qualitative reproduction. Furthermore, the quantitative reproduction of the widths could not be achieved and the quantitative comparison of the trajectories showed immense deviations. Therefore, the whole codes underlying physical theories were revised for the used energy and mass range and adapted if needed. This subsection will

report on applied code modifications. The semi-empirical approaches developed for otherwise not yet fully describable approaches are given and discussed. The comparison between experimental values, the simulations from the code of this work and from the external code will be given and discussed. Finally, a conclusion for the applicability and significance of the codes and especially their limitations will be discussed.

4.3.1.1 Adaption and revision of the in-house developed code

The simulation code was dedicated for the setup at the 6 MV Tandetron accelerator gas-filled magnet to give the final ion beam shape in the dispersive axis as a result. In a first step the code was simply adapted to match the different magnet properties, the used ion beam properties and furthermore for the use of helium gas. For comparison to the experimental values of this work, see subsec. 4.1.4 and 4.2.2, the code was extended to deliver not only the ion beam shape at the end of the gas-filled magnet but also at the angles corresponding to the ports of the 135° magnet. The simulation code uses a setup file in which all initial properties for the current simulation are defined which has to be changed between every performed simulation. Since revision of the code was planned, supporting python codes were written. One of them is dedicated to run parallel simulations of the given gas pressures and gas types of the performed experiments. The other supporting code analyzes the results and visualizes them for fast comparison. While the revision of the code for the used physical principles, the following modifications were made:

1. The used energy loss values were newly calculated using LISE++ with the formalism by Ziegler, see subsec. 2.1.1.

2. The used energy straggling was changed from energy independent Bohr straggling to the Yang straggling formula, see subsec. 2.1.2.

3. The formerly used tabulated angular straggling was adapted to the formula derived by Green, see subsec. 2.1.3. The calculations were performed for one atomic gas and subsequently adjusted to the particle number in the respective gas molecule.

4. The calculation of the mean charge state was adapted to compensate the formerly not considered gas density effect. It will be discussed in subsec. 4.3.1.2 in detail.

5. The charge state distribution was firstly adapted as described in subsec. 2.1.4. The given formula has to be further adapted, which will be discussed hereinafter.

The given modifications were applied to use the most suited approaches for the given beam properties used in Cologne from their given applicability. While the approach and the underlying effect for the mean charge state is discussed explicitly in subsec. 4.3.1.2, the modifications of the widths of the charge state distribution also needs more explanation. The widths of charge state distributions are usually only measured and no simple approach for their calculation is available. The used approach is based on the measurement of the reduced charge state distribution width in respect to the remaining bound electrons on the projectile, see subsec. 2.1.4. The data is given within a plot in the publication and was manually extracted for the simulation in this work. Thereby, the given data is manually parameterized and extrapolated if needed. Since the given reduced width is dedicated to solids, individual adjusting factors for nitrogen f_{N_2} and helium f_{He} had to be used with

dq_{new}=dq· f. The factors which best fitted the experiments were f_{N_2}=1.05 for N_2 and f_{He}=0.85 for He.

4.3.1.2 Gas density effect

The first performed simulations were in moderate agreement concerning the beam widths and showed extensive discrepancies concerning the beam trajectories of several centimeters. An example is given in fig. 4.11. Thereby, the systematic shift for the experimental values was already included in the start conditions of the simulations. The comparison showed that the deviations in beam position between simulation and experiment increase with passed gas mass. This is shown by the increase of deviation when increasing the flightpath through the magnet and more significantly if different pressures are compared. Thereby, higher pressures lead to significantly higher deviations. The observations indicated that the impact of the gas densities is either not implemented at one or several calculation steps, or is falsely neglected in calculation steps. The revision of the in-house developed code revealed that the used calculation for the mean charge state, also used in almost all former simulation codes dedicated to AMS applications, is not applicable to the real gas properties. The mainly used formalism, described in subsec. 2.1.4, have two given formulas dedicated to solid targets, often represented by carbon foils, and gas targets. The latter is explicitly described as diluted without further information. Looking at the respective used experiments and the dedication of the calculation for accelerator stripping gases, the usual pressure range is around 10^{-4} mbar. The impact of an increased gas mass, for example by increasing the pressure, on the charge changing processes was comprehensively investigated. An overview of the different works was created by Betz, [21]. It was found and concluded that after an ion-atom collision the ion is in an electronically excited state. In diluted gases the time between collisions exceeds the excitation time and the ion deexcites before the next collision. In dense gases the ion can undergo the next collision being excited which changes the electron loss and electron capture cross section. Thereby, it was observed that the electron loss cross section slightly increases while the electron capture cross section significantly decreases with increased target density. It is assumed that in the latter process the further excitation leads to a rapid Auger process, so that the electron capture cross section appears to be reduced. As a final result, total higher charge states are populated with increased target density. These assumptions were for example confirmed in the investigation of iodine ion beams where the cross sections and the resulting different charge state distributions for different target densities were measured, [71]. These results can explain the discrepancies between simulation and experimental values for the gas-filled magnet. The calculated mean charge state of the simulations are based on diluted gases which results in too low values for the presumed magnetic field so that the ions are drifting outwards. Thereby, the approximated averaged deviations of the mean charge states outlines for the considered cases between $\Delta q = +0.2$ up to a maximum of approximately $\Delta q = +1$ in dependence of gas type and gas pressure. Unfortunately, no trivial solution can be found for the implementation of this effect. In the current Monte Carlo code the whole simulation is based on this mean charge state, since it seemed to be a well-established calculable value. From that the cross sections are derived which impacts the traveled distance and therefore all following parameters. The correct physical approach would be to calculate the electron loss and capture cross section and derive all other values from there. High efforts were put into their description in the field of plasma physics. The theoretical calculation of these

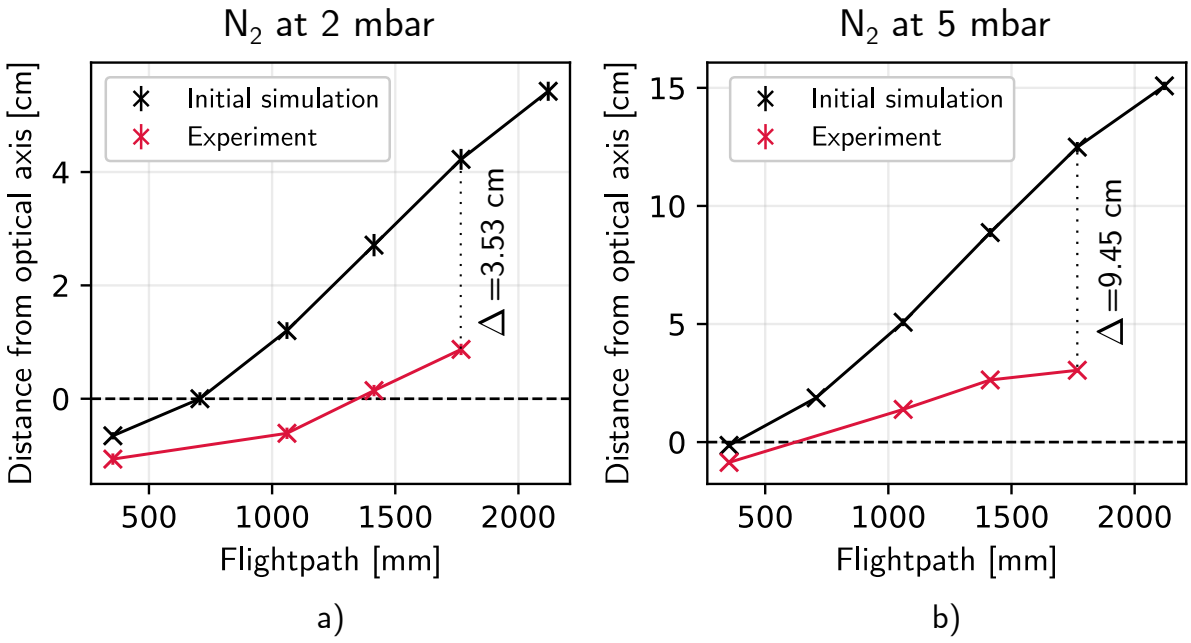

Figure 4.11: Comparison of experimental derived values for the ion beam trajectory to the initial simulations. Plot a) shows the comparison at 2 mbar nitrogen gas and plot b) at 5 mbar nitrogen gas. The deviations of several centimeters are significant. It was observed that the deviations increase with increasing flightpath and more significantly with increasing gas pressure. This indicated strongly that the gas pressure or gas density was falsely neglected in the initial simulations. It revealed that the gas density effect has to be considered in the calculations of the mean charge state influencing all remaining calculation steps.

cross sections becomes quite difficult due to their dependence on the atomic shell structure of the projectile ion and the gas atom or molecule. Numerical solutions were implemented in the CAPTURE and LOSS code which are not freely available but calculations can be requested, [25], [26]. Their results show good agreement in the comparison to experimental values. Unfortunately their usage is not applicable for the simulation of the gas-filled magnet since the ion parameters impacting theses cross sections change continuously throughout the gas-filled magnet. The number of required cross sections for every energy and possible charge change scenario would exceed even one ion-gas combination which does not consider different gas pressures. All stated approaches for semi-empirical formulas or scaling rules, [72], have been implemented in the current code but led not to success. Extensive investigations of the mean charge state dependencies were performed in Berkley, [70]. A formula for the mean charge state and a dedicated correction formula using the flight time of the ion for the gas density effect was derived. Unfortunately the investigated energy range significantly exceeds the used energies in Cologne. Therefore, in the scope of this chapter individual semi-empirical formulas were derived to adapt the simulation to the received experimental values. Therefore, in the first step a respective constant averaged shift Δq was added to the mean charge state calculated by the formula from Sayer, see subsec. 2.1.4, for each gas type and pressure. The shift was determined by manual trial for the best fit of the trajectory to each gas pressure and gas type:

$$\bar{q}_{new} = \bar{q}_{Sayer} + \Delta q \tag{4.2}$$

These determined shifts with the corresponding gas densities were then fitted with a polynomial function. In the first approach it was aimed for a combined function for both gases. Therefore, the initial charge state formula was replaced by the approach from Schiwietz, [30], which takes target properties into account. Subsequently, a fit over all received shift values accounting for the molecular structure of nitrogen was performed. The results reproduced the experimental values not sufficiently. The best results were achieved by the approach from Sayer and individual correction formulas for each gas type in dependence on the respective gas density n in $\frac{atoms}{cm^3}$ for the respective pressure and gas type.

$$\Delta q_{N_2} = -3.1627 \cdot 10^{-81} \cdot n^4 - 1.3825 \cdot 10^{-52} \cdot n^3 + 7.1711 \cdot 10^{-35} \cdot n^2 - 7.2537 \cdot 10^{-18} \cdot n + 0.55 \tag{4.3}$$

$$\Delta q_{He} = -1.062 \cdot 10^{-35} \cdot n^2 + 6.192 \cdot 10^{-18} \cdot n - 0.1176 \tag{4.4}$$

4.3.1.3 Comparison to external simulation code

Within this work not only the in-house developed simulation code was used but additionally the before mentioned well-established Monte Carlo code for gas-filled magnets, [69], [68], was used for simulations and compared. Initially used for an ENGE spectrograph, a version already adapted to the MLL setup which features the same gas-filled magnet design as Cologne, [32], was available[10]. Since both simulations will be shown in the comparison, their differences will be shortly explained. Therefore, the provided code will be referred to as external code hereinafter. While this code follows the same calculation procedure as the in-house code, it shows differences in individual calculations steps or used approaches.

1. Charge state distribution formula for the mean charge state.
   The external code has 4 different choices of formulas. Since the Sayer formalism was not available, it was chosen to use the formulas from Schiwietz which were similar in the case of carbon foils, see sec. 5.4.

2. Charge state distribution width.
   Since no easy theoretical or semi-empirical approach is available, the values are derived by fitting parameters from the equilibrium charge state formula and the capture cross section formula.

4.3.2 Results and comparison

The quality of the simulations is tested by the comparison between experimental values and simulated values of the beam widths within and after the gas-filled magnet, as well as the trajectory within the gas-filled magnet. Thereby, the values for helium and nitrogen gas-filling are compared quantitatively and qualitatively. At last the separation factor for different nitrogen gas pressures will be examined and compared to the simulation codes. All shown simulations were performed for 100000 particles to exclude statistical inaccuracies due to the Monte Carlo principle. Furthermore, only experimentally measured gas pressures from subsec. 4.1.4 and subsec. 4.2.2 were simulated

[10] Provided by Prof. Dr. Michael Paul

since a corresponding magnetic field is required. This subsection will firstly present the results of the simulations concerning the beam development in terms of width and position through the magnet and the beam width after passing the gas-filled magnet. Subsequently, a detailed discussion on these comparisons and the current limits of the simulations are given.

4.3.2.1 Ion beam profile width inside the gas-filled magnet

The results of the ion beam width of ^{60}Ni for both simulation types in comparison to the experimental values are visualized in fig. 4.12 for nitrogen gas (N_2) and in fig. 4.13 for helium gas (He). For the nitrogen gas pressures the shift of the minimum for each position with increasing

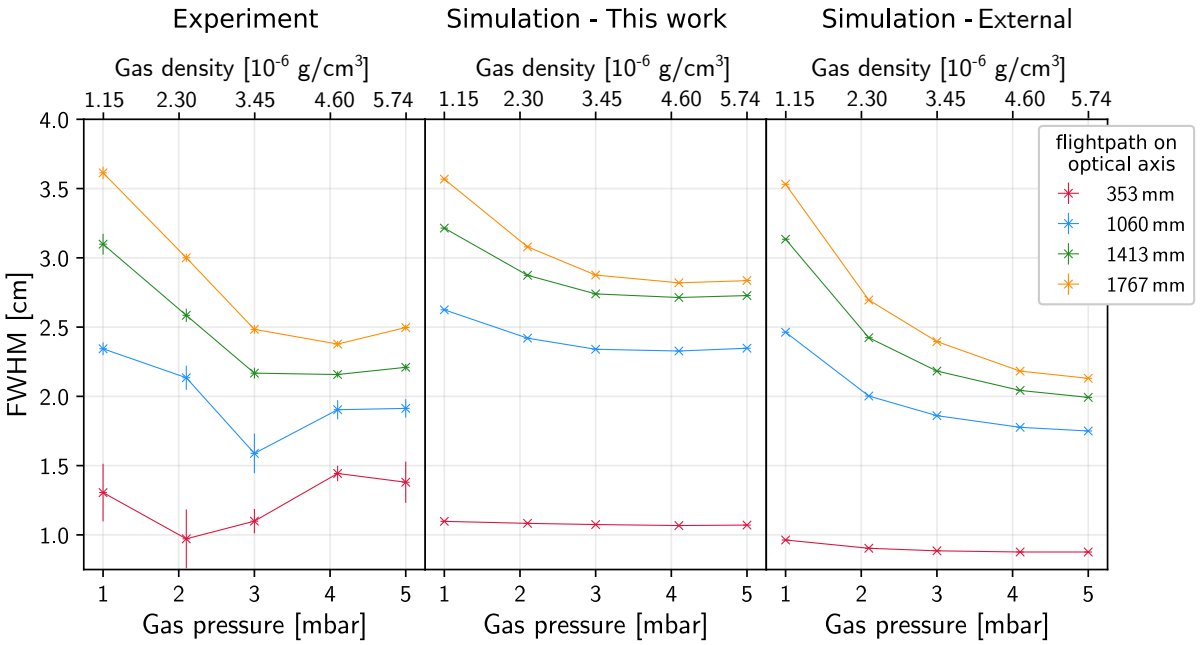

Figure 4.12: The plot shows the comparison of the experimental ion beam profile widths inside the GFM to the simulations from this works code and to the external code, for nitrogen gas. The shift of the minimum with the gas pressure is not reproduced by any of the codes. For the code of this work, every position has its minimum at 4 mbar and reproduces the last measured position qualitatively while the external code does not reproduce the minima. On the other hand the latter is quantitatively closer to the experimental values.

gas pressure is not reproduced by any of the codes. While the code from this work reproduces the width minimum at 4 mbar gas pressure, the external code does not reproduce a minimum in the gas pressure range. Therefore, qualitatively the code from this work reproduces the experiment better. However, quantitatively the external code shows on average a better agreement to the experimental data. For the helium gas the decreasing course of the widths with increasing gas pressure is mirrored by both codes, although the simulations decreases are steeper than the experimental one. While both codes are in sufficient quantitative agreement, the code of this work shows even closer agreement.

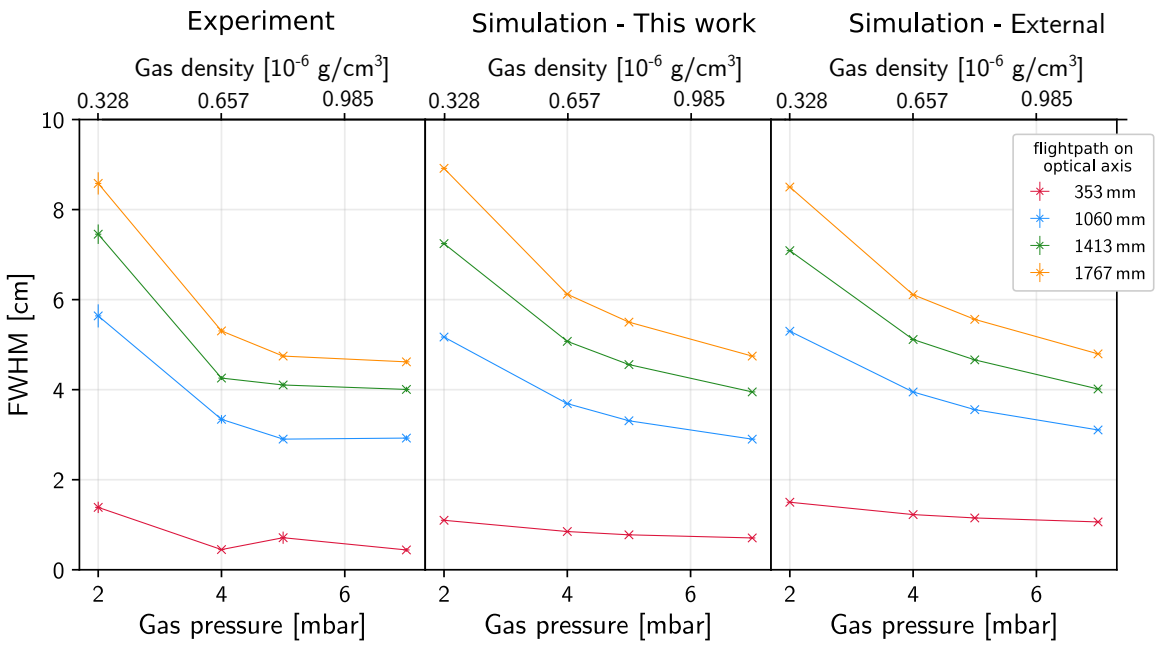

Figure 4.13: The plot shows the comparison of the experimental ion beam profile widths inside the GFM to the simulations from this works code and to the external code, for helium gas. The decreasing course with increasing gas pressure is mirrored by both simulations, although the decreases in the simulations are significantly steeper than in the experiment. Both simulations are in sufficient quantitative agreement.

4.3.2.2 Ion beam trajectory

The initial comparison between experimental trajectories and the simulation showed significant discrepancies. The reason is the gas density effect which highly influences the formed charge state distribution. Since many calculation steps in each code rely on the calculation of the mean charge state, it has high impact on every simulated parameter. However, the most direct impact can be seen on the simulation of the trajectories. The results of the simulation from this work with an adapted approach on the mean charge state and from the external code is shown in fig. 4.14 for nitrogen gas and fig. 4.15 for helium gas. The simulation additionally shows values for the second viewing port at 45° and for 135° at the end of the magnet. The black line within the figures represents the optical axis. Thereby, positive values refer to outer trajectories. For the simulation of the trajectory in nitrogen gas, it has to be remembered that a systematic shift was observed. The starting point and angle had to be slightly adjusted as seen in the parameter files in the appendix, subsec. 7.3.1. This is based on the assumption that the beam was not tuned centered and straightly within the first nitrogen measurement due to the large silicon detector in front of the magnet entrance window as explained in subsec. 4.1.4. All other simulations for the experiments used a centered start position and a straight direction due to the tuning procedure with the small silicon detector. With this and due to the adaption of the mean charge state, based on the experimental values, the code of this work reproduces the given trajectories in nitrogen sufficiently. In helium gas only the last measured position is reproduced quantitatively. Qualitatively all gas pressures except 4 mbar are reproduced sufficiently. The external code reproduces qualitative aspects like the increasing deviation from the optical axis with increasing gas pressure. The only exception to this is in helium gas for 7 mbar gas pressure which does not follow this trend in the experimental values and is therefore also not qualitatively reproduced. Quantitatively the external code is not able to

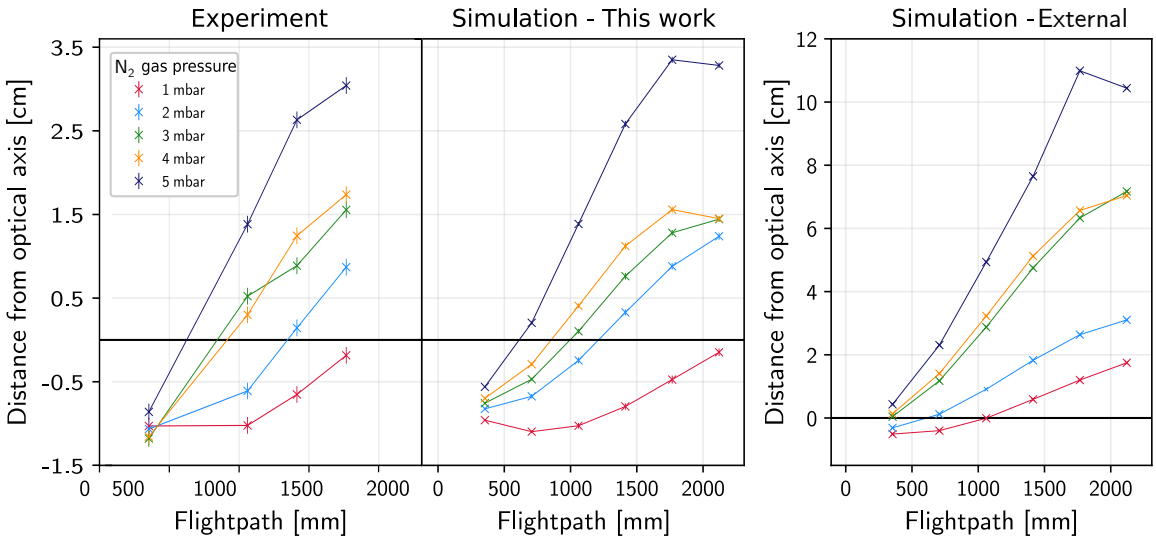

Figure 4.14: Comparison of the experimental ^{60}Ni beam trajectories in the GFM to simulations for nitrogen gas. The values are connected to guide the eye. The simulated points have additional values for the second viewing port at 45° and at 135°, the end of the magnet. The thick horizontal black line within the figures represents the optical axis. Positive values refer to outer trajectories. The difference in the adapted increase of the mean charge state is clearly visible. The trajectories of this work were fitted to the experimental results by deriving a semi-empirical formula using the gas density. With that, a sufficient reproduction of the trajectories is possible. The external code qualitatively reproduces the increased deviations with increasing gas pressures and the bending effect to the optical axis for later positions. Quantitatively the code does not reproduce the experimental values due to the already given reasons.

reproduce the trajectories due to the former given reasons. The deviation between simulation and experimental values become worse with increasing passed path in the gas and also with increased gas pressure as discussed in subsec. 4.3.1.2.

4.3.2.3 Ion beam profile width after the gas-filled magnet

While the measurements and simulations of the beam parameters within the gas-filled magnet are an important step to a better understanding of the process, the choice of the gas pressure and type for the experiment is only dependent on the beam shape and position values at its end. The comparison of the experimental results and the simulation code of the profiles after the gas-filled magnet are shown in fig. 4.16 a) for nitrogen, and b) for helium. For their comparison it has to be taken into account that the simulated values represent the results at an angle of 135° while the experimental values were captured after an additional gas path without magnetic field up to the detector. For nitrogen gas the results are qualitatively reproduced within their errors by the code of this work while not reproduced by the external code. Quantitatively both codes give significantly smaller widths than the experimental results. For helium gas the external code does qualitatively a better reproduction of the experimental results than the code of this work. Quantitatively both simulated results deviate significantly for small pressures and again for the two highest pressures. Thereby, the external code deviates less in both cases but is significantly closer at higher pressures. The quantitative deviations were expected since the measured and simulated positions are not equal. Different effects come into play after the particles leave the magnetic field up to the measurement

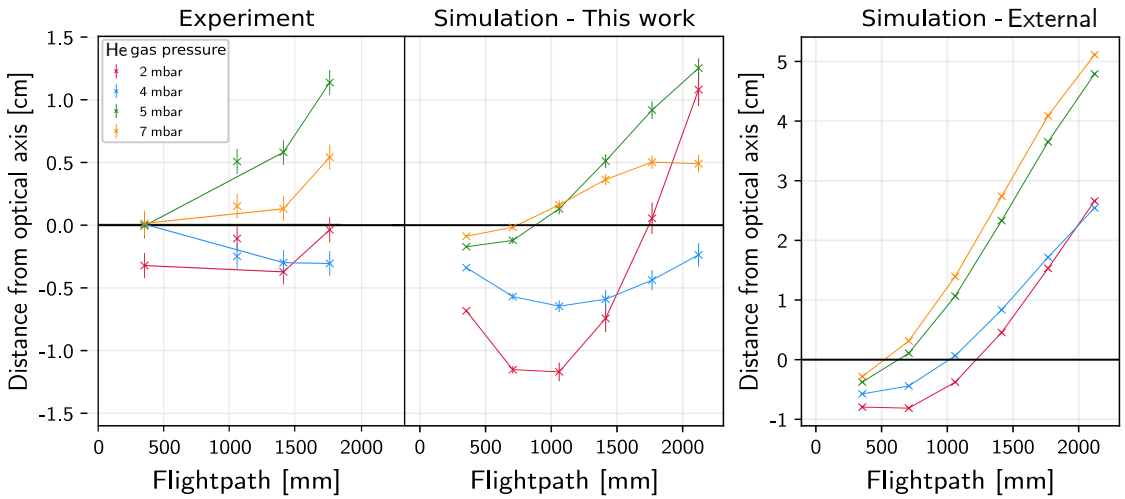

Figure 4.15: Comparison of the experimental ^{60}Ni beam trajectories in the GFM to simulations for helium gas. The values are connected to guide the eye. The trajectories in helium gas are not sufficiently reproduced by any of the codes. While the code revised in this work does not show the large deviations produced by the external code, qualitatively the trajectory shapes are not reproduced. The only position which is reproduced well is the last measured position. The external code is not able to reproduce the trajectories at all. Qualitative aspects like the increasing deviation from the optical axis with increasing gas pressure are mostly reproduced. One exception to this is in helium for 7 mbar gas pressure which does not follow this trend in the experimental values and is therefore also not qualitatively reproduced.

position. Firstly, the beam will experience a broadening effect due to angular straggling in the further gas path. Additionally, the particles will arrive at the edge of the magnetic field with an angle and a positional deviation. Therefore, they will experience a change in angle due to edge focusing by the magnet, [73]. Both effects have a higher impact on particles in nitrogen gas since they experience higher angular straggling and due to their higher positional deviation also a higher impact from the edge focusing. Therefore, it is also not possible to confidently evaluate the correctness of the simulation results. For the future, the simulations could be extended by the edge focusing calculations and an additional flightpath after the magnetic field to simulate the widths at the detector entrance.

4.3.3 Simulation of the separation factors

The experimental values of the measurement described in subsec. 4.2.4 were used to perform simulations with the in-house code and the external code to investigate if the qualitative factor of the separation can be reproduced. The comparison can be found in fig. 4.17. While both codes reproduce the dependence on the gas pressures qualitatively, the code revised in this work is closer to the experimental results. From this result it can be concluded that the revised simulation code revised in this work can be used more sufficiently for qualitative comparisons for nitrogen gas.

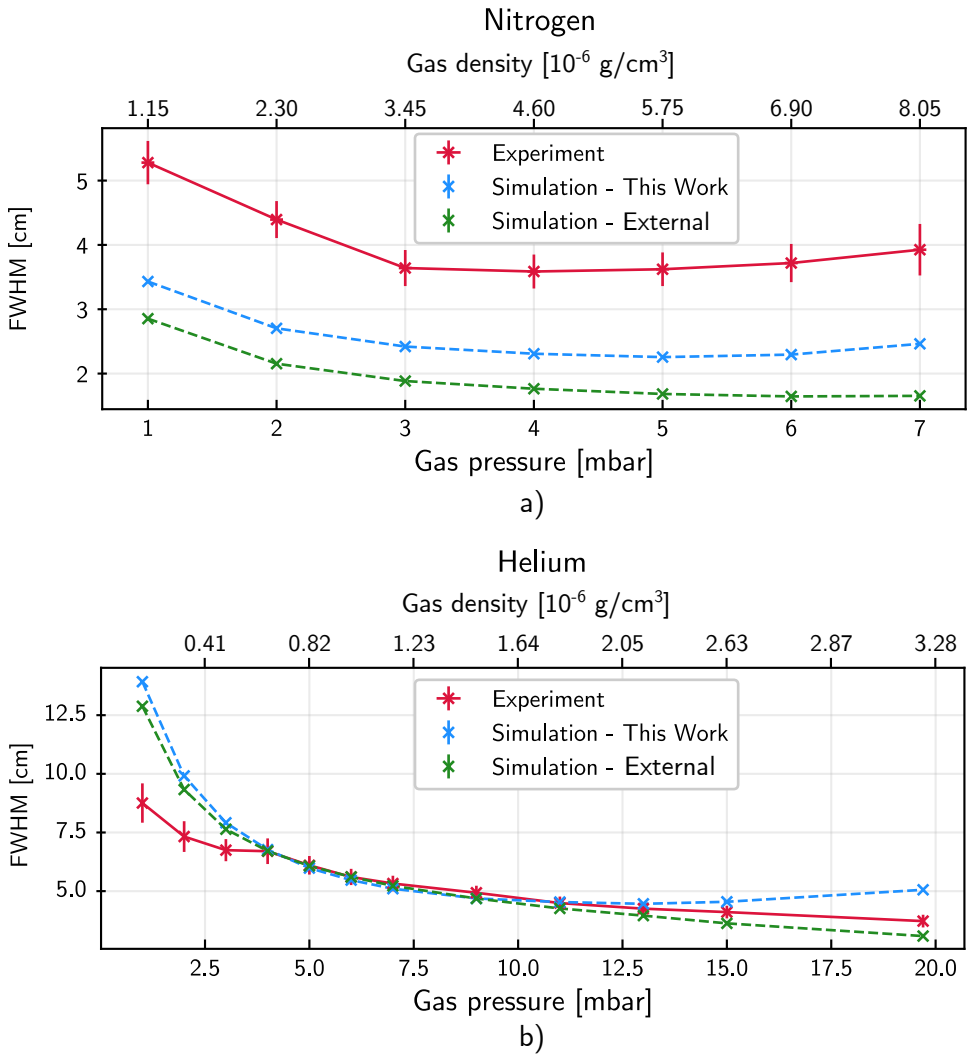

Figure 4.16: Comparison of the experimental ^{60}Ni beam widths after the GFM to simulations for nitrogen gas, a) and helium gas b).

4.3.4 Discussion and conclusion

While certain values are reproduced by either one or the other simulation, it can be concluded that the simulation codes do not achieve the complete reproduction of the inner gas-filled magnet processes. Thereby, the investigations and revision of the code of this work led to sufficient agreements for nitrogen gas and is therefore recommended for its simulations. The inner profile widths and trajectories were qualitatively and quantitatively sufficiently reproduced. Furthermore, the widths after the gas-filled magnet were at least qualitatively reproduced. For helium the quantitative reproduction for the code of this work was sufficient for the inner profiles and in case of low and high pressures not sufficient for the outer profiles. Without further information it would be recommended to use the external code for helium gas simulations for the widths and the code of this work for trajectories. In general the comparisons reveal the limits of the gas-filled magnet codes overall. The processes inside the gas-filled magnet have a complex character and combine a huge range of different physical effects. Due to the fact that there is no easy applicable theoretical or sufficient semi-empirical description for the mean charge state in dense gases or for the charge state distribution width in general, it is not possible to expect highly accurate quantitative results from these codes without further investigations. The significant discrepancies in the simulated

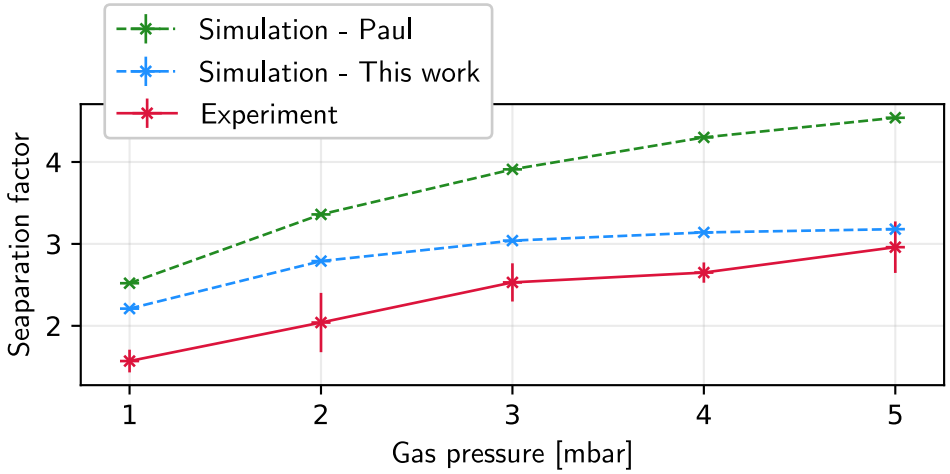

Figure 4.17: Comparison of the experimental measured separation factors of ^{60}Fe and ^{60}Ni after the GFM for different gas pressures to simulations. While both simulations are in qualitative agreement the code of this work is closer to the experimental results.

positions led to the revision of the code in the first place and the knowledge that the gas density effect has to be taken into account. Due to the complexity of this effect, it was only possible to receive an individual semi-empirical formula per gas type which is limited in its use. Secondly it revealed that the used width of the charge state distribution massively impacts the resulting ion beam width since subsequent calculations rely on this value. While the width calculations used in the external code can be used more generally, it relies on the mean charge which is demonstrably false. While the approach of this work uses a more sophisticated approach, it is based on results for solid materials and again adapted for the already measured gas types.
Overall the codes have limits in the prediction of absolute values. However, it can be concluded that the code of this work can be yet used for qualitative comparison of values like width development, trajectory development and even separation factor in nitrogen. Both codes are able to give a rough estimation of magnitude for the beam widths. While the code of this work is limited to the already measured gas pressures, the external code can be used to give a general rough quantitative comparison between gas types. Finally, at the current state of research for some of the necessary approaches, the codes can only be used to give an idea of measurement condition which subsequently has to be confirmed by experiment to be finally used.

5 Development of ^{60}Fe AMS measurements

The AMS setup at the 10 MV FN tandem accelerator in Cologne is dedicated to medium mass isotopes due to the higher achievable energies and concluding isobar separation in comparison to the 6 MV Tandetron accelerator AMS setup. First individual sample AMS measurements of ^{41}Ca and ^{53}Mn were performed using the degrader foil technique, [10]. The installment of a gas-filled magnet system enables significant improvement in the measurement technique by allowing higher transmission with high suppression of the isobar. A promising and interesting candidate for the first AMS measurement using the gas-filled magnet was the isotope ^{60}Fe. ^{60}Fe is currently only measurable by AMS with additional suppression steps on the high energy side, like a gas-filled magnet, due to the high amount of the stable isobar ^{60}Ni. Due to the ΔZ =2 to the isobar, a sufficient separation should be achievable with energies reachable in Cologne. First tests with the comparable stable isobars ^{58}Fe and ^{58}Ni showed sufficient separation in the system energy range, [33]. What is not taken into account is the immense difference in intensity between ^{60}Fe and ^{60}Ni which has to be overcome. Furthermore, even with sufficient separation, ^{60}Fe AMS measurements remain challenging due to the demand for lowest ratios in the range of ^{60}Fe/Fe $\approx 10^{-16}$ for certain applications. Since there is no measurable natural ^{60}Fe, the background level in the well established measurements is only dependent on the measurement duration. It has to be considered that each laboratory uses the highest reasonably achievable energy at its system which was at least 125 MeV, [42], and is currently around 170 MeV, [74] to guarantee full suppression of the isobar. This allowed measurements at the limits of AMS at isotopic ratios of around $1 \cdot 10^{-16}$ with background levels of 10^{-17} gained over several measurement periods. These demanding ratios require a fully developed system providing high ion beam output, stability, transmission and isobar suppression to provide sufficient statistics and lowest background. The developments of ^{60}Fe AMS measurements in Cologne were accompanied by general setup developments and gas-filled magnet investigations. Both were dedicated to improve the system to fulfill the demanding requirements for ^{60}Fe on the one side but also to allow reliable AMS measurements of any isotope of interest in general. Since these topics were described beforehand, see sec. 3.2 and chap. 4, this chapter will concentrate on the respective development of ^{60}Fe measurements in Cologne itself. The first section will shortly introduce the isotope of interest and its different applications with their ratio demands. Subsequently, the used standard materials and system characterization of values like extraction efficiency, stripping yields and overall transmission will be presented. The core of this chapter is the presentation of the performed ^{60}Fe standard and blank measurements. Thereby, a short report will be given on the initial individual sample measurements and a comprehensive report on the two sample sequence measurements with the current setup followed by a detailed discussion. Finally, a conclusion to the measurements in regards to the current status of ^{60}Fe measurements is given and current limits will be discussed.

5.1 Properties and applications of ^{60}Fe

The isotope ^{60}Fe is a long-lived β^- emitter with a half-life of $2.60 \cdot 10^6$ years, [8]. It lies near the valley of stability with its nearest stable isotope ^{58}Fe. The mass region including its stable isobar ^{60}Ni is shown in fig. 5.1. Since the isotope is not naturally produced on earth with measurable abundance, applications treat only extraterrestrial produced ^{60}Fe. These applications differ by their production origin which further leads to differences in the desired isotopic ratio values. The two prominent examples will be shortly discussed.

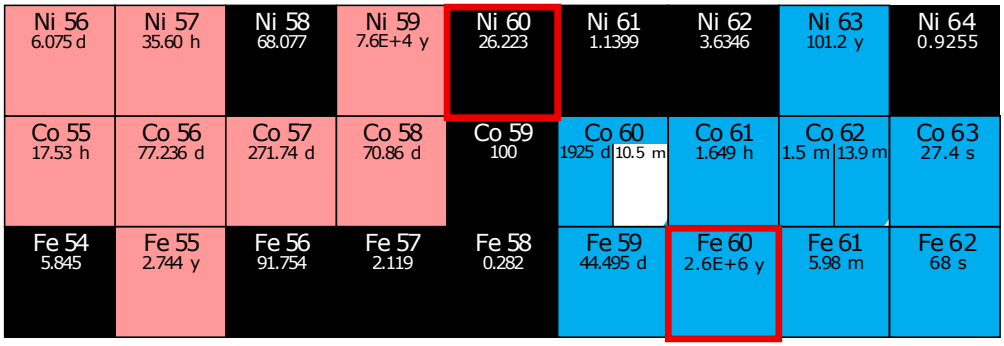

Figure 5.1: Cutout of the nuclide chart showing the mass region around mass 60 amu and the stable iron region. Indicated are the isotope of interest ^{60}Fe and its isobar ^{60}Ni.

- ^{60}Fe production in massive stars and supernova:
  In massive stars ^{60}Fe is produced during the last evolution stages or in supernovae via neutron capture on the unstable ^{59}Fe, [75], [76]. It is mainly produced at temperatures below $2 \cdot 10^9$ K and destroyed at higher temperatures by (γ,n) photodisintegrations and (p,n) reactions. For an efficient production of ^{60}Fe temperatures higher than $4 \cdot 10^8$ K are required yielding necessary neutron flux densities of $10^7\,\mathrm{cm}^{-3}$. A smaller composition is produced during the final explosion in regions which are heated up to $2.2 \cdot 10^9$ K. In dependence on the distance a certain fraction of the debris will enter the earths atmosphere despite the dominant part is shielded by the solar wind. The most significant evidence for identification of supernova debris are the live radioactive isotopes not produced naturally in measurable amounts on earth. Thereby, ^{60}Fe is a probable candidate since it is not produced in detectable amounts on earth but in extensive amounts contained in supernovae debris. An estimation of the accumulated amount on earth made clear that due to the high amount of stable iron the expected ^{60}Fe/Fe ratios are only measurable with AMS. Details on transport processes and calculations can be found in references [77] and [78]. Several scientific contributions report on ^{60}Fe signals determined with AMS in terrestrial reservoirs, [79], [80], [81], [41], [6], [82], [74]. For a sufficient resolution of these signals a sensitivity of ^{60}Fe/Fe of low 10^{-16} and an even smaller background level are required.

- ^{60}Fe production in iron meteorites:
  Meteorites are exposed to primary (protons) and secondary (protons and neutrons) cosmic ray particles. Thereby, ^{60}Fe is produced by spallation on ^{62}Ni and ^{64}Ni, [83], in respective iron meteorites. These consists mainly of iron and nickel material. Due to the low cross sections in an energy region below 1 GeV for this production path via protons, it is dominantly produced by neutrons. Therefore, it can be used as a measure for secondary neutron flux.

In combination with the measurement of ^{53}Mn, it gives information about the meteorite exposure history. Their combination is used for the investigation of galactic cosmic rays, [84]. The measured ratios range in the order of 10^{-15} to 10^{-14}, [83], [7]. The ^{60}Fe/Fe ratio differs between different iron meteorites due to the variation of their fractions of nickel and iron.

5.2 ^{60}Fe standard materials

Within the initiative ERAWAST (Exotic Radionuclides from Accelerator WAste for Science and Technology) the Paul-Scherrer institute (PSI) started a project in which secondary produced activities in setup components of high energy accelerator facilities are reused. The standard samples within this work were produced within this project and provided by the PSI. In the procedure a copper beam dump which was irradiated by high energetic protons for several decades and subsequently decommissioned for several years was processed. The contained iron material including around 10^{17} atoms of ^{60}Fe was chemically separated with respect to suppression of isobaric contents like nickel or copper whereby stable iron is added as carrier, [85]. By that, a solution was produced with a total of 10^{15} ^{60}Fe atoms. Its isotopic composition was derived by Multicollector-Inductively Coupled Plasma Mass Spectrometry (MC-ICPMS) measurements, [39]. By a dilution series of the initial solution, three standard samples of Fe_2O_3 powders were produced. Their specific ratios are given in tab. 5.1. Since the real sample ratios range between 10^{-16}- 10^{-14} dependent on the application, only the PSI-12 is used within sample sequence measurements, [7], when the measurement parameters are already established.

Name	^{60}Fe/Fe ratio
PSI-8	$1.029(3)\cdot10^{-8}$
PSI-10	$1.124(3)\cdot10^{-10}$
PSI-12	$1.242(3)\cdot10^{-12}$

Table 5.1: Standard material for ^{60}Fe AMS measurements used within this thesis and their given literature values, [40].

5.3 Iron oxide extraction

The ion beam extraction from the sample material is the first step of transmission throughout the system since only the particles, which are forming anions from the sample and are extracted out of the ion source, can be detected. An unavoidable loss has to be accepted since the material is sputtered in different molecular forms from which only one species of the extracted ion beam can be chosen by the low energy mass spectrometer. However, AMS measurements often profit from this circumstance. For ^{60}Fe AMS measurements, there are several advantages of the extraction of oxide molecules. Firstly, using a sample containing additional oxygen, for example added during sample preparation, the iron oxide anions produce a more intensive ion beam than the atomic iron. The spectrum over the respective mass ranges from an iron oxide sample can be seen in the upper

plot of fig. 5.2. In the measurement, the comparison between the two peaks of the most abundant component, ^{56}Fe, shows that the oxides ion beam current is a factor of 10 higher.

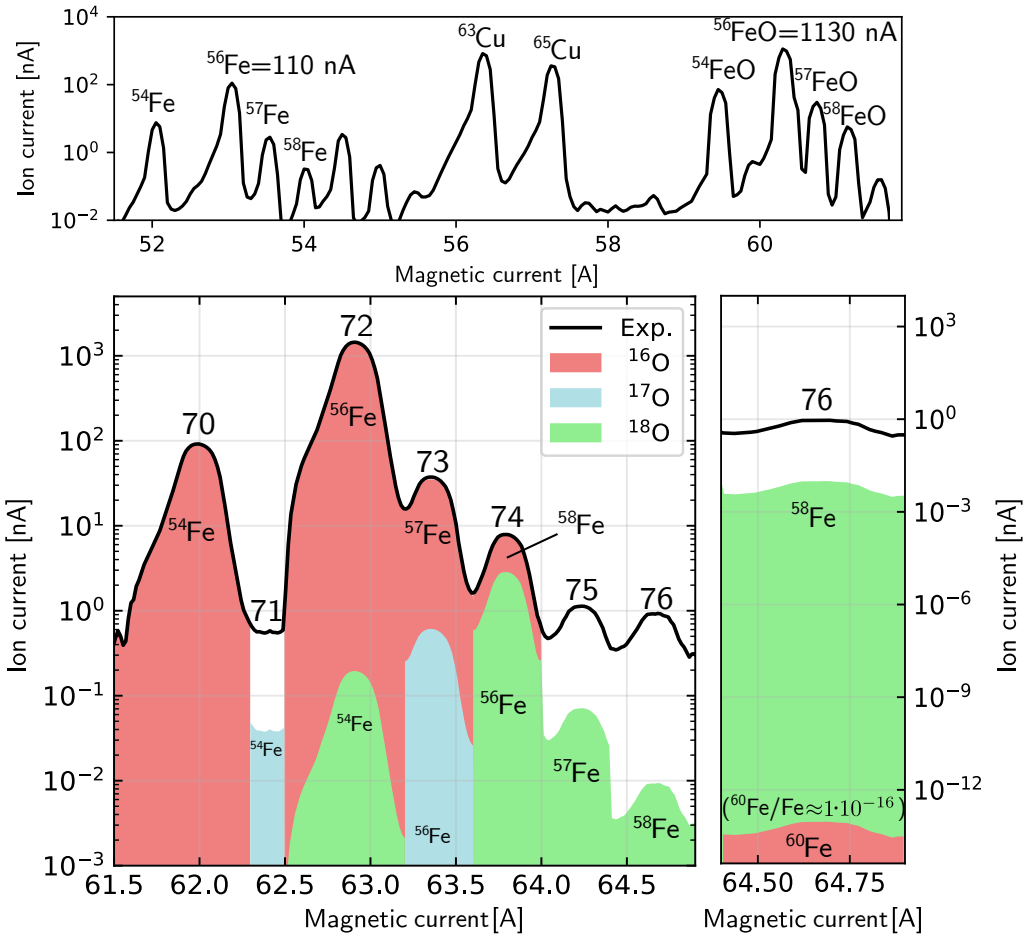

Figure 5.2: Analyzed iron anion spectra after the low energy magnet. The upper plot shows a linear-logarithmic mass spectrum consisting of the atomic iron region and the iron oxide region from Fe_2O_3 material. The iron oxide peaks have around 10 times higher intensities than the atomic iron anion peaks. The peaks in the middle of the regions are copper isotopes from the sample cathode. The lower left plot shows on a logarithmic y-axis the analyzed mass spectrum, containing mainly iron oxide molecules. The numbers above the peaks indicate the molecule mass. The different contents in each peak are indicated by the color scheme corresponding to the specific oxygen mass and complemented by the labels giving the corresponding iron mass. The right plot shows only the mass 76 peak and the estimated fraction of ^{60}Fe for a ratio of $^{60}\text{Fe/Fe} \approx 1 \cdot 10^{-16}$.

Furthermore, it is reported that the nickel background is suppressed by use of the oxide. Thereby, for equal iron oxide and nickel oxide amounts, the nickel extracted as an oxide is suppressed by a factor of 2 in comparison to its atomic extraction, [86]. The lower plots of fig. 5.2 show the mass spectrum of the iron oxide mass region. Thereby, it is shown which molecules contribute to the masses with their respective fractions. Finally, the ion current of ^{60}Fe for a ratio of $1 \cdot 10^{-16}$ ^{60}Fe/Fe within the background on mass 76 is indicated. The sample used for the extraction efficiency was filled with a mixture of iron oxide powder with silver powder in a mass relation of 1:2.8. The powder was pressed into the standard copper cathodes from *National Electrostatics Corporation* with 1.1 mm diameter opening, with the commercial pressing tool. With such a produced cathode, the extraction efficiency of iron oxide for the MC-SNICS ion source in Cologne was determined.

For that the enclosed sample material mass m_{all} is determined by the difference in weight of the empty and filled sample cathode. From that the content of iron atoms can be calculated. The mass of the Fe_2O_3 in the sample $m_{Fe_2O_3}$:

$$m_{Fe_2O_3} = m_{all} \cdot \frac{f_{Fe_2O_3}}{f_{Fe_2O_3} + f_{Ag}} \tag{5.1}$$

The values $f_{Fe_2O_3}$ and f_{Ag} are the contingents of iron and silver from the mixing process. The amount of substance of Fe_2O_3, $n_{Fe_2O_3}$, can be calculated by use of its mean molar mass $M_{Fe_2O_3} = 159.688\,\frac{\mathrm{g}}{\mathrm{mol}}$, [65]. From that the amount of substance of iron n_{Fe} can be determined and finally the amount of included iron atoms $N_{incl.,Fe}$. Since only one individual mass is analyzed from the low energy mass spectrum, the number of iron with mass 56 is calculated by using its natural abundance $F_{56} = 91.754\,\%$, [87]:

$$n_{Fe_2O_3} = \frac{m_{Fe_2O_3}}{M_{Fe_2O_3}} \tag{5.2}$$

$$n_{Fe} = 2 \cdot n_{Fe_2O_3} \tag{5.3}$$

$$N_{incl.,Fe} = N_A \cdot n_{Fe} = N_A \cdot 2 \cdot n_{Fe_2O_3} = N_A \cdot 2 \cdot \frac{m_{Fe_2O_3}}{M_{Fe_2O_3}} \tag{5.4}$$

$$N_{incl.,^{56}Fe} = F_{56} \cdot N_{incl.,Fe} \tag{5.5}$$

The extracted ions are determined by measuring the $^{56}Fe^{16}O$ ion beam on mass 72 after the low energy analyzing magnet in a Faraday cup. The value was logged by the control software once per minute. The ion beam current I is then partially integrated over the captured intervals of $\Delta t = 60\,\mathrm{s}$ to determine the captured charge and subsequently summarized for the total charge Q. From this the number of extracted ions is calculated. Since on mass 72 not only $^{56}Fe^{16}O$ is measured but also $^{54}Fe^{18}O$, see fig. 5.2 or the values in the appendix in tab. 7.4.1, the measured current is corrected by the real $^{56}Fe^{16}O$ fraction $F_{(m=72,^{56}Fe^{16}O)} = 99.987\%$. The final value for the extracted ^{56}Fe ions is derived:

$$N_{extr.,Fe} = N_{A\,Fe^{A\prime}O^-} = \frac{Q}{e} = \frac{\sum_{i=t0}^{i=tmax} I_i \cdot \Delta t}{e} \tag{5.6}$$

$$N_{extr.,^{56}Fe} = F_{(m=72,^{56}Fe^{16}O)} \cdot N_{extr.,Fe} \tag{5.7}$$

Finally, the efficiency is determined by:

$$\epsilon = \frac{N_{extr.,^{56}Fe}}{N_{incl.,^{56}Fe}} \tag{5.8}$$

For the efficiency measurement Fe_2O_3 powder was mixed with silver powder in a ratio of 1:2.8 ($f_{Fe_2O_3} : f_{Ag}$) and pressed into a copper cathode. The included sample material was weighed to m_{all}=18.9 mg. The $^{56}Fe^{16}O^-$ was prior tuned with a separate sample which was subsequently switched to the efficiency sample. The captured ion beam current is shown in fig. 5.3. The efficiency over the whole measurement time of 24.17 hours was ϵ=0.9%. Since the cathodes are not sputtered empty the given efficiency is a lower limit. Within real measurements the sample is switched after a certain decrease in output to achieve as much statistics in the given amount of measurement time as possible. The duration of one measurement lies in the region of around 5-10 hours which would lead to a reachable efficiency of $\epsilon_{5-10\,h}$=0.30-0.51% which is in a comparable magnitude to other

laboratories, [41], [42].

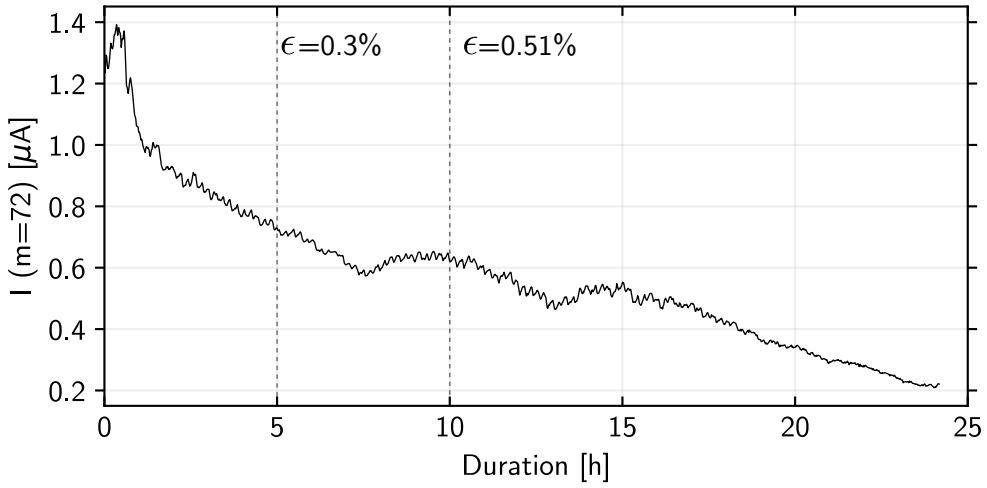

Figure 5.3: Efficiency measurement after the low energy analyzing magnet of mass=72, mainly $^{56}Fe^{16}O^{-}$, from Fe_2O_3. The Fe_2O_3 powder was mixed with silver in a ratio of 1:2.8 and the sample material was weighed to 18.9 mg.

5.4 Stripping charge state distribution

The choice of charge state has a high influence on the final AMS measurement. If the isobar separation is sufficiently possible, the charge state with the highest yield is chosen to achieve the highest statistics per equal measured time. Since the choice of charge state also determines the isotopes final energy, it can be favorable or even necessary to use a less abundant higher charge state to achieve better isobar separation. For the iron measurements the charge state distribution was measured with a macroscopic ion beam of ^{54}Fe. The charge state fractions were measured at the FC ANA and identified with the well-defined magnetic field at the high energy analyzing magnet. Since the chosen charge states have different $\frac{p}{q}$ values the magnetic lenses in front of the analyzing magnet were adjusted. The measured charge state distribution can be found in fig. 5.4 a). The resulting measured charge state fractions were compared to semi-empirical formulas of Sayer [28], Dmitriev [29] and Schiwietz [30], see fig. 5.4 b). While the calculations are in good agreement with each other, the experimental values are shifted by $\Delta q = +1$. The experimental values for the charge state distribution were repeatedly testified over the course of several measurements. Similar observations for the charge state distribution of iron were reported before, [88]. As a compromise between available energy for isobar separation and high statistics, the 10^{+} charge state is used for the measurements. The sum over the particle rate of the different fractions can be directly compared to the current on the FC LE to gain the transmission between them, including the transmission through the accelerator. For the shown values the transmission of the whole iron beam was 29%. The smaller value in comparison to proton or atomic carbon ion beam with around 50% can be explained due to the iron injection as iron oxide which causes coulomb explosions when using foil stripper material.

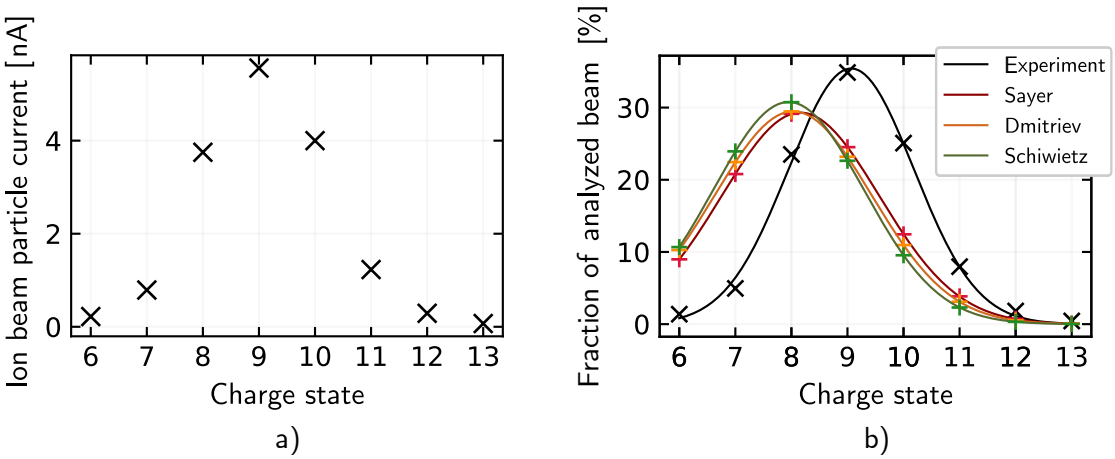

Figure 5.4: Charge state distribution measurement of ^{54}Fe injected as ^{54}Fe^{16}O at a terminal voltage of TV=8.85 MV. Plot a) shows the measured charge distribution derived by the measured particle current. The particle current is derived by the electric current divided by the respective charge state. Plot b) shows the fraction of the measured charge states from the whole identified iron beam and the corresponding values taken from calculations with the semi-empirical formulas from Sayer, Dmitriev and Schiwietz. While all calculated distributions are in good agreement the experimental values show a shift of $\Delta q = +1$.

5.5 Tuning procedures and stable isotope transmission

For the setup tuning for ^{60}Fe particles, two different procedures were used. In both, macroscopic ion beams, so-called pilot beams, reflecting the respective discrimination values are used to determine all system component settings up to the last Faraday cup. Subsequently, a microscopic particle beam with equal properties to the isotope of interest is used for the remaining flightpath up to the detector. The used particle beam can be the isotope of interest itself from standard material. Since memory effect should be minimized the alternative by use of the respective isobar from blank material should be used. The difference of both used procedures is the choice of used stable isotope as macroscopic beam. The first version reflects the tuning procedure of the initial performed standard material measurements, [10]. Thereby, a ^{58}Fe^{10+} ion beam was chosen since it was also the stable reference isotope during the final measurement. It was injected twice with different energies, firstly matching the $\frac{E}{q}$ value and secondly matching the $\frac{p}{q}$ value. By that, the corresponding components were tuned, see subsec. 3.2.3.2 for comparison. In a second version ^{54}Fe^{9+} was chosen as pilot beam whereby only one energy has been used since it matches the $\frac{E}{q}$ and $\frac{p}{q}$ values almost exactly. In both procedures, the beam was tuned to the FC HE III which is between the quadrupole lens III and the gas-filled magnet entrance. The achieved transmission for a stable iron beam, ^{54}Fe^{10+}, can be found in tab. 5.2. The transmission on the low energy side was 93% and the transmissions on the high energy side are near to 100%. The largest loss can be observed from the FC LE to the FC ANA with a transmission of 7.14%. From the FC LE up to the FC HE III 6.44% of the ion beam was transported, which includes the unavoidable loss by the charge state fraction of 25%. From the last available Faraday cup, the FC HE III, the beam has to be tuned to the gas ionization detector. Therefore, in the next tuning step the low energy mass spectrometer is set to mass 76 to inject ^{60}Ni^{16}O from a blank material. The isobar ^{60}Ni mirrors the tuning properties of ^{60}Fe. It is further used to tune the beam to the entrance of the magnet

Position	I($^{54}Fe^{10+}$)[nA]	Transmission to last position[%]	Total transmission[%]
FC Magnet	45	-	-
FC LE	42	93.33	93.33
FC ANA	30	7.14	6.67
FC HE I	29	96.67	6.44
FC HE II	29	100.00	6.44
FC HE III	29	100.00	6.44

Table 5.2: The table lists the electrical measured ion beam currents at each cup and the transmission between the different Faraday cup positions along the beam line for the iron pilot beam. Thereby, it differed between the transmission to the last position and the total transmission from the FC Magnet as the start. The transmissions on the high energy side are not divided by the charge state fraction of 24% for the used 10+.

where a silicon detector is installed as a reference. An analog ratemeter can be used for tuning but it is favored to use the data acquisition coupling as soon as the ^{60}Ni is identified in the recorded silicon energy spectrum. Thereby, it can be excluded to tune a different interference through the gas-filled magnet. In the last step, the ^{60}Ni is tuned into the gas ionization detector by tracing the gas-filled magnet and step-wise fine tune the high energy mass spectrometer. Since ^{60}Fe loses less energy than ^{60}Ni and therefore needs a higher magnetic field, it can be found at a 6-7 A higher magnet current in the used energy and gas pressure range. When switched to standard material, the ^{60}Fe particle rate is conclusively tuned with the help functions within the control software. A final set of parameters used in the measurements of subsec. 5.6 can be found in the appendix in tab. 7.6. At last, the stable reference isotope beam can be captured within the offset-cup which is positioned at +75.1 mm in comparison to the optical axis and fine-tuned by help of remotely controlled piezo-motors.

5.6 ^{60}Fe AMS measurements in Cologne

This section will present the performed sample sequence ^{60}Fe AMS measurements for two different window sizes of the gas ionization detector. Between the first performed measurements of ^{60}Fe and the current status, extensive effort has been put into the overall AMS system stability and reproducibility to even allow the measurement of sample sequences. An overall increase in the reachable statistics, to allow low-level measurement, was gained. Furthermore, systematic investigation of the gas-filled magnet inner processes and the gas settings were conducted and their results were applied in the current measurements. However, in the initial measurements a higher terminal voltage of 9.3 MV and conclusively higher energies were usable. For the measurements of the current status this was not possible due to the limiting voltage stability of the accelerator at terminal voltages over 9 MV without using slit control. Therefore, this section will firstly report on the initially performed AMS measurements and their limits. Subsequently, the current status is presented and which limitations were overcome. A detailed discussion of the current measurements and a comparison to the initial status is given. Finally a conclusion is drawn and current limits are discussed as well as a short outlook is given for the next steps.

5.6.1 Initial status of ^{60}Fe AMS measurements

Within the first ^{60}Fe standard material measurements it quickly became clear that the stability and reproducibility is not sufficient for the desired low-level AMS measurements or measurements of related sample sequences over a long-term measurement. Nevertheless it was possible to determine the initial status of the ^{60}Fe measurements with special respect to the achievable transmission, statistics and isobar suppression and separation. This subsection will report on these results.

5.6.1.1 Conduction, analysis and results

Within the former state, it was not possible to measure sequences within the first performed measurement periods. The stability did often not allow to measure under identical conditions over several hours and the reproducibility did often not allow to seamlessly continue the next day. However, it was possible to measure occasionally at least one sample of the different standard and blank materials in a row. In prior, the beam was tuned using ^{58}Fe as described in subsec. 5.5. The nitrogen gas pressure was set to 3 mbar which was chosen in respect to good energetic isobar separation in the gas ionization detector. The 5 anode gas ionization detector was used after the gas-filled magnet with a 2 cm x 2 cm SiN window with 1000 nm thickness as in former tests. For the analysis, the energy loss curves of ^{60}Fe and ^{60}Ni were evaluated to determine the anode configuration for optimal separation. Therefore, the crossing point of the energy loss curves was determined, see fig. 5.5. The experimental values are given in arbitrary channel values since no energy loss calibration could be easily made. Additionally, it has to be considered that in the former anode structures the anodes were not geometrically identical, see subsec. 7.4.2 in appendix. Since their experimental signal calibration was done by a pulser for the following electronics, their size-difference was not taken into account. For the determination of the energy loss curves the individual anode signals were evaluated. The respective peaks are identified by comparison between standard and blank sample measurements. The crossing point of both curves can be found between the third and fourth anode which was considered in the final analysis. The measured curves and the corresponding calculations with LISE++ with the formalism by Ziegler can be found in fig. 5.5. For the calculations, the ion energy loss within the magnet entrance window, the magnet inner gas distance, the detector entrance window and the energy loss on the different anodes were calculated. For the shown values the energy loss was calculated for the length of the respective anode. It has to be taken into account that energy loss within the dead volume in front of the detector will mostly be captured by anode 1, therefore both contributions were summed for the first entry within the calculations. Furthermore, it was later found that the displayed magnet gas pressure value at the setup did not equal the real gas pressure and differed to a second probe by +2 mbar. The comparison of the captured energy loss with calculations, assuming the displayed value of 3 mbar and an assumed value of 1 mbar, indicated that the lower value was the real one. While in the latter the crossing point is qualitatively reproduced, the overall curves are not reproduced due to the applied experimental calibration method. The gas pressure probe was replaced by a calibrated one in the current status, which was again independently testified with a second probe.

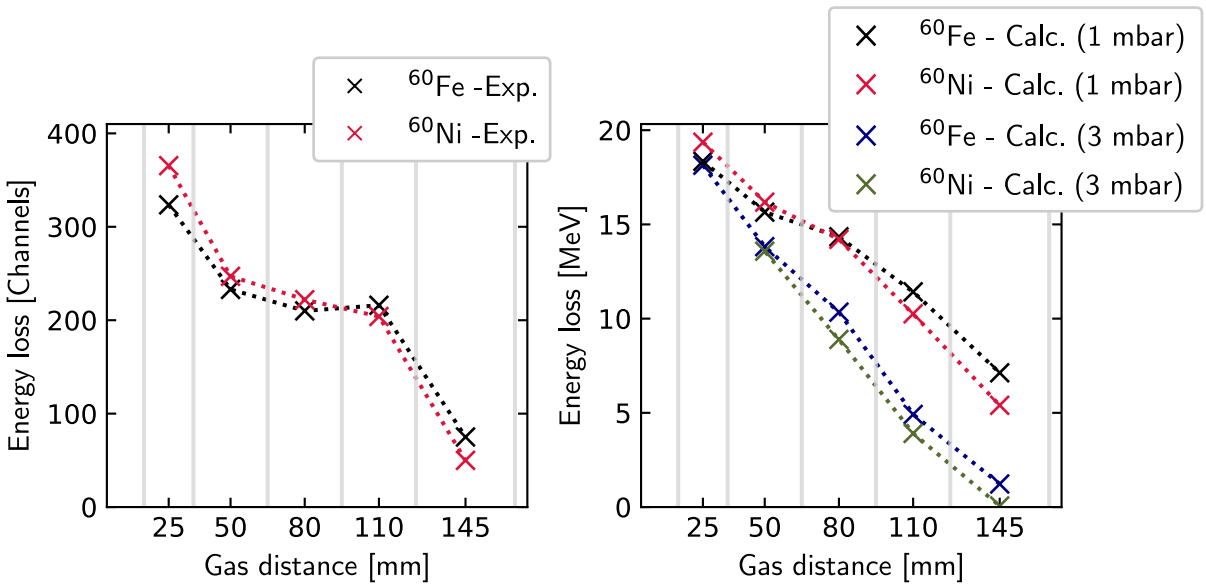

Figure 5.5: Plot a) shows the energy loss measurement of ^{60}Fe and ^{60}Ni in the gas ionization detector at 42 mbar isobutane gas pressure. The data points' x-positions indicate the middle of the respective anodes, the vertical lines their width. The gaps between the anodes are neglected. The crossing point is between the third and fourth anode. Plot b) shows the calculated curves by use of LISE++ with the formalism by Ziegler. Thereby, the prior energy loss is calculated beforehand. For the first position the energy loss of the prior dead volume is summed to the first anode. It was assumed that the displayed gas pressure of 3 mbar for the magnet was not correct but was assumed to be 1 mbar. The calculation of the integrated differential energy loss curves for 1 or 3 mbar nitrogen gas pressure show that the former qualitatively represents the crossing point better. Since the experimental calibration of the anodes by a pulser signal does not account for their different size the qualitative reproduction of their curves by calculations are not sufficiently possible.

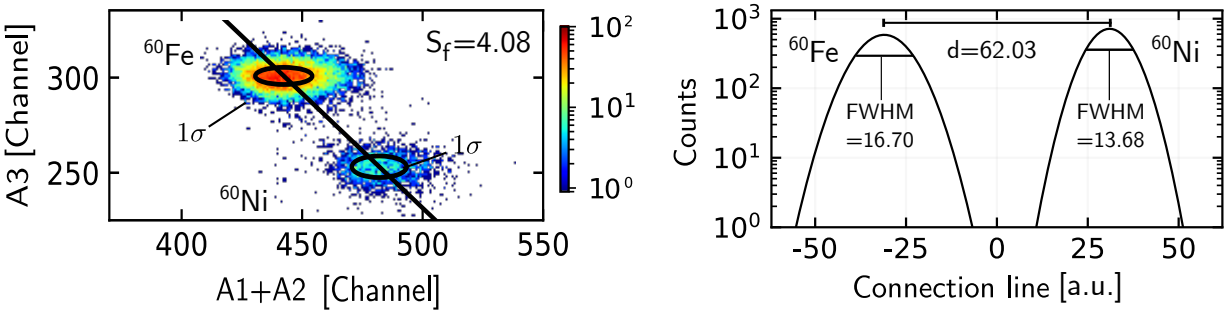

Figure 5.6: The figure shows the achieved separation in the detector spectrum in the example measurement. Plot a) shows the analyzed two-dimensional spectrum with the respective σ ellipses for each distribution, the connection line between the means and the intersections of connection line and ellipses. The separation factor between the peaks is S_f=4.08. Plot b) shows corresponding fitted Gaussian distributions on the projection of the connection line for equal amounts.

For the analysis, a two-dimensional spectrum comparing the energy loss between the sum of the second and third anode to the sum of the fourth and fifth anode was used. The first anode signal was not usable due to its signal disturbance. The respective separation parameters and a visualization of

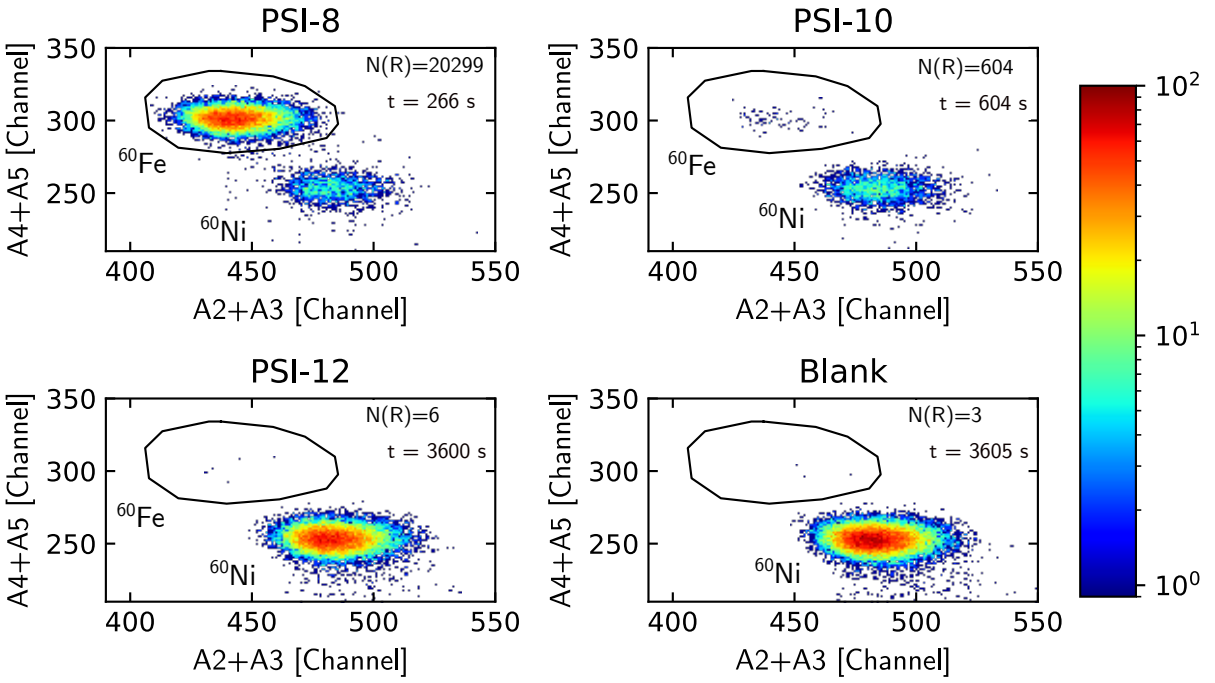

Figure 5.7: The figure shows a successful example of ^{60}Fe AMS measurements of standard and blank material. The ROI is indicated by the black lined region. While the separation between ^{60}Fe and ^{60}Ni was sufficient the achievable statistics is significantly too low to gain reasonable measurement duration for the desired ratios.

their two-dimensional fit can be found in fig. 5.6 a) while the fitted distribution on the projection of the connection line and the receptive Gaussian parameters is shown in fig. 5.6 b). The separation factor was determined to S_f=4.08 and no further offline analysis was required for final results. While the separation was sufficient, the achieved statistics were more than a magnitude lower than reasonable measurement times for ^{60}Fe/Fe$\approx 10^{-16}$ would require. To summarize over the course of the several performed individual measurements the averaged captured stable isotope current of ^{58}Fe^{10+} was 150 pA. This is impacted by the performance of the ion source, the low energy side transmission and the transmission through the accelerator up to the offset-cups. An example of a successful measurement can be seen in fig. 5.7 which resulted in the best correction factor achieved in an individual measurement series from the initial measurements of c_f=5-6 which translates to a transmission of the high energy mass spectrometer of 20-17%. The average achieved correction factor was around 8 which translates to a high energy side transmission, including the gas-filled magnet, and the isotope identification within the detector of 12.5%. To set these values in relation, the measurement of one count of a sample with a ^{60}Fe/Fe ratio of $1 \cdot 10^{-16}$ would need 27.69 days of pure measurement time on average. The isotopic ratio for a sample with a ^{60}Fe/Fe ratio of $1 \cdot 10^{-14}$ would need 6.64 hours. However, the best achieved background level was a corrected ratio of $6.55^{+4.99}_{-2.24} \cdot 10^{-14}$. It has to be taken into account that the high background level was probably caused by memory effect. Due to the low statistics, the ^{60}Fe particle beam tuning was exclusively performed with the PSI-8 with a ratio in the order of 10^{-8} due to the low achievable statistics and because only manual tuning was available. Furthermore, due to the non-reproducibility and instability of several ion-optical components a transmission improvement or investigation would not have been possible with lower particle rates. It can be assumed that the background would

not have hindered measurements in the range of 10^{-14} if the usage of only the lowest standard for tuning would have been possible. In conclusion, the main limitations were the insufficient statistics, the missing reproducibility and moreover the overall system stability. This hindered any related sample sequence measurements in general and in combination with low statistics did not allow long-term, low-level isotopic ratio measurements. Furthermore, the combination of instability and low statistics hindered systematic investigation and improvement of the AMS measurements themselves. Therefore, it was decided to overcome these limitations by systematic investigations and developments of the whole setup in respect to the problems, see sec. 3.2 and chap. 4.

5.6.2 Current status of ^{60}Fe AMS measurements

This section will report on the current status of ^{60}Fe AMS measurements at the 10 MV setup. After the extensive investigations and developments of the setup, first long-term measurements and sample sequence measurements became available. This section will report on the latest setup modifications and the measurement of two sample sequences consisting of standard and blank materials using different-sized detector entrance windows. The results will be presented and discussed subsequently.

5.6.2.1 Setup developments, measurement conduction and data analysis

In comparison to the initial experiment and by the finding of the beam shape investigations some final modifications were done to the gas-filled magnet setup. The existing magnet entrance foil setup was replaced. Formerly, it could be chosen between a large round 2µm thick Mylar window with a diameter of 58 mm or to use a small $12 \times 12\,\mathrm{mm}^2$ squared SiN foil which was mounted to a slightly larger rod inserted into the magnet by 250 mm. While the Mylar window causes large unnecessary energy loss, it can be assumed that the rod setup reduces the transmission since the beam is impacted by the magnetic field within the small rod which could hinder the ions to pass the window. Therefore, a 200 nm thick squared SiN foil with $10 \times 10\,\mathrm{mm}^2$ is yet mounted at the entrance adapter flange of the magnet. Therefore, an available inlet for the magnet entrance was redesigned so that it equals the detector entrance mounting. Therefore, each already available detector entrance window can be used for the gas-filled magnet entrance. Furthermore, a new adapter was built to shorten the gas distance after the gas-filled magnet. It connects the magnet exit flange directly to the detector only limited by the space which is necessary for mounting. For the experiment, three standard materials and one blank material were available. Thereby, the highest standard, PSI-8, was only measured once in the beginning of the measurement week and avoided afterwards. This was possible since the measurements of the other standards provided enough statistics for sufficient tuning and determination of the correction factor. In the first half of the experiment the two lower standards were used and in the second half even only the lowest standard was used to minimize ion source memory effect as much as possible. In the following the two effects of cross talk and memory effect will be referred to as memory effect since both could cause the described impacts, see subsec. 5.6.5.4 for a clarification of their difference. Thereby, at least two samples of each standard were equipped which were evenly distributed along the wheel. An equal number of blank samples were available consisting of already mounted samples which were

not sputtered in former measurements and newly produced blank samples. The measurement was conducted manually with an identical procedure as for the carbon standard material measurement, see subsec. 3.2.3.3. All available individual samples were measured. For the measurement, two different detector entrance windows were used. First the formerly used 1000 nm thick 2 cm x 2 cm SiN foil. This allows a direct comparison to the initial measurements and also allows higher gas pressures for optimized separation. Otherwise, the investigations of the beam shape showed that a part of the beam is cut at the window. Therefore, a second larger window, a round 2 µm thick Mylar window with a diameter of 4.5 cm was used to compensate for the broader beam in the second part of the measurement. As for the initial experiments the analysis used two-dimensional energy loss spectra for identification. Equally, the energy loss curves were analyzed and the two-dimensional spectra were chosen for best separation qualities. For the final identified particles an additional two-dimensional ROI was used. The energy loss curves and the respective chosen spectra can be found in the individual subsections concerning the different windows.

5.6.3 Results by use of the small detector entrance window

For the first part of the measurement the smaller detector entrance window was used. A detector pressure of 37.5 mbar isobutane gas was chosen. The captured energy loss curves and the theoretical calculations of ^{60}Fe and ^{60}Ni can be found in fig. 5.8. The crossing point from the experimental

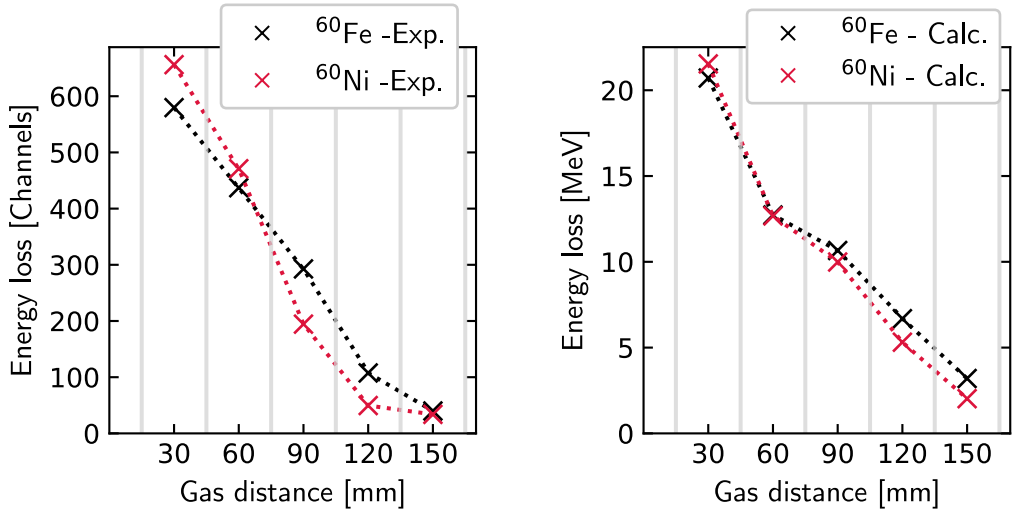

Figure 5.8: Plot a) shows the energy loss measurement of ^{60}Fe and ^{60}Ni in the gas ionization detector by the analysis of the individual anode signals of a standard sample. The smaller SiN entrance window was used which allowed an optimized inner gas pressure of 37.5 mbar. The chosen x-values indicate the middle of the individual anodes, the vertical lines their width. The crossing point can be found near to the middle of the second anode. Plot b) shows the calculated curves by use of LISE++ with the formalism by Ziegler. Thereby, the prior energy loss is calculated beforehand. The values represent the integrated differential energy loss over the anode length in beam direction. The energy loss of the dead volume is summed to the first anode since the produced signals will be captured mainly by the first anode, see subsec. 3.2.2.

values can be found shortly ahead of the middle of the second anode which is in agreement with the calculated values. Discrepancies can occur since the calculated ^{60}Ni component refers to the

primary beam which is positionally separated. The fraction of the ^{60}Ni ions which reach the detector in the experiment will have lower energy. Derived from the results, two-dimensional spectra which show the third anode in comparison to the sum of the first two anodes were used for analysis. The alternative two-dimensional spectra combination of the first anode against the third was excluded. Even if the separation between ^{60}Fe and ^{60}Ni would be slightly better, the separation to other interfering components became worse. The fitted separation properties between ^{60}Fe and ^{60}Ni can be found in fig. 5.9. The additional interferences are discussed in more detail due to their impact

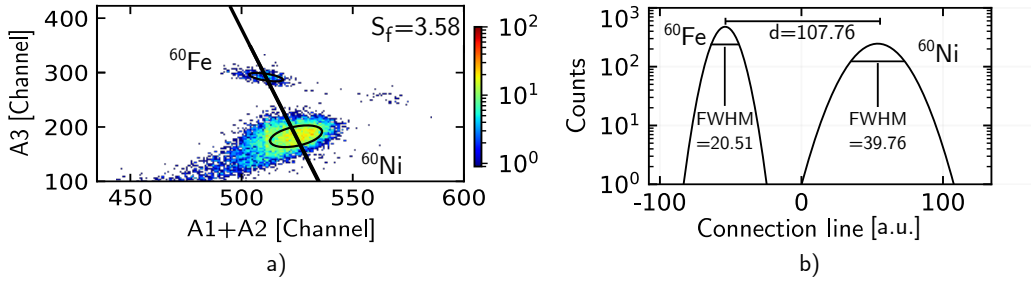

Figure 5.9: The figure shows the achieved separation in a combined spectrum of the highest standard and blank example measurements at 37.5 mbar isobutane gas pressure. Plot a) shows the overlap of the analyzed two-dimensional spectra with the respective σ ellipses for each distribution, the connection line between the means and the intersection of the connection line and ellipses. The separation factor between the peaks is S_f=3.58. Plot b) shows the corresponding fitted Gaussian distributions on the projection of the connection line for equal amount of ^{60}Fe and ^{60}Ni.

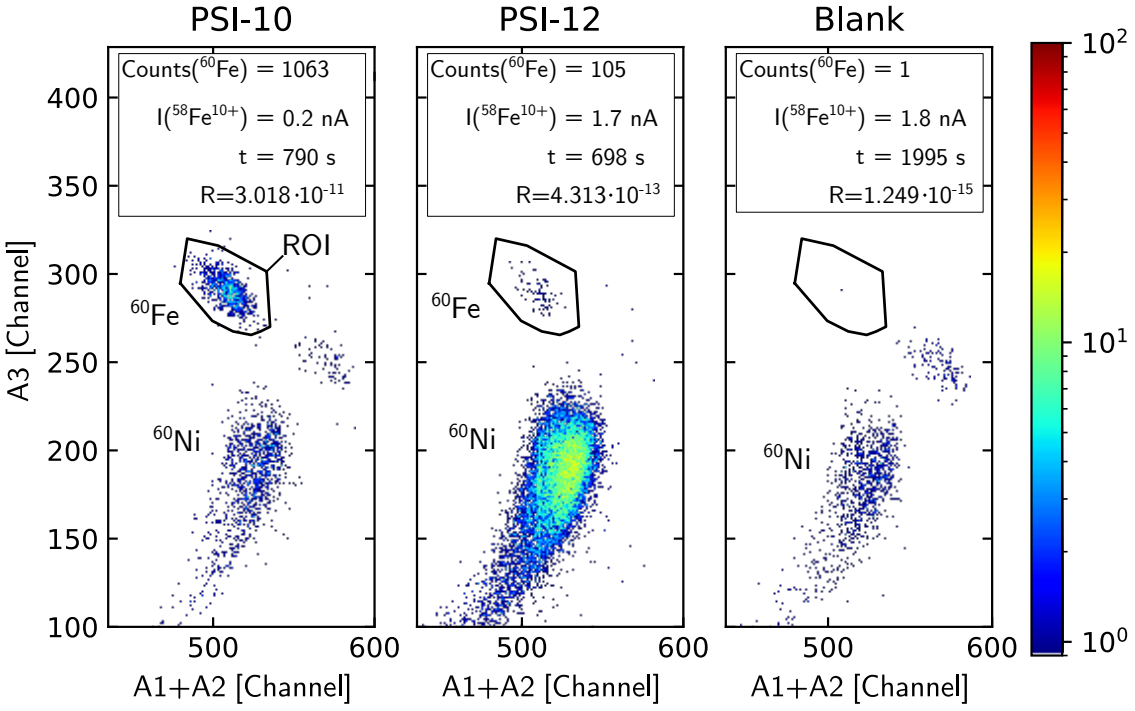

Figure 5.10: Examples of the gas ionization detector spectra used for particle identification of ^{60}Fe for three measured materials. The two-dimensional spectra show the signal from the third anode against the summed signals from the first and second anode to use the crossover of the energy loss measurements. Within these spectra a ROI is represented by the black frame.

by using the large window in subsec. 5.6.5.5. The final identification was done by a two-dimensional ROI. An example measurement of two measured standard materials and one blank can be found

in fig. 5.10. The uncorrected values of the individual measured samples can be found in fig. 5.11. It revealed that the former equipped blank samples result in almost a magnitude higher blank

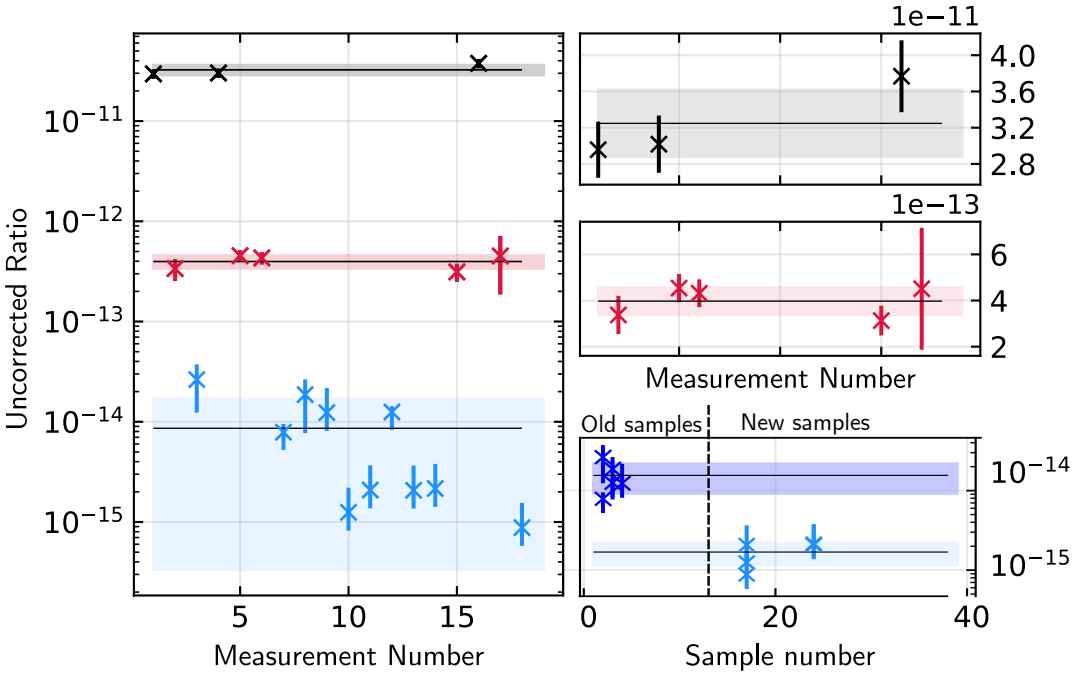

Figure 5.11: The left logarithmic plot shows the individual uncorrected ^{60}Fe/Fe ratios in order of their measurement by use of the small detector entrance window. The black ones correspond to the PSI-10 material, the red ones to the PSI-12 material and the blue values indicate the blank samples. Thereby, all measurements were performed subsequently to each other in order of the given number with exception of the last blank measurement. It was performed after two days in which only the PSI-12 was used as a standard. The upper two right plots show zoomed in versions of the two standard ratios on a linear scale. The lowest right plot shows the blank values in dependence of the respective sample number. It revealed that the former equipped blanks (positions under 10, indicated in dark blue in the lower right plot) result in an around one magnitude higher ratio than the newly produced ones (position 17 and 24). This can be traced back to memory effect of the formerly used high standard material PSI-8. The horizontal lines in all plots indicate the mean value and the underlying boxes indicate the standard deviation.

level than the newly produced ones. This can be traced back to former experiments where the highest available standard, PSI-8, was used extensively for tuning. The PSI-10 shows a standard deviation of 11.35%, the PSI-12 of 15.08%, the new blank samples of 31.01% and the old blanks of 41.17%. These individual values were processed as described in subsec. 3.2.3.3 to receive the final isotopic ratio result in tab. 5.3. By use of the smaller detector entrance window a correction factors of 3.52(2) was achieved corresponding to a transmission of 28.41%. This comes close to the calculated value of 23% on basis of the beam profile measurement in subsec. 4.2.3. Therefore, it can be assumed that the highest transmission loss occurs at the detector entrance window. By that, a corrected blank level by using newly produced samples of $4.53^{+3.85}_{-1.46}\cdot10^{-15}$ was achieved. It is assumed that the blank level is caused by memory effect due to the use of the PSI-10 material with a ratio of almost 5 magnitudes higher than the measured blank level. A corresponding investigation and its discussion can be found in subsec. 5.6.5.4.

Material	Meas. ^{60}Fe/Fe Ratio	c_f	Corr. ^{60}Fe/Fe Ratio
PSI-10	$3.17(19)\cdot10^{-11}$	3.54(22)	$1.124(3)\cdot10^{-10}$
PSI-12	$3.93(32)\cdot10^{-13}$	3.16(81)	$1.242(3)\cdot10^{-12}$
Blank$_{\text{old}}$	$1.25^{+0.47}_{-0.33}\cdot10^{-14}$		$4.41^{+1.89}_{-1.46}\cdot10^{-14}$
Blank$_{\text{new}}$	$1.29^{+1.09}_{-0.41}\cdot10^{-15}$		$4.53^{+3.85}_{-1.46}\cdot10^{-15}$

Table 5.3: Measured ratios for the three materials. The correction factors of the two standard materials are equal within their error and resulted in a final averaged factor for the measurements of $c_f = 3.52(21)$. The formerly equipped blank samples show a magnitude higher background caused by memory effect from former experiments where the PSI-8 were used.

5.6.4 Results by use of the large detector entrance window

For the second part of the measurement the large detector window with a diameter of 4.5 cm was used. Thereby, it was not possible to reach an optimal detector pressure due to the stability of the window. A detector pressure of 30 mbar isobutane gas was used. The captured energy loss curves and the theoretical calculations of ^{60}Fe and ^{60}Ni can be found in fig. 5.12. The crossing point from the experimental values can be found in the beginning of the second anode which is in good agreement with the calculations. Discrepancies can occur due to the same reasons for the ^{60}Ni energy as for the small window. Furthermore, the signal produced in the dead volume does not only reach the first anode but in dependence of the y-position also the second one. This effect has more impact by use of the large window. Due to the same reasons as for the small window an equally chosen two-dimensional spectrum and an adjusted two-dimensional ROI was used for analysis.

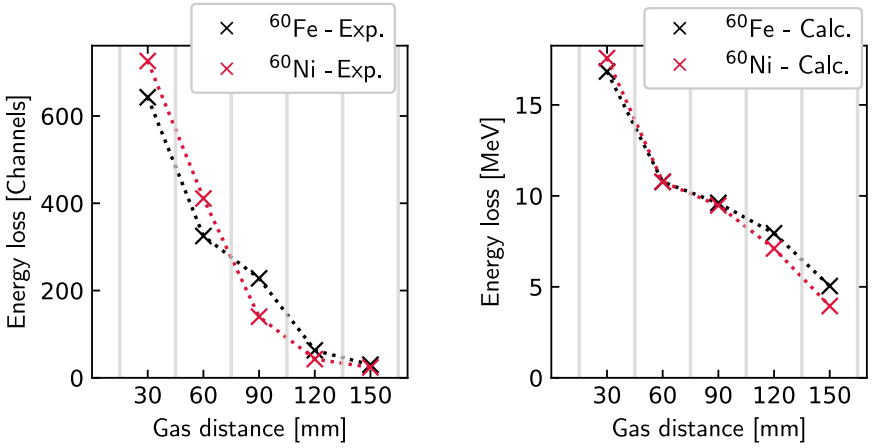

Figure 5.12: Plot a) shows the energy loss measurement of ^{60}Fe and ^{60}Ni in the gas ionization detector. The larger Mylar entrance window was used which only allowed a gas pressure of 30 mbar isobutane gas. The chosen x-values indicate the middle of the individual anodes, the vertical lines their width. The crossing point can be found at the beginning of the second anode. Plot b) shows the calculated values by use of LISE++ with the formalism by Ziegler. Thereby, the prior energy loss was calculated beforehand. The values are the integrated differential energy losses over the anode length. The energy loss within the dead volume is summed to the first anode.

The visualized separation can be found in fig. 5.13. Thereby, the separation factor is S_f=3.02 which is lower than for the small window. This has different reasons. Firstly, by using the larger window,

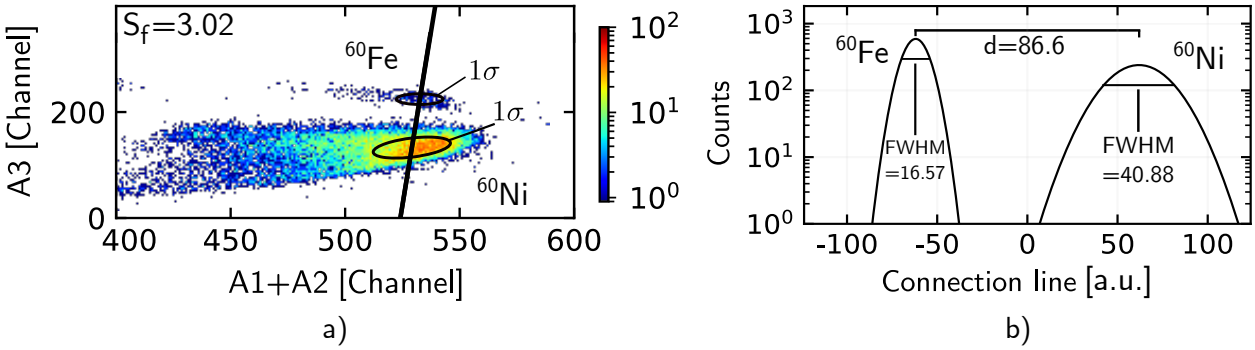

Figure 5.13: The figure shows the achieved separation in the example measurement at 30 mbar isobutane gas pressure. Plot a) shows the analyzed two-dimensional spectrum with the respective σ ellipses for each distribution, the connection line between the means and the intersections between the connection line and ellipses. The separation factor between the peaks is S_f=3.02. Plot b) shows corresponding fitted Gaussian distributions on the projection of the connection line for equal amount of ^{60}Fe and ^{60}Ni.

a higher fraction of ^{60}Ni will enter the detector. Furthermore, the energy of the additional ^{60}Ni fraction is closer to the energy of the main ^{60}Ni peak. Therefore, the energy difference of the new fraction to ^{60}Fe will be lower and the separation will worsen. Furthermore, the not optimized gas pressure leads unavoidably to a worse separation especially on the first anode, due to the height dependence on the signals. An example of the different measured material spectra can be found in fig. 5.14. The individual measured ratios are visualized in fig. 5.15. Within these measurements the PSI-10 was only measured once and then avoided to minimize memory effect since the measurement of the PSI-12 provided enough statistic. The PSI-12 ratios have a standard deviation of 12.71% while the blank samples have 35.56%. The final results can be found in tab. 5.4. A correction factor of 2.22(6) was achieved which translates to a transmission of 45.11%. This value is lower than the extrapolated value of 65% from the beam profile measurements in subsec. 4.2.3. The corrected blank value is $1.46^{+0.47}_{-0.30}\cdot10^{-14}$ and therefore 3.23 times higher than for the smaller window. Since these are the already corrected values it is assumed that an additional factor other than memory effect does have an impact by use of the larger window. A more detailed discussion can be found in subsec. 5.6.5.5.

Material	Meas. ^{60}Fe/Fe Ratio	c_f	Corr. ^{60}Fe/Fe Ratio
PSI-10	$5.08(13)\cdot10^{-11}$	2.21(6)	$1.124(3)\cdot10^{-10}$
PSI-12	$4.92(19)\cdot10^{-13}$	2.53(62)	$1.242(3)\cdot10^{-12}$
Blank	$6.60^{+2.13}_{-1.36}\cdot10^{-15}$		$1.46^{+0.47}_{-0.30}\cdot10^{-14}$

Table 5.4: Measured ratios for the three materials by use of the large detector entrance window. The correction factors of the two standards are equal within their error and resulted in a final correction factor for the measurements of $c_f = 2.22(5)$. The higher corrected blank value in comparison to the value when using the smaller window indicates that these signals have additional sources other than memory effect.

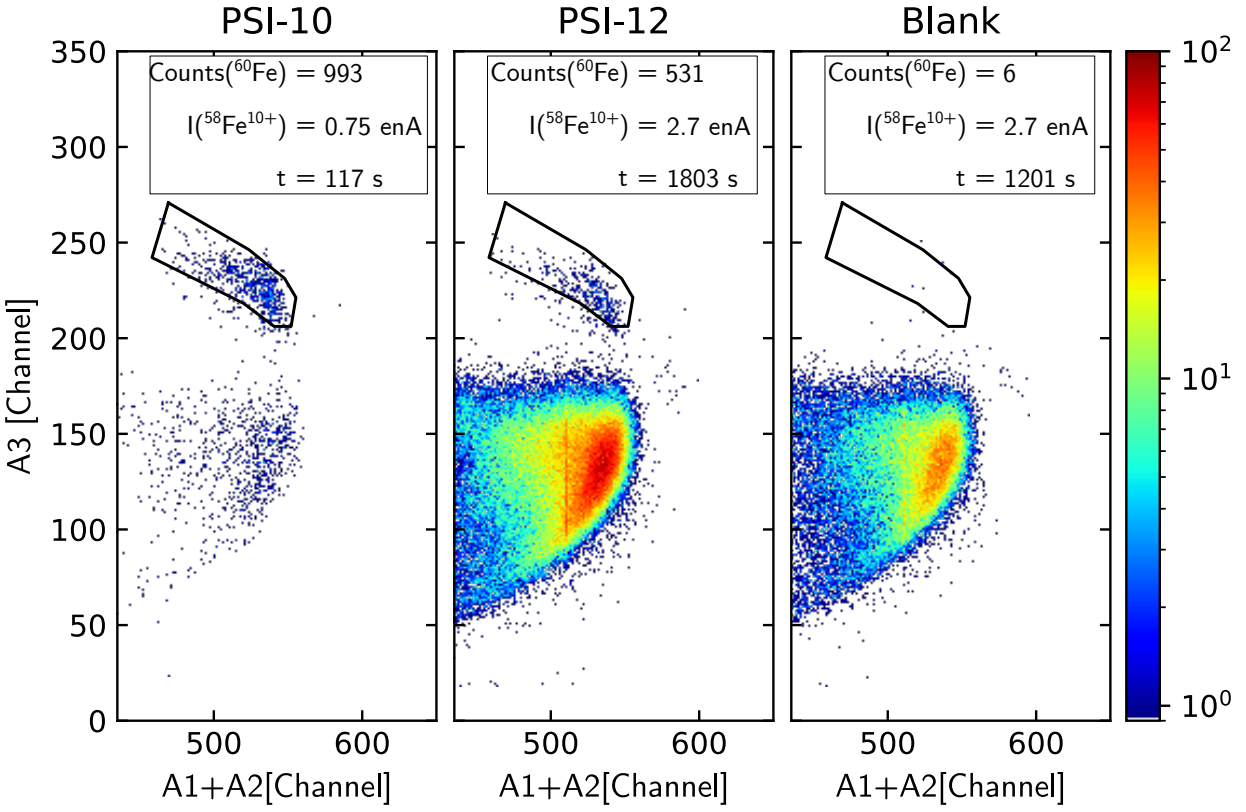

Figure 5.14: Examples of the gas ionization detector spectra used for particle identification of ^{60}Fe for three measured materials. The two-dimensional spectra show the signal from the third anode against the summed signals from the first and second anode to use the crossover of the energy loss measurement. Within these spectra a ROI is represented by the black frame.

5.6.5 Discussion

A sample sequence measurement of ^{60}Fe standard and blank material could successfully be conducted. This section will discuss the results of the measurements. Firstly, a comparison is drawn between initial and current status. Subsequently, a detailed discussion is given for the differences in using the different-sized detector entrance windows.

5.6.5.1 Comparison between initial and current status

In the first part of the discussion a comparison between initial measurements and current status is drawn since the former status was the motivation for the extensive development on the setup. Besides the general possibility to measure sample sequences and achieved reproducibility over several days a quantitative comparison can be found in tab. 5.5. For low-level AMS measurements like for ^{60}Fe the key factors for the feasibility is defined by the achievable statistics and the background level. For the initial measurements the ion source output and the transmission up to the offset-cup manifested in an averaged stable isotope current of $\bar{I}(^{58}Fe^{10+}) = 0.15\,\text{nA}$. Assuming perfect transmission and identification afterwards the measurement of 1 count of a $1 \cdot 10^{-16}$ ^{60}Fe/Fe ratio would statistically need 3.42 days on average. Combined with the former achieved correction factors between 5 and 8 increases the measurement duration to 17.31 - 27.69 days for a single count.

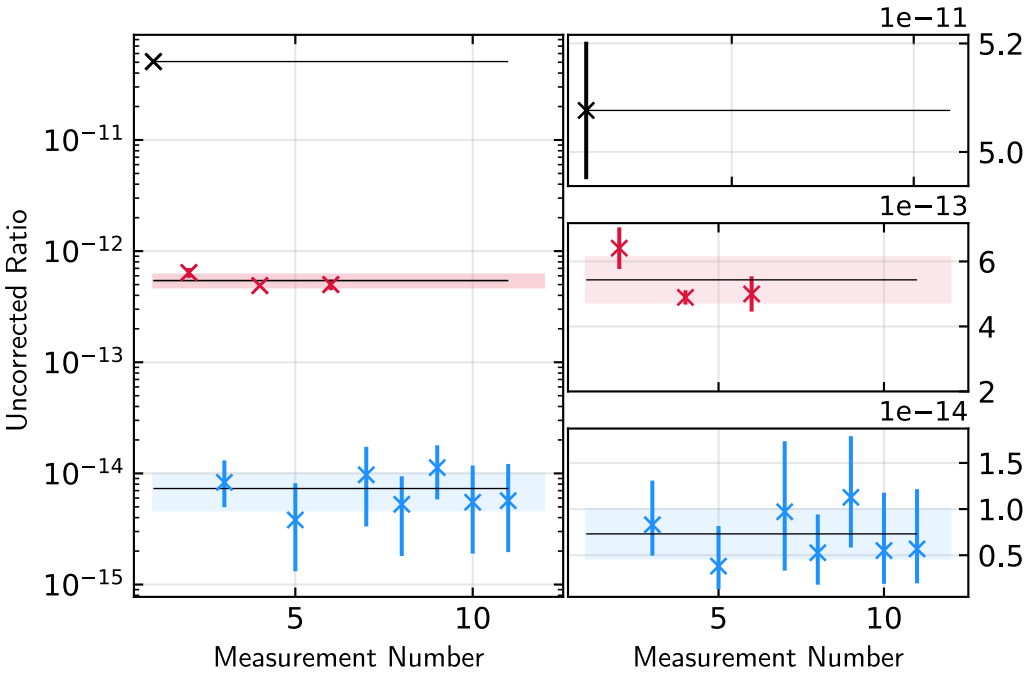

Figure 5.15: The left logarithmic plot shows the single uncorrected ^{60}Fe/Fe ratios in order of their measurement. Thereby, the black value corresponds to the PSI-10 sample, the red values to the PSI-12 material and the blue values indicate the blank samples. The PSI-10 was only used once and then neglected to avoid further memory effect and only newly produced blank samples were measured. Therefore, no scatter region is given for the PSI-10. The right plots show zoomed in versions of the two standard ratios and the blank level on a linear scale. The horizontal lines in all plots indicate the mean value and the underlying boxes indicate the standard deviation.

Thereby, the mandatory intermediate standard sample and blank sample measurements are not included. Since a lower background level needs an even higher measurement duration, a sequence measurement would not have been feasible even with a stable setup. In comparison to the current status, an increase of the measured stable isotope current of around 720%, factor 8, to an averaged current of $\bar{I}(^{58}Fe^{10+}) = 1.25\,nA$ was achieved. This, in addition to an improvement of the high energy mass spectrometer transmission leads to a hypothetical measurement duration for 1 count of a $1 \cdot 10^{-16}$ ^{60}Fe/Fe ratio of 35.66 hours (1.49 days) by use of the small window or only 22.49 hours (0.94 days) for the large window. This is a decrease of measurement time of 94.63% or 96.62% which corresponds to a factor of around 20. The stable reference current is a mean value averaged over a long measurement time including other investigations and including the end of the sample life span. Therefore, it can be assumed that by using newly produced samples, the measurement time can be decreased even further. Thereby, it revealed that the achieved transmission mirrored the observations from the beam profile measurements of ^{60}Fe. It can be assumed that latest transmission losses are still caused by the entrance window of the detector. Reversely this means that the transport transmission can be further increased by enlarging the detector entrance window which requires a redesign of the current gas ionization detector. For this consideration the second factor for feasibility, the achievable background level, comes into play. Concerning the pure separation factors the value is slightly lowered from the initial to the current status using the small window. The most probable explanation is that in the current measurements only a terminal volt-

Value	Initial	Current (Small window)	Current (Large window)
$\bar{I}(^{58}Fe^{10+})$	0.15 nA	1.23 nA	
$\overline{c_f}$	8|12.5%	3.52|28%	2.22|45%
corr. b_g	$6.55^{+11.53}_{-4.16}\cdot10^{-14}$	$4.53^{+3.85}_{-1.46}\cdot10^{-15}$	$1.46^{+0.47}_{-0.30}\cdot10^{-14}$
S_f	4.08	3.58	3.02
t(R=$1\cdot10^{-14}$, 1 event)	6.64 h	22.73 m	13.49 m
t(R=$1\cdot10^{-16}$, 1 event)	27.69 d	1.49 d	22.49 h

Table 5.5: The table presents a quantitative comparison of relevant values of ^{60}Fe AMS measurements between the initial and current status with both gas ionization detector entrance window options. Thereby, the averaged stable isotope current mirrors the ion source output and the transmission up to the offset-cup position. The correction factor of initial and current status is given as well as the corresponding transmission and the corrected blank level.

age of 8.9 MV instead of 9.3 MV was achievable and therefore the final energy is 4.31% lower in the current measurements. This again leads to worsening of the differential energy loss separation. In both cases of initial and current status with small window, the separations are sufficient. It is further assumed that the corrected blank levels of former $6.55^{+11.53}_{-4.16}\cdot10^{-14}$ and current $4.53^{+3.85}_{-1.46}\cdot10^{-15}$ are caused by memory effect of standards higher than the PSI-12, see subsec. 5.6.5.4. In the former case the PSI-8 was extensively used and in the beginning of the latest measurements also the PSI-10 was used several times. In the future, for every performed AMS measurement, the ion source and sample wheel should be cleaned and new samples should be produced. When only using the PSI-12 no memory effect is expected as it is commonly used in other laboratories, [41]. Thereby, a lower background level becomes achievable in case of using the small detector entrance window. In the use of the large detector window the PSI-10 was only measured once and avoided afterwards which should further decrease the memory effect. The measurements revealed a higher corrected background level than with the small window by a factor of 3 but still a factor of 5 smaller than for the initial status. A detailed discussion on the background level using the larger window can be found in subsec. 5.6.5.5.

5.6.5.2 Total efficiency of ^{60}Fe

The total efficiency of the AMS system represents which fraction of the isotopes of interest within the sample material will be identified in the detector after being transported through the system. The first fraction is the extraction efficiency ϵ in the ion source. For 5 hours of measurement it results to $\epsilon_{eff} = 0.3\%$, see subsec. 5.3. The low energy side transmission for iron oxide was around $T_{LE} = 93\%$, the transmission through the accelerator of $T_{Acc} = 28\%$ and the charge state fraction of the used 10^+ charge state was $f = 25\%$. By use of the small detector window a transmission up to the detector of $T_{HE} = 27\%$ was achieved. With these values the total efficiency can be calculated to:

$$\epsilon_{tot} = \epsilon \cdot T_{LE} \cdot T_{Acc} \cdot f \cdot T_{HE,small\,window} = 0.55 \cdot 10^{-4} \tag{5.9}$$

5.6.5.3 ^{60}Ni suppression

The suppression of the interfering isobar is of special importance to access lowest isotopic ratios since no reasonable background correction can be applied when only few counts are available in the real signal. This subsection will report on the achieved ^{60}Ni suppression for the current setup. Thereby, the final value composes from suppression in the ion source, the gas-filled magnet and the gas ionization detector. The ion source suppression resulted in a factor of $S_{Ion\,source} = 2$, see subsec. 5.3. The suppression in the gas-filled magnet was investigated within the former described experiment for the separation investigations, see subsec. 4.2.4. Therefore, the count rate within the detector with the small detector entrance window was captured while the magnetic field was traced. Thereby, a combination of ^{60}Ni and ^{60}Fe peak and the individual ^{60}Fe peak were captured consecutively. The measurements can be found in fig. 5.16. The data show the ^{60}Ni and ^{60}Fe distributions. The ^{60}Ni count rate was derived by subtracting the separately measured ^{60}Fe count rate from the total detector count rate. Since the ^{60}Ni peak was not exclusively captured, the resulting difference could also include other interferences. Therefore, the suppression of ^{60}Ni could be higher than the given values in this section which thereby has to be considered as a lower limit. The final suppression value is calculated by the maximum ^{60}Ni count rate divided by the averaged background count rate within the magnetic field ^{60}Fe region. The values for the different pressures can be found in tab. 5.6. The suppression value of at least $4.91 \cdot 10^2$ at 3 mbar nitrogen gas pressure will be used for the final calculation. For the detector suppression all measured blank samples

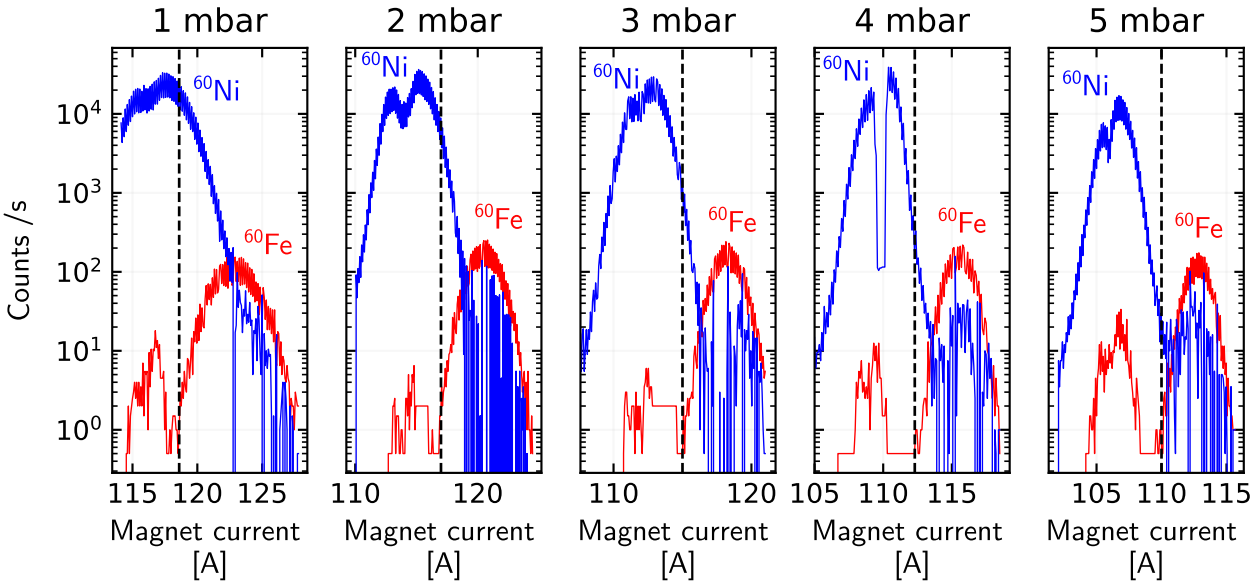

Figure 5.16: The plots show the ^{60}Ni and ^{60}Fe count rates measured in the gas ionization detector by varying the magnetic field of the GFM. The ^{60}Ni count rate, in blue, was derived by subtracting the separately measured ^{60}Fe count rate, in red, from the total detector count rate. The original measurements were presented in subsec. 4.2.4. Each plot represents one nitrogen gas pressure. The suppression is calculated by the maximum ^{60}Ni count rate divided by the averaged ^{60}Ni count rate within the ^{60}Fe region indicated by the black dotted lines.

were used for investigation. For the suppression value determination the factor between the counts in the region of interest to the main ^{60}Ni peak is used. The results for both windows can be found in tab. 5.7. By investigating the ^{60}Ni count rate to the count rate within the ^{60}Fe ROI, no linear correlation was found, which could have been assumed if the background is only ^{60}Ni particles.

Magnet gas pressure (N_2)	1 mbar	2 mbar	3 mbar	4 mbar	5 mbar
^{60}Ni/s on ^{60}Ni pos.	33160	36495	29445	389556	17049
^{60}Ni/s on ^{60}Fe pos.	2150	386	60	24.6	12.4
Suppression S_{GFM}	$1.54 \cdot 10^1$	$9.45 \cdot 10^1$	$4.91 \cdot 10^2$	$1.58 \cdot 10^3$	$1.37 \cdot 10^3$

Table 5.6: Lower limits for the ^{60}Ni suppression by the GFM for different nitrogen gas pressures.

Window type	Small window	Large window
Suppression $S_{I_{Det.}}$	$1.9(4) \cdot 10^4$	$1.3(5) \cdot 10^4$

Table 5.7: Lower limits for the ^{60}Ni suppression by the gas ionization detector for both window sizes. For the values, the measured blank samples were analyzed and the factor between determined ^{60}Ni counts and counts within the ^{60}Fe ROI is taken as the suppression factor. Since the ^{60}Fe and ^{60}Ni count rates do not show a linear correlation, it can be assumed that the ^{60}Fe ROI counts are not ^{60}Ni but have other sources, so that the given suppression values are only lower limits.

Therefore, it is assumed that the background counts have also different sources, so that the given suppression values are only lower limits. Since the suppression by the gas-filled magnet was only determined by using the smaller window, a final suppression limit is only given for the case of the small detector entrance window.

$$S_I = S_{Ion\,source} \cdot S_{GFM} \cdot S_{I_{Det.}} = 2 \cdot 4.91 \cdot 10^2 \cdot 1.9 \cdot 10^4 > 1.86 \cdot 10^7 \tag{5.10}$$

It results to a magnitude of at least 10^7 suppression of ^{60}Ni at the Cologne 10 MV AMS setup.

5.6.5.4 ^{60}Fe cross talk effect

In low-level AMS measurements only few counts are available in the final sample spectra, therefore a background-correction is not possible and each possible contamination has to be avoided. Another possibility is remained ^{60}Fe from high concentration samples which is referred to as cross talk for samples measured subsequently or memory effect for a long-term effect of ion source contamination. Both lead, when occurred, to unavoidable background. While cross talk should decrease in reasonable time, memory effects can occur until the source is cleaned. Its effect was clearly seen at the former equipped blank samples which were already in use when the highest ^{60}Fe, in the order of ^{60}Fe/Fe=10^{-8}, was extensively used. Even months later the samples show a significantly higher background level, see subsec. 5.6.3. Also in the beginning of the current experiment the middle standard, in the order of ^{60}Fe/Fe=10^{-10}, was used to find optimal parameters for the setups transmission. For investigating a possible memory effect, the three available standard materials were measured in ascending order at the end of the measurement period. Thereby, each was measured until at least hundred counts were reached and subsequently the same blank sample was measured after each. The measurement values can be found in tab. 5.8, the ratio results can be found in fig. 5.17. All ratios refer to ^{60}Fe/Fe ratios. The use of the PSI-12 with a ratio of $1.242(3) \cdot 10^{-12}$ has no measurable influence on the background level. The corrected blank ratio was $2.774^{+4.887}_{-1.771} \cdot 10^{-15}$ which lies a factor of 1.77 below the corrected blank level formerly measured with

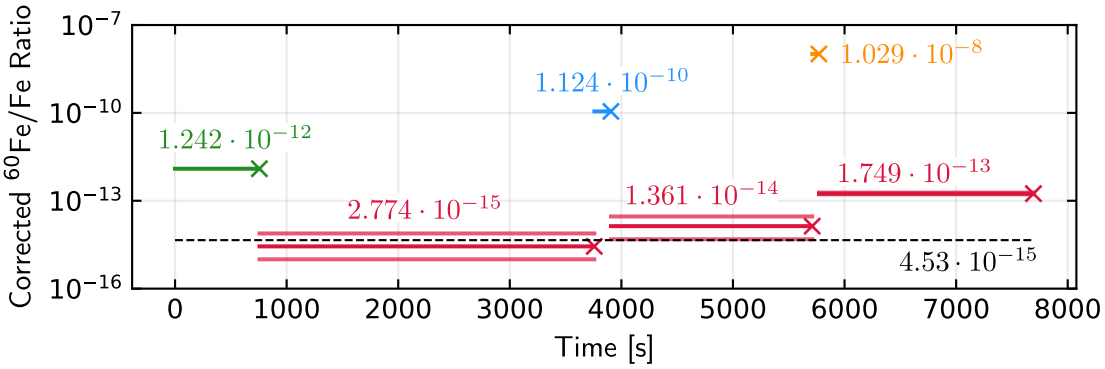

Figure 5.17: Investigation of cross talk for ^{60}Fe using the small detector window. For the measurement each of the three available standard materials were used for a respective duration to achieve at least several hundred counts in the detector. Subsequently, the same blank sample was measured. The markers indicate the end of each measurement and the resulting value while the line indicate the measurement duration on this corrected ratio level. This simplification is valid since none of the measurements showed duration-related changes in their ratios in the offline analysis. The black dotted line defines the formerly averaged measured blank value by use of the small detector window. In the former 48 hours before this test measurement, almost only the PSI-12 was used as a standard reference. The first given blank measurement lies beneath the former value but is still equal within its error. It can be assumed that the PSI-12 does not produce cross talk in the measured ratio range of 10^{-15}. By use of the PSI-10 an increase of one magnitude in blank level was observed. The agreement within the statistical error of the first two blank values indicate that the first blank measurement is still influenced by the PSI-10 even if the influence decreased. The second blank value lies 4 orders of magnitude beneath the PSI-10. By use of the PSI-8 an additional increase of one magnitude in blank level is observed while the absolute value lies 5 orders of magnitude beneath the PSI-8.

the small detector window but is equal within its statistical error. After the use of the PSI-10 standard with a ratio of $1.124(3) \cdot 10^{-10}$ the blank level increased by a factor of 5.19 to $1.361^{+1.555}_{-0.876} \cdot 10^{-14}$. The two blank measurements are only just in agreement within their error. This indicates that the first measured blank value is still influenced by the former PSI-10 measurement. The smaller value of the first blank value shows the slow decrease of the impact of the PSI-10. It can be expected that after cleaning the ion source and the production of new cathodes even smaller blank levels will be reached when only the PSI-12 is used as a standard. The effect of even shortest measurement duration of higher standards are significant. By use of the PSI-8 standard with a ratio of $1.1029(3) \cdot 10^{-8}$ it increased by an additional factor of 11.61 to $1.749(318) \cdot 10^{-13}$. Thereby, the blank level after the PSI-10 was around 4 orders of magnitude lower than the measured standard and for the PSI-8 around 5 orders of magnitude lower. Over the subsequent blank measurement duration, no relief of this effect within the measurement time was observed. Due to the improved reproducibility, general increased statistics and the developed particle rate tuning options future ^{60}Fe experiments should only make use of the PSI-12 with newly produced blank samples. The tuning procedure should mainly be done by use of the isobar from blank material as formerly described.

Standard	Ratio	t[s] (std)	Counts (std)	t[s] (blank)	Counts (blank)	Corr. blank level
PSI-12	$1.242(3)\cdot10^{-12}$	757	132(12)	3001	$1^{+1.76}_{-0.65}$	$2.774^{+4.887}_{-1.777}\cdot10^{-15}$
PSI-10	$1.124(3)\cdot10^{-10}$	149	975(31.22)	1804	$2^{+2.268}_{-1.31}$	$1.361^{+1.555}_{-0.876}\cdot10^{-14}$
PSI-8	$1.029(3)\cdot10^{-8}$	60	65550(256)	1923	31(5.57)	$1.749(318)\cdot10^{-13}$

Table 5.8: Results from the memory and cross talk investigations for ^{60}Fe. The table presents the used standard material with their corresponding measurement time and counts as well as the subsequent achieved corrected blank level.

5.6.5.5 ^{60}Fe background level using the large window

By using a larger detector window, the AMS measurements of standard and blank materials showed that the transmission is increased while also the background level increased. With that, the corrected background level resulted to $1.46^{+0.47}_{-0.30}\cdot10^{-14}$ which does not allow to measure ratios desired in recent applications. Due to the increase in the already corrected background level an additional effect other than cross talk or memory effect has to be assumed. Therefore, it seems likely that when enlarging the window for higher transmission the effect would become even more severe. The investigations on the additional background will be discussed in this subsection. Within the measurement, it was firstly ensured that the difference is not solely caused by the not optimized gas pressure or by use of the Mylar material. Therefore, the Mylar window size was artificially reduced to the same size and form as the smaller SiN window by attaching a non-permeable material. This resulted in an increased correction value of 3.78(38) and a corrected blank value of $6.6^{+7.8}_{-4.5}\cdot10^{-15}$ which is almost similar to the value formerly achieved by the small window. Therefore, it can be excluded that the window material or the used gas pressure solely causes the increased background. In a next step, an offline χ^2 analysis was performed, as described in subsec. 2.4.2, to investigate the background signals and improve the background level if possible. A high standard was used to define the one-dimensional cuts on the individual signals and determine the expectation values for the analysis. The analysis was then performed for the measurements using the small window and large window for comparison. Therefore, the lowest standard and blank measurements of each option were summed to receive more statistics for the analysis. The resulting χ^2 distributions can be found in fig. 5.18. Thereby, the distributions are given with and without formerly applied one-dimensional gates. By these cuts the main fraction of the isobar ^{60}Ni is rejected. It is clearly seen that the background can not be reduced without rejecting significant parts of ^{60}Fe which leads in the end to an equal or even worse corrected background level. An exemplary cut is visualized and its application on the final two-dimensional spectra can be found in the appendix subsec. 7.4.5. Additionally, it was tried to fit the χ^2 distributions. The comparison of these distribution shapes was reportedly used to finally testify the ^{60}Fe in the sample, [41]. Otherwise deviating distributions could give conclusion about the source of background. Due to the low statistics in the blank, the errors of the fitted values were too large for a significant comparison. When comparing both spectra visually, it shows that blank data appears up to a value of around $\chi^2 = 7.5$ and then again above $\chi^2 = 10$ in both spectra. It is assumed that the higher fraction is corresponding to ^{60}Ni. In case of the small window the lower fraction is assumed to be real ^{60}Fe from memory effect.

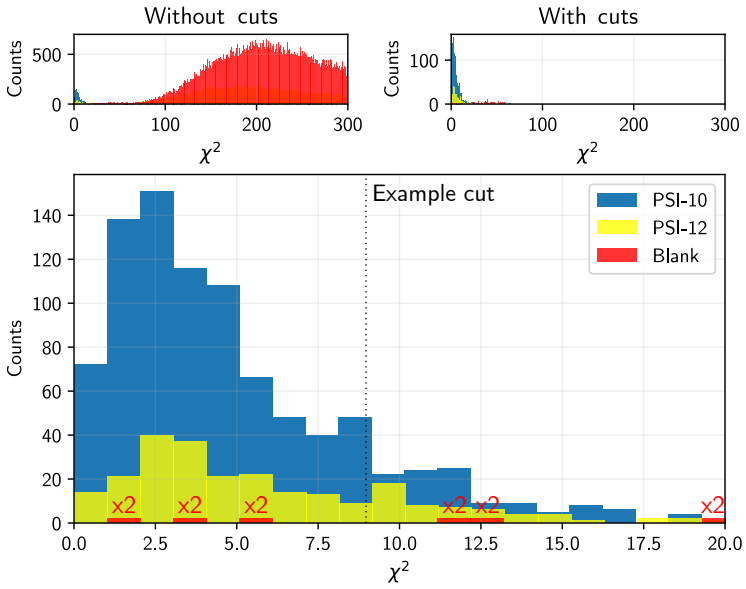

a)

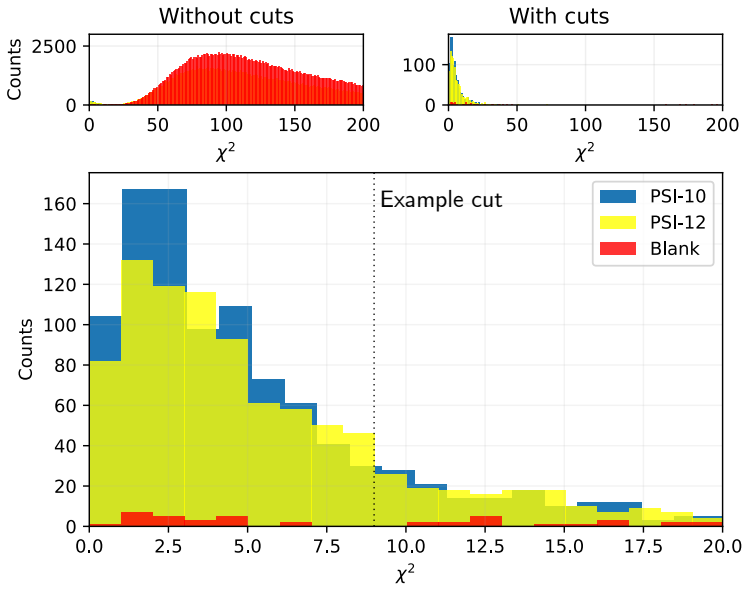

b)

Figure 5.18: The histograms show the resulting distributions of the χ^2 analysis for the small window, a), and the large window, b). In each plot the upper left histogram shows the χ^2 distribution of all events, the upper right histogram with applied one-dimensional cuts on the individual anode signals and the lower histogram is a zoomed in version of the right upper histogram. In plot a) the data from the blank is doubled (indicated by 'x2') for visualization. It is clearly seen that each cut-off condition will also reject significant fractions of ^{60}Fe which again leads to equal or even worse corrected background level. An exemplary cut is indicated. The corresponding final spectra with applied conditions can be found in the appendix in subsec. 7.4.5. When comparing both spectra it shows that blank data appears up to a χ^2 of around 7.5 and then again above χ^2 =10. It is assumed that the higher fraction is corresponding to ^{60}Ni. In case of the small window the lower fraction is assumed to be real ^{60}Fe from memory effect. For the large window the χ^2 shape of the blank data mirrors the χ^2 shape of the standards up to a value of χ^2 =4. An additional small increase at χ^2 =4 and at χ^2 =6 can be observed, which could be caused by an interference component.

For the large window the χ^2 shape of the blank data mirrors the χ^2 shape of the standards up to a value of $\chi^2 = 4$. An additional small increase at $\chi^2 = 4$ and at $\chi^2 = 6$ can be observed, which could be caused by an interference component. However, due to the low statistics no confident conclusion can be given. With this results, the impact of using the large window, besides higher transmission itself, has to be discussed. Thereby, two main aspects have to be considered. Due to the positional separation by the gas-filled magnet the detector window can be seen as a cut condition within this position spectrum. When enlarging this cut, it is possible that new interferences enter the detector. One option is the unavoidable larger fraction of the isobar ^{60}Ni. It has to be considered that on each individual position after the gas-filled magnet, the incoming particles will again have a gaussian-like energy distribution. By dealing with different particle positions on the focal plane, the energy distributions mean will be shifted. This means the additional ^{60}Ni which enters the detector is closer in energy to the main ^{60}Ni than the former edge of the ^{60}Ni position distribution. Therefore, the enlarging of the positional cut will lead to worse energy separation between isotope and isobar. A second option are completely different $\frac{m}{q}$ interferences which were previously positionally suppressed by use of the small window. Comparing spectra from other institutes measuring ^{60}Fe, such interferences were also extensively observed, [41]. They are rejected by the offline analysis. For other laboratories this process is simplified by the significantly higher used energies and the good energy resolution of the dedicated detectors for these measurements for every window type which will be the second discussed aspect. For the used detector in Cologne it was already investigated that the current detector design is challenged for wide y-distributed particle beams. In the case of the small detector window this effect was almost negligible and all anodes could be used for discrimination, see subsec. 3.2.2. Two main problems occurred during the current ^{60}Fe measurements using the large window. The first is the effect of the inhomogeneous electric field in the large dead volume prior to the anode structure of the detector. This led to a significant y-dependence in the energy loss signals on the first two anodes. This worsens the resolution drastically. The second point is the not optimized detector pressure due to the window stability. This led to a slight overshooting of the particles over the last anodes which has a similar effect as in the front of the detector and worsens the resolution dominantly on the last, but also slightly on the second last anode. Besides the increasingly difficult energy separability due to the plain enlargement of the window the third anode showed no further impact. This statement is mirrored by the determined separation factor for ^{60}Ni and ^{60}Fe, see subsec. 5.6.4. It was not significantly lowered since the separation mostly relies on the third anode. This is different for other appearing signals. A third component was already seen in the spectra using the small window and was mostly separated by the energy loss on the first two anodes, see red indicated area in fig. 5.19 a). By use of the large window this component is only slightly separated on the first two anodes and again also less separated on the third anode, see red indicated area in fig. 5.19 b). When considering the shape of the ^{60}Ni and ^{60}Fe components, it can be assumed that the tail of this component can interfere the ^{60}Fe ROI and thereby the blank level. Reported interferences in other laboratories were ^{59}Co and ^{76}Se, [42]. Other possible interferences which could pass the low energy mass spectrometer on mass 76 and at specific energies the high energy mas spectrometer are ^{60}Co, ^{63}Cu and ^{65}Cu. The energy losses of all these possibilities were calculated by use of LISE++ with the formalism by Ziegler and compared to the calculated values of ^{60}Fe and ^{60}Ni. By comparing the values from the sum of the first two anodes and the individual value of the third anode, it can be determined if it fits the experimentally observed interference. From the given possibilities none fitted the experimental

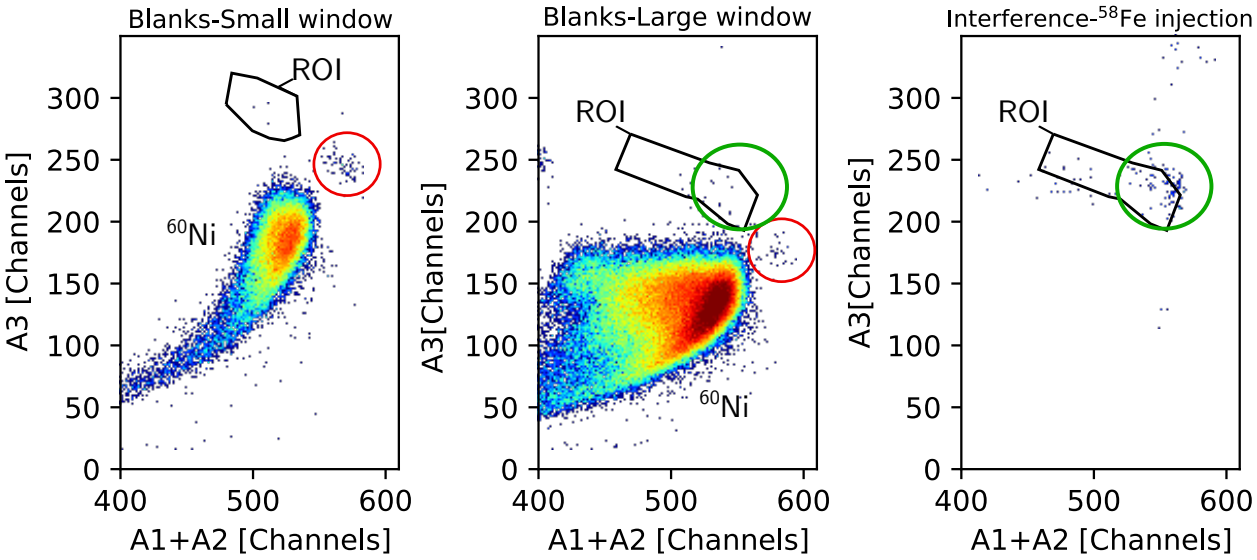

Figure 5.19: The left and middle plots show the gas ionization detector spectra of all summed blank measurements for both entrance window sizes respectively. The right plot shows an interference measured with the large entrance window when injecting the stable isotope (^{58}Fe^{16}O) on the low energy side.

values so that this component remained unidentified. Furthermore, it revealed that when injecting the stable reference isotope, ^{58}Fe^{16}O, on the low energy side, a significant signal is observed in the detector, see green indicated area in fig. 5.19 c). It is assumed that this is ^{58}Fe with higher energy from a charge change in the high energy section of the accelerator, from 11^+ to 10^+ , similar to the interference discussed in the ^{14}C measurements in subsec. 3.2.3.5. Thereby, it would pass the high energy analyzing magnet straightly. The assumption is supported by the fact that ^{58}Fe also passes on the injected rare isotope molecule mass 76 as ^{58}Fe^{18}O. An estimation of the counting rate which could be expected from memory effect and ^{58}Fe interference corresponds to 88% of background rate. The full discussion can be found in the appendix subsec. 7.4.4. An identification of the interferences could be achieved by positioning the existing in-beam projectile x-ray setup at the position of the gas ionization detector and measure the x-rays of the background particles. It has to be mentioned that due to the respective efficiencies a measurement over several hours up to a day would be necessary for confident results. While the identification of the interference components support the planning of further improvement steps, it is not mandatory. If the large window should be used in the future, two tasks have to be tackled. The first task is the gas ionization detector. Thereby, as a short-term requirement, a larger stable entrance window should be acquired to allow the optimal gas pressure to be used. The more difficult task is the y-dependence of the energy resolution of the gas ionization detector. A rough and easy approach would be to position the anode structure as near as possible to the detector entrance window to minimize the dead volume in front. Over a longer time the detector should be replaced by a newly designed one which should be inspired by the detectors used in other laboratories after gas-filled magnets, [32], [89]. A difference is the width of these detectors with wider anodes as the currently used ones in Cologne. Especially the entrance has to be adapted to allow larger entrance windows. Therefore, the inner structure has to be enlarged in its height since currently ions could collide with the cathode when the larger window is used, compare subsec. 3.1.2. Since even more impact of interferences can be expected by use of a larger window, a further separation step should be introduced. Thereby,

the position could be determined by using split anodes. These were removed due to their low-resolution energy loss signals. For their usage this resolution should be investigated to estimate if the gained position signal balances the worse differential energy loss separation. Another option is a time-of-flight measurement through the gas-filled magnet. A test measurement was performed prior to the current measurements. Therefore, a rudimentary time-of-flight setup was used. The stop detector from the initial time-of-flight setup, [10], was used as start detector and a silicon detector was attached to the back of the gas ionization detector as stop signal. The results for a standard and a blank material can be found in fig. 5.20 which shows the energy loss over all anodes of the gas ionization detector in comparison to the flight time. The first anode was neglected since

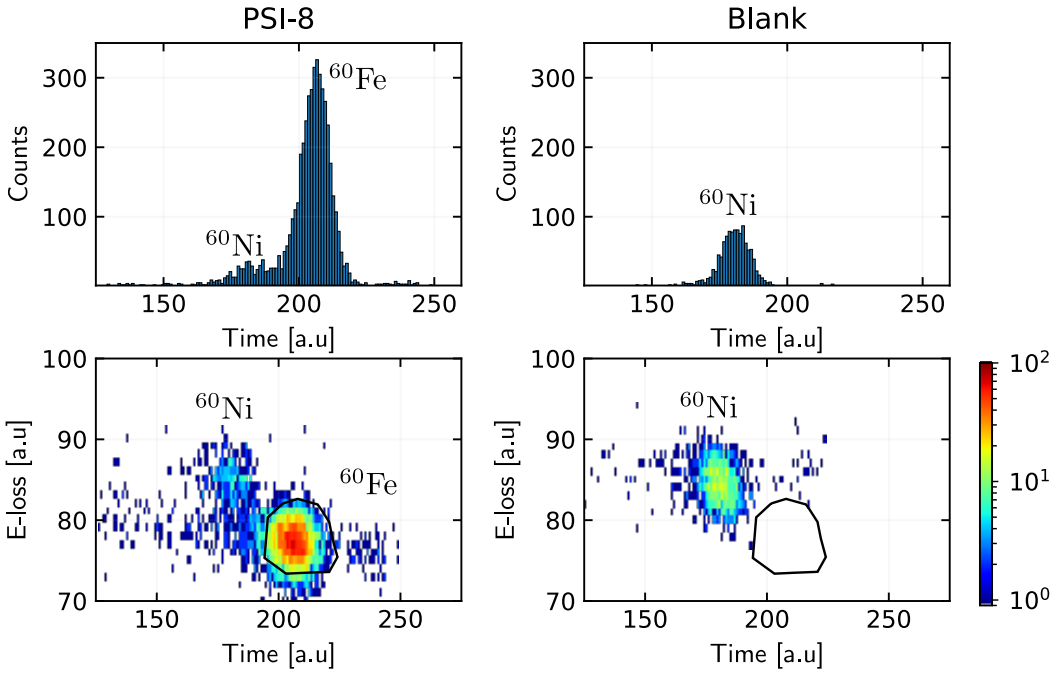

Figure 5.20: Example of one-dimensional time-of-flight spectrum and two-dimensional spectrum of a standard and a blank measurement, comparing the time-of-flight signal through the gas-filled magnet to the energy losses over the anodes of the gas ionization detector. It shows that the time-of-flight measurement through the GFM gives an additional uncorrelated step of separation in comparison to the energy loss separation.

its improvement was not applied yet and the signal was disturbed. It shows that the separation in the time-of-flight adds an additional separation step to the energy separation since a long flight time correlates to small energies. Since in these measurements the small detector window was used which showed sufficient separation in the energy loss signal on its own, the setup was not present during the latest measurements with the large window. Furthermore, since the silicon detector was attached at the end of the gas ionization detector, the gas pressure had to be lowered so that the particles reach the end of the detector chamber. This leads to a disturbed signals on the last anodes and worsens the overall energy loss resolution. Therefore, a more elaborated setup should be designed.

5.6.6 Limits and Conclusion

The feasibility of an AMS measurement can be limited by statistics to achieve reasonable measurement times or the background level if it exceeds or equals the real sample statistics so that no background correction is possible. In terms of statistics, and therefore needed measurement duration, the current status of the Cologne 10 MV AMS system should allow AMS measurements down to a ratio of ^{60}Fe/Fe $=10^{-16}$. For comparison a measurement of antarctic snow samples, of the closed Munich 14 MV MP tandem AMS system, will be discussed in the following, [42]. A measurement duration of 50 hours is given for the measurement of 5 counts of a ^{60}Fe/Fe ratio of $0.55{\cdot}10^{-15}$, 5 counts of a ^{60}Fe/Fe ratio of $0.9{\cdot}10^{-15}$ and a blank level of $0.25{\cdot}10^{-15}$. For comparison the determined averaged stable isotope current of 1.23 nA of $^{58}Fe^{10+}$ and the higher correction factor of 3.52 for the small detector window from the last measurement are taken. Thereby, a measurement duration of 66 hours would be needed which is in comparable range to the duration in Munich. Since the determined stable reference current of 1.23 nA of $^{58}Fe^{10+}$ is an average over a long measurement time, it can be assumed that by using newly produced samples, the measurement time can even be decreased. Therefore, the desired ratios for ^{60}Fe in terms of statistics became possible. Concerning the background level the current measured corrected background level of $4.53^{+3.85}_{-1.46}{\cdot}10^{-15}$ for the small window and the even higher level of $1.46^{+0.47}_{-0.30}{\cdot}10^{-14}$ using the large window does not allow to measure ratios of ^{60}Fe/Fe $=10^{-16}$ ratios. The former would allow the measurement of meteorites with ratios around 10^{-14}. If the assumption stays true that the background level using the small window can be traced back to memory effect, this limit will decrease. Therefore, it is recommended to clean the source and use new samples for every new measurement. Furthermore, it is recommended to use the small detector window for further experiments due to the suppression of interferences until measurements are planned which are limited at this exact transmission loss.

6 Summary and Outlook

6.1 Summary

Over the course of this thesis, ^{60}Fe AMS measurements were successfully developed at the Cologne 10 MV AMS system. Therefore, an extensive range of investigations and developments were performed to enable the mandatory stability to measure long-term low level isotopic ratios. Within these investigations the ion source stability and its output was significantly improved. Furthermore, the transmission through the whole system was highly increased. This is mirrored by the comparison of initial to latest conducted ^{60}Fe AMS measurements, in which the macroscopic stable isotope beam current at the offset-cups was increased by a factor of 8. By including the transmission improvement up to the particle detector a decrease in measurement time of at least 94.63%, a factor of around 20, is achieved. The achievable statistics enable the measurement of one event of a $1 \cdot 10^{-16}$ ^{60}Fe/Fe ratio within 1.49 days which is comparable to well-established larger AMS setups. The systems ability of long term measurement of mandatory sample sequences was testified in a successfully conducted ^{14}C AMS measurement. With that, a correction factor of c_f =1.20(5) (83% HE transmission) was achieved which is in comparable range as for the established measurements at the Cologne 6 MV AMS system with a factor of c_f = 1.19 (84% HE transmission). The corrected background value was $^{14}C/^{13}C=4.52^{+0.78}_{-0.58}\cdot 10^{-13}$. This can be extrapolated to a background level of $^{14}C/^{12}C=4.62\cdot 10^{-15}$. Furthermore, the particle data acquisition was coupled to the 10 MV AMS control system which allows that data acquisition inputs like detector signals can be logged and traced and even recorded as an average over time within the control software. Within this thesis, it is used for the silicon detector rate and gas ionization detector rate, whereby it is possible to use data acquisition conditions to investigate only specific separated isotopic components. For the first time, it is possible to sufficiently tune lowest particle rates which could previously not be tuned efficiently or systematically by hand. Additionally, with this coupling, first automatic AMS measurements of ^{60}Fe were possible which reproduced the manual measurement results for ^{60}Fe by use fo the small detector window. For the corresponding automatic measurements of ^{14}C an interference occurred while injecting the stable reference isotope which interfered with the chosen ROI, resulting in deviating results for the blank measurement.

Detailed investigations of the particle beam behavior inside and after the gas-filled magnet were conducted. Thereby, for the first time the dispersive beam shape and trajectory were captured on its flightpath through the gas-filled magnet. For that a ^{60}Ni particle beam, from ^{60}Fe blank material, was used as a close reference to ^{60}Fe. The measurements were conducted for helium and nitrogen gas for a certain range of pressures. The particles deviation from the magnet optical axis intermediately through their gas flightpath to outer trajectories was measured for the first time. The deviation increases with increased pressure and is stronger for nitrogen than for helium. The beam widths in nitrogen gas show the characteristic shape featuring a minimum in dependence of

the gas pressure, representing the interplay between narrowing due to more frequent charge fluctuations against angular straggling. For the first time, it was observed that this minimum shifts with the flightpath. In the measured helium gas pressure range the widths were significantly broader and no minimum was observed. In a follow-up experiment two-dimensional beam shapes were investigated to determine the optimal gas parameters for the ^{60}Fe measurements. From that, the beam widths in the dispersive and non dispersive axis were extracted. For helium the angular straggling was as expected significantly lower than for nitrogen. However, in the dispersive axis, which is the crucial parameter for positional separation by the gas-filled magnet, the nitrogen is favorable. It was also calculated that for the gas pressures where the x-widths in helium and nitrogen become comparable, the beam experiences a 10 MeV higher energy loss in helium. Therefore, the optimal gas type is nitrogen at a pressure of 3 mbar in terms of transmission for a subsequent symmetrical detector entrance window. Concerning the separation between ^{60}Fe and ^{60}Ni their combined peaks were measured by the gas ionization detector particle rate and subsequently the individual ^{60}Fe particle rate by using a ROI condition. These values were used to determine the separation factor which increases for nitrogen gas in the range up to 5 mbar with increasing gas pressure. Overall, besides the explicit prior measurements dedicated to ^{60}Fe, the measurements and findings are important steps to an improved understanding of the processes of beam behavior within the gas-filled magnet. Since the measurement of the inner profiles is time-consuming, in terms of AMS measurements, it is sufficient to perform the investigations after the gas-filled magnet which are faster and therefore enable easy measurements of a wider range of gas types and pressures. The experimental results were simulated by an in-house developed and an available external simulation code, [69], [68], and subsequently compared. After observing significant deviations in the trajectories, it was found that the gas density effect in dense gases was not considered in these simulation codes before. Since all further calculations are based on this value the in-house code was completely revised in terms of the used approaches to match the measurement conditions best. Thereby, due to the complexity of the topic and a gap in the current research state, the gas density effect and also the charge state distribution width were only adapted as semi-empirical formulas to match the experimental results for the inner magnet measurements. A formula for the gas density effect was included while the charge distribution widths are adapted by respective factors. Thereby, no gas-independent adaption was found but explicit ones for each gas type. With that, the measurements from the inner beam developments were sufficiently reproduced for nitrogen while the values for the follow-up experiment were only qualitatively reproduced with the revised code. For helium the reproduction was sufficient for the inner measurements and could not accurately reproduce the experimental values after the gas-filled magnet. The external code did not reproduce the nitrogen results but reproduced the helium results after the magnet sufficiently. While both codes show qualitative reproduction of the separation factors, the revised code was noticeably closer. Overall the codes can not be used for precise prediction of the beam development for arbitrary conditions. They are capable of giving an estimation for the quantitative width and a qualitative comparison between different ions and gas types. Due to the former experimental work the code in this work is capable of sufficient simulations using nitrogen gas.

Finally, ^{60}Fe AMS measurements were developed. Key parameters of the iron measurements at the current system were determined beforehand. For a typical measurement duration of a sample, an extraction efficiency of $\epsilon_{5-10\,h} = 0.3 - 0.51\%$ for $^{56}Fe^{16}O^-$ was achieved. With the chosen 10^+ charge state a transmission of 6.44% through the system from the first to the last Faraday cup

was reached. The system provides a suppression of the isobar ^{60}Ni in the order of 10^7. All given values are in a comparable range with well-established measurements at larger AMS facilities. For the first time, successful AMS measurements using the new gas-filled magnet of the Cologne setup were conducted within this work. Thereby, sample sequences were measured including different ^{60}Fe standard and blank samples. Two sequences were measured using different sized detector entrance windows. For the smaller window a transmission from the measurement position of the stable reference isotope to the identification of ^{60}Fe of 28.41% was achieved. The corrected background level was $4.53^{+3.85}_{-1.46}\cdot10^{-15}$. Further measurements investigating the remaining memory effect after using high isotopic ratios highly points to memory effect or cross talk as source of the background level using the small detector window. With the larger window a transmission of 45.11% and a corrected background level of $1.46^{+0.47}_{-0.30}\cdot10^{-14}$ was measured. It is assumed that the increased background level is caused by additional interferences since the window, as a cut condition to the gas-filled magnet separation, was enlarged. Furthermore, the separation ability of the detector worsens by use of the large window in the current detector layout. By use of the small detector window the measurement of applications with ratios of ^{60}Fe/Fe=10^{-14} like for certain iron meteorites are easily possible. The measurement of lowest ratios of ^{60}Fe/Fe=10^{-16} is statistically possible and would be enabled when the assumption of memory effect as a background source is confirmed.

6.2 Outlook

In conclusion, the beam output and transmission through the system overall is sufficient. One topic which has to be improved in the future is the reproducible positioning of the sample wheel, as well as the correction of its eccentricity. For that, motors are already in use which can be remotely controlled and delivered promising results in the first tests[11]. Systematic investigations should be performed to guarantee a minimization of the sample wheel dependence. In terms of stability, the AMS system itself shows a high level of reproducibility and stability. The remaining topic which has to be investigated is the accelerator itself. Since no slit control can be used during long-term measurements of particles beams, the accelerator stability using generating voltmeter (GVM) control and especially its influence on the interference suppression of the high energy mass spectrometer has to be investigated. Therefore, systematic measurements could be conducted, investigating the impact of small terminal voltage shifts on the separability of the high energy mass spectrometer. Systematic investigation of the background components spectra like in subsec. 3.2.3.5 overall or in terms of terminal voltage shifts could be conducted. Thereby, the measurement should also be conducted subsequently after the ESA. For the further investigation of the gas-filled magnet processes, extensive experimental work is necessary for an applicable description of the different density effects. In a first step, to further improve the simulations, the mean charge state and width in dependence of the gas type and gas pressure for different well-defined energies should be investigated. Therefore, a new setup has to be designed which would provide a differentially pumped chamber capable of holding gas pressures in the millibar region, see [90] for an example setup. The differential pumping is necessary since every entrance or exit foil would destroy the gas-dependent charge state distribution. An alternative to this could be the use of so-called jet targets, [21]. A subsequent separation component like a MSA or ESA would be necessary. Such

[11] G. Hackenberg, PhD thesis, not submitted

a setup could also be used to measure electron capture and loss cross sections. In all cases the simulation could only be improved if a semi-empirical or theoretical formula could be derived. It is not possible to measure each necessary combination of energies and initial charge which are found in the gas-filled magnet. The current detector units within the gas-filled magnet can be further used for beam inspections during measurements. In the current state the external code could be further used to simulate other gas types and gives a quality estimation of their usability. The revised in-house code could be used to simulate other ion beam species in nitrogen gas.
Concerning the status of ^{60}Fe AMS measurements, the assumption of the background level source by memory effect has to be proven if ratio measurements down to 10^{-16} are desired. Thereby, it is important that the whole source is cleaned beforehand, all samples are newly produced in ascending order and only the lowest standard is used as a reference. For the usage of the large detector window the gas ionization detector has to be further improved to achieve y-independent energy loss signals with good resolution on all anodes. In long-term the outer and inner detector layout has to be enlarged for the use of larger windows. Furthermore, a more stable entrance window has to be acquired. With a larger detector window it is unavoidable that further interferences and a higher fractions of the isobar enters the detector. For the interferences, it will be sufficient to introduce a further suppression step like a position signal by split anodes. For that an improvement of the energy loss signal of these anodes has to be achieved so that the further suppression does not come at a cost of differential energy loss separation. Another option would be the construction of an additional time-of-flight setup through the gas-filled magnet. For the isobaric fraction it should be sufficient to solve the y-dependence and apply an optimized gas pressure. For each individual isotope it has to be decided if the additional transmission with the larger window is required or if the small window with the inherently lower interferences is sufficient.

7 Appendix

7.1 Basic Concepts

7.1.1 Python implementation of the separation properties determination

```
import matplotlib.pyplot as plt
import matplotlib.colors as col
import numpy as np
import math

#For ellipse
from matplotlib import patches

#For fitting
import astropy
from astropy.modeling.models import Gaussian2D
from astropy.modeling.fitting import LevMarLSQFitter
from astropy.convolution import Gaussian2DKernel
from astropy.convolution import convolve

#Package for plotting by me
from support import plotsettings
#Package provides by G. Hackenberg
from eventdata import Listdata

#Define folder for saving the final plot
dir="Placeholder/"
#Definde folder of data
data="Placeholder"

#Get Dataframe from the measurement
all=Listdata(data+'190319_7.lst').data

#Get Dataframes for single anodes

anode1=all["ch1"]
anode2=all["ch2"]
```

```
anode3=all["ch3"]
anode4=all["ch4"]
anode5=all["ch5"]

#Define spectra division
anodestart=(anode3+anode2)
anodeend=(anode4+anode5)

pltset=plotsettings.Plotsettings()
pltset.plotsize("34half")

fig, axs= plt.subplots(nrows=1,ncols= 1 ,sharey="row",figsize=(pltset.
    figsizew, pltset.figsizeh/2),constrained_layout=True)
axs.xaxis.set_tick_params(direction = 'in',right=True)
axs.yaxis.set_tick_params(direction = 'in',top=True)
axs.set_xlim(370,550)
axs.set_ylim(200,350)
axs.set_xlabel("A1+A2[Channel]",fontname=pltset.font,fontsize=pltset.
    fontsizelabels)
axs.set_ylabel("A3[Channel]",fontname=pltset.font,fontsize=pltset.
    fontsizelabels)
xedges= np.arange((1024+1))
yedges= np.arange((1024+1))

#Define histogram binning
bin_list = np.linspace(0, 1024, 1024)
h = np.histogram2d(anodestart,anodeend,bins=bin_list)[0]
h=h.T

data=np.asarray(h).ravel()

#Define model
kernel = Gaussian2DKernel(x_stddev=1)
astropy_conv = convolve(data.reshape(1023, 1023), kernel)

notnans = np.isfinite(data.reshape(1023, 1023))

x, y = np.meshgrid(bin_list[0:1023], bin_list[0:1023])

#Fit
fitter = LevMarLSQFitter()
c1_init = Gaussian2D(amplitude=1000, x_mean=440, y_mean=300,cov_matrix=
    None)
```

```
c1_fit = fitter(c1_init, x[notnans], y[notnans], data.reshape(1023,
    1023)[notnans])

#Plot
im=axs.imshow(h, origin = "lower",cmap=plotsettings.newcmp, norm = col.
    LogNorm(vmin=0.9,vmax=100), aspect='auto', interpolation='none',
    rasterized=True)

sigma_x=round(c1_fit.x_fwhm/2.3548,3)
sigma_y=round(c1_fit.y_fwhm/2.3548,3)
ellipses=patches.Ellipse([c1_fit.x_mean[0],c1_fit.y_mean[0]],sigma_x*2,
    sigma_y*2,angle=math.degrees(c1_fit.theta[0]),label="FWHM␣ellipses␣
    of␣$^{60}$Fe␣",linewidth=1,edgecolor='red',facecolor="None")
axs.add_patch(ellipses)



#Fit second isotope
c2_init = Gaussian2D(amplitude=1000, x_mean=470, y_mean=260,cov_matrix=
    None)
c2_fit = fitter(c2_init, x[notnans], y[notnans], data.reshape(1023,
    1023)[notnans])

#Plot
im=axs.imshow(h, origin = "lower",cmap=plotsettings.newcmp, norm = col.
    LogNorm(vmin=0.9,vmax=100), aspect='auto', interpolation='none',
    rasterized=True)

sigma_x2=round(c2_fit.x_fwhm/2.3548,3)
sigma_y2=round(c2_fit.y_fwhm/2.3548,3)
ellipses=patches.Ellipse([c2_fit.x_mean[0],c2_fit.y_mean[0]],sigma_x2
    *2,sigma_y2*2,angle=math.degrees(c2_fit.theta[0]),label="FWHM␣
    ellipses␣of␣$^{60}$Fe␣",linewidth=1,edgecolor='red',facecolor="None"
    )
axs.add_patch(ellipses)

#Calculate distance between means
d = np.sqrt((c2_fit.x_mean[0] - c1_fit.x_mean[0])**2 + (c2_fit.y_mean
    [0] - c1_fit.y_mean[0])**2)

mu_x=c1_fit.x_mean[0]
mu_y=c1_fit.y_mean[0]
mu_x2=c2_fit.x_mean[0]
mu_y2=c2_fit.y_mean[0]
```

```
#Calculate correlation paarmeter
p2=    (math.tan(c2_fit.theta[0]*2)*(sigma_x2**2-sigma_y2**2)/(2*
    sigma_x2*sigma_y2))
p=   (math.tan(c1_fit.theta[0]*2)*(sigma_x**2-sigma_y**2)/(2*sigma_x*
    sigma_y))

#Define linear function for connection line
m = (c2_fit.y_mean[0]-c1_fit.y_mean[0])/(c2_fit.x_mean[0]-c1_fit.x_mean
    [0])
n = c1_fit.y_mean[0] - (m*c1_fit.x_mean[0])

def f1(x):
return(m*x+n)

#Calculate intersetcion x-points
x11 = (np.sqrt((sigma_x2**2)*(sigma_y2**2)*(mu_x2**2*m**2*p2**2-mu_x2
    **2*m**2-2*mu_x2*mu_y2*m*p2**2+2*mu_x2*mu_y2*m+2*mu_x2*m*n*p2**2-2*
    mu_x2*m*n+(sigma_x2**2)*m**2-2*(sigma_x2)*(sigma_y2)*m*p2+mu_y2**2*
    p2**2-mu_y2**2-2*mu_y2*n*p2**2+2*mu_y2*n+(sigma_y2**2)+n**2*p2**2-n
    **2))-mu_x2*(sigma_x2)*(sigma_y2)*m*p2+mu_x2*(sigma_y2**2)+(sigma_x2
    **2)*mu_y2*m-(sigma_x2**2)*m*n-(sigma_x2)*mu_y2*(sigma_y2)*p2+(
    sigma_x2)*(sigma_y2)*n*p2)/((sigma_x2**2)*m**2-2*(sigma_x2)*(
    sigma_y2)*m*p2+(sigma_y2**2))
x12 = (-np.sqrt((sigma_x2**2)*(sigma_y2**2)*(mu_x2**2*m**2*p2**2-mu_x2
    **2*m**2-2*mu_x2*mu_y2*m*p2**2+2*mu_x2*mu_y2*m+2*mu_x2*m*n*p2**2-2*
    mu_x2*m*n+(sigma_x2**2)*m**2-2*(sigma_x2)*(sigma_y2)*m*p2+mu_y2**2*
    p2**2-mu_y2**2-2*mu_y2*n*p2**2+2*mu_y2*n+(sigma_y2**2)+n**2*p2**2-n
    **2))-mu_x2*(sigma_x2)*(sigma_y2)*m*p2+mu_x2*(sigma_y2**2)+(sigma_x2
    **2)*mu_y2*m-(sigma_x2**2)*m*n-(sigma_x2)*mu_y2*(sigma_y2)*p2+(
    sigma_x2)*(sigma_y2)*n*p2)/((sigma_x2**2)*m**2-2*(sigma_x2)*(
    sigma_y2)*m*p2+(sigma_y2**2))
x21 = (np.sqrt((sigma_x**2)*(sigma_y**2)*(mu_x**2*m**2*p**2-mu_x**2*m
    **2-2*mu_x*mu_y*m*p**2+2*mu_x*mu_y*m+2*mu_x*m*n*p**2-2*mu_x*m*n+(
    sigma_x**2)*m**2-2*(sigma_x)*(sigma_y)*m*p+mu_y**2*p**2-mu_y**2-2*
    mu_y*n*p**2+2*mu_y*n+(sigma_y**2)+n**2*p**2-n**2))-mu_x*(sigma_x)*(
    sigma_y)*m*p+mu_x*(sigma_y**2)+(sigma_x**2)*mu_y*m-(sigma_x**2)*m*n
    -(sigma_x)*mu_y*(sigma_y)*p+(sigma_x)*(sigma_y)*n*p)/((sigma_x**2)*m
    **2-2*(sigma_x)*(sigma_y)*m*p+(sigma_y**2))
x22 = (-np.sqrt((sigma_x**2)*(sigma_y**2)*(mu_x**2*m**2*p**2-mu_x**2*m
    **2-2*mu_x*mu_y*m*p**2+2*mu_x*mu_y*m+2*mu_x*m*n*p**2-2*mu_x*m*n+(
    sigma_x**2)*m**2-2*(sigma_x)*(sigma_y)*m*p+mu_y**2*p**2-mu_y**2-2*
    mu_y*n*p**2+2*mu_y*n+(sigma_y**2)+n**2*p**2-n**2))-mu_x*(sigma_x)*(
    sigma_y)*m*p+mu_x*(sigma_y**2)+(sigma_x**2)*mu_y*m-(sigma_x**2)*m*n
    -(sigma_x)*mu_y*(sigma_y)*p+(sigma_x)*(sigma_y)*n*p)/((sigma_x**2)*m
```

```
    **2-2*(sigma_x)*(sigma_y)*m*p+(sigma_y**2))

#Calculate intersection values and distance between mean and
    intersetion
y11 = f1(x11)
y12 = f1(x12)
s1 = np.sqrt((x12 - x11)**2 + (y12 - y11)**2)/2

y21 = f1(x21)
y22 = f1(x22)
s2 = np.sqrt((x22 - x21)**2 + (y22 - y21)**2)/2

#Plot connection line
x12=np.arange(400,600,1)
y12=f1(x12)
axs.plot(x12,y12,linestyle="-",color="black")

FWHM = 2.4538*0.5*(s1+s2)
sf = d / FWHM
print(s1)
print(s2)
print(d)
print(FWHM)
print(sf)
plt.savefig(dir+Placeholder)
plt.show()
```

7.1.2 Confidence intervals for small counting statistics

Events	low. lim.	up. lim.	low. lim. ^{12}C	up. lim. ^{12}C	low. lim. ^{60}Fe	up. lim. ^{60}Fe
0	0	1.29	0.00	1.38	0.00	1.46
1	0.37	2.75	0.36	2.75	0.35	2.76
2	0.74	4.25	0.73	4.26	0.69	4.28
3	1.1	5.3	1.08	5.32	1.03	5.36
4	2.34	6.78	2.30	6.80	2.21	6.86
5	2.75	7.81	2.71	7.85	2.59	7.94
6	3.82	9.28	3.75	9.32	3.59	9.43
7	4.25	10.3	4.18	10.36	4.00	10.51
8	5.3	11.3	5.21	11.38	4.98	11.57
9	6.33	12.79	6.21	12.88	5.92	13.09
10	6.78	13.81	6.66	13.91	6.36	14.17
11	7.81	14.82	7.66	14.95	7.30	15.25
12	7.83	16.29	7.69	16.42	7.36	16.75
13	9.28	17.3	9.10	17.46	8.67	17.83
14	10.3	18.32	10.09	18.50	9.60	18.93
15	11.32	19.32	11.08	19.53	10.52	20.02
16	12.33	20.8	12.06	21.01	11.43	21.52
17	12.79	21.81	12.52	22.05	11.89	22.61
18	13.81	22.82	13.51	23.08	12.81	23.71
19	14.82	23.82	14.48	24.11	13.72	24.80
20	15.83	25.3	15.46	25.60	14.62	26.30

Table 7.1: Confidence intervals for small event numbers. Columns 2 and 3 give the upper and lower limit by Feldman et al., [44], which were taken from [41]. As in [41] proposed, the remaining uncertainties are added quadratically to receive adjusted limits which are shown in columns 4 and 5 for carbon and 6 and 7 for iron. An exception to this is for 0 events where 0.09 is added to the carbon upper limit and 0.17 is added to the iron upper limit. These were used in the analysis within this thesis.

7.2 Experimental Setup and Developments

7.2.1 Limioptic code for the current 10 MV AMS setup in Cologne

The LIMIOPTIC2 code of the current 10 MV AMS setup in Cologne is given below. The red colored lines indicate modifications to the setup.

```
AddBeam(7.76,7.84,7.76,7.84,0,0,10)

 #MC - SNICS
AddDrift(1, 1, 0.0146)
AddDrift(1, 1, 0.0146)
AddDrift(1,1,0.1787)
AddThinLens(0.2990,0.2990,68) ; Name("EL01");
AddDrift(1,1,0.1787)

AddWaist(); Name("WAIST"); Name("Waist sputter");
AddSlit(0,10,0,10)

 #Injector

 #ESA
AddDrift(1,1,.435)
AddESD(100,1,math.radians(90),0.435,0.435,0,45) ; Name("ESA");
AddDrift(1,1,0.435)
AddWaist(); Name("WAIST");
AddSlit(0,10,0,10)

# 90 degree magnet
AddDrift(1,1,0.8)
AddEdgeFocusing(0.435, 3.6068,-0.01, 50)
AddMSA(10, 1, 0.435, math.radians(90.), 50); Name("MSA");
AddEdgeFocusing(0.435, 3.6068,-0.01, 50)
AddDrift(1,1,0.870)
AddWaist(); Name("WAIST");
AddSlit(0,10,0,10)

# Preacceleration
AddDrift(1,1,0.656+0.0000)
AddVBFN(97.e2,75.e3,0.342) ; Name("VB");
AddDrift(1,1,0.617-0.0000)

# LE
```

```
# New Einzel lens
AddThinLens(4.0500,4.0500,100) ; Name("El0.1");
AddDrift(1,1,0.150+0.150+0.3)

AddDrift(1,1,1.448)

# Duplasmatron source housing
AddDrift(1,1,1.103)

 #20 degree magnet
AddDrift(1,1,0.56)
#Ende Magnet
AddDrift(1,1,0.637)

# EL I
AddThinLens(1.0100,1.0100,100) ; Name("EL1");
# Blende

AddDrift(1,1,1.308)
AddWaist(); Name("WAIST");
AddSlit(0,10,0,10)
Name("Blende");
AddDrift(1,1,1.019)

# EL II
AddThinLens(0.5100,0.5100,100); Name("EL2");
AddDrift(1,1,.503)
AddWaist(); Name("WAIST");
AddDrift(1,1,0.3)

# EL III
AddThinLens(0.1000,0.1000,100); Name("EL3");
AddDrift(1,1,.37)

 #Tandem
AddFNAccNeu(9.5e6, 75000, 10, b =1.1400, b1 = -1., b2 = -1., D1 = .088,
     factor1 = 1., factor2 = 1., beamprofile = False,addwaist=True) ;
    Name("fn");

#  HE
AddDrift(1, 1, .9)

# Q0
AddQuadrupolAxFoc(10, 1,3.7400, .315, 30) ;  Name("Q1");
```

```
AddDrift(1, 1, .02)
AddQuadrupolRadFoc(10, 1, 3.8200, .315, 30)
AddDrift(1, 1, 2.45)

 #Objekt slits first 90 degree magnet
AddSlit(0,10,0,10)
AddDrift(1, 1, 2.92193)
AddWaist(); Name("waist");
AddSlit(0,10,0,10)

 #Second 90 degree magnet
AddDrift(1, 1,2.208 )

 #Magnet
AddEdgeFocusing(1.104,math.radians(28.8), .5, 60)
AddMSA(10, 1, 1.104, math.radians(90.), 60) ; Name("MSA");
AddEdgeFocusing(1.104, math.radians(28.8), .5, 60)

AddDrift(1, 1, 2.208)
AddWaist()
AddSlit(0,10,0,10)
AddDrift(1, 1, 3.142)

#QD0

AddQuadrupolAxFoc(10, 1,5.5000, .300, 30)
AddQuadrupolRadFoc(10,1,5.6900, .300, 30) ; Name("qd0");

AddDrift(1, 1,3.15)

AddWaist(); Name("WAIST");
AddSlit(0,10,0,10)

 #ESA

 #QD1

AddDrift(1, 1,0.775)
AddQuadrupolRadFoc(10, 1,9.8785, .300, 30) ; Name("qd1");
AddQuadrupolAxFoc(10, 1,6.9984, .300, 30)

 #ESA
AddDrift(1, 1, .2)
AddESD(10, 1, math.radians(30), 3.5, 1.e9, 0., 15)
```

```
AddDrift(1, 1, .2)

AddQuadrupolAxFoc(10, 1,6.9984, .300, 30) ; Name("qd2");
AddQuadrupolRadFoc(10, 1,9.8785, .300, 30)

 #QD2
AddDrift(1, 1, 0.775)
AddWaist(); Name("WAIST");
AddSlit(0,10,0,10)

# ToF

 #QD2
AddDrift(1, 1, 2.077)
AddQuadrupolRadFoc(10, 1,7.4959, .300, 36.5) ; Name("qd3");
AddQuadrupolAxFoc(10, 1,7.4617, .300, 36.5)

AddDrift(1, 1, 2.077/2);Name("TOF");

 #135 Grad Magnet

AddDrift(1, 1, 2.077/2)
AddWaist(); Name("WAIST");
AddSlit(0,10,0,10)
```

7.2.2 Limioptic simulation for the current 10 MV AMS setup in Cologne

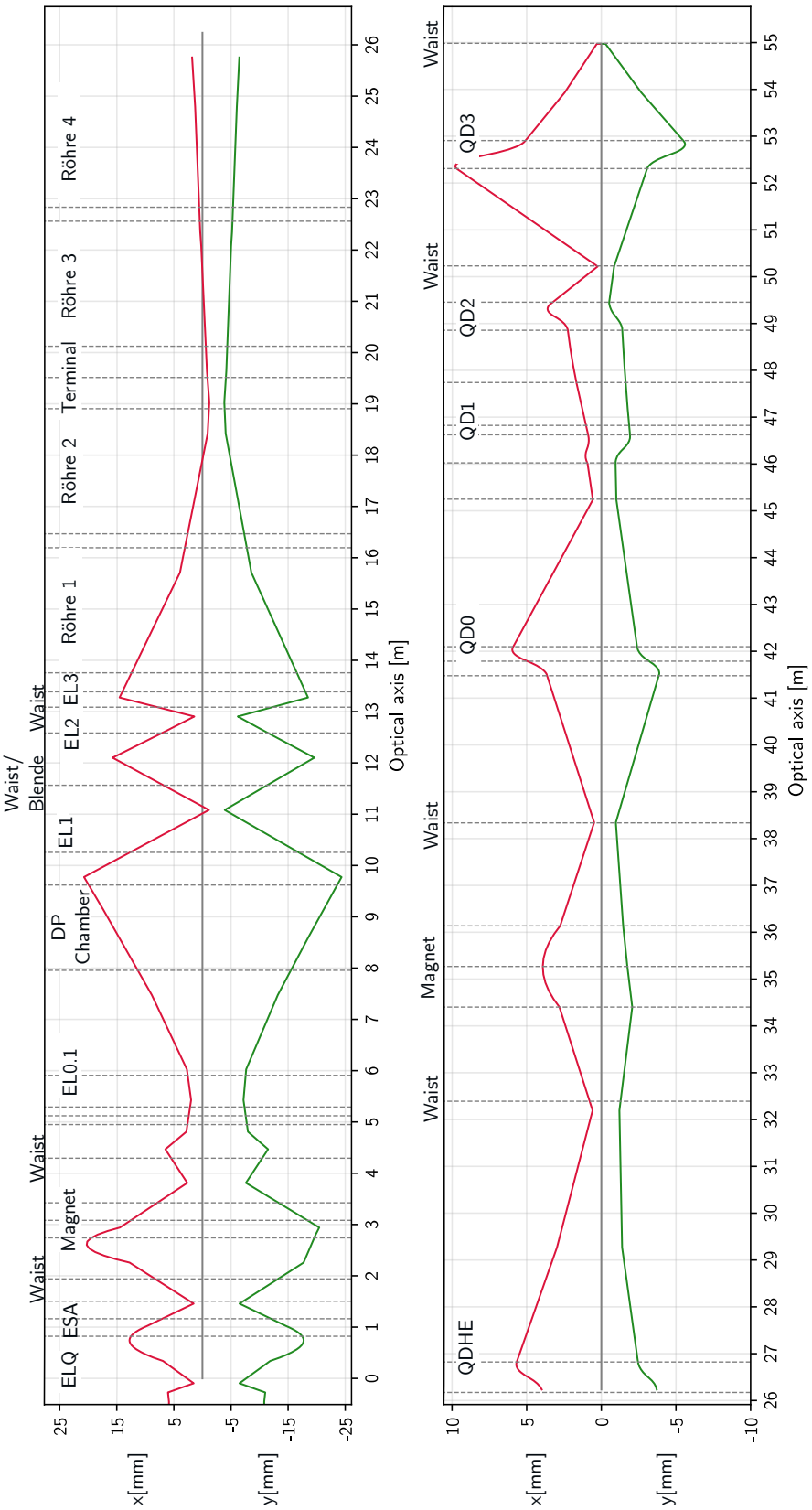

Figure 7.1: Ion-optical simulation of the current AMS setup at the 10 MV tandem accelerator. The view is split in the red colored dispersive x-axis and the green colored non-dispersive y-axis.

7.2.3 Parameter set of $^{48}Ti^{8+}$ (64.31 MeV) from the pilot beams of $^{47}Ti^{8+}$

Section	Component	Value	
Ion Source	Ionizer Curr.	24.8	A
	Sputter Volt.	5098	V
	Sputter Curr.	-	mA
	Oven Curr.	0.6	A
	Oven Temp.	-	°C
	Cesiumfocus	4902	V
	Extraction	11997	V
	Einzel lens	1962	V
	Y-steerer	15.99	V
	X-Slits	±5	mm
Injector	ESA Volt.	1710	V
	LE Magnet	52.33	A
	Bouncer 1 (^{47}TiH)	1414	V
	Bouncer 2 (^{48}TiH)	1039	V
	X-steerer 1	13.75	V
	Y-steerer 1	-17.71	V
	X-steerer 2	-16.24	V
	Y-steerer 2	-33.48	V
	Pre-Acceleration	60.54	kV
	Einzel Lens 0.1	15	kV
	X-Slits (ESA)	±5	mm
	Y-Slits (ESA)	±10	mm
	X-Slits (Magnet)	±3	mm
	Y-Slits (Magnet)	±10	mm
LE side	X-steerer 1	0.55	kV
	X-steerer 2	-0.82	kV
	Y-steerer 1	0.0	kV
	Y-steerer 2	-0.62	kV
	Einzel Lens 1	47.96	kV
	Einzel Lens 2	46.5	kV
	Einzel Lens 3	8	kV
	X-Slits (LE)	open	

Section	Component	Value	
Acc.	Terminal Volt.	6.984	MV
	Term. Steerer	-10	a.u.
HE	Quadr. Lens 1	0.413	A
	Quadr. Lens 2	0.427	A
	X-steerer 1	0.01	kV
	Y-steerer 1	-0.01	kV
	X-steerer 2	3.24	kV
	Y-steerer 2	0.01	kV
HEM	Magnet	8964	G
	of. cup 1	-	mm
	Aperture	3	mm
	Slits	±4	mm
HEE	QD01	10.8	A
	QD02	10.6	A
	QD 1	12	A
	QD 2	12.5	A
	QD 3	24.5	A
	QD 4	15.3	A
	Slits bf. ESA	open	
	Slits af. ESA	open	
	ESA Volt.	68.2	kV

Table 7.2: Parameter set determined in the tuning routine test with $^{48}Ti^{7+}$ for $^{48}Ti^{8+}$ (64.31 MeV) shown in subsec. 3.2.1.7.

7.2.4 Parameter set of $^{14}C^{4+}$ (35.57 MeV)

Section	Component	Value	
Ion Source	Ionizer Curr.	25	A
	Sputter Volt.	5098	V
	Sputter Curr.	0.29	mA
	Oven Curr.	0.65	A
	Oven Temp.	100	°C
	Cesiumfocus	4860	V
	Extraction	11943	V
	Einzel lens	2237	V
	Y-steerer	-55.07	V
	X-Slits	±5	mm
Injector	ESA Volt.	1710	V
	LE Magnet	27.19	A
	Bouncer 1 (^{14}C)	214	V
	Bouncer 2 (^{13}C)	1536	V
	X-steerer 1	-31.38	V
	Y-steerer 1	-13.47	V
	X-steerer 2	11.74	V
	Y-steerer 2	50.97	V
	Pre-Acceleration	64.75	kV
	Einzel Lens 0.1	15	kV
	X-Slits (ESA)	±5	mm
	Y-Slits (ESA)	±10	mm
	X-Slits (Magnet)	±3	mm
	Y-Slits (Magnet)	±10	mm
LE side	X-steerer 1	0.07	kV
	X-steerer 2	-0.03	kV
	Y-steerer 1	0.22	kV
	Y-steerer 2	-0.58	kV
	Einzel Lens 1	15	kV
	Einzel Lens 2	15	kV
	Einzel Lens 3	15	kV
	X-Slits (LE)	open	

Section	Component	Value	
Acc.	Terminal Volt.	7.030	MV
	Term. Steerer	-10	a.u.
HE	Quadr. Lens 1	0.331	A
	Quadr. Lens 2	0.337	A
	X-steerer 1	0.01	kV
	Y-steerer 1	0.01	kV
	X-steerer 2	3.06	kV
	Y-steerer 2	0.01	kV
HEM	Magnet	7300	G
	of. cup 1	+160	mm
	Aperture	3	mm
	Slits	±4	mm
HEE	QD01	8.6	A
	QD02	8.6	A
	QD 1	15.4	A
	QD 2	17.1	A
	QD 3	12.99	A
	QD 4	9.0	A
	Slits bf. ESA	open	
	Slits af. ESA	±6	mm
	ESA Volt.	76.19	kV
Det.	Gas pressure	42	mbar
	Gas type	Isobut.	
	Window type	SiN	
	Window type	8x8	mm^2
	Window thickn.	150	nm
	Anode Volt.	500	V
	Frisch grid	250	V

Table 7.3: Parameter set used for $^{14}C^{4+}$ (35.57 MeV) in the measurements shown in subsec. 3.2.3.3

7.3 Investigation of the 135° gas-filled magnet

7.3.1 Exemplary parameter files for the simulations

7.3.2 Nitrogen gas inner profile

```
<config>
<Ionproperties>
<type>Ni</type>
<Zp>28</Zp>
<Ap>60</Ap>
<Ep>87.86</Ep>
<Epv>100</Epv>
<dEp>0.0583</dEp>
<x>-894</x>
<dx>3</dx>
<alpha>0.7</alpha>
<dalpha>0.01</dalpha>
<q>11</q>
<qn>21</qn>
<n>100000</n>
<dqn>1.51</dqn>
</Ionproperties>
<Magnet>
<B>0.6805</B>
<GasDensity>5</GasDensity>
<Atomnumber>2</Atomnumber>
<Gastype>N</Gastype>
<GasA>14</GasA>
<GasZ>7</GasZ>
</Magnet>
<filedir>
<name>Result\Ni\100000\Januar_Stickstoff\OhneRandfeld</name>
</filedir>
<outputcondition>
<trajectory>true</trajectory>
<ytrajectory>false</ytrajectory>
<all>true</all>
<angle>135</angle>
</outputcondition>
<fringe>
<apply>false</apply>
</fringe>
<window>
```

```
<windowpos>0</windowpos>
</window>
</config>
```

7.3.3 Nitrogen gas outer profile

```
<config>
<Ionproperties>
<type>Ni</type>
<Zp>28</Zp>
<Ap>60</Ap>
<Ep>87.86</Ep>
<Epv>100</Epv>
<dEp>0.0583</dEp>
<x>-900</x>
<dx>3.0</dx>
<alpha>0.0</alpha>
<dalpha>0.004</dalpha>
<q>11</q>
<qn>21</qn>
<n>100000</n>
<dqn>1.51</dqn>
</Ionproperties>
<Magnet>
<B>0.64012</B>
<GasDensity>7</GasDensity>
<Atomnumber>2</Atomnumber>
<Gastype>N</Gastype>
<GasA>14</GasA>
<GasZ>7</GasZ>
</Magnet>
<filedir>
<name>Result\Ni\100000\Mai_Stickstoff\OhneRandfeld</name>
</filedir>
<outputcondition>
<trajectory>false</trajectory>
<ytrajectory>false</ytrajectory>
<all>true</all>
<angle>135</angle>
</outputcondition>
<fringe>
<apply>false</apply>
</fringe>
<window>
```

<windowpos>0</windowpos>
</window>
</config>

7.3.4 Helium gas

<config>
<Ionproperties>
<type>Ni</type>
<Zp>28</Zp>
<Ap>60</Ap>
<Ep>87.86</Ep>
<Epv>100</Epv>
<dEp>0.0583</dEp>
<x>−900</x>
<dx>1</dx>
<alpha>−0.0</alpha>
<dalpha>0.0037</dalpha>
<q>11</q>
<qn>21</qn>
<n>100000</n>
<dqn>1.51</dqn>
</Ionproperties>
<Magnet>
<B>0.7131</B>
<GasDensity>19.7</GasDensity>
<Atomnumber>1</Atomnumber>
<Gastype>He</Gastype>
<GasA>4</GasA>
<GasZ>2</GasZ>
</Magnet>
<filedir>
<name>Result\Ni\100000\Mai_Helium\OhneRandfeld</name>
</filedir>
<outputcondition>
<trajectory>true</trajectory>
<ytrajectory>false</ytrajectory>
<all>true</all>
<angle>135</angle>
</outputcondition>
<fringe>
<apply>false</apply>
</fringe>
<window>

```
<windowpos>0</windowpos>
</window>
</config>
```

7.4 Development of ^{60}Fe AMS measurements

7.4.1 Individual and combined fractions of iron oxide low energy mass spectrum

Oxygen		Iron	
Mass	[%]	Mass	[%]
16	99.757	54	5.845
17	0.038	55	-
18	0.205	56	91.754
		57	2.119
		58	0.282

Table 7.4: The table presents the abundances of iron and oxygen which combines to the mass spectrum found in tab. 7.5. The abundances were taken from reference [87].

Mass		^{54}Fe	^{56}Fe	^{57}Fe	^{58}Fe	$\text{Sum}_{\text{calc.}}$	$\text{Sum}_{\text{meas.}}$
70		^{54}Fe^{16}O					
	[%]	100				5.831	6.0922
71		^{54}Fe^{17}O					
	[%]	100				0.002	0.035
72		^{54}Fe^{18}O	^{56}Fe^{16}O				
	[%]	0.013	99.987			91.546	90.937
73			^{56}Fe^{17}O	^{57}Fe^{16}O			
	[%]		1.707	98.293		2.151	2.2307
74			^{56}Fe^{18}O	^{57}Fe^{17}O	^{58}Fe^{16}O		
	[%]		39.9984	0.180	59.822	0.470	0.500
75				^{57}Fe^{18}O	^{58}Fe^{17}O		
	[%]			97.469	2.531	0.004	0.071
76					^{58}Fe^{18}O		
	[%]				100	0.001	0.058

Table 7.5: The table presents the components of the low energy mass spectrum over the range of iron oxide with their respective fractions. The last two columns give the fractions of each mass by calculations in comparison to the measured ones. The values agree very well. Besides the experimental uncertainties one reason for discrepancies could be the neglection of possible hydride combinations. Additionally molecules containing ^{63}Cu or ^{65}Cu could impact this mass region.

7.4.2 Anode structure layouts

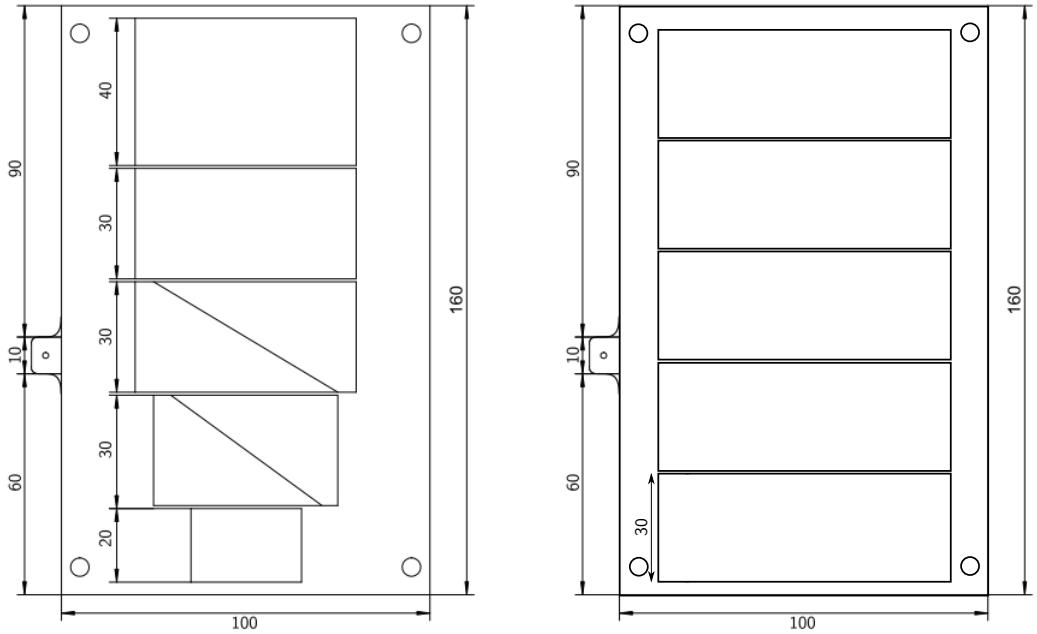

a) b)

Figure 7.2: Anode layouts of the 5 anode gas ionization detector. In the former layout, a), the anodes are geometrically different which made a calibration difficult. The new anode structure, b), provides equally sized and shaped anodes which can be easily calibrated by an external pulser signal. Drawing a) is taken from [33] while drawing b) is adapted from the former.

7.4.3 Parameter set of $^{60}Fe^{10+}$ (96.07 MeV)

Section	Component	Value	
Ion Source	Ionizer	25	A
	Sputter Volt.	5098	V
	Sputter Curr.	0.98	mA
	Oven Curr.	0.75	A
	Oven Temp.	100	°C
	Cesiumfocus	4248	V
	Extraction	12000	V
	Einzel lens	2142	V
	Y-steerer	-159.68	V
	X-Slits	±5	mm
Injector	ESA Volt.	1708	V
	LE Magnet	63.82	A
	Bounc. 1:$^{60}Fe^{16}O$	234	V
	Bounc. 2:$^{58}Fe^{16}O$	700	V
	X-steerer 1	178.91	V
	Y-steerer 1	250	V
	X-steerer 2	-96.22	V
	Y-steerer 2	-52	V
	Pre-Acceleration	65.2	kV
	Einzel Lens 0.1	15	kV
	X-Slits (ESA)	±5	mm
	Y-Slits (ESA)	±10	mm
	X-Slits (Magnet)	±3	mm
	Y-Slits (Magnet)	±10	mm
LE side	X-steerer 1	0.25	kV
	X-steerer 2	-0.3	kV
	Y-steerer 1	1.47	kV
	Y-steerer 2	-1.34	kV
	Einzel Lens 1	40.43	kV
	Einzel Lens 2	54	kV
	Einzel Lens 3	0	kV
	X-Slits (LE)	open	

Section	Component	Value	
Acc.	Terminal Volt.	8.864	MV
	Term. Steerer	-10	a.u.
HE side	Quadr. Lens 1	0.452	A
	Quadr. Lens 2	0.469	A
	X-steerer 1	0.01	kV
	Y-steerer 1	-0.01	kV
	X-steerer 2	3.43	kV
	Y-steerer 2	-1.4	kV
HEM	Magnet	9959	G
	Of. cup 1	+75.1	mm
	Aperture	3	mm
	Slits	±4	mm
HEE	QD0 1	11.3	A
	QD0 2	11.5	A
	QD 1	7.6	A
	QD 2	16.3	A
	QD 3	21	A
	QD 4	14.7	A
	QD 5	15.05	A
	QD 6	15.59	A
	Slits bf. ESA	open	mm
	Slits af. ESA	±6	mm
	ESA Volt.	82.16	kV
GFM	Gas type	N_2	
	Gas pressure	3	mbar
Det.	Pressure	42	mbar
	Gas type	Isobut.	
	Window area	20x20	mm^2
	Window type	SiN	
	Window thickn.	1000	nm
	Anode Volt.	500	V
	Slits	open	

Table 7.6: List of the parameter set used for $^{60}Fe^{10+}$ (96.07 MeV) in the measurements shown in subsec. 5.6.

7.4.4 Possibility of ^{58}Fe interference using the large detector window

Within the ^{60}Fe AMS measurements using the large detector window, it revealed that a significant background signal can be measured within the ROI when injecting the stable isotope $^{58}Fe^{16}O$ from blank material on the low energy side. Hereinafter the possibility of an additional interference

of ^{58}Fe when using the large window will be discussed. Thereby, it is assumed that in the blank sample measurements using the small window only real ^{60}Fe lies within the ROI caused by memory effect or cross talk, in the following only referred to as memory effect. By use of the large window it is assumed that the background is caused by memory effect and an additional rate by interference. By this assumption, the large windows background count rate should be the sum of the count rate measured from the memory effect and the additional fraction expected by ^{58}Fe. In terms of memory effect by use of the small window a normalized uncorrected count rate of $3.76{\cdot}10^{-4}$ $\frac{\text{counts}}{\text{s}{\cdot}\text{nA}}$ was measured at a correction factor of 3.52. By use of the bigger window with a correction factor of 2.22 the uncorrected count rate caused by memory effect would increase to an uncorrected count rate of $5.97{\cdot}10^{-4}\,\frac{\text{counts}}{\text{s}{\cdot}\text{nA}}$. For the calculations of the expected count rate caused by ^{58}Fe, the interference measurement can be investigated where only the stable molecule mass 74 (^{58}Fe^{16}O) was injected into the accelerator. It results in an uncorrected count rate of $3.73{\cdot}10^{-1}\,\frac{\text{counts}}{\text{s}{\cdot}\text{nA}}$. To estimate the count rate of ^{58}Fe when injecting mass 76 (^{58}Fe^{18}O) the analysis of the low energy iron oxide spectrum can be taken into account. The factor between the amount of ^{58}Fe when injected as ^{58}Fe^{16}O on mass 74 and the fraction on mass 76 as ^{58}Fe^{18}O is 465.51. Therefore, a count rate of $\frac{3.73{\cdot}10^{-1}\,\frac{\text{counts}}{\text{s}{\cdot}\text{nA}}}{465.51} = 8{\cdot}10^{-4}\,\frac{\text{counts}}{\text{s}{\cdot}\text{nA}}$ can be expected. The sum of the expected count rate from the memory effect and from the interference is $1.44{\cdot}10^{-3}\,\frac{\text{counts}}{\text{s}{\cdot}\text{nA}}$ which is results in 89% (38%(memory effect)+51% (^{58}Fe)) of the real count rate measured in the blank levels when using the large window. This would lead to the conclusion that a third, not identified, interference causes the remaining 11%. Furthermore, similar to the analysis of ^{14}C, see subsec. 3.2.3.5, it was determined which ion beam properties ^{58}Fe must have to cause the interference. The most probable candidate would be ^{58}Fe^{10+} with the same $\frac{\text{p}}{\text{q}}$ value corresponding to an energy of 99.38 MeV by recharge processes in the high energy accelerator tube. For its investigation, the gas ionization spectra of the third anode of a single standard sample, the summed spectra for all measured blanks as well as all interference measurements were analyzed, see spectra in fig. 7.3. The experimental values are compared to calculations of the energy loss of ^{60}Fe^{10+} with the used beam energy of 96.07 MeV and the proposed interference component, see tab. 7.7. Thereby, the fitted experimental values are calibrated to the calculated ^{60}Fe^{10+} component. With that the values calculated value of the interference matches the experimental value. However, the distributions also overlap fully within

Spectrum	Isotope	E_{ini} [MeV]	E-loss(A3) [MeV]	Meas. $\mu\|\sigma$ [Channel]	Cal. μ [MeV]
Standard	^{60}Fe^{10+}	96.07	10.858	215.9(8)|11.9(10)	10.858
Interference	^{58}Fe^{10+}	99.38	11.559	229.6(16)|12.5(14)	11.561

Table 7.7: Comparison of the energy loss of ^{60}Fe and the interference component. While the means of ^{60}Fe and the interference component do clearly differ an overlap within their 1σ interval of both distributions is observed.

their 1σ interval. Considering the blank spectra, the signals are equally distributed in the respective area of the assumed overlap, see fig. 7.3. A smallest increase can be observed on the position of the interference peak. The superposition of the two distributions normalized to the count rate of the blank is shown and does not contradict the data. However due to the low statistics no confident conclusion can be drawn.

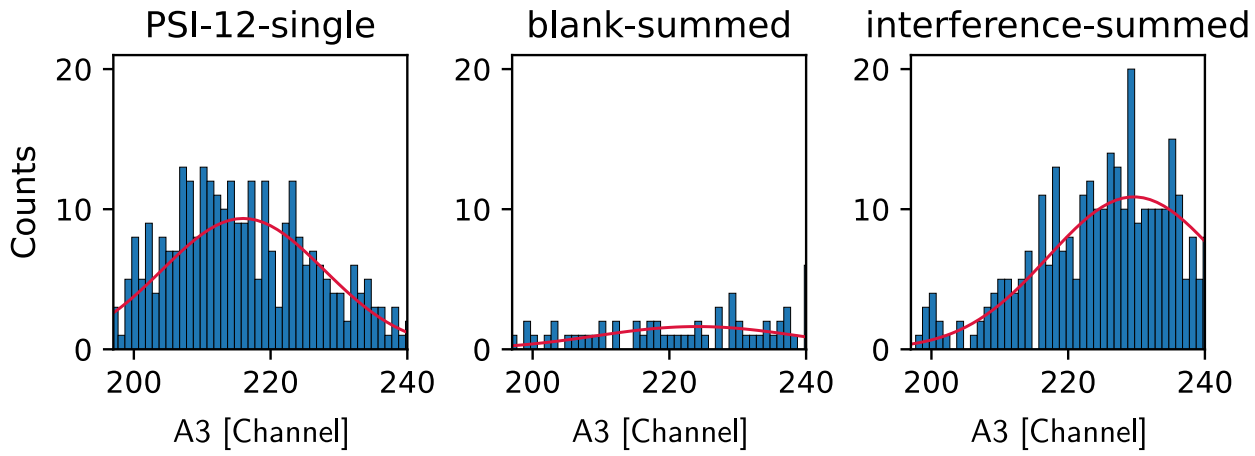

Figure 7.3: Spectra of the third anode with the highest separation of the gas ionization detector by use of the large detector window. Thereby, an individual standard sample measurement (left), the summed spectra from all blanks (middle) and the summed interference measurements (right) are shown. The red lines for the standard and interference spectra indicate their fitted Gaussian distributions. The ^{60}Fe and the interference component show different energies but overlap significantly within their 1σ. The summed blanks show mainly an equal distribution. One smallest increase on position of the interference can be seen. The red line represents a superposition from the other two Gaussian distributions with their respective assumed fractions and normalized to the measured background count rate. The calculated curve does not contradict the data but due to the low statistics no confident solution can be drawn.

7.4.5 ^{60}Fe spectra resulting from the χ^2-analysis

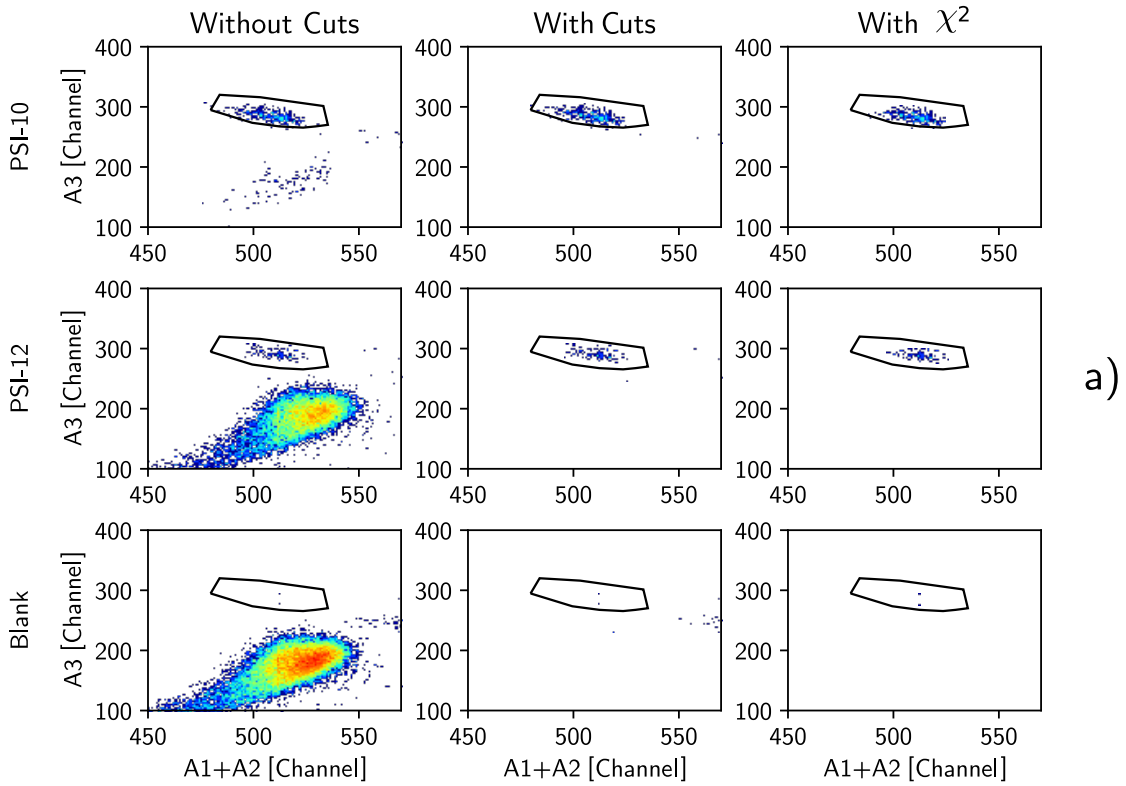

Figure 7.4: Continued on next page.

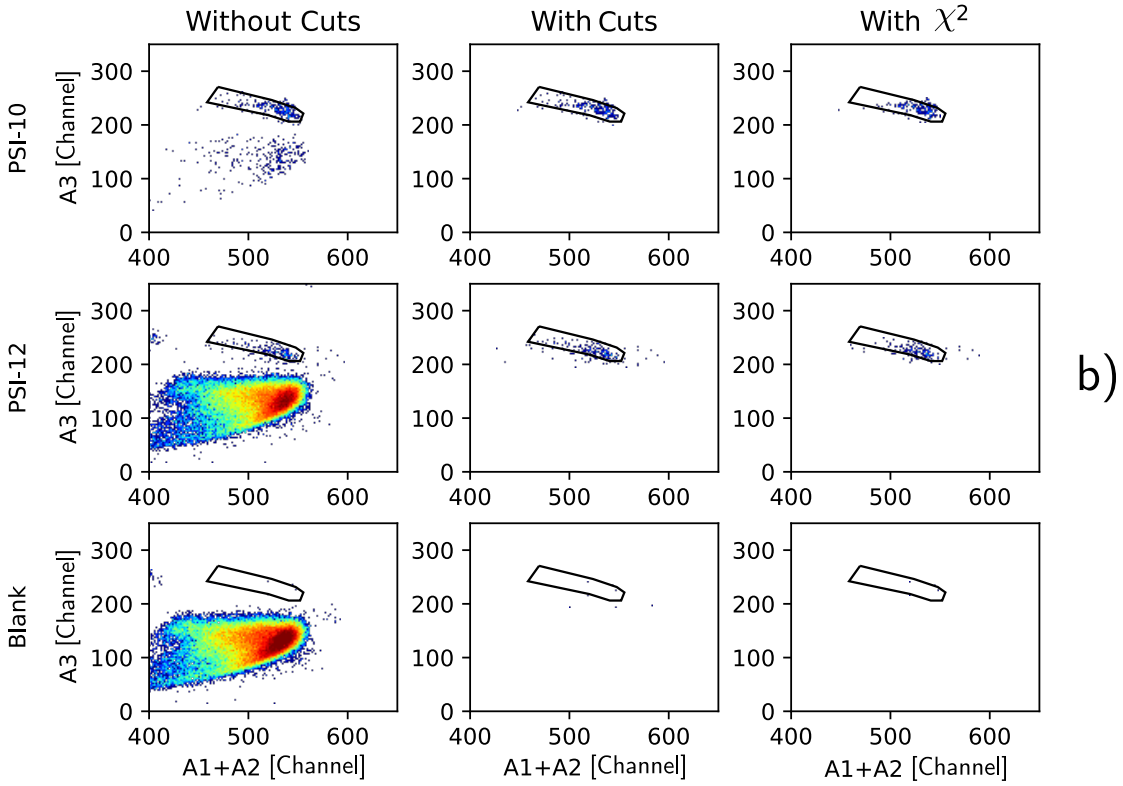

Spectra resulting from the χ^2 analysis for the small window, a), and the large window, b). Each individual spectrum shows the energy loss signal on the third anode in dependence of the energy loss signal on the sum of the first two anodes. Each row corresponds to one material. Each column corresponds to one step of the analysis. The first columns show the spectra without prior conditions. The second columns show the impact of the one-dimensional cuts on each individual anode and the third columns show the spectra after a cut at χ^2=9.

List of Figures

List of Tables

Bibliography

[1] A.J.T. Jull and G.S. Burr. Accelerator mass spectrometry: Is the future bigger or smaller? *Earth and Planetary Science Letters*, 243(3-4):305–325, 2006.

[2] R. Hellborg and G. Skog. Accelerator mass spectrometry. *Mass Spectrometry Reviews*, 27(5):398–427, 2008.

[3] K. Hain, M. Martschini, F. Gülce, M. Honda, M. Lachner, J.and Kern, F. Pitters, J.and Quinto, A. Sakaguchi, P. Steier, A. Wiederin, A. Wieser, A. Yokoyama, and R. Golser. Developing Accelerator Mass Spectrometry Capabilities for Anthropogenic Radionuclide Analysis to Extend the Set of Oceanographic Tracers. *Frontiers in Marine Science*, 9(March):1–17, 2022.

[4] F. Quinto, M. Lagos, M. Plaschke, T. Schäfer, H. Geckeis, and P. Steier. *Accelerator mass spectrometry (AMS)*, volume 7709 of *KIT Scientific Reports*, pages 71–73. KIT Scientific Publishing, 2015.

[5] A. Wallner, K. Buczak, I. Dillman, J. Feige, F. Käppeler, G. Korschinek, C. Lederer, A. Mengoni, U. Ott, M. Paul, G. Schätzel, P. Steier, and H. P. Trautvetter. AMS Applications in Nuclear Astrophysics : New Results for ^{13}C(n,γ)^{14}C and ^{14}N(n,p)^{14}C. pages 115–120, 2012.

[6] A. Wallner, J. Feige, N. Kinoshita, M. Paul, L. K. Fifield, R. Golser, M. Honda, U. Linnemann, H. Matsuzaki, S. Merchel, G. Rugel, S. G. Tims, P. Steier, T. Yamagata, and S. R. Winkler. Recent near-Earth supernovae probed by global deposition of interstellar radioactive ^{60}Fe. *Nature*, 532(7597):69–72, 2016.

[7] I. Leya, J. C. David, T. Faestermann, M. Froehlich, N. Kivel, D. Koll, S. Korschinek, G.and McIntyre, S. Merchel, S.and Pavetich, G. Rugel, D. Schumann, T. Smith, and A. Wallner. ^{53}Mn and ^{60}Fe in iron meteorites—New data and model calculations. *Meteoritics and Planetary Science*, 55(4):818–831, 2020.

[8] A. Wallner, M. Bichler, K. Buczak, R. Dressler, L. K. Fifield, D. Schumann, J. H. Sterba, S. G. Tims, G. Wallner, and W. Kutschera. Settling the half-life of Fe 60: Fundamental for a versatile astrophysical chronometer. *Physical Review Letters*, 114(4):1–6, 2015.

[9] K. Knie, T. Faestermann, G. Korschinek, G. Rugel, W. Rühm, and C. Wallner. High-sensitivity AMS for heavy nuclides at the Munich Tandem accelerator. *Nuclear Instruments and Methods in Physics Research Section B: Beam Interactions with Materials and Atoms*, 172(1-4):717–720, 2000.

[10] M. Schiffer. *Ein dediziertes Beschleuniger-Massenspektrometer für mittelschwere Radionuklide am Kölner FN-Tandembeschleuniger*. PhD thesis, University of Cologne, 2017.

[11] N. Bohr. On the theory of the decrease of velocity of moving electrified particles on passing through matter. *Philosophical Magazine*, 6(20):10–31, 1913.

[12] H. Bethe. Zur Theorie des Durchgangs schneller Korpuskularstrahlen durch Materie. *Annalen der Physik*, 397(3):325–400, 1930.

[13] F. Bloch. Zur Bremsung rasch bewegter Teilchen beim Durchgang durch Materie. *Annalen der Physik*, 408(3):285–320, 1933.

[14] O.B. Tarasov and D. Bazin. LISE++: Radioactive beam production with in-flight separators. *Nuclear Instruments and Methods in Physics Research Section B: Beam Interactions with Materials and Atoms*, 266(19-20):4657–4664, 2008.

[15] W.K. Chu and J.F. Ziegler. Chapter: Energy Loss and Energy Straggling. *Ion Beam Handbook for Material Analysis*, pages 1–19, 1977.

[16] N. Bohr. The penetration of atomic particles through matter. *Mathematisk-fysiske Meddelelser*, XVIII(8):1–144, 1948.

[17] Q. Yang, D. J. O'Connor, and Zhonglie Wang. Empirical formulae for energy loss straggling of ions in matter. *Nuclear Inst. and Methods in Physics Research, B*, 61(2):149–155, 1991.

[18] L. Meyer. Plural and multiple scattering of low-energy heavy particles in solids. *Physica Status Solidi (B)*, 44(1):253–268, 1971.

[19] K. Green and D. Burch. Multiple Scattering of Heavy Ion. *Annual report of nuclear physics laboratory, University of Washington*, pages 46–47, 1976.

[20] P. Sigmund and K. B. Winterbon. Small-Angle Multiple Scattering of Ions in the Screened Coloumb Region. *Nuclear Instruments & Methods*, 119:541–557, 1974.

[21] H.-D. Betz. Charge states and charge-changing cross sections of fast heavy ions penetrating through gaseous and solid media. *Reviews of Modern Physics*, 44(8):465–539, 1972.

[22] Inga Tolstikhina, Imai Makoto, Nicolas Winckler, and Shevelko Viacheslav. *Basic Atomic Interactions of Accelerated Heavy Ions in Matter*, volume 4. Springer, 2018.

[23] C. Feuerstein. *Improvement of measurement capabilities at the Cologne Accelerator Mass Spectrometer*. PhD thesis, University of Cologne, 2016.

[24] A. S. Schlachter, J. W. Stearns, W. G Graham, K. H. Berkner, R. V. Pyle, and J. A. Tanis. Electron capture for fast highly charged ions in gas targets: An empirical scaling rule. *Journal of Chemical Information and Modeling*, 53(9):1689–1699, 1983.

[25] V. P. Shevelko. Charge exchange in collisions between heavy low-charged ions. *Technical Physics*, 46(10):1225–1234, 2001.

[26] V. P. Shevelko, I. Yu Tolstikhina, and Th Stöhlker. Stripping of fast heavy low-charged ions in gaseous targets. *Nuclear Instruments and Methods in Physics Research, Section B: Beam Interactions with Materials and Atoms*, 184:295–308, 2001.

[27] N. Winckler, A. Rybalchenko, V. P. Shevelko, M. Al-Turany, T. Kollegger, and Th Stöhlker. BREIT code: Analytical solution of the balance rate equations for charge-state evolutions of heavy-ion beams in matter. *Nuclear Instruments and Methods in Physics Research, Section B: Beam Interactions with Materials and Atoms*, 392:67–73, 2017.

[28] R. O. Sayer. Semi-empirical formulas for heavy-ion stripping data. *Revue de Physique Appliquee*, 12(10):1543–1546, 1977.

[29] I. S. Dmitriev and V. S. Nikolaev. Semi-Empirical Method for the Calculation of the Equilibrium Distribution of Charges in a Fast-Ion Beam. *Soviet Physics Jetp*, 20(2):615–623, 1965.

[30] G Schiwietz. Improved charge-state formulas. *Nuclear Instruments and Methods in Physics Research B*, 177:125–131, 2001.

[31] M. Martschini, J. Buchriegler, P. Collon, W. Kutschera, J. Lachner, W. Lu, A. Priller, P. Steier, and R. Golser. Isobar separation of ^{93}Zr and ^{93}Nb at 24 MeV with a new multi-anode ionization chamber. *Nuclear Instruments and Methods in Physics Research, Section B: Beam Interactions with Materials and Atoms*, 361:201–206, 2015.

[32] K. Knie. *Beschleunigermassenspektrometrie mit Isobarenseparation in einem dedizierten gasgefüllten Magneten*. PhD thesis, TU Munich, 1997.

[33] R. Spanier. *A 135° Gas-Filled Magnet at the Cologne 10 MV AMS FN-Tandem Accelerator Setup and the use of ^{41}Ca as a Reference Nuclide for Nuclear Waste Management*. PhD thesis, University of Cologne, 2019.

[34] R. Middleton. A Negative-Ion Cookbook. *open source*, 1990.

[35] G. Rugel, T. Faestermann, K. Knie, G. Korschinek, A.A. Marchetti, J.E. McAninch, W. Rühm, T. Straume, and C. Wallner. Accelerator mass spectrometry of ^{63}Ni using a gas-filled magnet at the Munich Tandem Laboratory. *Nuclear Instruments and Methods in Physics Research Section B: Beam Interactions with Materials and Atoms*, 172:934–938, 2000.

[36] A. M. Miltenberger, K.-U.and Müller, M. Suter, H.-A. Synal, and C. Vockenhuber. Accelerator mass spectrometry of ^{26}Al at 6 MV using AlO^- ions and a gas-filled magnet. *Nuclear Instruments and Methods in Physics Research Section B: Beam Interactions with Materials and Atoms*, 406:272–277, 2017.

[37] K. Knie, T. Faestermann, and G. Korschinek. AMS at the Munich gas-filled analyzing magnet system GAMS. *Nuclear Instruments and Methods in Physics Research Section B: Beam Interactions with Materials and Atoms*, 123(1-4):128–131, 1997.

[38] M. Schiffer, R. Spanier, C. Müller-gatermann, S. Herb, C. Feuerstein, G. Hackenberg, M. Marock, S. Heinze, A. Stolz, A. Dewald, and S. Binnie. The first (^{53}Mn / ^{55}Mn) isotopic ratio measurements at the Cologne FN Tandem Accelerator. *Nuclear Inst. and Methods in Physics Research, B*, 437:87–92, 2018.

[39] N. Kivel, D. Schumann, and I. Günther-Leopold. Quantification of 60Fe atoms by MC-ICP-MS for the redetermination of the half-life. *Analytical and Bioanalytical Chemistry*, 405(9):2965–2972, 2013.

[40] D. Schumann and N. Kivel. Preparation of a ^{60}Fe standard for accelerator mass spectrometery (AMS). Technical report, 2016.

[41] P. Ludwig. *Search for supernova ^{60}Fe in the Earth's microfossil record.* PhD thesis, TU Munich, 2015.

[42] D. Koll. Search for Recent ^{60}Fe Deposition in Antarctica with AMS. Master's thesis, TU Munich, 2018.

[43] G. F. Knoll. *Radiation Detection and Measurement.* John Wiley & Sons,Inc., 3 edition, 1999.

[44] G. J. Feldman and R. D. Cousins. Unified approach to the classical statistical analysis of small signals. *Physical Review D - Particles, Fields, Gravitation and Cosmology*, 57(7):3873–3889, 1998.

[45] M. Schiffer. Aufbau eines Injektors für Massenspektrometrie am Kölner FN Tandembeschleuniger. Diploma, University of Cologne, 2012.

[46] R. Altenkirch. Setting the new ams-injector at the fn-tandem accelerator into operation and first performance test. Master thesis.

[47] S. Herb. Automation of AMS measurements at the Cologne 10 MV FN Tandem Accelerator. Master thesis, University of Cologne, 2018.

[48] A. Stolz. Untersuchung der Ionenoptik des Kölner AMS-Massenspektrometers und Vergleich unterschiedlicher Betriebsmodi für ausgesuchte Radioisotope. Diploma, University of Cologne, 2012.

[49] P. Wasserburger. Simulation und Optimierung des Laser-Ionen-Aufbaus an VERA. Diploma, University of Vienna, 2018.

[50] G. Hackenberg. Entwicklungsarbeiten zur Massenspektrometrie am CologneAMS für $^{41}CaH_2$-Proben und einen Gasionisationsdetektor. Master thesis, University of Cologne, 2019.

[51] National Electrostatics Corporation. MC-SNICS Ion Source- Instruction Manual. Technical report.

[52] A. Stolz. *Einrichtung und Weiterentwicklung eines $^{14}CO_2$-Systems am 6 MV TANDETRON Beschleuniger des CologneAMS.* PhD thesis, University of Cologne, 2019.

[53] H. Wiedemann. *Particle accelerator physics*, volume 4. Springer, 2019.

[54] L. Netterdon. *Constraining nuclear-physics input for explosive nucleosynthesis processes via in-beam γ -ray spectroscopy and the activation technique.* PhD thesis, University of Cologne, 2015.

[55] H. Wollnik. *Optics of Charged Particles.* Academic Press, 1987.

[56] Danfysik A/S. Manual-Beam profile monitor 517-System 5000. Technical report, 1984.

[57] P. Steier. *Exploring the limits of VERA: A universal facility for accelerator mass spectrometry.* PhD thesis, University of Vienna, 2000.

[58] D. Manura and D. Dahl. *SIMION 7.0 User Manual*.

[59] H. A. Synal, M. Stocker, and M. Suter. MICADAS: A new compact radiocarbon AMS system. *Nuclear Instruments and Methods in Physics Research, Section B: Beam Interactions with Materials and Atoms*, 259(1):7–13, 2007.

[60] Kr. E. Stenström, G. Skog, E. Georgiadou, J. Genberg, and A. Johansson. A guide to radiocarbon units and calculations. *Lund University, Department of Physics, Division of Nuclear Physics Internal Report*, 2011.

[61] J Rethemeyer, M Gierga, S Heinze, A Stolz, A Wotte, P Wischhöfer, S Berg, JO Melchert, and A Dewald. Current Sample Preparation and Analytical Capabilities of the Radiocarbon Laboratory at CologneAMS. *Radiocarbon*, 61(5):1449–1460, 2019.

[62] W. G. Mook and J. Van Der Plicht. Reporting ^{14}C activities and concentrations. *Radiocarbon*, 41(3):227–239, 1999.

[63] M. Le Clercq, J. van der Pflicht , and M. Gröning. New ^{14}C Reference Materials with activities of 15 an 50 pmC. *Radiocarbon , Volume 40 , Issue 1: 16th International Radiocarbon Conference*, 40(1):295–297, 1998.

[64] W. Kutschera. The Half-Life of 14 C-Why Is It So Long? . *Radiocarbon*, 61(5):1135–1142, 2019.

[65] D. R. Lide. *CRC Handbook of Chemistry and Physics*, volume 84. CRC Press, 2003.

[66] A. Steinhof. Chapter 8: Accelerator Mass Spectrometry of Radiocarbon. In *Radiocarbon and Climate Change: Mechanisms, Applications and Laboratory Techniques*, pages 253–278. Springer, 2016.

[67] FAST ComTec GmbH. *Multiparameter Data Acquisition System-User Manual*, 2014.

[68] M. Paul. Separation of isobars with a gas-filled magnet. *Nuclear Instruments and Methods in Physics Research Section B: Beam Interactions with Materials and Atoms*, 52(3-4):315–321, 1990.

[69] Michael Paul, Bruce G. Glagola, Waiter Henning, Jorg G Keller, Waiter Kutschera, Zenhao Liu, Karl Ernst Rehm, Bernhard Schneck, and Rolf H Siemssen. Heavy ion separation with a gas-filled magnetic spectrograph. 277, 1989.

[70] K. E. Gregorich. Simulation of recoil trajectories in gas-filled magnetic separators. *Nuclear Instruments and Methods in Physics Research, Section A: Accelerators, Spectrometers, Detectors and Associated Equipment*, 711:47–59, 2013.

[71] B. Franzke, N. Angert, and Ch. Schmelzer. Charge exchange of fast iodine ions in a dense jet of carbon dioxide. *IEEE Transactions on Nuclear Science*, 19(2):266–271, 1972.

[72] V. P. Shevelko. One-electron capture in collisions of fast ions with atoms. 287:19–26, 1978.

[73] F. Hinterberger. Physik der Teilchenbeschleuniger und Ionenoptik. *Physik der Teilchenbeschleuniger und Ionenoptik*, 1997.

[74] A. Wallner, J. Feige, L. K. Fifield, M. B. Froehlich, R. Golser, M. A.C. Hotchkis, D. Koll, G. Leckenby, M. Martschini, S. Merchel, S. Panjkov, S. Pavetich, G. Rugel, and S. G. Tims. 60Fe deposition during the late Pleistocene and the Holocene echoes past supernova activity. *Proceedings of the National Academy of Sciences of the United States of America*, 117(36):21873–21879, 2020.

[75] J. Feige. The connection between the local bubble and the ^{60}Fe anomaly in the deep sea hydrogenetic ferromanganese crust. Magisterarbeit, University of Vienna, 2010.

[76] M. Limongi and A. Chieffi. Nucleosynthesis of 60Fe in massive stars. *New Astronomy Reviews*, 50(7-8):474–476, 2006.

[77] J. Ellis, B. D. Fields, and D. N. Schramm. Geological Isotope Anomalies as Signatures of Nearby Supernovae. *The Astrophysical Journal*, 470:1227, 1996.

[78] T. Athanassiadou and B.D. Fields. Penetration of nearby supernova dust in the inner solar system. *New Astronomy*, 16(4):229–241, 2011.

[79] K. Knie, G. Korschinek, T. Faestermann, C. Wallner, J. Scholten, and W. Hillebrandt. Indication for Supernova Produced ^{60}Fe Activity on Earth. *Physical Review Letters*, 83(1):18–21, 1999.

[80] K. Knie, G. Korschinek, T. Faestermann, E. A. Dorfi, G. Rugel, and A. Wallner. ^{60}Fe anomaly in a deep-sea manganese crust and implications for a nearby supernova source. *Physical Review Letters*, 93(17):1–4, 2004.

[81] C. Fitoussi, G. M. Raisbeck, K. Knie, G. Korschinek, T. Faestermann, S. Goriely, D. Lunney, M. Poutivtsev, G. Rugel, C. Waelbroeck, and A. Wallner. Search for supernova-produced ^{60}Fe in a marine sediment. *Physical Review Letters*, 101(12):121101, 2008.

[82] D. Koll, G. Korschinek, T. Faestermann, J.M. Gómez-Gumán, S. Kipfstuhl, S. Merchel, and J. M Welch. Interstellar 60 Fe in Antarctica. *Physical Review Letters*, 123(7):72701, 2019.

[83] K. Knie, S. Merchel, G. Korschinek, T. Faestermann, U. Herpers, M. Gloris, and Michel R. Accelerator mass spectrometry measurements and model calculations of iron-60 production rates in meteorites. *Meteorites & Planetary Science*, 34:729–734, 1999.

[84] T. Smith, D. L. Cook, S. Merchel, G. Pavetich, S.and Rugel, A. Scharf, and I. Leya. The constancy of galactic cosmic rays as recorded by cosmogenic nuclides in iron meteorites. *Meteoritics and Planetary Science*, 54(12):2951–2976, 2019.

[85] Dorothea Schumann and Jörg Neuhausen. Accelerator waste as a source for exotic radionuclides. *Journal of Physics G: Nuclear and Particle Physics*, 35(1), 2008.

[86] M. Zhang, Y.and He, F. Wang, Q. Zhao, J. Liu, S. Wu, K. Li, Q. You, K. Dong, and S. Jiang. Developing the measurement of 60Fe with AMS at CIAE. *Nuclear Instruments and Methods in Physics Research Section B: Beam Interactions with Materials and Atoms*, 2018.

[87] Brookhaven National Laboratory National Nuclear Data Center. Nudat (nuclear structure and decay data). open source.

[88] P. W. E. Gartenmann. *Untersuchung von anthropogenem ^{60}Fe und anderen mittelschweren Radionukliden mit Beschleunigermassenspektrometrie.* PhD thesis, ETH Zürich, 1999.

[89] M. Martschini, L. K. Fifield, M. B. Froehlich, G. Leckenby, S. Pavetich, S.G. Tims, B. Tranter, and A. Wallner. New and upgraded ionization chambers for AMS at the Australian National University. *Nuclear Instruments and Methods in Physics Research Section B: Beam Interactions with Materials and Atoms*, 438:141–147, 2019.

[90] S. Lee, R. Corliss, I. Friščić, R. Alarcon, S. Aulenbacher, J. Balewski, S. Benson, J. C. Bernauer, J. Bessuille, J. Boyce, J. Coleman, D. Douglas, C. S. Epstein, P. Fisher, S. Frierson, M. Garçon, J. Grames, D. Hasell, C. Hernandez-Garcia, E. Ihloff, R. Johnston, K. Jordan, R. Kazimi, J. Kelsey, M. Kohl, A. Liyanage, M. McCaughan, R. G. Milner, P. Moran, J. Nazeer, D. Palumbo, M. Poelker, G. Randall, S. G. Steadman, C. Tennant, C. Tschalär, C. Vidal, C. Vogel, Y. Wang, and S. Zhang. Design and operation of a windowless gas target internal to a solenoidal magnet for use with a megawatt electron beam. *Nuclear Instruments and Methods in Physics Research, Section A: Accelerators, Spectrometers, Detectors and Associated Equipment*, 939(March):46–54, 2019.

Danksagung

Prof. Dr. Alfred Dewald danke ich für die Betretung meiner Arbeit und die mir gegebenen Möglichkeiten jederzeit selbstständig meine Ziele und Interessen verfolgen zu können. Ich danke ihm für sein unschätzbares, umfassendes Wissen zur Beschleunigerphysik und dass er mich gelehrt hat die Dinge grundlegend zu hinterfragen und wirklich verstehen zu wollen.

Prof. Dr. Andreas Zilges danke ich für seine Bereitschaft, diese Arbeit als Prüfer zu bewerten.

Prof. Dr. Tibor Dunai danke ich für den Vorsitz der Prüfungskommission.

Dr. Markus Schiffer danke ich für seine immer währende Unterstützung und Richtungsweisung in meiner wissenschaftlichen Arbeit, in der er mir mit seinem großen, wissenschaftlichen Talent als Vorbild dient. Ich danke ihm für die unzähligen großen und kleinen Gespräche und Diskussionen, die mich maßgeblich vorangetrieben haben und ohne diese ich nicht so weit gekommen wäre, wie ich bin. Du wirst in mir immer eine Verbündete und Freundin haben.

Gereon Hackenberg danke ich für die zahllosen gemeinsamen Stunden bei Experimenten, in denen nur das gemeinsame Arbeiten und Lachen die langen Tage und Nächte erträglich und erfolgreiche Ergebnisse möglich machten. Ich danke ihm für seine guten Ideen, sein handwerkliches Geschick und unsere gute Kompatibilität im gemeinsamen Arbeiten. Einen Kollegen und Freund wie dich kann man sich nur wünschen.

Dr. Richard Spanier danke ich dafür, dass er nie müde wurde mir die technischen Grundlagen der AMS und Beschleunigerphysik beizubringen. Ich danke ihm für die vielen, schönen gemeinsamen Jahre im Büro, in der Lehre, auf Dienstreisen und vor allem im Tiefkeller.

Dr. Stefan Heinze danke ich für die vielen interessanten Gespräche, die mir bei physikalischen Problemen, aber auch in meiner persönlichen Entwicklung, immer wieder neue Perspektiven gezeigt haben.

Dr. Alexander Stolz danke ich für seine gute Laune und seinen Enthusiasmus zur wissenschaftlichen Arbeit, mit der er die Gruppenatmosphäre bereicherte. Ich danke ihm, dass ich von ihm Lernen konnte, dass manchmal eine entspannte, unbesorgtere Einstellung der Schlüssel zum Erfolg ist.

Dr. Claus Müller-Gatermann danke ich für ein stetig offenes Ohr und seine immer währenden Bemühungen dem Institut und bei Bedarf auch mir mit Rat und Tat zur Seite zu stehen.

Alle ehemaligen und aktuellen Mitglieder der AMS-Gruppe danke ich dafür, dass sie meiner Arbeit den Weg bereitet haben und unsere Gruppe weiterbrachten.

Dem Kölner Beschleuniger-Operateursteam, Frank Bielau, Otto Rudolph, Sebastian Brünsing, und Viktor Rehl, und dem ehemaligen Operateur Albert Wedel danke ich dafür, dass sie mir bei kleinen und großen Problemen oft tatkräftig zur Seite standen.

Stefan Thiel und den Mitarbeitern der Feinmechanik-Werkstatt danke ich für die vielen kleinen und größeren hergestellten Bauteile, ohne die der Aufbau nie hätte verbessert werden können. Ich habe immer ein offenes, interessiertes Ohr, Enthusiasmus für die Entwicklungen und schnelle Hilfe, wenn diese nötig war, gefunden.

Christoph Görgen und den Mitarbeiten der Elektronik-Werkstatt, insbesondere Guido Richardt, danke ich, dass ich immer Rat und sorgfältige Beratung bekommen habe, sodass die bereitgestellte Lösung und die angefertigten Elektroniken genau auf die Lösung meiner Probleme zugeschnitten waren.

Besonderer Dank:

Ein besonderer Dank geht an meine Familie, besonders an meine Mutter Johanna Herb und meinen Vater Wilfried Herb, die mich zu jeder Zeit bedingungslos in jeglicher Hinsicht unterstützt haben und immer an mich geglaubt haben. Ich danke meinem Bruder Marc Herb, der mir das Leben als Wissenschaftler vorgelebt hat und der mit seiner Leidenschaft für diese eine große Inspiration für mich ist. Ich danke meiner Cousine Sabine Derichsweiler und danke in liebevoller Erinnerung meiner Tante Helga Derichsweiler, die mir zusätzlich zu meiner Mutter, als starke Frauenrollen in meinem Leben gezeigt haben, dass mir keine Grenzen gesetzt sind.
Einen ganz besonderen Dank, wenn nicht sogar den Größten, möchte ich an meinen Partner Michael Weinert richten, der trotz einer großen Reihe an Einbußen in unserer gemeinsamen Zeit mir immer zur Seite stand. Ich danke ihm, dass er mir tagtäglich den Rücken freigehalten hat um mir mein Arbeitspensum zu ermöglichen und dass er mich in den schwierigsten Zeiten aufgefangen und wieder aufgebaut hat.

Eidesstattliche Erklärung

Ich versichere, dass ich die von mir vorgelegte Dissertation selbständig angefertigt, die benutzten Quellen und Hilfsmittel vollständig angegeben und die Stellen der Arbeit - einschließlich Tabellen, Karten und Abbildungen -, die anderen Werken im Wortlaut oder dem Sinn nach entnommen sind, in jedem Einzelfall als Entlehnung kenntlich gemacht habe; dass diese Dissertation noch keiner anderen Fakultät oder Universität zur Prüfung vorgelegen hat; dass sie - abgesehen von unten angegebenen Teilpublikationen - noch nicht veröffentlicht worden ist, sowie, dass ich eine solche Veröffentlichung vor Abschluss des Promotionsverfahrens nicht vornehmen werde. Die Bestimmungen der Promotionsordnung sind mir bekannt. Die von mir vorgelegte Dissertation ist von apl. Prof. Dr. Alfred Dewald betreut worden.

Teilpublikationen

S. Herb, M. Schiffer, R. Spanier , S. Heinze, A. Stolz, L. Bussmann, G. Hackenberg, D. Schumann, N. Kivel, A. Dewald.
First AMS measurements of ^{60}Fe/Fe isotopic ratios at the Cologne 10 MV tandem accelerator
Nuclear Instruments and Methods in Physics Research, Section B: Beam Interactions with Materials and Atoms, **461**. (2019).

04.01.2023, Köln
Datum, Ort

(Susan Herb)